University of Trento
Department of Physics

Thesis
Submitted to the
Doctoral School in Physics
by

Riccardo Franchi

In candidature for the degree of
Philosophiae Doctor - Dottore di ricerca

The taiji and infinity-loop microresonators: examples of non-hermitian photonic systems

Supervisor: Prof. Lorenzo Pavesi

35°PhD cycle

June 1, 2023

Supervisor:
Prof. Lorenzo Pavesi

Co-Supervisors:
Dr. Stefano Biasi
Dr. Mher Ghulinyan

Members of the committee:
Prof. Stefan Rotter - Vienna University of Technology
Prof. Vittorio M.N. Passaro - Politecnico di Bari
Dr. Alessandro Roggero - University of Trento

Acknowledgements

I cannot start without expressing my gratitude to my supervisor, Prof. Lorenzo Pavesi, for guiding me through these years, but at the same time allowing me the freedom to follow freely my passion for scientific research. Thanks to your advice, I have grown and become more scientifically mature.

A big thank you goes to Stefano Biasi, with whom I have established a wonderful collaboration. In fact, in the last few years we have been discussing physics almost every day. Thanks to you I have learned so much and I hope that our friendship can last. You are a talented researcher and I hope you will have the opportunity to achieve all your goals.

I am also grateful to have worked with Mher Ghulinyan, Iacopo Carusotto, Claudio Castellan, Alberto Muñoz de las Heras, Filippo Mione, Diego Piciocchi, Davide Bazzanella, Lorenzo Cerini, Marco Peretti and Martino Bernard. With you I have had interesting scientific discussions and shared many hours in the laboratory.

I also thank all the past and present members of the *Nanoscience Laboratory* research group, the *SPIE Student Chapter* of the University of Trento, the *Sensors and Devices* group of the FBK and the *Experimental Gravitation* group. I have shared many good moments with you, scientific and otherwise. Having lunch together, if possible in the garden, has always been an important part of the day. I would especially like to thank Davide Bazzanella, Matteo Sanna, Giovanni Donati, Clara Zaccaria, Gioele Piccoli, Nicolò Leone, Alessio Baldazzi and Michele Valentini for the good times we spent together.

Thanks also to the laboratory technician Enrico Moser and to all the staff of the electronic and mechanical workshop, who helped me to realize some components of the experimental setup.

Special thanks to my climbing friends: Davide Bazzanella, Jacopo Rossi, Marco

Tomasi, Federica Falagiarda, Vittorio Chiavegato, Stefano Biasi, Paolo Bettotti, Chiara Piotto, ... Thanks for all the fun and good times together!!!

The next lines are in Italian and are addressed to my family.
Un ringraziamento molto sentito a tutta la mia famiglia per avermi supportato, ma soprattutto sopportato in questi anni e principalmente in questo ultimo periodo. Tengo a nominarvi tutti perché, almeno per ora, siete le persone più importanti della mia vita: mamma Carla, papà Marco, Matteo, Maurizio, Fulvia, nonna Emma e per ultimo, solo per la sua giovane età, il mio nipotino Andrea.
Vi voglio tanto bene!!!

Riccardo Franchi

Abstract

This thesis theoretically and experimentally studies the characteristics of integrated microresonators (MRs) built by passive (no gain) and non-magnetic materials and characterized by both Hermitian and non-Hermitian Hamiltonians. In particular, I have studied three different microresonators: a typical Microring Resonator (MR), a Taiji Microresonator (TJMR), which consists of a microresonator with an embedded S-shaped waveguide, and a new geometry called the Infinity-Loop Microresonator (ILMR), which is characterized by a microresonator shaped like the infinity symbol coupled at two points to the bus waveguide.

To get an accurate picture of the three devices, they were modeled using both the transfer matrix method and the temporal coupled mode theory. Neglecting propagation losses, the MR is described by a Hermitian Hamiltonian, while the TJMR and the ILMR are described by a non-Hermitian one. An important difference between Hermitian and non-Hermitian systems concerns their degeneracies. Hermitian degeneracies are called Diabolic Points (DPs) and are characterized by coincident eigenvalues and mutually orthogonal eigenvectors. In contrast, non-Hermitian degeneracies are called Exceptional Points (EPs). At the EP, both the eigenvalues and the eigenvectors coalesce. The MR is at a DP instead, and the TJMR and the ILMR are at an EP. Since the TJMR and ILMR are at an EP, they have interesting features such as the possibility of being unidirectional reflectors. Here, it is shown experimentally how in the case of the TJMR this degeneracy can also be used to break Lorentz reciprocity in the nonlinear regime (high incident laser powers), discussing the effect of the Fabry-Perot of the bus waveguide facets.

The effect of backscattering, mainly due to the waveguide surface-wall roughness, on the microresonators is also studied. This phenomenon induces simultaneous excitation of the clockwise and counterclockwise modes, leading to eigenvalue splitting. This splitting makes the use of typical quality factor estimation methods unfeasible. To overcome this problem and mitigate the negative effects of backscattering, a new experimental technique called interferometric excitation is introduced. This technique involves coherent excitation of the microresonator from both sides of the bus waveguide, allowing selective excitation of a single supermode. By adjusting the relative phase and amplitude between the excitation fields, the splitting in the transmission spectrum can be eliminated, resulting in improved quality factors and eigenvalue measurements. It is shown that this interferometric technique can be exploited under both stationary and dynamic conditions of time evolution.

The thesis also investigates the sensing performance of the three microresonators as a function of a backscattering perturbation, which could be caused, for example, by the presence of a molecule or particle near the microresonator waveguide. It is shown that the ILMR has better performance in terms of responsivity and sensitivity than the other two microresonators. In fact, it has both the enhanced sensitivity due to the square root dependence of the splitting on the perturbation (characteristic of EPs) and the ability to completely eliminate the region of insensitivity as the backscattering perturbation approaches zero, which is present in both the other two microresonators.

To validate the models used, they were compared with experimental measurements both in the linear regime and, for TJMR, also in the nonlinear regime, with excellent agreement.

Contents

Acronyms

InGaAs indium gallium arsenide. 61

SiON silicon oxynitride. 90, 92, 93, 97, 100

SiO$_2$ silica. 6, 7, 62, 97, 118, 119, 154, 166, 190

SiO$_x$ silicon oxide. 97

Si silicon. 6, 62, 97, 116, 154, 155, 175, 190

2D two-dimensional. 169

3D three-dimensional. 51–53, 55, 57, 126

ALPI ERC-PoC ALPI Project. 188

AS Alignment Stage. 60, 61, 95, 96

BACKUP BACKUP project: Unveiling the relationship between brain connectivity and function by integrated photonics. 185, 188

BPSG borophosphosilicate. 97

BS backscattering. 8–10, 12, 20, 24–36, 39–41, 43, 45, 48, 50, 52, 53, 55, 56, 58, 59, 64, 66–68, 70, 77, 78, 116–123, 125, 126, 131, 133, 135, 137, 141–145, 152, 153, 157–160, 166, 171, 175–177, 187, 188

BWG bus waveguide. 7

C *constructive*-like. 98–103, 107, 108, 110, 112–114

CCW counterclockwise. 7, 19, 21, 25–27, 29, 30, 35–37, 49, 54, 56, 78–80, 93–95, 100, 102, 104, 105, 107–109, 111, 117, 118, 134, 159, 167, 169, 176

CMOS Complementary Metal-Oxide Semiconductor. 6

CMT Coupled Mode Theory. 190, 191

CPA Coherent Perfect Absorption. 147–150, 164, 177

CR crossing. 6

CRD Cavity Ring-Down. 48, 54, 56

CROW coupled resonators optical waveguides. 186, 187

CW clockwise. 7, 19, 21, 25–27, 29, 30, 35–37, 52, 54, 56, 78–80, 93, 95, 100, 104, 105, 107–109, 111, 117, 118, 134, 159, 167, 169, 176

CWTL Continuous Wave Tunable Laser. 60, 62, 71, 95, 96

D *destructive*-like. 99, 100, 102, 103, 107, 108, 110, 112–114

DL Delay Line. 60, 61

DP Diabolic Point. 5, 7, 8, 11, 21, 31, 32, 123, 124, 161, 176, 177

EDFA Erbium Doped Fiber Amplifier. 95, 96

EF Enhancement Factor. 18, 23, 24, 94, 102, 112, 139–141

EP Exceptional Point. 5–10, 77–79, 116, 123–126, 128, 133, 135–137, 139, 143–145, 147, 150, 158, 161, 163, 164, 166, 176–178, 187

ER Extinction Ratio. 17, 18, 23, 24, 27, 29, 120

F *Fano*-like. 98, 99, 102, 103, 107, 108, 110, 112–114

FCA Free Carrier Absorption. 93

FCD Free Carrier Dispersion. 93

FP Fabry-Pérot. 9, 62, 63, 77, 82, 89–91, 94, 98, 100, 102, 104, 106–113, 115, 116

FPC Fiber Polarization Controller. 60, 61, 95, 96

FPO Fabry-Pérot Oscillation. 89–91

FS Fiber Splitter. 60

FSR Free Spectral Range. 17–19, 22, 35, 91, 98

FWHM Full Width at Half Maximum. 17, 18, 22, 23, 36, 39–41, 45, 48, 59, 63, 64, 70, 75, 81, 128, 176

GND ground. 188, 190

GRT grating. 6

ILMR Infinity-Loop Microresonator. 7–10, 133–151, 153–166, 175, 177, 178, 185–187

IRC Infrared Camera. 60, 62

laser light amplification by stimulated emission of radiation. 60, 77, 92, 95

MMI Multi-Mode Interferometer. 6, 71

MR Microresonator. 6–25, 27–34, 36, 40–59, 62–70, 72–75, 77–79, 81, 84, 88, 93, 94, 105, 106, 116, 119, 120, 122, 123, 125, 126, 128, 134, 136, 141, 151, 159–178, 187, 188, 193

MZI Mach Zhender Interferometer. 71, 187

OC Optical Circulator. 60, 61, 95, 96, 194

OI Optical Isolator. 60, 95, 96

PC Personal Computer. 60–62, 95

PD photodetector. 60–62, 95, 96, 193, 194

PECVD Plasma-Enhanced Chemical Vapor Deposition. 97

PELM Photonic Extreme Learning Machine. 185, 186, 188

PicoScope PC Oscilloscope. 60, 62

PID Proportional–Integral–Derivative controller. 60, 61

PSWO particle swarm optimization. 120

Q Quality Factor. 8, 9, 18, 19, 23, 24, 30, 39, 40, 45, 48, 50, 54, 56, 58, 59, 63, 64, 66, 68, 70, 75, 78, 81, 116, 119–123, 128, 141, 166, 175, 176, 178

SCISSOR side-coupled integrated sequences of resonators. 186, 187

SOI Silicon-on-Insulator. 62

TC Temperature Controller. 60

TCMT Temporal Coupled Mode Theory. 7, 9, 19, 25, 35, 37, 48, 67, 69, 77, 78, 82, 85, 116, 123, 133, 135, 141, 150, 152, 154, 156, 157, 171, 175, 176

TE Tranverse Electric. 61, 62, 119

TJMR Taiji Microresonator. 7–10, 77–79, 81–87, 89–102, 104–131, 133–137, 141, 142, 151, 159–178, 185–187

TM Tranverse Magnetic. 97

TMM Transfer Matrix Method. 7, 9, 12, 19, 22, 23, 33, 35, 77, 82, 85, 86, 91, 104, 105, 133, 150, 152, 154, 157, 171, 175, 191

TO Thermo Optic. 8, 104, 105

TOE Thermo Optic Effect. 93, 94, 100

TPA Two Photon Absorption. 93

VOA Variable Optical Attenuator. 60–62, 193, 194

WG waveguide. 6–8, 10, 12–14, 17, 24, 25, 30, 34, 49, 61–66, 68, 77–79, 81–84, 90–95, 97, 104–107, 111, 116, 118–120, 122, 124, 127, 133, 134, 139, 141, 143, 151, 152, 154, 155, 170–172, 175–178, 187, 190, 191

Introduction

Classical and quantum systems are usually described by Hermitian and non-Hermitian Hamiltonians. Hermitian Hamiltonians describe isolated systems, characterized by energy conservation. The Hermiticity of these systems ensures the presence of only real-valued energy eigenvalues. Unlike Hermitian systems, the non-Hermitian ones are open systems and therefore exhibit loss and/or gain. They do not conserve energy and can therefore exhibit interesting asymmetric couplings between the levels of the system. In general, the eigenvalues of these systems are complex, i.e. they have an imaginary part (corresponding to losses and gains) that is not zero. In 1998 Bender and Boettcher show in [1, 2] that even non-Hermitian systems can have only real eigenvalues if the Hamiltonian satisfies the parity time symmetry (PT-symmetry). In these special cases, the system is not isolated, the modes of the system exchange their energy, and the losses are perfectly balanced by the presence of gains. Although PT-symmetric systems are not isolated, they are in equilibrium and their energy levels are real as in a Hermitian system [1, 2]. This has led to a great interest in the study of these special non-Hermitian systems [2, 3, 4, 5]. These systems have been studied in different areas such as in optics [6, 7, 8, 9, 10, 11, 12, 13, 14, 15, 16, 17, 18, 19, 20], in microwave cavities [21, 22], superconductivity [23, 24], atomic diffusion [25], electronic circuits [26, 27], mechanical systems [28] and graphene [29, 30].

Another important difference between Hermitian and non-Hermitian systems concerns their degeneracies. Hermitian degeneracies are called Diabolic Points (DPs) and are characterized by coincident eigenvalues and mutually orthogonal eigenvectors [4]. In contrast, non-Hermitian degeneracies are called Exceptional Points (EPs). At the EP both the eigenvalues and the eigenvectors coalesce [4, 31, 32, 3]. Both DPs and EPs have been studied in many different physical systems.

In particular, the coalescence of the eigenstates present at an EP has been studied in several fields, such as in optics [33, 34, 35, 36, 37, 38, 6, 39], in the microwave Physics [40, 41], in atom-cavity systems [42], and in acoustic systems [43]. In addition, the EP can be used for different applications or devices, such as enhanced sensors [35, 44, 45, 46, 32, 47, 48, 49, 50], unidirectional reflectors (unidirectional invisibility) [11, 51, 34, 52, 14], chiral transmission [53, 54, 55, 56, 57, 58], loss-induced transparency [6], lasers (unidirectional lasers, chiral lasers, single-mode lasers, PT-lasers, loss-induced suppression and revival of lasing, laser line width broadening) [55, 59, 36, 60, 61, 55, 62, 20, 63, 64, 65, 66, 67, 68], topological devices (topological lasers, topological energy transfer) [69, 70, 71], EP-based gyroscopes [72, 73, 74, 75], asymmetric mode switching devices [76, 41], and non-reciprocal optical components which show a violation of the Lorentz reciprocity theorem (unidirectional transmission devices) [39, 77, 78, 79, 80].

A powerful platform for studying Hermitian and non-Hermitian physics is integrated photonics, because of its miniaturization and the ability to have loss and gain. Integrated photonics is based on waveguides (WGs) of a material with a high refractive index, we used silicon (Si) with a cross section of 450 nm × 220 nm, surrounded by a material with a low refractive index, such as silica (SiO_2). The waveguides, as the name suggests, guide light and are used to construct the basic components of integrated optical circuits. Light, as an electromagnetic field, is not completely confined within the core of the WG. The field in the WG cladding is called the evanescent field and is used to exchange optical power from one WG to a nearby WG, i.e. to couple WGs. WGs are arranged in several geometries: the Microresonator (MR, composed of a closed WG coupled to a bus waveguide) [81, 82], the Multi-Mode Interferometer (MMI) [83], the WGs coupler, the Wavelength-Division Multiplexing (WDM) device [84], the crossing (CR) [85, 86, 87, 88] and the grating (GRT) [89, 90, 91]. These structures can be implemented in regions of the order of 500 μm^2. Consequently, using photonic chip fabrication techniques, such as Complementary Metal-Oxide Semiconductor (CMOS) technology, one can fabricate miniaturized structures that are very stable and facilitate the experimental characterization of Hermitian and non-Hermitian phenomena.

Light propagation in the integrated WGs is subject to power losses that make the system a characteristic non-Hermitian system. In fact, the study of many phenomena characteristic of EPs and many of the devices listed above use integrated optics and optics in general. By appropriately engineering the integrated structures, losses can be reduced or controlled through the use of the evanescent field coupling between different WGs. An example of a tailored made non-Hermitian system in a fully integrated device is the Taiji Microresonator (TJMR) [52, 36]. The TJMR consists of a microresonator with an embedded S-shaped WG which induces a unidirectional coupling between the microresonator counter-propagating modes (the clockwise and the counterclockwise ones), see Fig. 1 (b). Other optical non-Hermitian systems described in the literature are for example the SiO_2 micro-toroid cavity with two silica nano-tips [35], two microresonators coupled together and with two bus waveguides (BWGs) [92], a microresonator coupled to a waveguide with at one end a symmetric reflector [57, 48, 49]. By using these devices, the physics of EPs can be studied.

My thesis aims to study integrated Microresonators (MRs) characterized by both a Hermitian and a non-Hermitian Hamiltonian, built by passive (no gain) and non-magnetic materials. In particular, I studied three different microresonators: the microring resonator (MR), the TJMR [52] and a new geometry called Infinity-Loop Microresonator (ILMR) [93], see Fig. 1.

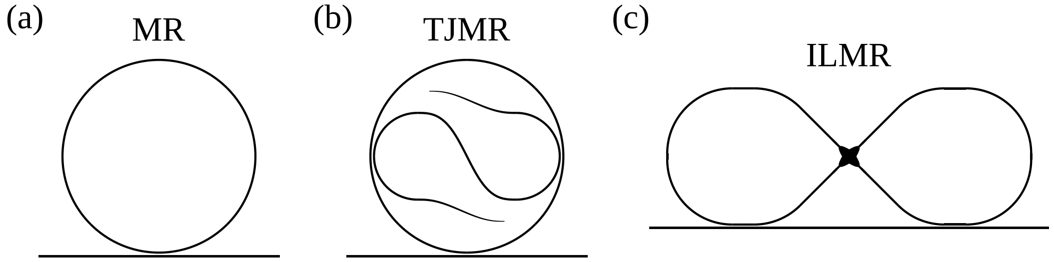

Figure 1: Sketch of a microring resonator (MR) (a), a Taiji Microresonator (TJMR) (d), and a Infinity-Loop Microresonator (ILMR) (c). In all three microresonators, the field within them is coupled via a bus waveguide (straight line in the three panels).

The three MRs are modeled with a Transfer Matrix Method (TMM) and a Temporal Coupled Mode Theory (TCMT). In the TCMT, a MR is described as a two-level system. These correspond to its two counterpropagating modes, the clockwise (CW) and the counterclockwise (CCW) ones. Through the TCMT, we derive the Hamiltonian of the system. Neglecting propagation losses, this turns out to be Hermitian for the MR, while it is non-Hermitian for the TJMR and the ILMR. Therefore, the MR is at a DP, while the TJMR and ILMR are at an EP. Since the TJMR and the ILMR are at an EP, they have interesting features such as the possibility of being unidirectional reflectors and the possibility of breaking Lorentz reciprocity when used in the nonlinear (high power) regime.

These MRs are also studied when perturbed by Hermitian and non-Hermitian backscattering (BS). Indeed, the MRs integrated with a high quality factor (in silicon $Q > 50,000$ [47]) show a non-negligible coupling between the two counterpropagating modes caused by the BS. The BS is mainly due to the roughness of the lateral surfaces of the WGs. Other causes of BS are the coupling regions between the WGs or the presence of molecules/particles near the core of the WGs [94, 95, 47, 48, 96, 97, 35, 98, 99, 100, 101, 102, 103]. The BS causes a splitting of the eigenvalues of the system, which leads to a splitting of the resonance. In this work, the behavior of the three MRs is studied as a function of the BS strength. This last can also be considered as a perturbation to the ideal MR, thus the MR can be also studied as a sensor. In particular, the three devices are compared and a linear dependence of the eigenvalue splitting as a function of the perturbation near the DP and a square root dependence near the EP (enhanced sensitivity) [35, 47] are reported.

The BS splitting resonance reduces the Quality Factor (Q) of the resonator. In this work we see how to solve this problem using interferometric excitation [102, 103]. We call interferometric excitation a new technique that involves a simultaneous coherent excitation of the MR from both sides of a bus waveguide. With interferometric excitation, by varying the relative phase between the two excitation fields, a single supermode of the system relative to one of the two eigenvalues can be excited. In this way, in the transmission, one no longer observes a splitting, but a single Lorentzian dip corresponding to one of the two eigenvalues. Using this technique it is then possible to increase the Q of the MR and measure directly the eigenvalues of the system from the spectrum. We also see that this technique is valid not only for the steady-state spectral response, but also for the temporal response.

The TJMR is studied theoretically and experimentally in the linear regime (low power), but also in the nonlinear regime (high power), where the Thermo Optic (TO) effect becomes relevant. In this case, an increase in the optical intensity inside the microresonator is followed by an increase in its temperature and, consequently, in its refractive index. The increase in the refractive index causes a redshift of the resonant frequency. A Hermitian MR being symmetrical, has always a transmission response independent of the microresonator excitation direction. On the other hand, the TJMR is a non-Hermitian chiral structure characterized by an asymmetrical coupling between the two counterpropagating modes. Therefore, it has different transmissions depending on the excitation direction. This means that the TJMR in the nonlinear regime can break the Lorentz reciprocity theorem [77, 78].

The study of the ILMR, which consists of an infinity-shaped closed WG coupled with a bus waveguide [see Fig. 1 (c)], is also reported. Due to its peculiar geometry, the coupling occurs at two points that correspond to the two infinity-shaped microresonator lobes. This causes particular Riemann sheets [41, 3, 104, 4, 105, 106]. In particular, the Riemann surfaces given by the eigenvalues of the system as well as those obtained from the transmission and reflection spectra are presented. We compute the sensitivity of a ILMR used as a sensor and compare it with those of a MR and a TJMR.

My thesis is organized as follows.

Chapter 1 studies the spectral and temporal responses of an ideal and non-ideal MR, that is characterized by a Hermitian or non-Hermitian BS. The system is modeled with the TMM and the TCMT. The behavior of the MR as a function of a Hermitian backscattering perturbation is presented in order to study the sensitivity near a diabolic point. A new method to excite individually the supermodes of the system, named the interferometric excitation [102, 103], is also presented. Here we study the spectral response in both the steady state and transient (time response) regimes. Finally, experimental measurements are reported to verify experimentally the theoretical models.

Chapter 2 introduces the TJMR by using the formalism introduced in the previous chapter. It is demonstrated that it works at an Exceptional Point (EP), is a unidirectional reflector, and that in the nonlinear (high power) regime it breaks the Lorentz reciprocity by showing different transmissions depending on the excitation direction. This chapter also includes in the model the Fabry-Pérot (FP) cavity [107] created by reflections from the ends of the bus waveguide. It is then studied how the interaction between the FP cavity and the TJMR modifies the main properties of the TJMR (unidirectional reflection, non-reciprocal transmission) [78]. Then, the backscattering is introduced to study the sensing enhancement of the EP. The influence of the characteristic TJMR parameters such as backscattering coefficient as a function of the TJMR Q-factors is studied [47]. Finally, experimental measurements validating the theoretical analysis are reported.

Chapter 3 analyzes a new integrated structure at an EP, the ILMR [93]. Here the ILMR is modeled with both the TCMT and the TMM. Spectral responses of different ILMRs, geometrically symmetric or asymmetric, are reported, showing that the ILMR can exhibit completely different reflections (unidirectional reflection, like the TJMR) or identical reflections, remaining at an EP. In addition, the Riemann sheets of the ILMR and its efficiency in sensing BS perturbations are studied.

Chapter 4 discusses the main differences between the three analyzed structures (the MR, the TJMR, and the ILMR). In particular, the greater tunability and efficiency in detecting small BS perturbations of the ILMR compared to the normal MR and the TJMR is highlighted.

Chapter 5 reports a first study of topological matrices of TJMRs. In particular, it presents the structures designed to study topologically protected edge states [108, 109, 69].

The "Conclusions and Perspectives" chapter reports the final considerations and future prospects of this research project.

The "Publications" chapter lists the publications made during my academic career.

Appendix A describes the sample designs in which I participated. It also reports the procedure used to simulate and then design the coupling regions between WGs.

Appendix B describes the experimental procedure used to perform the interferometric excitation measurements.

Chapter 1

Microring Resonator

This chapter describes the microring resonator [82, 96, 110, 111, 112, 81]. It is one of the most important components in integrated optics and is used in various applications. For example, it can be used as a sensor to detect temperature changes [113], to detect the concentration of a contaminant [114, 115, 116, 113, 117, 35], to detect strain [118], to detect magnetic field [119] and to detect acceleration [120]. In addition, it is also used as a tunable photonic element to filter a signal [121], and to address signals of different wavelengths in different waveguides [122].

In Sec. 1.1 its geometry is described and two models are developed that can describe its behavior and, in particular, its spectral responses. After the description of the ideal MR and the explanation of all the characteristic parameters of this type of MR, we move on to the introduction of backscattering (Sec. 1.2). This is a process caused by the presence of surface-wall roughness, which couples the propagating and the counter-propagating waves. Then, the evolution of the eigenvalues of the system around a DP is described.

In Sec. 1.3 a new methodology is described to be able to derive both the real and imaginary parts of the eigenvalues directly from the experimental spectrum. This is useful when the eigenvalues of the MR differ due to backscattering and two dips/peaks appear in the transmission spectra. This technique is called *interferometric excitation* and consists in the simultaneous excitation of the two modes of a MR by the use of two coherent fields having a specific relative phase ($\pm\pi/2$) and a ratio between the input intensities which is related to the coupling coefficients between the two propagating modes.

In Sec. 1.4, in order to have a more complete description of MR, the study of the time response of a MR, first ideal and then non-ideal in the presence of BS, is reported.

Finally, Sec. 1.5 describes the experimental setup used to perform both single-side excitation and interferometric excitation measurements. In addition, experimental measurements on integrated silicon MRs are reported. It is then shown that the models and techniques presented in this section provide an excellent description of the experimental results we measured.

Part of this chapter is derived from [102, 103, 93].

1.1 Design and theoretical model

The standard MRs consists of a closed waveguide (WG) that can be coupled to one or more WGs in such a way that light can be fed into and extracted from it. There are a variety of MR geometries, but the most common ones are the ring-shaped or racetrack-shaped geometries, see Fig. 1.1. These MRs are theoretically equivalent, since the coefficients describing them are the same. Therefore, in the following we will use the most common MR, the microring resonator, as a standard.

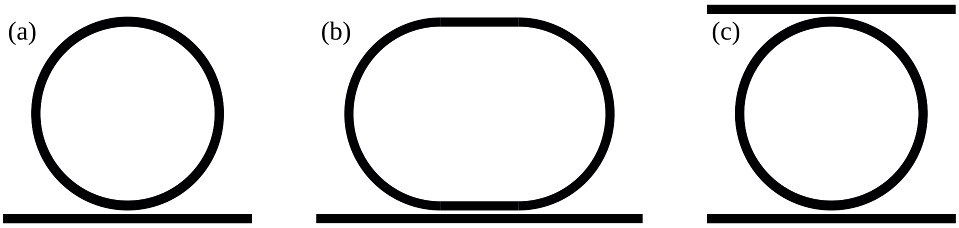

Figure 1.1: Sketches of the microring resonator, (a) and (c), and the racetrack microresonator (b). In (a) and (b) the microresonator is shown in the all-pass configuration, whereas in (c) the microring resonator is represented in the add-and-drop configuration.

Typically, a MR is coupled to one or two WGs. Specifically, if it is coupled to only one bus waveguide then it is in the all-pass configuration, see Fig. 1.1 (a), while if it is coupled to two WGs it is in the add-drop configuration, see Fig. 1.1 (c). The following is a study of a microring resonator in the all-pass configuration, see Fig. 1.1 (a).

1.1.1 Transfer Matrix Method

One way to describe a microring resonator is to use the TMM [107, 82, 81]. The idea behind this method is to write down all the relationships between the fields inside and outside the MR. Then, by solving the system of equations, the fields exiting from the bus waveguide are obtained.

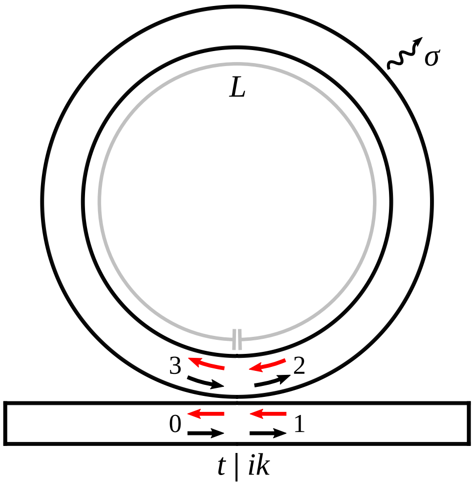

Figure 1.2: Sketches of the microring resonator in the all-pass configuration. The black arrows indicate the E_n fields, where $n = 0, ..., 3$, and their propagation direction. The red arrows instead identify the E_{nr} fields, which have opposite propagation directions. L is the perimeter of the microresonator measured at the center of the waveguide. All parameters are described in the text.

With the help of Fig. 1.2 we write the equations that link the fields in the different sections of the MR:

$$\begin{cases} E_1 = tE_0 + ikE_3 \\ E_2 = tE_3 + ikE_0 \\ E_3 = \sigma e^{i\psi} E_2 \\ E_{0r} = tE_{1r} + ikE_{2r} \\ E_{2r} = \sigma e^{i\psi} E_{3r} \\ E_{3r} = tE_{2r} + ikE_{1r} \end{cases} \tag{1.1}$$

$$\psi := \frac{2\pi}{\lambda} n_{\text{eff}} L\,, \quad \sigma := e^{-\alpha L}\,, \quad L := 2\pi R\,, \tag{1.2}$$

where t and ik are the transmission and coupling coefficients between the bus waveguide and the microring resonator. ψ is the phase acquired by the field as it travels one lap of the MR, λ is the wavelength of the input field, n_{eff} is the effective mode index of the WG, σ^2 is the percentage of intensity remaining after a round trip ($0 \leqslant \sigma \leqslant 1$, related to propagation losses), α is the propagation loss coefficient, L is the perimeter of the MR, and R is its radius. Since the system is passive, t and

k must be between 0 and 1 and must also satisfy the inequality $k^2 + t^2 \leqslant 1$. The imaginary unit in front of the coefficient k is used to account for the phase acquired by the field when it passes from one WG to another.

The field E_n, with $n = 0, ..., 3$, is the field at the black arrow with the number n given in Fig. 1.2. Furthermore, the direction of the arrow corresponds to the propagation direction of the field. Similarly, the field E_{nr} is related to the red colored arrows shown in Fig. 1.2. Therefore, it is possible to excite the system via the E_0 and E_{1r} fields from left and right, respectively. Instead, the output fields are E_1 and E_{0r} from right and left, respectively. To make the following formulas clearer and easier to interpret, we use the following definitions:

$$E_{\text{in,L}} := E_0 \,, \qquad E_{\text{out,R}} := E_1 \,, \tag{1.3}$$

$$E_{\text{out,L}} := E_{0r} \,, \qquad E_{\text{in,R}} := E_{1r} \,. \tag{1.4}$$

Solving the system of equations in Eq. 1.1 yields the following fields:

$$E_{\text{out,R}} = E_{\text{in,L}} \left(t - \frac{k^2 \sigma}{e^{-i\psi} - t\sigma} \right) , \tag{1.5}$$

$$E_{\text{out,L}} = E_{\text{in,R}} \left(t - \frac{k^2 \sigma}{e^{-i\psi} - t\sigma} \right) , \tag{1.6}$$

$$E_2 = E_{\text{in,L}} \frac{ike^{-i\psi}}{e^{-i\psi} - t\sigma} \,. \tag{1.7}$$

Therefore, the scattering matrix ($\mathbf{S}_{\text{MR}}$) of the MR is [107]:

$$\begin{pmatrix} E_{\text{out,L}} \\ E_{\text{out,R}} \end{pmatrix} = \mathbf{S}_{\text{MR}} \begin{pmatrix} E_{\text{in,L}} \\ E_{\text{in,R}} \end{pmatrix} , \tag{1.8}$$

$$\mathbf{S}_{\text{MR}} = \begin{pmatrix} 0 & t - \frac{k^2\sigma}{e^{-i\psi} - t\sigma} \\ t - \frac{k^2\sigma}{e^{-i\psi} - t\sigma} & 0 \end{pmatrix} . \tag{1.9}$$

Since in this ideal model we have neglected any phenomena that could cause backreflection of the electromagnetic field, the MR will show zero reflection. In fact, in Eq. (1.5) we observe that $E_{\text{out,R}}$ depends only on the input field $E_{\text{in,L}}$ and is independent of the field $E_{\text{in,R}}$. Similarly, $E_{\text{out,L}}$ depends only on $E_{\text{in,R}}$, see Eq. (1.6). Moreover, the transmission by exciting the MR from right or left is equal. Therefore, as expected, the Lorentz Reciprocity Theorem is satisfied. These considerations can be deduced directly from the scattering matrix [Eq. (1.9)]; in fact, the elements on the diagonal are zero and those on the antidiagonal are equal.

The intensity transmission T is equal to:

$$T = \frac{|E_{out,R}|^2}{|E_{in,L}|^2} = \frac{|E_{out,L}|^2}{|E_{in,R}|^2} = (k^2 + t^2) - \frac{k^2\left(1 - \left(k^2 + t^2\right)\sigma^2\right)}{1 - 2\sigma t \cos[\psi] + \sigma^2 t^2} \tag{1.10}$$

Assuming zero losses in the coupling ($k^2 + t^2 = 1$), we obtain [82, 81]:

$$T = \frac{t^2 - 2\sigma t \cos[\psi] + \sigma^2}{1 - 2\sigma t \cos[\psi] + \sigma^2 t^2} = 1 - \frac{\left(1 - t^2\right)\left(1 - \sigma^2\right)}{1 - 2\sigma t \cos[\psi] + \sigma^2 t^2}\,, \tag{1.11}$$

$$T = 1 - \frac{k^2 g^2}{1 - 2\sigma t \cos[\psi] + \sigma^2 t^2}\,, \tag{1.12}$$

where we introduced the new variable $g^2 := 1 - \sigma^2$ which describes the amount of loss in a round trip.

Equations (1.5), (1.6) and (1.11) show that the spectral responses are periodic in ψ. In particular, T has minima equal to:

$$T_{min} = \frac{(t - \sigma)^2}{(1 - t\sigma)^2} \quad \text{at} \quad \psi = 2\pi m \quad \text{with} \quad m \in \mathbb{N}^+\,, \tag{1.13}$$

at resonance, and maxima equal to:

$$T_{max} = \frac{(t + \sigma)^2}{(1 + t\sigma)^2} \quad \text{at} \quad \psi = \pi + 2\pi m \quad \text{with} \quad m \in \mathbb{N}^+\,, \tag{1.14}$$

at anti-resonance. At resonance, the internal field inside the resonator is maximum ($k^2/(1 - t\sigma)^2$), and the field coming out of the MR makes destructive interference with the field propagating along the bus waveguide. The MR is at resonance when the optical path ($n_{eff}L$) is a multiple of the wavelength:

$$\lambda_{res} = \frac{n_{eff}L}{m}\,, \quad m \in \mathbb{N}^+\,. \tag{1.15}$$

Equation 1.13 shows that zero transmission at resonance can be obtained if $t = \sigma$ or equivalently if $k^2 = g^2$. This condition corresponds to the critical-coupling regime where the transmission coefficient t of the coupling is equal to the propagation coefficient σ, or rather where the power coupled to the MR is equal to the power lost in a round trip. On the other hand, if $t > \sigma$ ($k^2 < g^2$) then the MR is in the under-coupling regime, while if $t < \sigma$ ($k^2 > g^2$) then the MR is in the over-coupling regime.

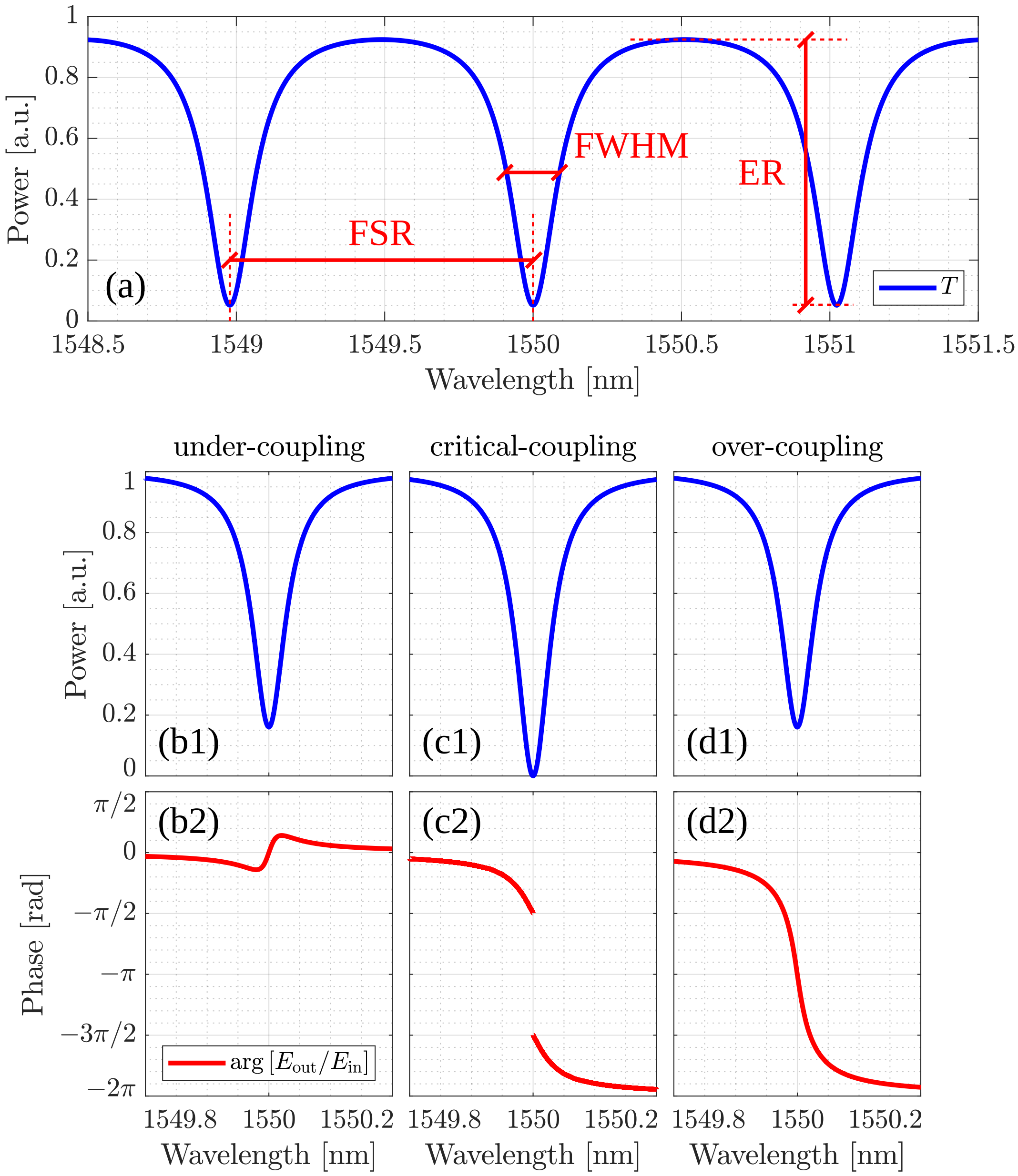

Figure 1.3: Transmission response of the MR as a function of the wavelength. In (a) are reported the name of the most important features of the spectral transmission. Panels (b), (c), and (d) refer to the three coupling regimes of the MR, under-coupling, critical-coupling, and over-coupling, respectively. (b1), (c1), and (d1) show the intensity transmission (T). (b2), (c2), and (d2) report the phase of the output field ($\arg\left[E_{\mathrm{out,R}}/E_{\mathrm{in,L}}\right] = \arg\left[E_{\mathrm{out,L}}/E_{\mathrm{in,R}}\right]$). For panel (a) we used $\lambda_{\mathrm{res}} = 1550$ nm, $n_{\mathrm{eff}}[\lambda_{\mathrm{res}}] \simeq 2.35$, $L = 1000$ μm, $Q \simeq 8.1 \times 10^3$, $t = 0.8$ and $\sigma = 0.7$. For panels (b), (c) and (d) we used $\lambda_{\mathrm{res}} = 1550$ nm, $n_{\mathrm{eff}}[\lambda_{\mathrm{res}}] \simeq 2.36$, $L = 50$ μm, $t\sigma = 0.995^2 \simeq 0.99$ and $Q \simeq 2.4 \times 10^4$. For (b1) and (b2) $t = 0.997$ and $\sigma \simeq 0.0774$. For (c1) and (c2) $t = \sigma = 0.995$. For (d1) and (d2) $t \simeq 0.0774$ and $\sigma = 0.997$.

As can be seen from Eq. (1.11) and Eq. (1.5), the intensity transmission is independent of the exchange of the t and σ parameters [see Fig. 1.3 (b1) and (d1)], while the output electric field is affected by the exchange. Therefore, the only way to distinguish the over-coupling regime from the under-coupling regime, when we can only measure the outgoing fields in the stationary regime around a resonance, is to measure not only the field intensity but also its phase. In fact, as observed in Fig. 1.3, the phase of the outgoing field has a different trend in the three regimes. In critical-coupling, it is observed that the transmission intensity has a spectral dip that reaches zero at resonance, see Fig. 1.3 (c1). In fact, at resonance, the field coming out of the MR has a π phase difference with respect to the field propagating in the bus waveguide (destructive interference). In the critical-coupling regime, since the intensities of the field exiting the MR and the one propagating in the bus waveguide are equal, complete destructive interference occurs, resulting in a zero intensity output. Therefore, the phase at resonance is undefined and there is a jump of π in phase, as shown in Fig. 1.3 (c2). In contrast, in the under-coupling regime, since the coupling with the resonator is smaller, the outgoing field intensity of the MR is smaller than that of the field that continues into the bus waveguide, so at resonance there will be non-zero transmission and the phase of the outgoing field will be 0 (the field that remains in the bus waveguide wins), see Fig. 1.3 (b1) and (b2). Finally, in the over-coupling regime there is $k^2 > g^2$, so the field exiting the MR has a higher intensity than that continuing into the bus waveguide. Consequently, at resonance, the phase of the outgoing field will be equal to $-\pi$ and the intensity will be different from zero, see Fig. 1.3 (d1) and (d2).

The spectral characteristic parameters are the Full Width at Half Maximum (FWHM), the Free Spectral Range (FSR), and the Extinction Ratio (ER), see Fig. 1.3 (a). The FWHM of the resonance spectrum can be derived from Eq. (1.11) [82]:

$$\mathrm{FWHM} = \frac{\lambda_{res}^2 (1 - t\sigma)}{\pi n_g L \sqrt{t\sigma}}\,, \tag{1.16}$$

where n_g is the WG group index that is defined as:

$$n_g = n_{eff} - \lambda \frac{dn_{eff}}{d\lambda}\,. \tag{1.17}$$

The group index is related to the velocity with which the envelope of the wave propagates through the WG (group velocity) $v_g = c/n_g$, where c is the speed of light in vacuum. From Eq. (1.11) we can also derive the distance between two consecutive resonances:

$$\mathrm{FSR} = \frac{\lambda^2}{n_g L}\,, \tag{1.18}$$

which is inversely proportional to the perimeter of the MR. The ER is the ratio of the transmission intensity at anti-resonance to that at resonance. From Eq. (1.14) and Eq. (1.13) we get:

$$\mathrm{ER} = \frac{T_{max}}{T_{min}} = \frac{(t+\sigma)^2}{(1+t\sigma)^2}\frac{(1-t\sigma)^2}{(t-\sigma)^2}\,. \tag{1.19}$$

Other very important parameters that describe a MR are: the Quality Factor (Q), the Finesse, the Enhancement Factor (EF) and the round-trip time. The Q is a dimensionless quantity that describes the sharpness of the resonance. The Q has different definitions, which become equivalent for large values of Q [82, 81]:

$$Q = 2\pi\frac{\text{energy stored}}{\text{energy dissipated per cycle}}\,, \tag{1.20}$$

$$Q = \frac{\lambda_{res}}{\mathrm{FWHM}} = \frac{\pi n_g L\sqrt{t\sigma}}{\lambda_{res}(1-t\sigma)}\,. \tag{1.21}$$

The higher the Q, the better the MR will be. Equation (1.21) shows that Q and MR losses are linked. Larger Q are associated with smaller g (higher σ). The Finesse is defined as:

$$\mathrm{Finesse} = \frac{\mathrm{FSR}}{\mathrm{FWHM}} = \frac{\pi\sqrt{t\sigma}}{1-t\sigma}\,. \tag{1.22}$$

The enhancement factor is defined as the ratio between the power inside the MR and the input power at resonance, which we get from Eq. (1.7):

$$\mathrm{EF} \simeq \frac{k^2}{(1-t\sigma)^2}\,. \tag{1.23}$$

With equal losses, the EF is higher in the critical-coupling regime when $t = \sigma$.

The round-trip time is:

$$\tilde{\tau} = \frac{n_g L}{c}\,, \tag{1.24}$$

and the repetition frequency (its inverse) is:

$$\tilde{f} = \frac{c}{n_g L}\,. \tag{1.25}$$

Later we will see that this parameter turns out to be useful for linking equations derived by TMM to those derived by TCMT. Moreover, the FSR in angular frequency is:

$$\mathrm{FSR}_\omega = 2\pi\frac{c}{n_g L} = 2\pi\tilde{f}\,. \tag{1.26}$$

1.1.2 Temporal Mode Theory

Another way to describe the MR is by using the temporal mode theory [123, 124, 125, 126, 127]. In temporal mode theory the MR is described by its characteristic modes. The modes of a simple MR are the CW and CCW modes. The former describes the clockwise rotating field in the MR, while the latter describes the counterclockwise rotating field. The ideal MR has no backscattering and therefore the two counterpropagating modes do not interact. As in Sec. 1.1.1, the modes of the MR are characterized by intrinsic loss γ (propagation loss, material absorption, bending losses and scattering) and extrinsic loss Γ (loss due to the coupling with the bus waveguide), see Fig. 1.4. These two parameters, γ and Γ, are loss/coupling rates. In addition to the two modes CW and CCW, which we identify with α_{CW} and α_{CCW}, a key parameter is the resonance angular frequency of the MR, ω_0. Instead, ω is the angular frequency of the input wave. Unlike the method used in the previous subsection (TMM), the temporal mode theory only describes the behavior of the MR around a single resonance, so it will not be possible to observe the FSR using this technique. In addition, to accurately describe the MR, the loss and coupling rates must be small ($\gamma \ll \tilde{f} \ll \omega_0$ and $\Gamma \ll \tilde{f} \ll \omega_0$). This condition is typically satisfied for MR with high Q ($Q \gtrsim 10^3$).

Using the parameters just described and taking into account the conservation of energy near the coupling, we can write the system of equations describing the modes of the system [102]:

$$i\frac{d}{dt}\begin{pmatrix}\alpha_{CCW}\\ \alpha_{CW}\end{pmatrix} = \begin{pmatrix}\omega_0 - i\gamma_{tot} & 0\\ 0 & \omega_0 - i\gamma_{tot}\end{pmatrix}\begin{pmatrix}\alpha_{CCW}\\ \alpha_{CW}\end{pmatrix} - \sqrt{2\Gamma}\begin{pmatrix}E_{in,L}\\ E_{in,R}\end{pmatrix}, \tag{1.27}$$

where $\gamma_{tot} = \gamma + \Gamma$ is the total loss rate and $E_{in,L}$ ($E_{in,R}$) is the excitation field from the left (right) input of the bus waveguide. Thus, the Hamiltonian of the system is:

$$H = \begin{pmatrix}\omega_0 - i\gamma_{tot} & 0\\ 0 & \omega_0 - i\gamma_{tot}\end{pmatrix}. \tag{1.28}$$

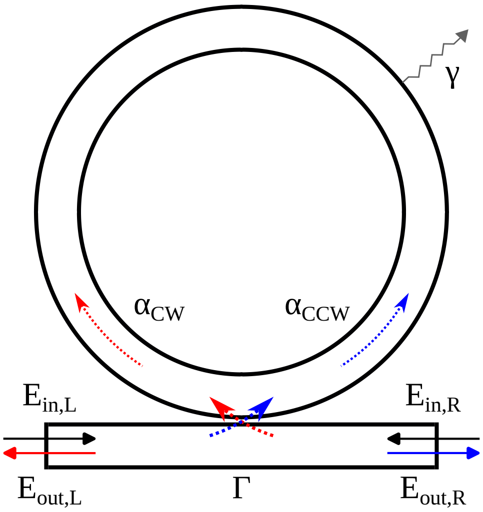

Figure 1.4: Sketches of the microring resonator in the all-pass configuration. γ and Γ are the intrinsic and the extrinsic damping rate. The index R, L refer to left and right. E_{in} and E_{out} are the input and the output fields, respectively. All parameters are described in more detail in the text.

The off-diagonal terms of the Hamiltonian are zero because in the ideal MR (without BS) the two counterpropagating modes do not interact. Note that γ and Γ are real numbers, so $\gamma_{tot} \in \mathbb{R}$. In particular, in the absence of gain, $[\gamma, \Gamma, \gamma_{tot}] \in \mathbb{R}^+$.

For the system to be completely Hermitian, its Hamiltonian must be equal to its conjugate transpose $H = H^\dagger$. From the Eq. (1.28) we see that the Hamiltonian is in fact non-Hermitian, $H \neq H^\dagger$. This is due to the presence of losses in the system. However, since the losses are the same for the two modes of the MR, the non-Hermiticity of the MR does not yield any special property. Therefore, since the two modes are equivalent and there is a symmetric (zero) coupling between them, we can consider the MR as a Hermitian system (Hermitian coupling between the modes of the MR).

Equation (1.28) shows that the eigenvalues of the system are two, degenerate and equal to:

$$\lambda_1 = \lambda_2 = \omega_0 - i\gamma_{tot} \, . \tag{1.29}$$

As expected, they are not real because the MR has losses. If we compute the eigenvectors instead, we get

$$v_1 = \begin{pmatrix} 1 \\ 0 \end{pmatrix} , \quad v_2 = \begin{pmatrix} 0 \\ 1 \end{pmatrix} \, . \tag{1.30}$$

Therefore the eigenvectors are orthogonal to each other, in fact, their inner product is zero $< \nu_1|\nu_2 >= 0$. Since the eigenvalues are degenerate and the eigenvectors are orthogonal, this means that the system is on a DP. Thus, an ideal MR works on a DP.

To derive the output fields, we must also write the equations that connect them to the input fields and to the internal modes of the MR [102]:

$$\begin{pmatrix} E_{\text{out},R} \\ E_{\text{out},L} \end{pmatrix} = \begin{pmatrix} E_{\text{in},L} \\ E_{\text{in},R} \end{pmatrix} + i\sqrt{2\Gamma} \begin{pmatrix} \alpha_{CCW} \\ \alpha_{CW} \end{pmatrix} , \tag{1.31}$$

where $E_{\text{out},R}$ and $E_{\text{out},L}$ are the electric fields at the right and left edge of the bus waveguide, respectively. Solving Eq. (1.27) and Eq. (1.31) in the steady state and assuming:

$$E_{\text{in},L} := \varepsilon_{\text{in},L}\, e^{-i\omega t} , \qquad E_{\text{in},R} := \varepsilon_{\text{in},R}\, e^{i\phi}\, e^{-i\omega t} , \tag{1.32}$$

$$\alpha_{CCW} := a_{CCW}\, e^{-i\omega t} , \qquad \alpha_{CW} := a_{CW}\, e^{-i\omega t} , \tag{1.33}$$

$$E_{\text{out},R} := \varepsilon_{\text{out},R}\, e^{-i\omega t} , \qquad E_{\text{out},L} := \varepsilon_{\text{out},L}\, e^{-i\omega t} , \tag{1.34}$$

we obtain:

$$\varepsilon_{\text{out},R} = \left(1 - \frac{2\Gamma}{-i\Delta\omega + \gamma_{\text{tot}}}\right) \varepsilon_{in,L} , \tag{1.35}$$

$$\varepsilon_{\text{out},L} = \left(1 - \frac{2\Gamma}{-i\Delta\omega + \gamma_{\text{tot}}}\right) e^{i\phi}\, \varepsilon_{\text{in},R} , \tag{1.36}$$

$$a_{CCW} = \frac{i\sqrt{2\Gamma}}{-i\Delta\omega + \gamma_{\text{tot}}} \varepsilon_{in,L} , \tag{1.37}$$

$$a_{CW} = \frac{i\sqrt{2\Gamma}}{-i\Delta\omega + \gamma_{\text{tot}}} e^{i\phi}\, \varepsilon_{\text{in},R} , \tag{1.38}$$

where $\Delta\omega = \omega - \omega_0$, ε is the input or output field amplitude, and ϕ is the phase difference between the incoming field from the right side of the bus waveguide and the incoming field from the left side.

As seen in Sec. 1.1.1, Eq. (1.35) and Eq. (1.36) show that $\varepsilon_{\text{out},R}$ is independent of $\varepsilon_{\text{in},R}$, and $\varepsilon_{\text{out},L}$ is independent of $\varepsilon_{\text{in},L}$. This is due to the absence of coupling between the two counterpropagating modes within the MR.

The transmission intensity can be easily derived by the Eq. (1.35) or the Eq. (1.36):

$$T = \left|\frac{\varepsilon_{\mathrm{out,R}}}{\varepsilon_{\mathrm{in,L}}}\right|^2 = \left|\frac{\varepsilon_{\mathrm{out,L}}}{\varepsilon_{\mathrm{in,R}}}\right|^2 = 1 - \frac{4\gamma\Gamma}{\Delta\omega^2 + \gamma_{\mathrm{tot}}^2} = 1 - \frac{4\gamma\Gamma}{\Delta\omega^2 + (\gamma+\Gamma)^2}\,. \tag{1.39}$$

Equation (1.39) shows that the spectral response of the MR is equal to 1 minus a Lorentzian with

$$\mathrm{FWHM}_\omega = 2\gamma_{\mathrm{tot}} = 2(\gamma+\Gamma)\,, \tag{1.40}$$

see Fig. 1.5 (FWHM_ω is the FWHM in the angular frequency spectrum). Moreover, as ensured by the Lorentz Reciprocity Theorem, the two transmission spectra are identical.

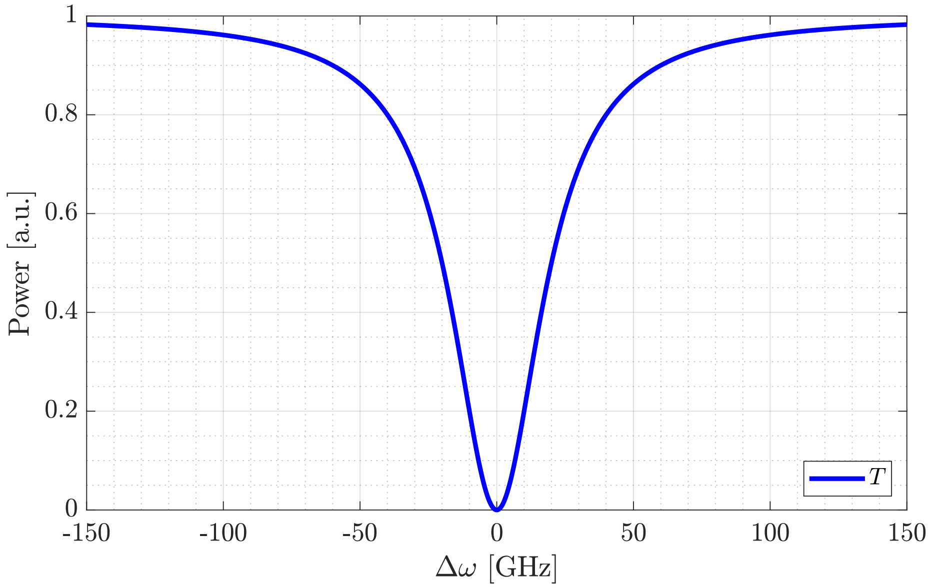

Figure 1.5: Graph of the spectral response of a MR. To create this plot, Eq. (1.39) was used. The used parameters are: $\gamma = \Gamma = 10$ GHz.

As before, we can distinguish between three coupling regimes of the MR. The critical-coupling regime is when the coupling rate is equal to the rate of intrinsic losses $\Gamma = \gamma$. By decreasing Γ ($\Gamma < \gamma$) one enters the under-coupling regime, while for higher Γ ($\Gamma > \gamma$) one is in the over-coupling regime.

The observations made in Sec. 1.1.1 can also be applied to this new formulation, except for the concept of FSR, in fact in temporal mode theory we focus on a single resonance.

It is possible to pass from the spectral response of Eq. (1.5) derived using TMM to that of Eq. (1.35) by assuming that $t \simeq 1$ ($k \ll 1$), $\sigma \simeq 1$ ($g \ll 1$). These assumptions are satisfied for MR with high Q and are equivalent to satisfying $\Gamma \ll \tilde{f}$ and $\gamma \ll \tilde{f}$. Therefore, starting from Eq. (1.5), making the following substitutions:

$$t \simeq 1 - \frac{\Gamma}{\tilde{f}}, \quad k \simeq \sqrt{\frac{2\Gamma}{\tilde{f}}}, \tag{1.41}$$

$$\sigma \simeq 1 - \frac{\gamma}{\tilde{f}}, \quad g \simeq \sqrt{\frac{2\gamma}{\tilde{f}}}, \tag{1.42}$$

$$t\sigma \simeq 1 - \frac{\gamma_{tot}}{\tilde{f}}, \tag{1.43}$$

$$\lambda_0 = \lambda_{res} = \frac{2\pi c}{\omega_0}, \quad \psi = \frac{\Delta\omega}{\tilde{f}}, \tag{1.44}$$

$$\tilde{f} := \frac{c}{n_g L} = \frac{c\,\mathrm{FSR}}{\lambda_0^2}, \quad \mathrm{FSR} := \frac{\lambda_0^2}{n_g L}, \tag{1.45}$$

and stopping at the first-order expansion, we get Eq. (1.35).

In conclusion, we have demonstrated that, if the following relations are satisfied ($k \ll 1$, $t \simeq 1$, $\sigma \simeq 1$) equivalent to ($\gamma_{tot} \ll \omega_0$ or better $\gamma_{tot} \ll \tilde{f}$), to move from the coefficients corresponding to TMM to those of temporal mode theory, it is sufficient to use the following relations:

$$\Gamma \simeq \tilde{f}(1-t), \quad \Gamma \simeq \tilde{f}k^2/2, \tag{1.46}$$

$$\gamma \simeq \tilde{f}(1-\sigma), \quad \gamma \simeq \tilde{f}g^2/2, \tag{1.47}$$

$$\gamma_{tot} \simeq \tilde{f}(1-t\sigma), \tag{1.48}$$

$$\tilde{f} := \frac{c}{n_g L} = \frac{c\,\mathrm{FSR}}{\lambda_0^2}, \quad \mathrm{FSR} := \frac{\lambda_0^2}{n_g L}. \tag{1.49}$$

With the temporal mode theory we can also derive the main characteristic parameters of a MR, the Q, the Extinction Ratio (ER) and the Enhancement Factor (EF) [102, 93, 128].

$$Q = \frac{\omega_0}{\mathrm{FWHM}_\omega} = \frac{\omega_0}{2\gamma_{tot}} = \frac{\omega_0}{2(\gamma+\Gamma)}, \tag{1.50}$$

$$\mathrm{ER} = \frac{\gamma_{tot}^2}{\gamma_{tot}^2 - 4\gamma\Gamma} = \frac{(\gamma+\Gamma)^2}{(\gamma-\Gamma)^2}, \tag{1.51}$$

$$\mathrm{EF} = \frac{2\Gamma\tilde{f}}{\gamma_{tot}^2} = \frac{2\Gamma\tilde{f}}{(\gamma+\Gamma)^2} = \frac{2\Gamma c}{n_g L(\gamma+\Gamma)^2}. \tag{1.52}$$

Thus, we can calculate these parameters directly using the coefficients of the temporal mode theory. Equation (1.51) and Eq. (1.52) show that the ER and EF are maximal in the critical-coupling regime ($\Gamma = \gamma$). Fig. 1.6 shows $\mathrm{EF}\cdot\gamma/\tilde{f}$ as a function of $\xi = \Gamma/\gamma$:

$$\mathrm{EF}\cdot\frac{\gamma}{\tilde{f}} = \frac{2\xi}{(1+\xi)^2}\,. \tag{1.53}$$

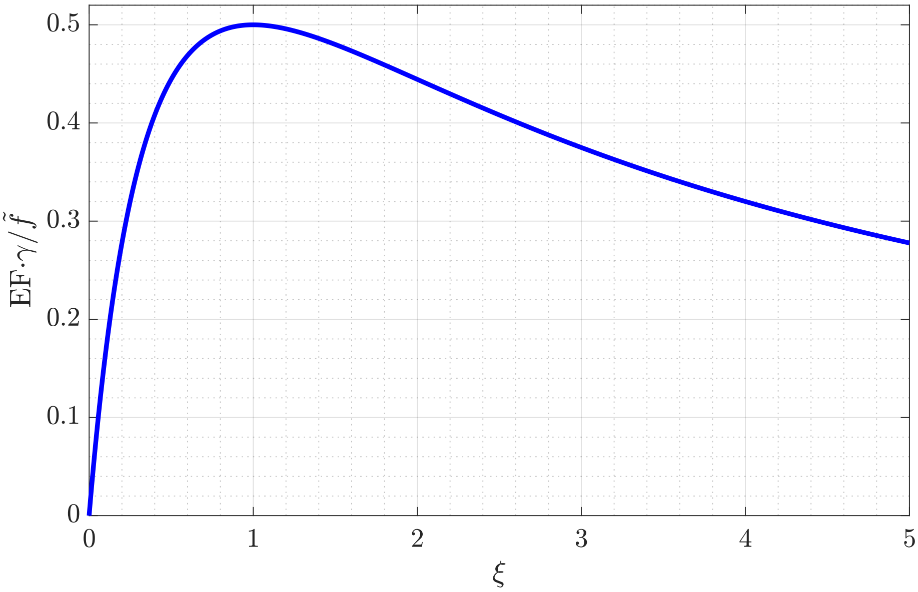

Figure 1.6: $\mathrm{EF}\cdot\gamma/\tilde{f}$ as a function of $\xi = \Gamma/\gamma$.

Fig. 1.6 shows that, keeping the intrinsic losses (γ) fixed, the EF is maximized for $\xi = 1$, which is the condition for having a critical-coupling, $\Gamma = \gamma$.

1.2 Backscattering and Diabolic Point

In the Sec. 1.1 we saw that in the ideal case there is no coupling between the counterpropagating modes of the MR. In a more realistic situation, especially for integrated MRs with high Q, the two modes exchange energy due to the backscattering (BS) [94, 95, 47, 96, 102, 103, 97, 48]. The latter is mainly due to the surface-wall roughness of the WGs. The surface-wall roughness is caused by the used fabrication method. The finite lithographic resolution and the etching process are not able to produce a smooth surface at the sides of the WG core, only a rough surface. Instead, polishing can produce a much smoother top surface. The roughness creates a change in the effective refractive index of the WG along the propagation direction of the wave, causing retroreflections and thus the BS.

1.2.1 Temporal Coupled Mode Theory

To include the BS in our model, we use the Temporal Coupled Mode Theory (TCMT) [123, 124, 125, 127]. We identify with $\beta_{BS,12}$ the coefficient describing the coupling rate from the α_{CW} mode to the α_{CCW} mode and with $\beta_{BS,21}$ from α_{CCW} to α_{CW}, see Fig. 1.7. To include this phenomenon in the model, we need to add the following term to the ideal MR [Eq. (1.27)]:

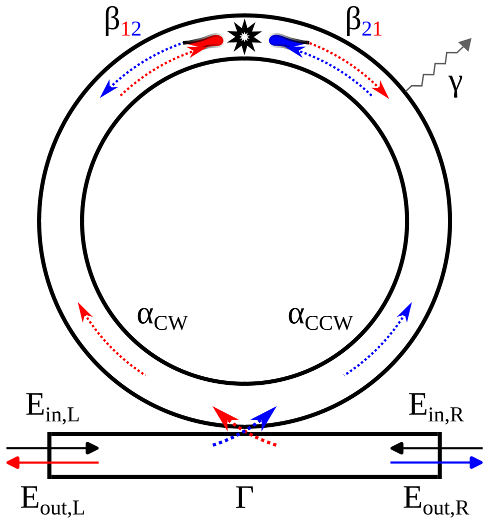

Figure 1.7: Sketch of the microring resonator with backscattering in the all-pass configuration. All the parameters are described in the text.

$$K\begin{pmatrix}\alpha_{CCW}\\ \alpha_{CW}\end{pmatrix} := \begin{pmatrix}0 & -i\beta_{BS,12}\\ -i\beta_{BS,21} & 0\end{pmatrix}\begin{pmatrix}\alpha_{CCW}\\ \alpha_{CW}\end{pmatrix}, \tag{1.54}$$

Consequently, the Hamiltonian of the MR becomes

$$H = \begin{pmatrix}\omega_0 - i\gamma_{tot} & -i\beta_{BS,12}\\ -i\beta_{BS,21} & \omega_0 - i\gamma_{tot}\end{pmatrix}. \tag{1.55}$$

As a result, the eigenvalues of the system are no longer degenerate [102]:

$$\lambda_{1/2} = \omega_0 \pm i\sqrt{\beta_{BS,12}\,\beta_{BS,21}} - i\gamma_{tot} \;\Rightarrow\; \lambda_1 \neq \lambda_2\,, \tag{1.56}$$

$$\begin{aligned} v_{1/2} &= \frac{1}{\sqrt{|\beta_{BS,12}|/|\beta_{BS,21}|+1}} \begin{pmatrix} \mp\sqrt{\frac{\beta_{BS,12}}{\beta_{BS,21}}} \\ 1 \end{pmatrix} \\ \Rightarrow < v_1|v_2 > &= \frac{1-|\beta_{BS,12}|/|\beta_{BS,21}|}{1+|\beta_{BS,12}|/|\beta_{BS,21}|}. \end{aligned} \tag{1.57}$$

where the inner product is defined as:

$$\left\langle \begin{pmatrix} x_1 \\ \vdots \\ x_n \end{pmatrix} \middle| \begin{pmatrix} y_1 \\ \vdots \\ y_n \end{pmatrix} \right\rangle = x^T y^* = \sum_{i=1}^{n} x_i y_i^* = x_1 y_1^* + \cdots + x_n y_n^*, \tag{1.58}$$

The BS can be classified into two categories, a Hermitian and a non-Hermitian scattering. This distinction can be made using the matrix K that couples the two modes [Eq. (1.54)]. If K is Hermitian ($\beta_{BS,21} = -\beta^*_{BS,12}$) then the BS is Hermitian, otherwise they are both non-Hermitian ($\beta_{BS,21} \neq -\beta^*_{BS,12}$).

We there get the following systems of equations:

$$i\frac{d}{dt}\begin{pmatrix} \alpha_{CCW} \\ \alpha_{CW} \end{pmatrix} = \begin{pmatrix} \omega_0 - i\gamma_{tot} & -i\beta_{BS,12} \\ -i\beta_{BS,21} & \omega_0 - i\gamma_{tot} \end{pmatrix} \begin{pmatrix} \alpha_{CCW} \\ \alpha_{CW} \end{pmatrix} - \sqrt{2\Gamma} \begin{pmatrix} E_{in,L} \\ E_{in,R} \end{pmatrix}, \tag{1.59}$$

$$\begin{pmatrix} E_{out,R} \\ E_{out,L} \end{pmatrix} = \begin{pmatrix} E_{in,L} \\ E_{in,R} \end{pmatrix} + i\sqrt{2\Gamma} \begin{pmatrix} \alpha_{CCW} \\ \alpha_{CW} \end{pmatrix}, \tag{1.60}$$

In the steady state, the solutions of Eq. (1.59) and Eq. (1.60) are

$$\begin{aligned} \varepsilon_{out,R} = &\left(1 - \frac{2\Gamma\left(-i\Delta\omega + \gamma_{tot}\right)}{\left(-i\Delta\omega + \gamma_{tot}\right)^2 - \beta_{BS,12}\beta_{BS,21}}\right) \varepsilon_{in,L} \\ &+ \left(\frac{2\Gamma\beta_{BS,12}}{\left(-i\Delta\omega + \gamma_{tot}\right)^2 - \beta_{BS,12}\beta_{BS,21}}\right) e^{i\phi}\varepsilon_{in,R}, \end{aligned} \tag{1.61}$$

$$\begin{aligned} \varepsilon_{out,L} = &\left(1 - \frac{2\Gamma\left(-i\Delta\omega + \gamma_{tot}\right)}{\left(-i\Delta\omega + \gamma_{tot}\right)^2 - \beta_{BS,12}\beta_{BS,21}}\right) e^{i\phi}\varepsilon_{in,R} \\ &+ \left(\frac{2\Gamma\beta_{BS,21}}{\left(-i\Delta\omega + \gamma_{tot}\right)^2 - \beta_{BS,12}\beta_{BS,21}}\right) \varepsilon_{in,L}, \end{aligned} \tag{1.62}$$

$$\begin{aligned} a_{CCW} =& \frac{\sqrt{2\Gamma}(\Delta\omega + i\gamma_{tot})}{(-i\Delta\omega + \gamma_{tot})^2 - \beta_{BS,12}\beta_{BS,21}} \varepsilon_{in,L} \\ & - \frac{i\sqrt{2\Gamma}\,\beta_{BS,12}}{(-i\Delta\omega + \gamma_{tot})^2 - \beta_{BS,12}\beta_{BS,21}} e^{i\phi}\varepsilon_{in,R}\,, \end{aligned} \tag{1.63}$$

$$\begin{aligned} a_{CW} =& \frac{\sqrt{2\Gamma}(\Delta\omega + i\gamma_{tot})}{(-i\Delta\omega + \gamma_{tot})^2 - \beta_{BS,12}\beta_{BS,21}} e^{i\phi}\varepsilon_{in,R} \\ & - \frac{i\sqrt{2\Gamma}\,\beta_{BS,21}}{(-i\Delta\omega + \gamma_{tot})^2 - \beta_{BS,12}\beta_{BS,21}} \varepsilon_{in,L}\,, \end{aligned} \tag{1.64}$$

Where we assumed the conditions given in Eq. (1.32), Eq. (1.33), and Eq. (1.34).

A simultaneous excitation of the system from both sides has been considered in the equations above. We can observe that the left(right) output fields are equal to the sum of the transmission of the system given by the incoming field from right(left) with the reflection of the MR given by the incoming field from left(right). With this strategy, it is straightforward to change the excitation side of the system. In fact, for a left excitation, it is sufficient to impose $\varepsilon_{in,L} \neq 0 \wedge \varepsilon_{in,R} = 0$, while for a right excitation $\varepsilon_{in,L} = 0 \wedge \varepsilon_{in,R} = 0$. In the following, we refer to the field at the o output when the device is excited from the i input as ε_{io}, where $i = L, R$ and $o = L, R$ (L stands for left and R stands for right).

In Fig. 1.8 we report the spectral responses of the MR when subjected to a Hermitian BS (a) or to a non-Hermitian BS (b).

In the presence of a Hermitian BS, the MR has symmetric spectral responses with respect to the axis where the detuning $\Delta\omega$ is zero, see Fig. 1.8 (a1). The two transmissions, the one related to the excitation from left and the one related to the excitation from right, are identical (Lorentz Reciprocity Theorem). The inclusion of the coupling terms between the counterpropagating modes ($\beta_{BS,12}$ and $\beta_{BS,21}$) leads to a doublet characterized by two dips in the spectral transmission. This splitting is a consequence of the interaction between the modes, which causes the separation of the two eigenvalues of the system. Figure 1.8 (a1) shows that in the Hermitian case the two dips are symmetrical and balanced, i.e. they have the same ER. In fact, in the case of the Hermitian BS, the losses of the supermodes describing the system are equal (the two eigenvalues have the same imaginary part). The presence of the Hermitian BS means that the reflection spectra are no longer equal to zero, in fact they show a symmetric spectral doublet (two peaks). In addition, since the BS is in this case Hermitian, the two reflections ($|\varepsilon_{LL}|^2$ and $|\varepsilon_{RR}|^2$) are equal.

The phase spectrum of the fields also changes when BS is present, see Fig. 1.8 (a2). In particular, in Fig. 1.3 only a sudden change at resonance is observed. In contrast,

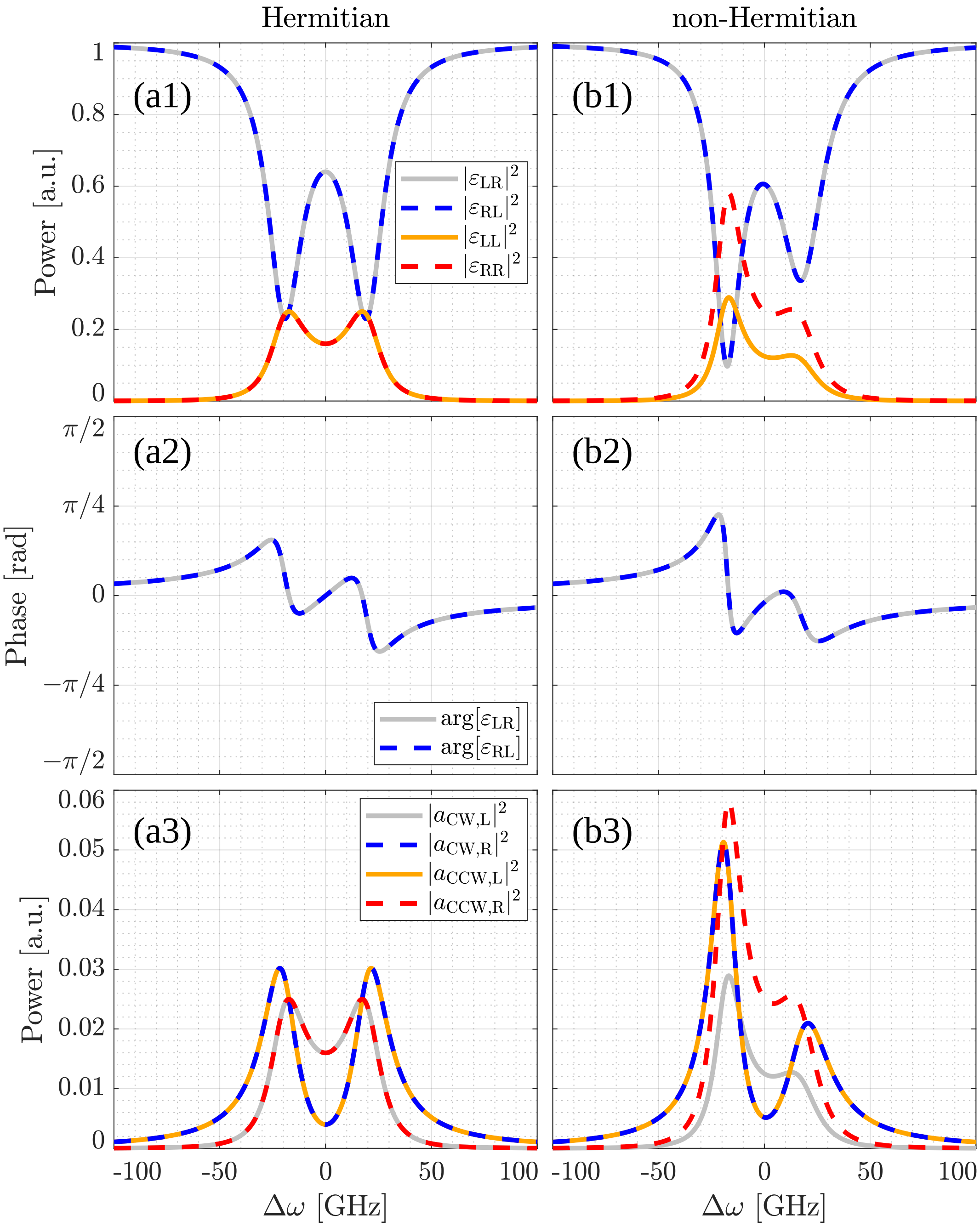

Figure 1.8: Spectral response of a MR with BS. Column (a) is characterized by a Hermitian BS ($\beta_{BS,12} = -\beta^*_{BS,21} = 20$ GHz). Column (b) has a non-Hemiltonian BS ($\beta_{BS,12} \neq -\beta^*_{BS,21}$, $\beta_{BS,12} = 22$ GHz, $\beta_{BS,21} = (-15+4i)$ GHz). The first row shows the spectral responses at the output ports of the system. The second shows the relative phases of the fields at the output ports of the system. The third row shows the intensities of the two counterpropagating modes as a function of the detuning $\Delta\omega$. The parameters used are $\gamma = 5$ GHz and $\Gamma = 5$ GHz.

in Fig. 1.8 (a2), since the eigenvalues of the system are no longer degenerate, two sudden changes are observed near the two minima of the spectral transmission.

Figure 1.8 (a3) shows the intensity of the two counterpropagating modes within the MR for both the left-side excitation ($|a_{CCW,L}|^2$ and $|a_{CW,L}|^2$) and the right-side excitation ($|a_{CW,R}|^2$ and $|a_{CCW,R}|^2$). Let us focus for the moment on $|a_{CCW,L}|^2$ and $|a_{CW,L}|^2$. Both spectra (CCW and CW) have two symmetrical peaks. Therefore, an eigenvalue of the system does not correspond to a CCW or a CW mode, but to a combination of them. Let us call the two combinations of these modes (a_{CCW} and a_{CW}) supermodes (s_1 and s_2). Note that the eigenvalues of the system correspond to the supermodes. Excitation from only one side of the MR does not excite only one supermode, but excites both simultaneously, in fact in transmission we observe a doublet. The two spectra ($|a_{CCW,L}|^2$ and $|a_{CW,L}|^2$) are different. In fact, by exciting from left the bus waveguide couples the light directly to the CCW mode that due to BS couples the light to the CW mode. For the right-side excitation, the results are equivalent; it is sufficient to exchange the CCW mode with the CW mode. Note that in the Hermitian case $|a_{CW,L}|^2 = |a_{CCW,R}|^2$ and $|a_{CW,R}|^2 = |a_{CCW,L}|^2$, see Fig. 1.8 (a3), Eq. (1.63) and Eq. (1.64).

Let us now consider the non-Hermitian case, see Fig. 1.8 (b). Even in the non-Hermitian case, the Lorentz Reciprocity Theorem ensures equality between the two transmissions of the system (when the system is excited from the left side or the right one). Also in the case of the non-Hermitian BS there are two dips in the transmission spectrum of the MR, see Fig. 1.8 (b1). However, this time the spectra are asymmetric with respect to the axis where the detuning is zero. In particular, the two dips are characterized by two different Extinction Ratios (ERs). For this reason, we will call this an unbalanced splitting. This asymmetry is caused by the non-Hermiticity of the BS, which creates an asymmetric coupling between the modes of the MR. The asymmetric coupling also causes an increase in the total losses of the system. Since the parameter γ also includes the losses given by the BS, in order to have no gain within the MR it is necessary that $|n| \leqslant \gamma$ [96, 102], where

$$h := i\frac{\beta_{tot,12} - \beta^*_{tot,21}}{2}\,, \qquad n := \frac{\beta_{tot,12} + \beta^*_{tot,21}}{2}\,, \tag{1.65}$$

are the Hermitian (h) and non-Hermitian (n) intermodal coupling coefficients [96, 102]. This formulation of the intermodal coupling coefficients allows to distinguish between the Hermitian and non-Hermitian part of the coefficients. Here $\beta_{tot,12}$ and $\beta_{tot,21}$ are the total coupling coefficients from the first mode (CW) to the second mode (CCW) and vice versa. In the case of a MR, $\beta_{\mathrm{tot},12} = \beta_{\mathrm{BS},12}$ and $\beta_{\mathrm{tot},21} = \beta_{\mathrm{BS},21}$. Note that to obtain $\beta_{\mathrm{tot},12}$ and $\beta_{\mathrm{tot},21}$ from the parameters h and n, it is sufficient to use the inverse definitions of Eq. (1.65):

$$\beta_{\mathrm{tot},12} := n - ih\,, \qquad\qquad \beta_{\mathrm{tot},21} := n^* - ih^*\,. \tag{1.66}$$

Fig. 1.8 (b1) shows that the reflections related to the excitation from the two sides show asymmetric splitting and also differ from each other. However, if we look more closely, we can see that the spectral shape of the two reflections is equivalent, and therefore the two reflections differ only by a multiplicative factor. In fact, from Eq. (1.61) and Eq. (1.62) we observe that $|\varepsilon_{\mathrm{LL}}|^2/|\varepsilon_{\mathrm{RR}}|^2 = |\beta_{\mathrm{BS},21}|^2/|\beta_{\mathrm{BS},12}|^2$. Then we can simply derive the ratio between the absolute values of the two BS coefficients from the ratio of the reflection intensities. This will be very useful in the Sec. 1.3 where we will present the interferometric excitation to excite the supermodes individually. The phase of the fields exiting the bus waveguide also shows asymmetry with respect to the axis where the detuning is zero, see Fig. 1.8 (b2). An asymmetry is also found in the modes within the MR, as shown in Fig. 1.8 (b3). Here we see that the modes have different spectral forms and that both are present at the two eigenvalues. Thus, even in the non-Hermitian case, the eigenvalues correspond to supermodes which are combinations of the two modes (α_{CCW} and α_{CW}). Panel (b3) of Fig. 1.8, Eq. (1.63) and Eq. (1.64) show that also in the non-Hermitian case $|a_{\mathrm{CW,R}}|^2 = |a_{\mathrm{CCW,L}}|^2$ and $|a_{\mathrm{CW,L}}|^2/|a_{\mathrm{CCW,R}}|^2 = |\beta_{\mathrm{BS},21}|^2/|\beta_{\mathrm{BS},12}|^2$.

Fig. 1.8 shows that the spectral definition of Q no longer has the same meaning when splitting occurs. Having two dips in the transmission spectrum makes it difficult to identify the Q or Qs of the system.

In summary, the coupling between the counterpropagating modes of the MR caused by the presence of the BS causes an Autler-Townes splitting doublet [129, 35]. The coupling between the two modes of the MR can also occur due to other causes, such as the punctual presence of one or more molecules/particles in the WG cladding of the MR [35, 98, 99, 100, 101]. This means that the splitting of the eigenvalues/transmission spectrum can be used to determine the BS and thus the presence of the molecules we want to detect. Therefore, we could consider the BS as a perturbation of the MR we want to measure. Assuming that the perturbation is Hermitian, i.e. $\delta\beta = \beta_{\mathrm{BS},12} = -\beta^*_{\mathrm{BS},21}$, we can observe the variation of the eigenvalues and the eigenvector as a function of $\delta\beta$. Equation (1.65), Eq. (1.56) and

Eq. (1.57) transform into:

$$h = i \cdot \delta\beta\,, \qquad n = 0\,, \tag{1.67}$$

$$\lambda_{1/2} = \omega_0 \mp |\delta\beta| - i\gamma_{\text{tot}} \;\Rightarrow\; \lambda_1 \neq \lambda_2\,,\, \Delta\lambda_{2-1} := \lambda_2 - \lambda_1 = 2|\delta\beta|\,, \tag{1.68}$$

$$\nu_{1/2} = \frac{1}{\sqrt{2}} \begin{pmatrix} \pm i\sqrt{\frac{\delta\beta}{\delta\beta^*}} \\ 1 \end{pmatrix} \;\Rightarrow\; <\nu_1|\nu_2>= 0\,. \tag{1.69}$$

Eq. (1.68) shows that only the real part of the eigenvalues changes as a function of the perturbation, while the imaginary part remains equal to the total losses of the system (γ_{tot}). In particular, the eigenvalue splitting is real and has a linear dependence on the perturbation $|\delta\beta|$. Moreover, the eigenvectors remain orthogonal to each other even for $\delta\beta \neq 0$, in fact their inner product is zero, as shown in Eq. (1.69). These equations also show that when the perturbation is zero, the MR is at a DP and the displacement from the latter produces a linear splitting of the eigenvalues as a function of $|\delta\beta|$.

To make the behavior of the eigenvalues as a function of the $\delta\beta$ perturbation clearer, we can represent Riemann surfaces [41, 3, 104, 4, 105, 106] in the complex field of the perturbation, see Fig. 1.9 (a).

Figure 1.9 (a) shows the Riemann sheets for the MR as a function of the real $\Re[\delta\beta]$ and the imaginary part $\Im[\delta\beta]$ of the Hermitian BS perturbation ($\delta\beta$). The eigenvalues of the MR form two cones around the DP, one corresponding to λ_1 and the other to λ_2, colored red and blue, respectively. Thus the Riemann surfaces have cylindrical symmetry and are symmetric with respect to the plane where $\Re[\lambda] = 0$.

Experimentally, using a single-side excitation, it is not possible to have a direct measure of the eigenvalues of the system. To derive the real part $\Re[\lambda]$ of the eigenvalues from the spectral response of the system (i.e. the actual observable of the system), it is common to calculate the spectral position of the two minima of the Autler-Townes splitting doublet. Figure 1.9 (b) shows the Riemann surfaces computed from the transmission spectra of the MR characterized by the BS perturbation $\delta\beta$. The orange and Dodger blue colors correspond to the positions of the two different transmission dips [see Fig. 1.8 and Fig. 1.9 (b)] and in this case refer to the eigenvalues λ_1 and λ_2. Here we can see that around the DP [around $(0, 0)$], it is not possible to identify two different spectral dips that cause a cancellation of the sensitivity of the MR with respect to a small BS perturbation, see also Fig. 1.9 (d). In fact, the spectral width of the dips causes the two dips to overlap. Outside this central region, there is a nonlinear trend of the positions of the minima as a function

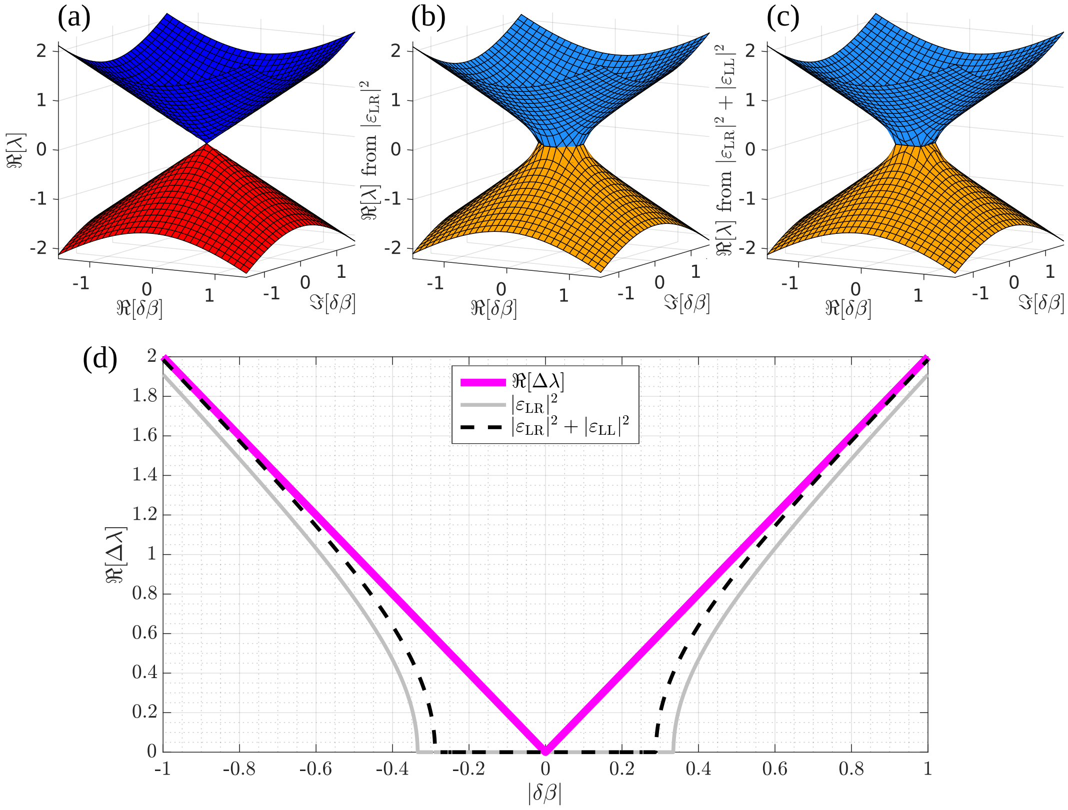

Figure 1.9: Riemann surfaces for the MR as a function of the real $\Re[\delta\beta]$ and the imaginary $\Im[\delta\beta]$ part of the Hermitian BS perturbation $(\delta\beta)$. (a) shows the map of the real $\Re[\lambda]$ part of the eigenvalues, in red $\Re[\lambda_1]$ and in blue $\Re[\lambda_2]$. Panels (b) and (c) represent the map of the positions of the spectral minima of the transmission intensity $(|\varepsilon_{\mathrm{LR}}|^2)$ and of the sum of the transmission intensity with the reflection intensity $(|\varepsilon_{\mathrm{LR}}|^2 + |\varepsilon_{\mathrm{LL}}|^2)$, respectively. The hole around the DP [around $(0,0)$] in panels (b) and (c) is due to the inability to distinguish two peaks. The colors orange and Dodger blue correspond to the positions of the two different dips and in this case refer to the eigenvalues λ_1 and λ_2. (d) shows in magenta, gray and black the splitting of the eigenvalues, the splitting of the doublets observed in the transmission spectra and the splitting observed in the $|\varepsilon_{\mathrm{LR}}|^2 + |\varepsilon_{\mathrm{LL}}|^2$ spectra as a function of $|\delta\beta|$, respectively. Here we use $\gamma = 1/4$ a.u. and $\Gamma = 1/4$ a.u..

of $\delta\beta$, which then tends to the ideal linear trend of the eigenvalues. To highlight this trend, given the cylindrical symmetry of the Riemann surfaces, we have plotted the splitting $\Re[\Delta\lambda]$ as a function of $|\delta\beta|$ in Figure 1.9 (d). We can see the linearity of the splitting of the eigenvalues and also the region where the spectral splitting does not faithfully describe the trend of the eigenvalues. To reduce as much as possible the region where no splitting can be observed, we found a trick: instead of using only the intensity in transmission $(|\varepsilon_{\mathrm{LR}}|^2)$, we can use the sum of the transmission intensity with the reflection intensity $(|\varepsilon_{\mathrm{LR}}|^2 + |\varepsilon_{\mathrm{LL}}|^2)$. This sum can be obtained by measuring the two intensities separately and then adding them. In Fig. 1.9 (c), the Riemann surfaces obtained from the sum of these intensities are shown. Panels (c) and (d) show that by using also the reflection component it is possible to reduce, but not eliminate, the region where the splitting does not appear in the spectrum and to still have higher sensitivity. Figure 1.9 (d) shows that both splittings computed using $|\varepsilon_{LR}|^2$ or $|\varepsilon_{LR}|^2 + |\varepsilon_{LL}|^2$ tend to the eigenvalues splitting as the perturbation $\delta\beta$ increases.

1.2.2 Backscattering in the Transfer Matrix Method

It is also possible to implement the BS using the TMM. Here, instead of having a uniform BS inside the MR, we model the BS as a point scatterer characterized by a transmission coefficient t_{BS} and two reflection coefficients $b_{BS,12}$ and $b_{BS,21}$, see Fig. 1.10.

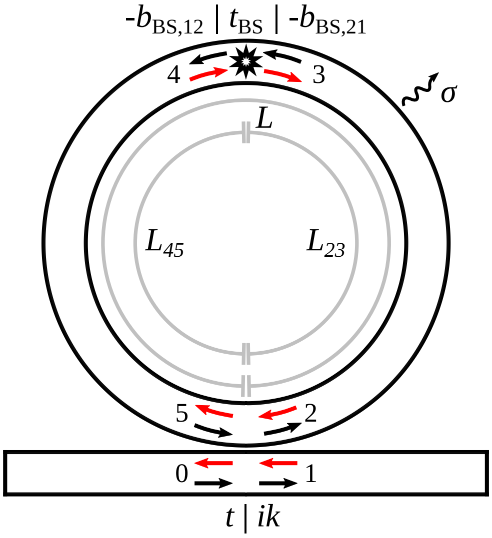

Figure 1.10: Sketches of a MR in all-pass configuration with a scatterer (black star) inside, simulating the BS. The black arrows identify the E_n fields, where $n = 0, ..., 5$, and their propagation directions. The red arrows instead identify the E_{nr} fields, which have opposite propagation directions. All parameters are described in the text.

The system of equations corresponding to the MR in Fig. 1.10 is as follows:

$$\begin{cases} E_1 = tE_0 + ikE_5 \\ E_2 = tE_5 + ikE_0 \\ E_3 = \sigma_{23} e^{i\psi_{23}} E_2 \\ E_4 = t_{BS} E_3 - b_{BS,12} E_{4r} \\ E_5 = \sigma_{45} e^{i\psi_{45}} E_4 \\ E_{0r} = tE_{1r} + ikE_{2r} \\ E_{2r} = \sigma_{23} e^{i\psi_{23}} E_{3r} \\ E_{3r} = t_{BS} E_{4r} - b_{BS,21} E_3 \\ E_{4r} = \sigma_{45} e^{i\psi_{45}} E_{5r} \\ E_{5r} = tE_{2r} + ikE_{1r} \end{cases} \tag{1.70}$$

$$\psi_{jl} := \frac{2\pi}{\lambda} n_{\text{eff}} L_{jl}\,, \quad \sigma_{jl} := e^{-\alpha L_{jl}}\,, \tag{1.71}$$

$$\psi := \frac{2\pi}{\lambda} n_{\text{eff}} L\,, \quad \sigma := e^{-\alpha L}\,, \quad L := 2\pi R\,, \tag{1.72}$$

For simplicity, we have assumed that there are no losses in the coupling between the bus waveguide and the MR ($t^2 + k^2 = 1$). The parameter L_{ij} identifies the WG length between the numbers i and j given in Fig. 1.10. From (1.70) we derive

$$\varepsilon_{LR} = \varepsilon_{RL} = \frac{1}{t}\left(1 - \frac{k^2\left(1 - \sigma t_{BS} t e^{i\psi}\right)}{\left(1 - \sigma t_{BS} t e^{i\psi}\right)^2 - b_{12} b_{21} \sigma^2 t^2 e^{2i\psi}}\right)\,, \tag{1.73}$$

$$\varepsilon_{LL} = \frac{k^2 b_{21} \sigma_{23}^2 e^{2i\psi_{23}}}{\left(1 - \sigma t_{BS} t e^{i\psi}\right)^2 - b_{12} b_{21} \sigma^2 t^2 e^{2i\psi}}\,, \tag{1.74}$$

$$\varepsilon_{RR} = \frac{k^2 b_{12} \sigma_{45}^2 e^{2i\psi_{45}}}{\left(1 - \sigma t_{BS} t e^{i\psi}\right)^2 - b_{12} b_{21} \sigma^2 t^2 e^{2i\psi}}\,, \tag{1.75}$$

$$\varepsilon_{out,R} = \varepsilon_{in,L} \varepsilon_{LR} + \varepsilon_{in,R} e^{i\phi} \varepsilon_{RR}\,, \tag{1.76}$$

$$\varepsilon_{out,L} = \varepsilon_{in,R} e^{i\phi} \varepsilon_{RL} + \varepsilon_{in,L} \varepsilon_{LL}\,. \tag{1.77}$$

In order to simplify the discussion, we impose the following conditions on the position of the scatterer inside the MR: $L_{23} = L_{45} = L/2$ ($\psi_{23} = \psi_{45} = \psi/2$ and $\sigma_{23} = \sigma_{45} = \sqrt{\sigma}$).

If the conditions describing a situation of "low" couplings ($k \ll 1$, $t \simeq 1$, $|b_{BS,12/21}| \ll 1$, $t_{BS} \simeq 1$, $\sigma \simeq 1$) are met, and performing the following substitutions [93]:

$$t \simeq 1 - \frac{\Gamma}{\tilde{f}}, \quad k \simeq \sqrt{\frac{2\Gamma}{\tilde{f}}} \tag{1.78}$$

$$t_{BS}\sigma \simeq 1 - \frac{\gamma}{\tilde{f}}, \quad \sigma := e^{-\alpha L} \tag{1.79}$$

$$b_{BS,12} \simeq \frac{\beta_{BS,12}}{\tilde{f}}, \quad b_{BS,21} \simeq \frac{\beta_{BS,21}}{\tilde{f}} \tag{1.80}$$

$$\tilde{f} := \frac{c}{n_g L} = \frac{c\ FSR}{\lambda_0^2}, \quad FSR := \frac{\lambda_0^2}{n_g L} \tag{1.81}$$

$$\psi = \frac{\Delta\omega}{\tilde{f}} \tag{1.82}$$

it is straightforward to verify that we get the same results derived through the TCMT equations, namely Eq. (1.61) and Eq. (1.62).

In conclusion, we have demonstrated that, if the following relations are satisfied ($k \ll 1$, $t \simeq 1$, $|b_{BS,12/21}| \ll 1$, $t_{BS}\sigma \simeq 1$) equivalent to ($\gamma_{tot}\&|\beta_{BS,12}|\&|\beta_{BS,21}| \ll \omega_0$ or better $\gamma_{tot}\&|\beta_{BS,12}|\&|\beta_{BS,21}| \ll \tilde{f}$), to move from a TCMT to a TMM model one has to use the following relations [93]:

$$\Gamma \simeq \tilde{f}(1-t), \quad \Gamma \simeq \tilde{f}k^2/2 \tag{1.83}$$

$$\gamma \simeq \tilde{f}(1-t_{BS}\sigma), \quad \sigma := e^{-\alpha L} \tag{1.84}$$

$$\gamma_{tot} \simeq \tilde{f}(1-tt_{BS}\sigma), \tag{1.85}$$

$$\beta_{BS,12} \simeq \tilde{f}b_{BS,12}, \quad \beta_{BS,21} \simeq \tilde{f}b_{BS,21} \tag{1.86}$$

$$\tilde{f} := \frac{c}{n_g L} = \frac{c\ FSR}{\lambda_0^2}, \quad FSR := \frac{\lambda_0^2}{n_g L}. \tag{1.87}$$

Note that these are the same equations found in Sec. 1.1.2 [Eq. (1.46), Eq. (1.47), Eq. (1.48), Eq. (1.49)] with the addition of Eq. (1.86) and of the term t_{BS} in Eq. (1.84) and in Eq. (1.85).

1.3 Interferometric excitation

In Sec. 1.2 we saw that the CW and CCW modes do not correspond to the eigenstates of the system. This is due to the existence of a coupling between the two modes. Therefore, in this section we want to find the supermodes of the system that correspond to the eigenvalues. We will find two supermodes which will not mutually exchange energy. We will also find a way to excite one supermode at a time so that the two eigenvalues are obtained separately in the spectral response. In particular, the real part of the eigenvalue will be the position of the dip minimum, while the imaginary part will be proportional to its FWHM.

To make this discussion as general as possible, let us identify with $\beta_{tot,12}$ and $\beta_{tot,21}$ the total coupling coefficients from the mode $\alpha_{CW} = \alpha_1$ to the mode $\alpha_{CCW} = \alpha_2$ and vice versa. In $\beta_{tot,12}$ and $\beta_{tot,21}$ there can be both contributions given by the BS and those given by the geometry of the system. In particular in this chapter, since the ideal MR has no couplings between modes, we will have that $\beta_{tot,12} = \beta_{BS,12}$ and $\beta_{tot,21} = \beta_{BS,21}$. From Eq. (1.59) and Eq. (1.60) we derive the general system of equations [102]:

$$i\frac{d}{dt}\begin{pmatrix}\alpha_{CCW}\\ \alpha_{CW}\end{pmatrix} = \begin{pmatrix}\omega_0 - i\gamma_{tot} & -i\beta_{tot,12}\\ -i\beta_{tot,21} & \omega_0 - i\gamma_{tot}\end{pmatrix}\begin{pmatrix}\alpha_{CCW}\\ \alpha_{CW}\end{pmatrix} - \sqrt{2\Gamma}\begin{pmatrix}E_{in,L}\\ E_{in,R}\end{pmatrix}, \tag{1.88}$$

$$\begin{pmatrix}E_{out,R}\\ E_{out,L}\end{pmatrix} = \begin{pmatrix}E_{in,L}\\ E_{in,R}\end{pmatrix} + i\sqrt{2\Gamma}\begin{pmatrix}\alpha_{CCW}\\ \alpha_{CW}\end{pmatrix}, \tag{1.89}$$

with the eigenvalues and eigenvectors equal to:

$$\lambda_{1/2} = \omega_0 \pm i\sqrt{\beta_{tot,12}\,\beta_{tot,21}} - i\gamma_{tot} \;\Rightarrow\; \lambda_1 \neq \lambda_2\,, \tag{1.90}$$

$$\begin{aligned} \nu_{1/2} &= \frac{1}{\sqrt{|\beta_{tot,12}|/|\beta_{tot,21}| + 1}}\begin{pmatrix}\mp\sqrt{\frac{\beta_{tot,12}}{\beta_{tot,21}}}\\ 1\end{pmatrix} \\ &\Rightarrow <\nu_1|\nu_2> = \frac{1 - |\beta_{tot,12}|/|\beta_{tot,21}|}{1 + |\beta_{tot,12}|/|\beta_{tot,21}|} \end{aligned} \tag{1.91}$$

equivalent to Eq. (1.56) and Eq. (1.57).

Taking advantage of the knowledge of the eigenvectors of the system, Eq. (1.91), we can change the basis to get a diagonal Hamiltonian. To do this we write down the supermodes of the system:

$$\mathfrak{s}_1 := \frac{1}{\sqrt{\tilde{2}}}\left(-\sqrt{\frac{\beta_{\mathrm{tot},21}}{\beta_{\mathrm{tot},12}}}\alpha_{\mathrm{CCW}} + \alpha_{\mathrm{CW}}\right), \tag{1.92}$$

$$\mathfrak{s}_2 := \frac{1}{\sqrt{\tilde{2}}}\left(+\sqrt{\frac{\beta_{\mathrm{tot},21}}{\beta_{\mathrm{tot},12}}}\alpha_{\mathrm{CCW}} + \alpha_{\mathrm{CW}}\right), \tag{1.93}$$

$$\tilde{2} := \frac{|\beta_{\mathrm{tot},21}|}{|\beta_{\mathrm{tot},12}|} + 1, \tag{1.94}$$

where $1/\sqrt{\tilde{2}}$ is the normalization of the supermodes. $\tilde{2}$ is equal to 2 if $|\beta_{\mathrm{tot},21}| = |\beta_{\mathrm{tot},12}|$. Note that the supermodes are a linear combination of the two α_{CW} and α_{CCW} modes. This combination also takes into account the different couplings $\beta_{\mathrm{tot},12}$ and $\beta_{\mathrm{tot},21}$.

Writing the TCMT equations with the supermodes $\mathfrak{s}_1$ and $\mathfrak{s}_2$ yields

$$i\frac{d}{dt}\begin{pmatrix}\mathfrak{s}_1\\ \mathfrak{s}_2\end{pmatrix} = \begin{pmatrix}\lambda_1 & 0\\ 0 & \lambda_2\end{pmatrix}\begin{pmatrix}\mathfrak{s}_1\\ \mathfrak{s}_2\end{pmatrix} - \sqrt{2\Gamma}\begin{pmatrix}\frac{-\sqrt{\beta_{\mathrm{tot},21}/\beta_{\mathrm{tot},12}}E_{\mathrm{in,L}}+E_{\mathrm{in,R}}}{\sqrt{\tilde{2}}}\\ \frac{+\sqrt{\beta_{\mathrm{tot},21}/\beta_{\mathrm{tot},12}}E_{\mathrm{in,L}}+E_{\mathrm{in,R}}}{\sqrt{\tilde{2}}}\end{pmatrix}, \tag{1.95}$$

$$\begin{pmatrix}E_{\mathrm{out,R}}\\ E_{\mathrm{out,L}}\end{pmatrix} = \begin{pmatrix}E_{\mathrm{in,L}}\\ E_{\mathrm{in,R}}\end{pmatrix} + i\sqrt{2\Gamma}\frac{\sqrt{\tilde{2}}}{2}\begin{pmatrix}-\sqrt{\frac{\beta_{\mathrm{tot},12}}{\beta_{\mathrm{tot},21}}} & \sqrt{\frac{\beta_{\mathrm{tot},12}}{\beta_{\mathrm{tot},21}}}\\ 1 & 1\end{pmatrix}\begin{pmatrix}\mathfrak{s}_1\\ \mathfrak{s}_2\end{pmatrix}, \tag{1.96}$$

where λ_1 and λ_2 are the eigenvalues of the system given in Eq. (1.90). To derive Eq. (1.96) we used the following relations:

$$\alpha_{\mathrm{CCW}} = \frac{\sqrt{\tilde{2}}}{2}\sqrt{\frac{\beta_{\mathrm{tot},12}}{\beta_{\mathrm{tot},21}}}\left(-\mathfrak{s}_1 + \mathfrak{s}_2\right), \tag{1.97}$$

$$\alpha_{\mathrm{CW}} = \frac{\sqrt{\tilde{2}}}{2}\left(\mathfrak{s}_1 + \mathfrak{s}_2\right). \tag{1.98}$$

As can be seen from Eq. (1.95), if the system is excited from only one side (left or right), the two supermodes are excited at the same time, leading to a doublet in the spectral response. On the other hand, to excite only one supermode, it is necessary to perform an interferometric excitation [102, 103], in which the system is excited from both sides with two coherent fields having a certain relative phase and a precise ratio between their intensities.

To excite only the supermode $\mathfrak{s}_1$, one must have:

$$\frac{+\sqrt{\beta_{\text{tot},21}/\beta_{\text{tot},12}}E_{\text{in},L} + E_{\text{in},R}}{\sqrt{2}} = 0 \tag{1.99}$$

$$\Rightarrow E_{\text{in},R} = \sqrt{\frac{\beta_{\text{tot},21}}{\beta_{\text{tot},12}}}E_{\text{in},L}e^{i(\pi+2\pi m)} \tag{1.100}$$

$$\Rightarrow \begin{cases} |E_{\text{in},R}| = \sqrt{\frac{|\beta_{\text{tot},21}|}{|\beta_{\text{tot},12}|}}|E_{\text{in},L}| \\ \Phi = \frac{\arg[\beta_{\text{tot},21}/\beta_{\text{tot},12}]}{2} + \pi + 2\pi m =: \Phi_1 \end{cases} \tag{1.101}$$

Instead, to excite only the second supermode ($\mathfrak{s}_2$), one must satisfy:

$$\frac{-\sqrt{\beta_{\text{tot},21}/\beta_{\text{tot},12}}E_{\text{in},L} + E_{\text{in},R}}{\sqrt{2}} = 0 \tag{1.102}$$

$$\Rightarrow E_{\text{in},R} = \sqrt{\frac{\beta_{\text{tot},21}}{\beta_{\text{tot},12}}}E_{\text{in},L}e^{i2\pi m} \tag{1.103}$$

$$\Rightarrow \begin{cases} |E_{\text{in},R}| = \sqrt{\frac{|\beta_{\text{tot},21}|}{|\beta_{\text{tot},12}|}}|E_{\text{in},L}| \\ \Phi = \frac{\arg[\beta_{\text{tot},21}/\beta_{\text{tot},12}]}{2} + 2\pi m =: \Phi_2 \end{cases} \tag{1.104}$$

where

$$\Phi := \arg\left[\frac{E_{\text{in},R}}{E_{\text{in},L}}\right], \quad \varphi_{12/21} := \arg\left[\beta_{\text{tot},12/21}\right], \quad m \in \mathbb{Z}. \tag{1.105}$$

Consequently, to excite the $\mathfrak{s}_1$ or $\mathfrak{s}_2$, the ratio of the intensities of the input fields must be equal to the square root of the ratio of the coupling coefficients:

$$\frac{|E_{\text{in},R}|}{|E_{\text{in},L}|} = \sqrt{\frac{|\beta_{\text{tot},21}|}{|\beta_{\text{tot},12}|}} \tag{1.106}$$

and the phase difference between the incoming field from right and the incoming field from left must be:

$$\Phi_{1/2} = \frac{\arg[\beta_{\text{tot},21}/\beta_{\text{tot},12}]}{2} + \frac{\pi}{2} \pm \frac{\pi}{2} + 2\pi m. \tag{1.107}$$

We further define the phases θ_1 and θ_2 as follows:

$$\theta_{1/2} := \Phi_{1/2} - \left(\frac{\arg[\beta_{\text{tot},21}/\beta_{\text{tot},12}]}{2} + \frac{\pi}{2}\right) = \pm\frac{\pi}{2} + 2\pi m. \tag{1.108}$$

It is important to note that to know the ratio between the two input intensities to be used ($|E_{\text{in,R}}|^2/|E_{\text{in,L}}|^2 = |\beta_{\text{tot},21}|/|\beta_{\text{tot},12}|$), it is sufficient to measure the ratio between the reflections in single-side excitation. In fact, as pointed out in Sec. 1.2.1, from Eq. (1.61) and Eq. (1.62) we have that $|\varepsilon_{\text{LL}}|^2/|\varepsilon_{\text{RR}}|^2 = |\beta_{\text{BS},21}|^2/|\beta_{\text{BS},12}|^2$ and therefore $|E_{\text{in,R}}|^2/|E_{\text{in,L}}|^2 = \sqrt{|\varepsilon_{\text{LL}}|^2/|\varepsilon_{\text{RR}}|^2}$.

By solving the system in the steady-state [Eq. (1.32), Eq. (1.34), and $s_{1/2} = \mathfrak{s}_{1/2}e^{-i\omega t}$] we get Eq. (1.61) and Eq. (1.62) (where $\beta_{\text{BS},12}$ and $\beta_{\text{BS},21}$ should be replaced with $\beta_{\text{tot},12}$ and $\beta_{\text{tot},21}$, respectively). Now by performing the interferometric excitation in order to excite only one of the two supermodes [Eq. (1.106) and Eq. (1.107)], we obtain [102]:

$$\begin{pmatrix} |\varepsilon_{\text{out,R}}|^2 \\ |\varepsilon_{\text{out,L}}|^2 \end{pmatrix} = \left(1 - \frac{4(\gamma \mp \tilde{\gamma})\Gamma}{(\Delta\omega \pm \tilde{\beta})^2 + (\gamma \mp \tilde{\gamma} + \Gamma)^2}\right) \begin{pmatrix} |\varepsilon_{\text{in,L}}|^2 \\ |\varepsilon_{\text{in,R}}|^2 \end{pmatrix}, \tag{1.109}$$
$$\tilde{\beta} := \sqrt{|\beta_{\text{tot},12}\beta_{\text{tot},21}|}\,\sin\left[\arg\left[\beta_{\text{tot},12}\beta_{\text{tot},21}\right]/2\right],$$
$$\tilde{\gamma} := \sqrt{|\beta_{\text{tot},12}\beta_{\text{tot},21}|}\,\cos\left[\arg\left[\beta_{\text{tot},12}\beta_{\text{tot},21}\right]/2\right].$$

Equation (1.109) shows that the responses in the case of interferometric excitation are characterized by a single Lorentzian dip. Therefore, this method allows us to transform a transmission doublet into a single Lorentzian. This Lorentzian is centered in $\mp\tilde{\beta}$ and its FWHM is equal to $2(\gamma \mp \tilde{\gamma} + \Gamma)$. We also note that the eigenvalues of the system [Eq. (1.90)] can also be written as a function of $\tilde{\beta}$ and $\tilde{\gamma}$, which yields:

$$\lambda_{1/2} = \omega_0 \mp \tilde{\beta} - i(\gamma_{\text{tot}} \mp \tilde{\gamma}) = \omega_0 \mp \tilde{\beta} - i(\gamma \mp \tilde{\gamma} + \Gamma). \tag{1.110}$$

Consequently, $\tilde{\beta}$ and $\tilde{\gamma}$ are the real and imaginary parts of the shifts of the eigenvalues with respect to $\omega_0 - i\gamma_{\text{tot}}$. Thus from Eq. (1.109) and Eq. (1.110) we see that the position of the Lorentzian corresponds to the real part of the eigenvalue, while its FWHM corresponds to twice the modulus of the imaginary part of the eigenvalue. Therefore, by the interferometric excitation, one can measure the eigenvalues of the system directly from the transmission spectrum. Note also that $\tilde{\gamma}$ is always positive, while $\tilde{\beta}$ can change sign as a function of $\beta_{\text{tot},12}$ and $\beta_{\text{tot},21}$.

The two Lorentzians described in Eq. (1.109) are closely related to the two eigenvalues of the system. Since we can separate their contribution in the transmission spectrum, their Qs can be calculated. As can also be seen from Eq. (1.110), in general the eigenvalues have a different imaginary part, consequently the two Lorentzians will have different FWHMs and different Qs. Using the spectral definition of Q [Eq. (1.50)], we get that the two Qs are approximately:

$$Q_{1/2} = \frac{\omega_0}{\mathrm{FWHM}_{1/2}} = \frac{\omega_0}{2(\gamma \mp \tilde{\gamma} + \Gamma)} \,. \tag{1.111}$$

It is worth noting that since $\tilde{\gamma} \geqslant 0$, the first supermode always has the maximum Q.

1.3.1 Hermitian Coupling

Let us consider the case of Hermitian coupling. Here, $\beta_{\mathrm{tot},12} = -\beta^*_{\mathrm{tot},21} = \beta$, $h = i\beta$ and $n = 0$, see Eq. (1.67). Under this condition, we have that Eq. (1.106) and Eq. (1.107) become:

$$\frac{|E_{\mathrm{in},R}|}{|E_{\mathrm{in},L}|} = 1 \,, \quad \phi_{1/2} = \frac{\arg\left[-(\beta^*)^2\right]}{2} + \frac{\pi}{2} \pm \frac{\pi}{2} + 2\pi m \,. \tag{1.112}$$

This means that to excite one of the supermodes one must use a symmetric interferometric excitation, i.e. the two input field intensities must be equal. To find the correct excitation phase, if one does not know $\arg\left[-(\beta^*)^2\right]$, it is sufficient to vary it until one observes a spectral response characterized by a single Lorentzian. Substituting the Hermitian coupling condition into Eq. (1.109) yields:

$$\begin{gathered} \beta_{\mathrm{tot},12} = -\beta^*_{\mathrm{tot},21} = \beta \quad \Rightarrow \quad \tilde{\beta} = |\beta| \,, \; \tilde{\gamma} = 0 \\ \Rightarrow \begin{pmatrix} |\varepsilon_{\mathrm{out},R}|^2 \\ |\varepsilon_{\mathrm{out},L}|^2 \end{pmatrix} = \left(1 - \frac{4\gamma\Gamma}{(\Delta\omega \pm \tilde{\beta})^2 + (\gamma+\Gamma)^2}\right) \begin{pmatrix} |\varepsilon_{\mathrm{in},L}|^2 \\ |\varepsilon_{\mathrm{in},R}|^2 \end{pmatrix} \,. \end{gathered} \tag{1.113}$$

Therefore, if one excites the first supermode ($\mathfrak{s}_1$), a Lorentzian centered at $\omega_0 - |\beta|$ will be measured. On the other hand, if one excites the second supermode ($\mathfrak{s}_2$), one will measure a Lorentzian centered at $\omega_0 + |\beta|$. Moreover, these two Lorentzians are characterized by the same FWHM $= 2(\gamma + \Gamma)$ as that of the ideal MR (without any coupling). Note that since the coupling is Hermitian, the total losses of the system remain the same as in the case of the ideal MR. Using the interferometric excitation, we can calculate the Q of the MR affected by BS, which in the case of Hermitian coupling is equal to that of an ideal MR:

$$Q_{1/2} = \frac{\omega_0}{2(\gamma + \Gamma)} \,. \tag{1.114}$$

To make it clear, we present in the following (Fig. 1.11) some graphs of the optical response of a MR having: $\Gamma = \gamma = 6.8$ GHz, $\beta_{\mathrm{tot},12} = -\beta^*_{\mathrm{tot},21} = \beta = 33.2$ GHz and $\omega_0 \simeq 2\pi \cdot 193$THz.

Panels (a1) and (a2) of Fig. 1.11 show the standard single-side excitation output spectral intensities, i.e., when $|\varepsilon_{\mathrm{in,L}}|^2 = 1$ mW and $|\varepsilon_{\mathrm{in,R}}|^2 = 0$ or when $|\varepsilon_{\mathrm{in,L}}|^2 = 0$ and $|\varepsilon_{\mathrm{in,R}}|^2 = 1$ mW, respectively. Hence, in the top graph, $|\varepsilon_{\mathrm{out,R}}|^2$ and $|\varepsilon_{\mathrm{out,L}}|^2$ are the transmitted and reflected intensities while the opposite applies to the bottom graph. The output intensities are not simple Lorentzians, but show a balanced doublet (same dip extinction ratios) due to the interaction between the counter-propagating modes in the MR. Figure 1.11 (a1) and Fig. 1.11 (a2) show equal transmission spectra and reflection spectra.

Using a symmetric (i.e. equal field intensities) interferometric excitation ($|\varepsilon_{\mathrm{in,L}}|^2 = |\varepsilon_{\mathrm{in,R}}|^2 = 1$ mW), $\varepsilon_{\mathrm{out,L}}$ and $\varepsilon_{\mathrm{out,R}}$ depend on θ. Panels (b1) and (b2) of Fig. 1.11 show the transmitted field intensities as a function of $\Delta\omega$ and θ. A rich dynamic is observed, with the transmitted intensities increasing or decreasing depending on the excitation conditions. Note that, since the sum of the input intensities is equal to 2 mW, it is expected to observe spectral regions where at least one transmitted intensity is greater than 1 mW. Moreover, by exciting simultaneously from both sides of the system, the Lorentz reciprocity theorem cannot be used, and in fact, the transmissions are generally different. Both phenomena (output intensity greater than 1 mW and different transmissions) would not be present if the MR was ideal (without BS). Figures 1.11 (c1)-(c4) show the transmission spectra for $\theta = \{\pm\pi, \pi/4, +\pi/2, -\pi/2\}$. Different transmission line shapes are observed at the bus waveguide outputs when the angle θ is changed. Note that when $\theta = \pm\pi/2$ the doublet merges into a single Lorentzian resonance and the two transmission spectra are identical. When $\theta = \pm\pi/2$ (Fig. 1.11 (c3), (c4)) the Lorentzian is centered in $\Delta\omega = \mp|\beta|$ (real part of the eigenvalue $\lambda_{1/2}$) and its FWHM is $2(\gamma + \Gamma)$ (absolute value of twice the imaginary part of $\lambda_{1/2}$). This means that in Fig. 1.11 (c3) we only excite the first supermode ($\mathfrak{s}_1$), while in Fig. 1.11 (c4) we only excite the second supermode ($\mathfrak{s}_2$). Note also that these spectral responses, except for a frequency shift, are equal to the spectral response of the ideal MR with the same coefficients γ and Γ. Note also that for $\theta = \pm\pi/2$ the MR has dips that reach zero in transmission, which is not the case when we use single-side excitation [Fig. 1.11 (a1) and (a2)]. Thus, since we have $\Gamma = \gamma$ and the BS is Hermitian, if we excite one of the two supermodes (via a symmetric interferometric excitation), we have the spectral response of the MR in the critical-coupling regime. Finally, note that by continuously varying the phase difference (ϕ corresponding to the variation of θ) between the input fields, it

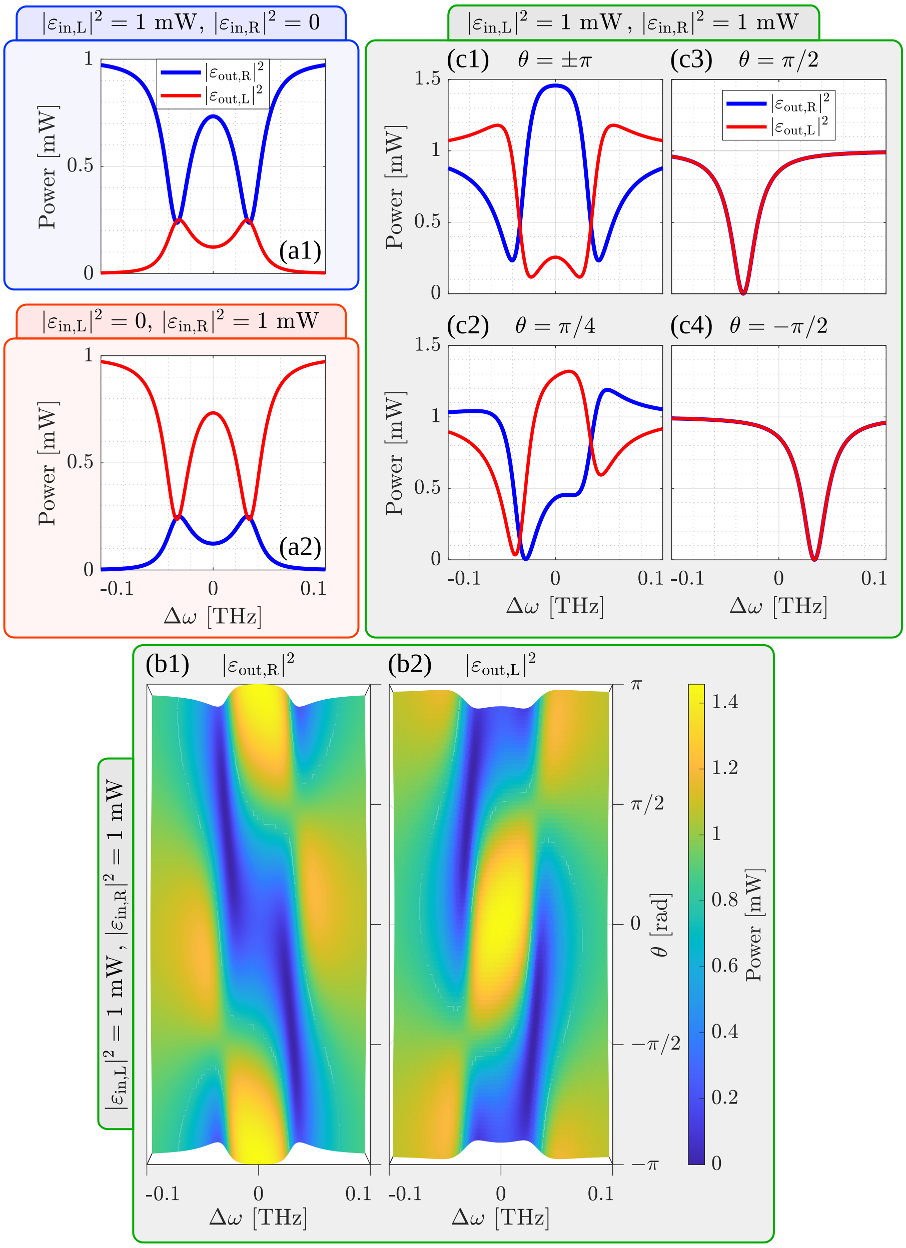

Figure 1.11: Spectral responses for a MR with a Hermitian coupling. Panels (a1) and (a2) report the transmission and reflection spectra for an excitation from the left and right input sides, respectively. Maps (b1) and (b2) show, respectively, the right and left output field intensities as a function of θ and $\Delta\omega$ for a symmetric interferometric excitation. (c1)-(c4) show the output field intensity spectrum for fixed values of $\theta = \{\pm\pi, \pi/4, \pi/2, -\pi/2\}$. The blue and red curves correspond to the right and the left output field intensities, respectively. The used coefficients are: $\Gamma = \gamma = 6.8$ GHz, $\beta_{\mathrm{tot},12} = -\beta^*_{\mathrm{tot},21} = 33.2$ GHz and $\omega_0 = 2\pi \cdot 193$ THz. [102]

is easy to tune the system so that only one supermode is excited, see Fig. 1.11 (b1) and Fig. 1.11 (b2).

1.3.2 Non-Hermitian Coupling

Let us consider the case of non-Hermitian coupling. Here, $\beta_{\mathrm{tot},12} \neq -\beta^*_{\mathrm{tot},21}$ and therefore $n \neq 0$, see Eq. (1.65). In this subsection, we will first observe what happens when we use a symmetric interferometric excitation in the case of a non-Hermitian BS, and then we will calculate the spectral responses when we use the asymmetric interferometric excitation characterized by the correct ratio between the intensities of the input fields (separate excitation of supermodes).

Let us now consider a MR characterized by a non-Hermitian BS and described by the following parameters: $\Gamma = \gamma = 6.8$ GHz, $\beta_{\mathrm{tot},12} = 20.2$ GHz, $\beta_{\mathrm{tot},21} = (-20.2 + 9i)$ GHz and $\omega_0 = 2\pi \cdot 193$ THz. In panels (a1) and (a2) of Fig. 1.12, the single-side excitation output spectral intensities are reported, i.e., when $|\varepsilon_{\mathrm{in},L}|^2 = 1$ mW and $|\varepsilon_{\mathrm{in},R}|^2 = 0$ or when $|\varepsilon_{\mathrm{in},L}|^2 = 0$ and $|\varepsilon_{\mathrm{in},R}|^2 = 1$ mW, respectively. Also with a non-Hermitian BS, the Lorentz reciprocity theorem ensures the same transitions. Instead, the reflections are different, as can be seen by comparing $|\varepsilon_{\mathrm{out},L}|^2$ of the panel (a1) and $|\varepsilon_{\mathrm{out},R}|^2$ of the panel (a2). Panels (b1)-(b2) and (c1)-(c4) describe the spectral responses of the system when symmetric interferometric excitation is used ($|\varepsilon_{\mathrm{in},L}|^2 = |\varepsilon_{\mathrm{in},R}|^2 = 1$ mW). A high variability of the transmission spectra is observed as the phase θ varies. Here, by varying θ one can obtain a spectrum very similar to that of a Lorentzian, see panels (c3) and (c4) of Fig. 1.12. Although for $\theta = \pm\pi/2$ the doublet seems to be almost completely merged into a single resonance, a small deformation is still present. This deformation results from the fact that we excite the system with two fields of equal intensity instead of taking into account the unbalance between the $\beta_{\mathrm{tot},12}$ and $\beta_{\mathrm{tot},21}$ couplings, see Eq. (1.106). To get the correct interferometric excitation so that the supermodes can be excited individually, it is necessary to satisfy Eq. (1.106). Note that symmetric interferometric excitation can be perfect even if the BS is non-Hermitian, but one needs equal absolute values of the two couplings ($|\beta_{\mathrm{tot},12}| = |\beta_{\mathrm{tot},21}|$).

In the general case, to obtain the excitation of only one supermode at a time, one must satisfy Eq. (1.106) and Eq. (1.107). Fig. 1.13 shows the spectral responses as the phase θ changes when the asymmetric interferometric excitation is used [Eq. (1.106) satisfied]. Panels (b1) and (b2) of Fig. 1.13 emphasize the fact that for $\theta = \pm\pi/2$ one is able to excite only the first/second supermode ($\mathfrak{s}_{1/2}$). In fact, the asymmetric

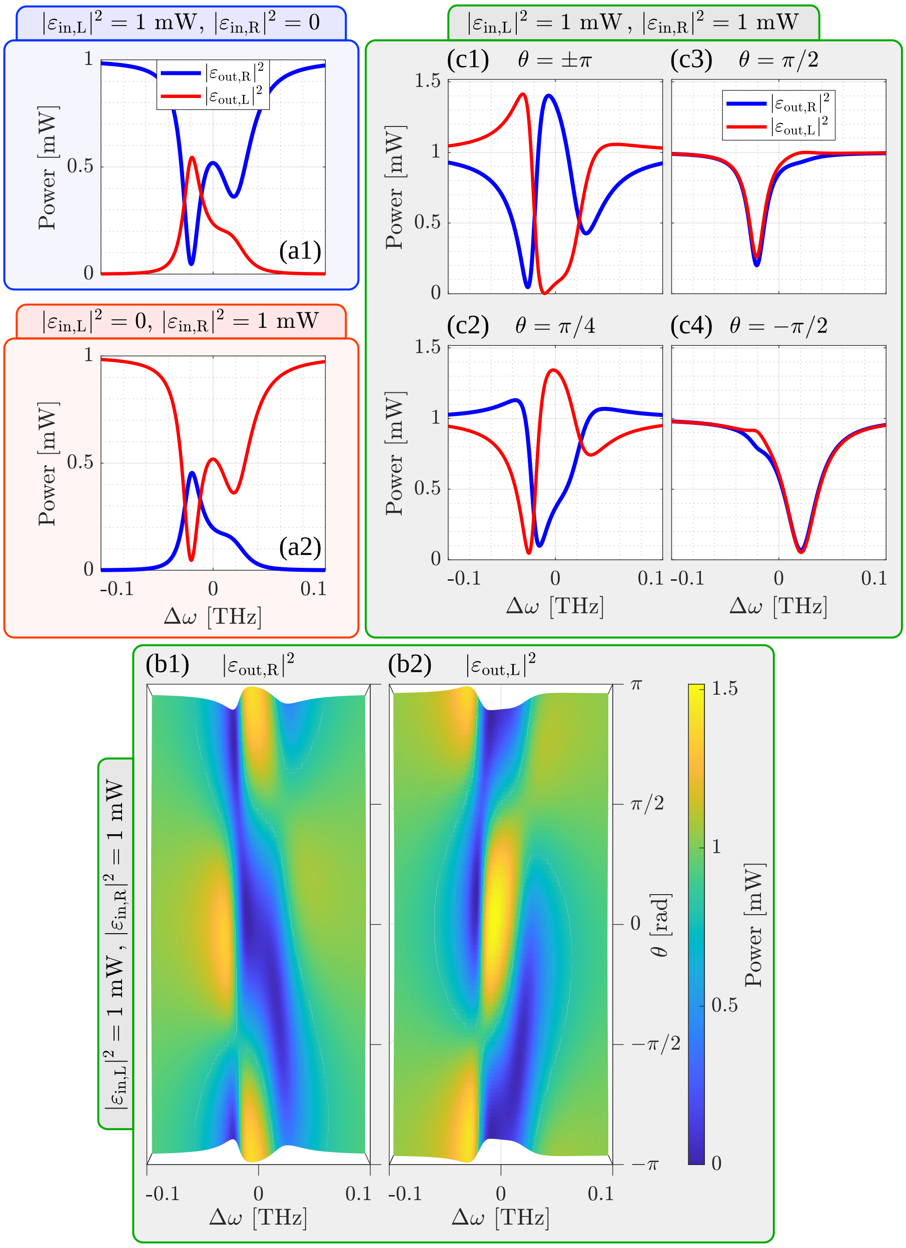

Figure 1.12: Spectral responses for a MR with a non-Hermitian coupling. Panels (a1) and (a2) report the transmission and reflection spectra for an excitation from the left and right input sides, respectively. Maps (b1) and (b2) show, respectively, the right and left output field intensities as a function of θ and $\Delta\omega$ for a symmetric interferometric excitation ($|\varepsilon_{\mathrm{in,L}}|^2 = |\varepsilon_{\mathrm{in,R}}|^2$). (c1)-(c4) show the output field intensity spectrum for fixed values of $\theta = \{\pm\pi, \pi/4, \pi/2, -\pi/2\}$. The blue and red curves correspond to the right and the left output field intensities, respectively. The used coefficients are: $\Gamma = \gamma = 6.8$ GHz, $\beta_{\mathrm{tot},12} = 20.2$ GHz, $\beta_{\mathrm{tot},21} = (-20.2 + 9i)$ GHz and $\omega_0 = 2\pi \cdot 193$ THz. [102]

doublets of Fig. 1.12 (a1) and (a2) merge into a single Lorentzian, see Fig. 1.13 (b1) and (b2). In panel (b1) of Fig. 1.13 it is observed that the two output spectra have the same spectral shape but different intensities. This is due to the different intensity of the two input fields, namely $|\varepsilon_{\mathrm{in,L}}|^2 = 1$ mW, while $|\varepsilon_{\mathrm{in,R}}|^2 \simeq 1.1$ mW.

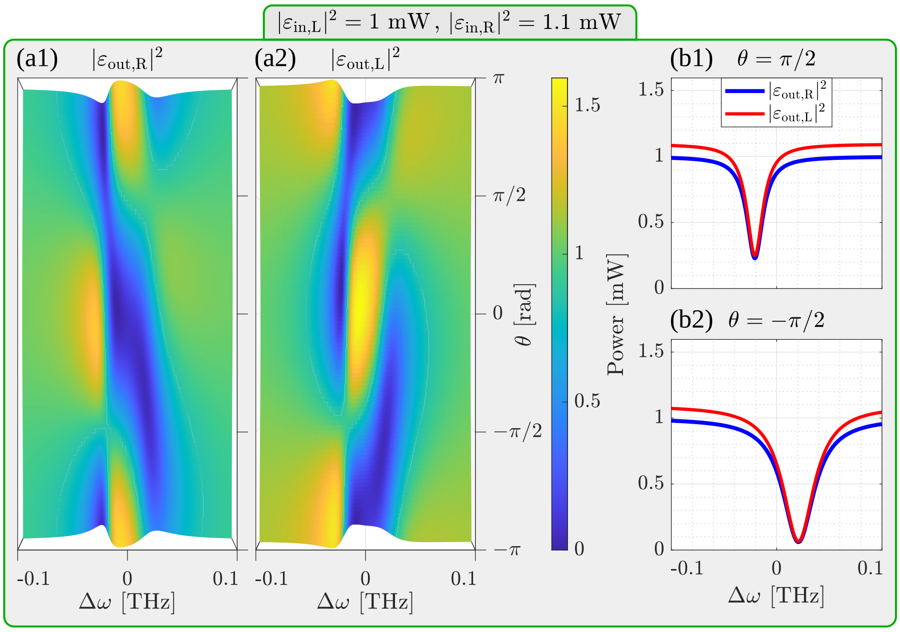

Figure 1.13: Spectral responses for a MR with a non-Hermitian coupling. Maps (a1) and (a2) show, respectively, the right and left output field intensities as a function of θ and $\Delta\omega$ for an asymmetric interferometric excitation [$|\varepsilon_{\mathrm{in,R}}|^2 = \sqrt{|\beta_{\mathrm{tot},21}|/|\beta_{\mathrm{tot},12}|}|\varepsilon_{\mathrm{in,L}}|^2$, Eq. (1.106) satisfied]. (b1) and (b2) show the output field intensity spectrum for fixed values of $\theta = \pm\pi/2$ (first and second supermode). The blue and red curves correspond to the right and the left output field intensities, respectively. The used coefficients are: $\Gamma = \gamma = 6.8$ GHz, $\beta_{\mathrm{tot},12} = 20.2$ GHz, $\beta_{\mathrm{tot},21} = (-20.2 + 9i)$ GHz and $\omega_0 = 2\pi \cdot 193$ THz. [102]

As in the case of the Hermitian coupling, we can measure directly from the spectrum the real part (position of the Lorentzian) and the imaginary part (minus half of the Lorentzian FWHM) of the eigenvalues. Note that since the BS is non-Hermitian, the FWHMs and thus the Qs of the two supermodes are different. Thus, the losses of the two supermodes are different, and in particular, for one they are less than γ_{tot}, while for the other they are greater than γ_{tot}. In Fig. 1.13, since $\Gamma = \gamma$, one supermode is in the over-coupling regime while the other is in the under-coupling regime (for more details see Sec. 1.4.2).

A special non-Hermitian case is when $\sin[\arg[\beta_{\mathrm{tot},12}\beta_{\mathrm{tot},21}]/2] = 1$. This condition can be satisfied if $\beta_{\mathrm{tot},21} = -r\beta^*_{\mathrm{tot},12}$ where $r > 0$ and $r \in \mathbb{R}$. In this situation,

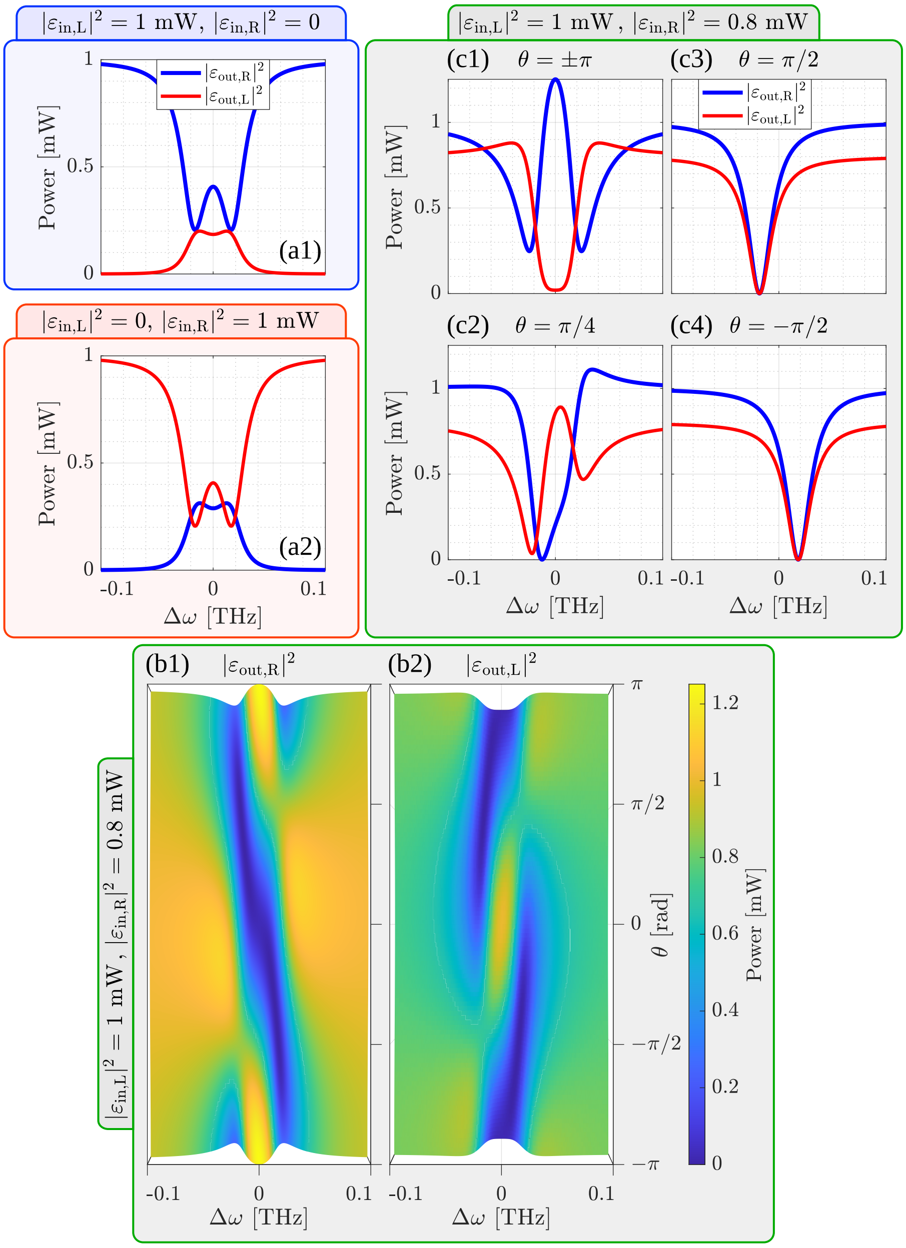

Figure 1.14: Spectral responses for a MR with a non-Hermitian coupling. Panels (a1) and (a2) report the transmission and reflection spectra for an excitation from the left and right input sides, respectively. Maps (b1) and (b2) show, respectively, the right and left output field intensities as a function of θ and $\Delta\omega$ for an asymmetric interferometric excitation [$|\varepsilon_{\text{in,R}}|^2 = \sqrt{|\beta_{\text{tot},21}|/|\beta_{\text{tot},12}|}\,|\varepsilon_{\text{in,L}}|^2$, Eq. (1.106) satisfied]. (c1)-(c4) show the output field intensity spectrum for fixed values of $\theta = \{\pm\pi, \pi/4, \pi/2, -\pi/2\}$. The blue and red curves correspond to the right and the left output field intensities, respectively. The used coefficients are: $\Gamma = \gamma = 6.8\,\text{GHz}$, $\beta_{\text{tot},12} = 20.2\,\text{GHz}$, $\beta_{\text{tot},21} = -0.8\beta_{\text{tot},12} = -16.16\,\text{GHz}$ and $\omega_0 = 2\pi \cdot 193$ THz.

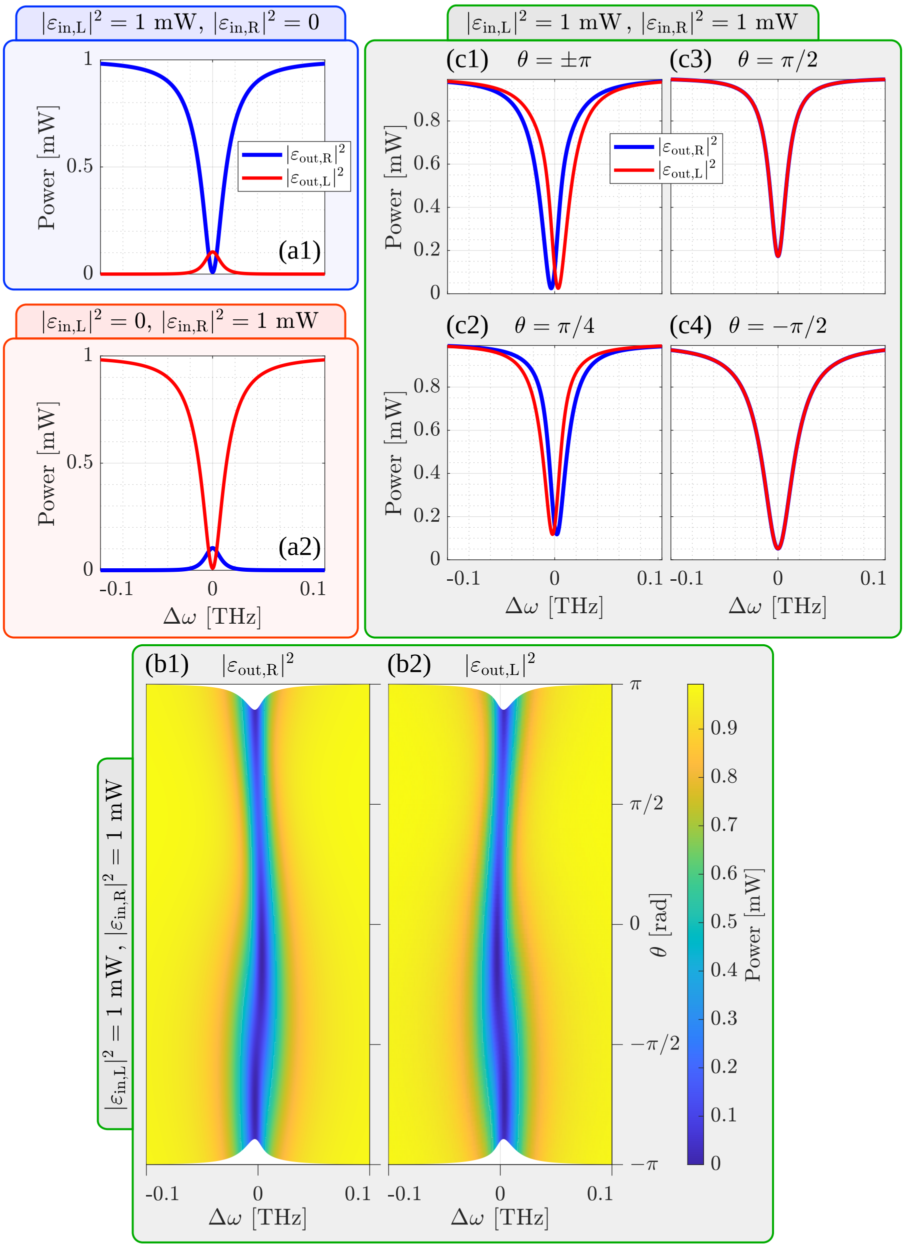

Figure 1.15: Spectral responses for a MR with a non-Hermitian coupling. Panels (a1) and (a2) report the transmission and reflection spectra for an excitation from the left and right input sides, respectively. Maps (b1) and (b2) show, respectively, the right and left output field intensities as a function of θ and $\Delta\omega$ for a symmetric interferometric excitation [$|\varepsilon_{\mathrm{in,R}}|^2 = |\varepsilon_{\mathrm{in,L}}|^2$, Eq. (1.106) satisfied]. (c1)-(c4) show the output field intensity spectrum for fixed values of $\theta = \{\pm\pi, \pi/4, \pi/2, -\pi/2\}$. The blue and red curves correspond to the right and the left output field intensities, respectively. The used coefficients are: $\Gamma = \gamma = 6.8$ GHz, $\beta_{\mathrm{tot},12} = 4$ GHz, $\beta_{\mathrm{tot},21} = \beta^*_{\mathrm{tot},12} = 4$ GHz and $\omega_0 = 2\pi \cdot 193$ THz.

$\tilde{\beta} = \sqrt{r}|\beta_{\text{tot},12}|$ and $\tilde{\gamma} = 0$, so the difference of the two eigenvalues would only be real and consequently the two Lorentzians would have the same FWHM, see Fig. 1.14.

Another special non-Hermitian case is when $|\beta_{\text{tot},12}| = |\beta_{\text{tot},21}|$, because as discussed before it is possible to use the symmetric interferometric excitation. Furthermore, when $\arg[\beta_{\text{tot},12}\beta_{\text{tot},21}] = 0$ (i.e. when $\sin[\arg[\beta_{\text{tot},12}\beta_{\text{tot},21}]/2] = 0$), then $\beta_{\text{tot},21} = \beta^*_{\text{tot},12}$, $\tilde{\beta} = 0$ and $\tilde{\gamma} = |\beta_{\text{tot},12}|$. In this situation, the difference of the two eigenvalues is only imaginary and consequently the two Lorentzians would be centered at ω_0 and the FWHMs would be different, see Fig. 1.15. In particular, one would have $|n| = \tilde{\gamma}$ and thus for the supermode with $\lambda_1 = \omega_0 - \tilde{\beta} - i(\gamma - \tilde{\gamma} + \Gamma) = \omega_0 - i(\gamma - |n| + \Gamma)$, using the interferometric excitation, one is able to completely remove the losses due to the non-Hermitian BS.

1.4 Time response

In the previous sections, we focused on the spectral responses of a MR with or without backscattering, analyzing only the steady state. In fact, we neglected the time dependence of the field amplitudes. In this section, we will calculate the time response of a MR from the equations of the TCMT. The study of the time response is important for resonators with ultra-high Q [110, 130, 131, 132]. In fact, in these cases, the resonance of the MR is spectrally too narrow, and therefore the Cavity Ring-Down (CRD) technique is used to determine the main characteristics of the MR [133, 103, 134]. This technique takes advantage of the fact that MRs with ultra-high Q have relatively long charge and discharge times which can be detected with fast detectors.

In Sec. 1.4.1 I will present the time response of a MR when it is excited on one side only (standard method). Then I will describe the three coupling regimes from the point of view of the time response. Next, I will introduce backscattering inside the MR, which will cause a distortion in the usual exponential discharge of the MR.

Finally, in order to derive the characteristic parameters of the two supermodes of the MR with BS, for example the Qs, I will use the interferometric excitation described in Sec. 1.3 also in the study of the time response.

1.4.1 Ideal microresonator

In an ideal MR the two counterpropagating modes are not coupled [Eq. (1.27)] and the MR has the same response in both transmission and reflection. Therefore, without loss of generality, we focus only on the CCW mode excited by the electric field $E_{in,L}$ coming from the left side of the WG. We therefore write

$$i\frac{d\alpha}{dt} = (\omega_0 - i\gamma_{tot})\alpha - \sqrt{2\Gamma}\,E_{in,L}\,, \tag{1.115}$$

$$E_{out,L} = E_{in,L} + i\,\sqrt{2\Gamma}\,\alpha\,. \tag{1.116}$$

To compute the time response of the MR, we solve the system of Eq. (1.115) using Green's function $G[t]$. This function is defined as the solution of a differential equation when its forcing is equal to a Dirac delta function ($\delta[t]$) [135]. Thus, using an impulse excitation from left ($E_{in,L}[t] = \varepsilon_{in,L}\delta[t-t']$, where $\varepsilon_{in,L}$ is the input field amplitude) and taking the Fourier transform of Eq. (1.115), one obtains the spectral Green's function $G[\omega]$ [110]:

$$G[\omega] = -\frac{1}{\sqrt{2\pi}}\frac{\sqrt{2\Gamma}}{\Delta\omega + i\gamma_{tot}}\varepsilon_{in,L}e^{i\omega t'}\,. \tag{1.117}$$

Then the spectral Green's function of the output fields is determined by substituting this solution into Eq. (1.116):

$$G_{out,R}[\omega] = \frac{1}{\sqrt{2\pi}}\varepsilon_{in,L}e^{i\omega t'}\left(1 - \frac{2\Gamma}{-i\Delta\omega + \gamma_{tot}}\right)\,. \tag{1.118}$$

The inverse Fourier transform of $G_{out,R}[\omega]$ is:

$$G_{out,R}[t-t'] = \varepsilon_{in,L}\left(\delta[t-t'] - 2\Gamma\,\Theta[t-t']e^{-i(\omega_0 - i\gamma_{tot})(t-t')}\right)\,, \tag{1.119}$$

where $\Theta[t]$ is the Heaviside function. Now, to obtain $E_{out,R}[t]$, we need to do the convolution of $G_{out,R}[t]$ with the exciting function, $\xi_{in}[t]$:

$$E_{out,R}[t] = \int_{-\infty}^{\infty} G_{out,R}[t-t']\,\xi_{in}[t']dt'\,. \tag{1.120}$$

Let us consider a MR excited by a continuous-wave light pulse of angular frequency ω and a duration equal to Δt [$\xi_{in}[t] = (\Theta[t] - \Theta[t-\Delta t])e^{-i\omega t}$]. We obtain:

$$\begin{aligned} E_{\text{out,R}}[t] = \; & \varepsilon_{\text{in,L}} e^{-i\omega t}\left\{\Theta[t]\left(1-\frac{2\Gamma(1-e^{i(\Delta\omega+i\gamma_{\text{tot}})t})}{-i\Delta\omega+\gamma_{\text{tot}}}\right)\right. \\ & \left.-\Theta[t-\Delta t]\left(1-\frac{2\Gamma(1-e^{i(\Delta\omega+i\gamma_{\text{tot}})(t-\Delta t)})}{-i\Delta\omega+\gamma_{\text{tot}}}\right)\right\}. \end{aligned} \tag{1.121}$$

Figure 1.16 shows $|E_{\text{out,R}}|^2$ as a function of time and frequency detuning for the three coupling conditions. In (a), (b) and (c) the output responses of a MR in the over-, critical- and under-coupling regime are shown. Figure 1.16 shows that for all three coupling regimes, since the square pulse arrives at $t = 0$, the outgoing field quickly reaches 1 and then decays exponentially. After this, the time responses for the three regimes change. In the case of over-coupling, the outgoing field arrives at 0 and then rises again, stopping at the value previously obtained in the stationary regime. This behavior is due to the fact that at the cancellation of the outgoing field, there is a complete destructive interference between the field exiting the MR and that continuing in the bus waveguide. However, immediately thereafter, in the over-coupling regime ($\Gamma > \gamma$), the field coming out of the MR dominates over that continuing in the bus waveguide, causing an increase in $|E_{\text{out,R}}|^2$ and an abrupt change in the phase of the outgoing field at the value of π. In contrast, in the critical-coupling regime ($\Gamma = \gamma$), $|E_{\text{out,R}}|^2$ tends exponentially to 0 (value corresponding to the steady state). Also in the under-coupling regime, the intensity of the outgoing field tends exponentially to the value previously found in the steady state, which this time is not zero. Moreover, in the under-coupling regime, the field does not acquire any phase during the charging of the MR.

At the end of the rectangular pulse of duration Δt, the interference between the field exiting the MR and the field continuing in the bus waveguide is no longer present. In particular, at the time Δt, a sudden positive change of $|E_{\text{out,R}}|^2$ and an exponential discharge of the MR are observed. In all three cases, the outgoing field has a π phase. In the over-coupling regime a peak with an intensity greater than 1 is observed, in the critical-coupling regime the peak reaches 1 and finally in the under-coupling regime the peak remains below 1.

By studying the charge and discharge of the MR, it is easy to derive the important parameters of the MR, such as γ, Γ, and Q. This technique is called the cavity ring-down technique.

1.4.2 Microresonator with backscattering

To derive the time response of a MR with BS we can follow the steps described in Sec. 1.4.1 starting from Eq. (1.88) and Eq. (1.89).

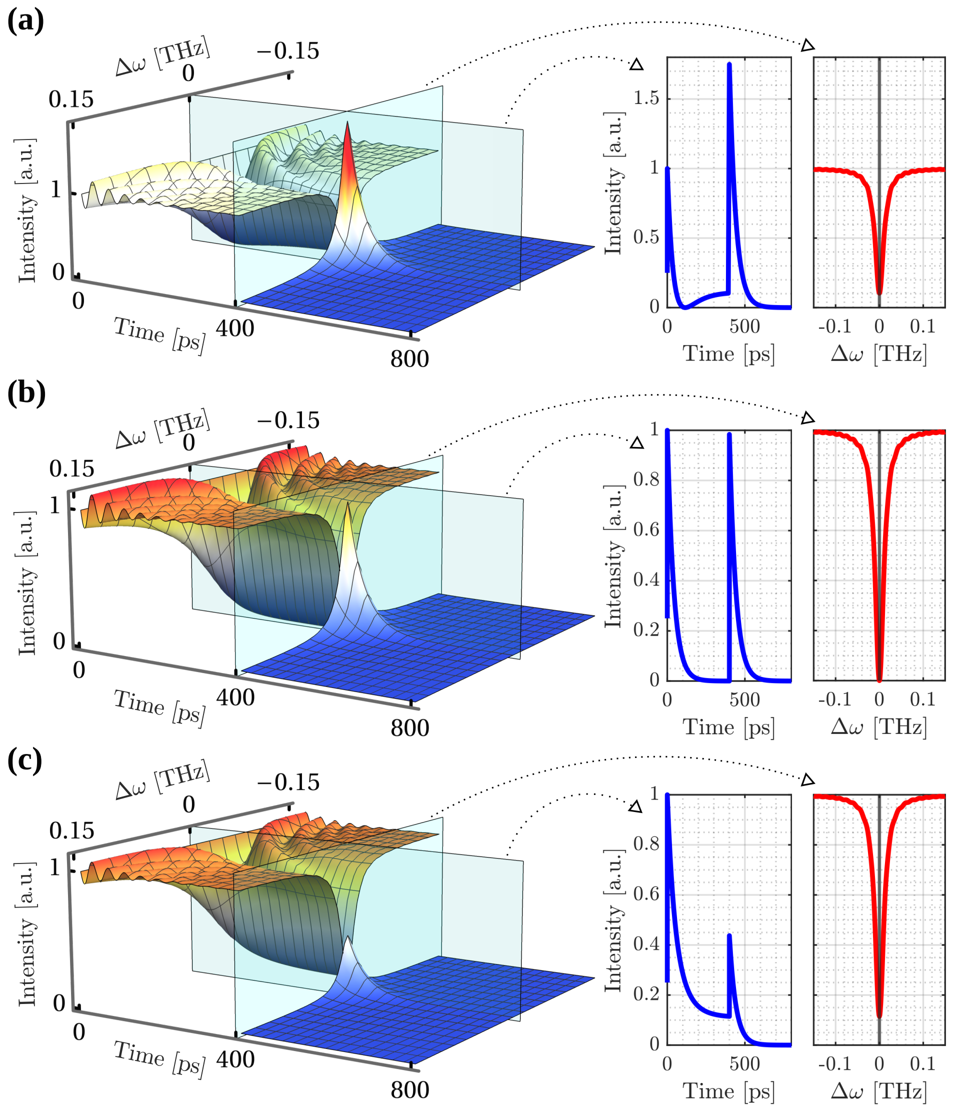

Figure 1.16: (a), (b) and (c) show the time response for an ideal MR in the over-, critical- and under-coupling regimes when a left side excitation with a rectangular pulse shape ($\Delta t = 400$ ps) is used. The input time pulse of intensity 1 a.u. starts at time $t = 0$ and ends at $t = \Delta t$. The first column shows $|E_{\mathrm{out,R}}|^2$ as a function of $\Delta\omega$ and time in a three-dimensional (3D) plot. The second column shows the time response of the MR at $\Delta\omega = 0$. The third column reports the spectral response of the MR at $t \simeq \Delta t$ (quasi-stationary regime). The used parameters are: (a) $\Gamma = 8$ GHz $> \gamma = 4$ GHz, (b) $\Gamma = 6$ GHz $= \gamma = 6$ GHz and (c) $\Gamma = 4$ GHz $< \gamma = 8$ GHz.

The first step is the calculation of the spectral Green's function [103]:

$$\begin{aligned} G_{\text{out},R}[\omega] = &\ \frac{1}{\sqrt{2\pi}}\varepsilon_{\text{in},L}e^{i\omega t'}\left(1-\frac{2\Gamma(-i\Delta\omega+\gamma_{\text{tot}})}{(-i\Delta\omega+\gamma_{\text{tot}})^2-\beta_{\text{tot},12}\beta_{\text{tot},21}}\right) \\ &+\frac{1}{\sqrt{2\pi}}\varepsilon_{\text{in},R}e^{i\omega t'}\left(\frac{2\Gamma\beta_{\text{tot},12}}{(-i\Delta\omega+\gamma_{\text{tot}})^2-\beta_{\text{tot},12}\beta_{\text{tot},21}}\right)e^{i\phi}\,. \end{aligned} \tag{1.122}$$

Then its Fourier transform is calculated:

$$\begin{aligned} G_{\text{out},R}[t-t'] = &\ \varepsilon_{\text{in},L}\left\{\delta[t-t']-\Gamma\Theta[t-t']\left(e^{-i(t-t')\lambda_1}+e^{-i(t-t')\lambda_2}\right)\right\} \\ &+\sqrt{\frac{\beta_{\text{tot},12}}{\beta_{\text{tot},21}}}\varepsilon_{\text{in},R}\Gamma\Theta[t-t']\left(e^{-i(t-t')\lambda_2}-e^{-i(t-t')\lambda_1}\right)e^{i\phi}\,, \end{aligned} \tag{1.123}$$

where $\lambda_{1/2}=\omega_0-i\gamma_{\text{tot}}\pm i\sqrt{\beta_{\text{tot},12}\beta_{\text{tot},21}}$ are the system eigenvalues, see Eq. (1.90). Then, the convolution of $G_{\text{out},R}[t]$ with the exciting function, $\xi_{\text{in}}[t]$, yields to $E_{\text{out},R}[t]$.

Let us excite the MR by a CW pulse of light of angular frequency ω and a duration equal to Δt [$\xi_{\text{in}}[t]=(\Theta[t]-\Theta[t-\Delta t])e^{-i\omega t}$]. We obtain:

$$\begin{aligned} E_{\text{out},R}[t] = &\ e^{-i\omega t}\Bigg\{\Theta[t]\Bigg\{\varepsilon_{\text{in},L}\left(1+\frac{\Gamma(e^{-it\sigma^-}-1)}{i\sigma^-}+\frac{\Gamma(e^{-it\sigma^+}-1)}{i\sigma^+}\right) \\ &+\varepsilon_{\text{in},R}\sqrt{\frac{\beta_{12}}{\beta_{21}}}e^{i\phi}\Gamma\left(\frac{e^{-it\sigma^+}-1}{i\sigma^+}-\frac{e^{-it\sigma^-}-1}{i\sigma^-}\right)\Bigg\} \\ &-\Theta[t-\Delta t]\Bigg\{\varepsilon_{\text{in},L}\left(1+\frac{\Gamma(e^{i(\Delta t-t)\sigma^-}-1)}{i\sigma^-}+\frac{\Gamma(e^{i(\Delta t-t)\sigma^+}-1)}{i\sigma^+}\right) \\ &+\varepsilon_{\text{in},R}\sqrt{\frac{\beta_{12}}{\beta_{21}}}e^{i\phi}\Gamma\left(\frac{(e^{i(\Delta t-t)\sigma^+}-1)}{i\sigma^+}-\frac{(e^{i(\Delta t-t)\sigma^-}-1)}{i\sigma^-}\right)\Bigg\}\Bigg\}, \end{aligned} \tag{1.124}$$

where $\sigma^-=\lambda_1-\omega$ and $\sigma^+=\lambda_2-\omega$.

Single side excitation

The Eq. (1.124) can be used either for an interferometric excitation or for a single-side excitation. For example, to use Eq. (1.124) as a single-side excitation, it is sufficient to set $\varepsilon_{\text{in},L}=1$ a.u. and $\varepsilon_{\text{in},R}=0$.

Figure 1.17 shows $|E_{\text{out},R}|^2$ as a function of the time and the frequency detuning ($\Delta\omega$). In the first row, (a), the graphs corresponding to a MR with a Hermitian BS are shown. Instead, the MR of the second row, (b), is characterized by a non-Hermitian BS. In Fig. 1.17, the first column shows the 3D plots of $|E_{\text{out},R}|^2$, while in the second, the blue curves show the time behavior of $|E_{\text{out},R}[t]|^2$ for $\Delta\omega$ indicated by the vertical black lines in the third column, where the line scans for $|E_{\text{out},R}[\Delta\omega]|^2$ at $t=399$ ps (red curves) are reported, i.e., close to the end of the square pulse.

Figure 1.17 shows that in both cases (Hermitian and non-Hermitian BS) the tem-

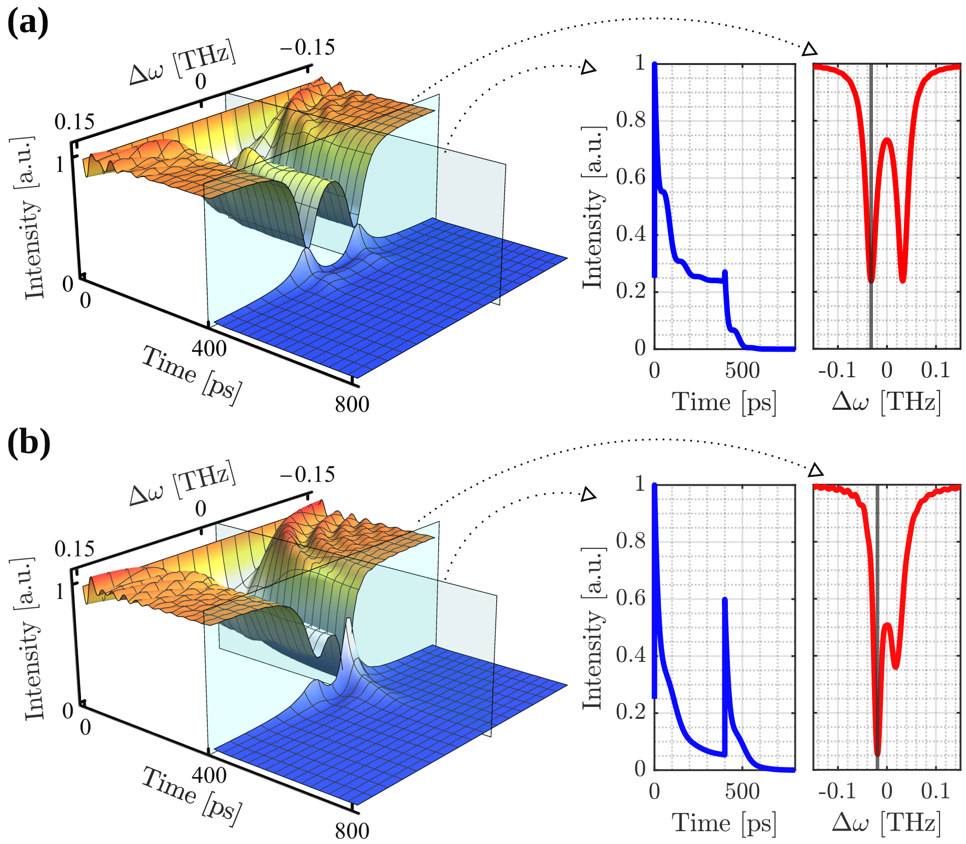

Figure 1.17: (a) and (b) show the time response of a MR characterized by a Hermitian and non-Hermitian BS, respectively. Here, a single-side excitation with a rectangular pulse shape ($\Delta t = 400$ ps) is used. The input time pulse of intensity 1 a.u. starts at time $t = 0$ and ends at $t = \Delta t$. The first column shows $|E_{\mathrm{out},R}|^2$ as a function of $\Delta\omega$ and time in a 3D plot. The second column of panels (a) and (b) shows the time response of the MR at $\Delta\omega$ equal to -33.2 GHz and -19.3 GHz, respectively. The third column reports the spectral response of the MR at $t \simeq \Delta t$ (quasi-stationary regime). The MR parameters in panel (a) are $\Gamma = \gamma = 6.8$ GHz and $\beta_{\mathrm{tot},12} = -\beta_{\mathrm{tot},21} = \beta = 33.2$ GHz. Instead, the MR parameters in panel (b) are $\Gamma = \gamma = 6.8$ GHz, $\beta_{\mathrm{tot},12} = 20.2$ GHz and $\beta_{\mathrm{tot},21} = (-20.2 + 9i)$ GHz. [103]

poral response shows an exponential trend that is superimposed by an oscillatory pattern. The latter is caused by the continuous energy exchange between the CW and CCW modes. This continuous oscillation does not allow to unambiguously determine the characteristic parameters of the MR. In fact, fitting the charging or discharging of the MR with a simple exponential decay leads to errors in parameter estimation. Therefore, the estimation of the Q by the CRD method will also not be accurate.

Interferometric excitation

One way to overcome the continuous energy exchange between the counterpropagating modes of the MR is to use the interferometric excitation method [103, 102]. In particular, as we have seen in Sec. 1.3, it is possible to excite one of the two supermodes of the MR individually by exciting the system from both sides and with a certain relationship between the phases and between the amplitudes of the two fields. The supermodes of the MR do not interact, therefore no energy exchange occurs and the oscillatory pattern is not present.

Hermitian coupling In the case where the backscattering is Hermitian ($\beta_{\mathrm{tot},12} = -\beta^*_{\mathrm{tot},21} = \beta$), the amplitude of the two fields entering from the left and right into the bus waveguide must be equal ($\varepsilon_{\mathrm{in,L}} = \varepsilon_{\mathrm{in,R}} = \varepsilon_{\mathrm{in}}$).

Figure 1.18 (a) shows that by fixing $\phi = \frac{8}{5}\pi$ and with $\Gamma = \gamma$, a preferential exchange of energy towards a given supermode is induced. For this value of ϕ, an unbalanced doublet (different spectral dips) is obtained. In addition, $\phi = \frac{8}{5}\pi$ does not avoid the intensity oscillation during the time evolution, see the temporal profile. The asymmetric excitation of the two supermodes is also observed in the discharge ($t > \Delta t$). Indeed, when the inputs are switched off, the outgoing intensity field exhibits a larger peak for the negative supermode ($\Delta\omega < 0$) than for the positive one ($\Delta\omega > 0$).

As seen in Sec. 1.3, to excite a single supermode it is necessary to satisfy not only the relation between the intensities of the incoming fields, but also a specific phase relation. In particular, to excite the first supermode corresponding to the eigenvalue $\lambda_1 = \omega_0 - |\beta| - i(\gamma + \Gamma)$ [see Eq. (1.110) and Eq. (1.113)] it is necessary to satisfy Eq. (1.107) and thus have $\theta = +\pi/2 + 2\pi m$ (with $m \in \mathbb{Z}$), see Eq. (1.108). On the other hand, to excite only the second supermode, $\mathfrak{s}_2$, which corresponds to $\lambda_2 = \omega_0 + |\beta| - i(\gamma + \Gamma)$, one needs $\theta = -\pi/2 + 2\pi m$, see Eq. (1.108).

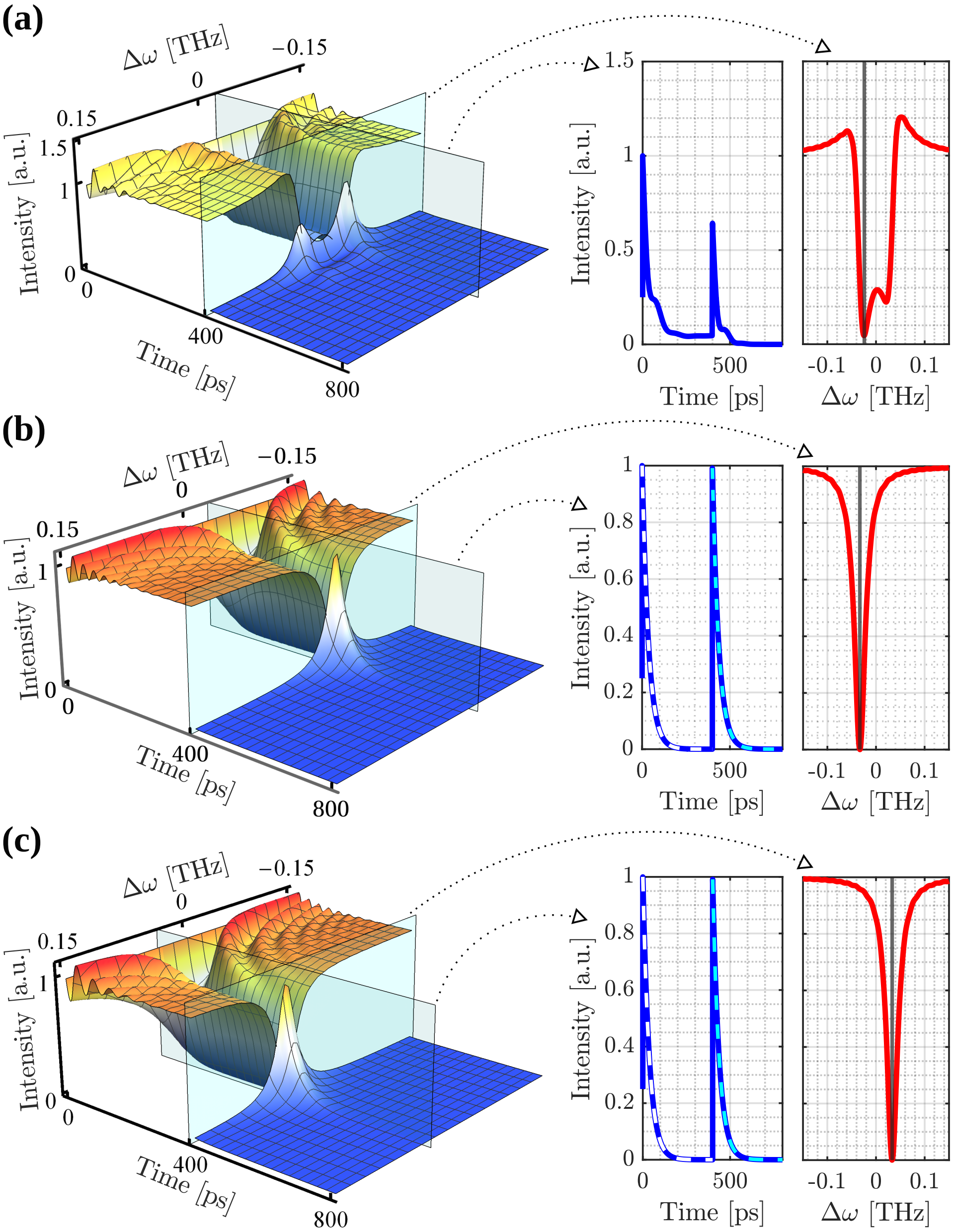

Figure 1.18: Time response of a MR characterized by a Hermitian BS when an interferometric excitation with a rectangular pulse shape ($\Delta t = 400$ ps) is used. The input time pulse of intensity 1 a.u. starts at time $t = 0$ and ends at $t = \Delta t$. In (a), (b) and (c) the phase θ is equal to $\pi/10$, $+\pi/2$ and $-\pi/2$, respectively. The first column shows $|E_{out,R}|^2$ as a function of $\Delta\omega$ and time in a 3D plot. The second column of panels (a), (b) and (c) shows the time response of the MR at $\Delta\omega = -24$ GHz and at the resonant frequency of the first or second supermode ($\Delta\omega = \mp\beta = \mp 33.2$ GHz), respectively. The dashed lines underline the perfect exponential decay. The third column reports the spectral response of the MR at $t \simeq \Delta t$ (quasi-stationary regime). The MR parameters are $\Gamma = \gamma = 6.8$ GHz and $\beta_{tot,12} = -\beta_{tot,21} = \beta = 33.2$ GHz. [103]

Panels (b) and (c) of Fig. 1.18 show the interferometric excitation of the first and the second supermode, respectively. Here, a single dip/peak in the transmission is observed during both charging and discharging of the MR. In addition, the oscillations due to the interference between the two supermodes are no longer present. Therefore, it is possible to use the interferometric CRD technique to extrapolate the MR parameters, such as the Q, by an exponential fit. In fact, using: $\varepsilon_{\mathrm{in},R} = \varepsilon_{\mathrm{in},L} = \varepsilon_{\mathrm{in}}$ and $\phi_{1/2} = \frac{\arg[\beta_{\mathrm{tot},21}/\beta_{\mathrm{tot},12}]}{2} + \frac{\pi}{2} \pm \frac{\pi}{2} + 2\pi m$ $(m \in \mathbb{Z})$, Eq. (1.124) reduces to:

$$\begin{aligned}|E_{\mathrm{out},R}[t]|^2 = \varepsilon_{\mathrm{in}}^2 \Bigg| &\Theta[t] \frac{\gamma-\Gamma-i(\Delta\omega\pm|\beta|)+2\Gamma e^{-t(-i(\Delta\omega\pm|\beta|)+\gamma+\Gamma)}}{\gamma+\Gamma-i(\Delta\omega\pm|\beta|)} \\ &- \Theta[t-\Delta t] \frac{\gamma-\Gamma-i(\Delta\omega\pm|\beta|)+2\Gamma e^{-(t-\Delta t)(-i(\Delta\omega\pm|\beta|)+\gamma+\Gamma)}}{\gamma+\Gamma-i(\Delta\omega\pm|\beta|)} \Bigg|^2 .\end{aligned} \tag{1.125}$$

Considering only the MR discharge ($t > \Delta t$):

$$|E_{\mathrm{out},R}[t]|^2 = e^{-2(\gamma+\Gamma)t} \left(\frac{4\varepsilon_{\mathrm{in}}^2 \Gamma^2 \left(1+e^{2\Delta t(\gamma+\Gamma)} - 2e^{\Delta t(\gamma+\Gamma)} \cos[\Delta\omega\pm|\beta|]\right)}{(\gamma+\Gamma)^2+(\Delta\omega\pm|\beta|)^2} \right) , \tag{1.126}$$

namely, the product of a constant by an exponential decay function with a time constant $\tau_{\mathrm{ph}} = \frac{1}{2(\gamma+\Gamma)} = \frac{Q}{\omega_0}$, see dashed cyan line in Fig. 1.18 (b) and (c). Note that the discharge of the MR follows a simple exponential decay even for $\Delta\omega \neq \mp|\beta|$. This is interesting experimentally because it relaxes the requirement for high-precision spectral control of the input frequency in CRD measurements.

In Fig. 1.18, given that $\Gamma = \gamma$ and the BS is Hermitian, we have that both supermodes have the same Q and furthermore are in the critical-coupling regime, in fact in the stationary regime ($t \simeq \Delta t$) at zero detuning ($\Delta\omega = 0$) the transmission is zero.

Non-Hermitian coupling In the non-Hermitian case the CW and the CCW modes have two different coupling rates $\beta_{\mathrm{tot},12}$ and $\beta_{\mathrm{tot},21}$. As explained in Sec. 1.3, to excite one of the two supermodes individually, it is necessary to excite the system simultaneously from both sides (interferometric excitation), satisfying Eq. (1.106), Eq. (1.107) and Eq. (1.108), namely $\frac{|\varepsilon_{\mathrm{in},R}|}{|\varepsilon_{\mathrm{in},L}|} = \sqrt{\frac{|\beta_{\mathrm{tot},21}|}{|\beta_{\mathrm{tot},12}|}}$, $\phi_{1/2} = \frac{\arg[\beta_{\mathrm{tot},21}/\beta_{\mathrm{tot},12}]}{2} + \frac{\pi}{2} \pm \frac{\pi}{2} + 2\pi m$, and $\theta_{1/2} = \pm\frac{\pi}{2} + 2\pi m$ $(m \in \mathbb{Z})$. Under these conditions, the transmission doublet merges into a single Lorentzian, see Fig. 1.19.

Even in the non-Hermitian case, the temporal response of the MR no longer shows the intensity oscillations. Furthermore, for $\Delta\omega < 0$ (panel (a) of Fig. 1.19) the typical behavior of a MR in the over-coupling regime is observed [110, 103]. In fact, the outgoing intensity reaches a zero value before the steady state and

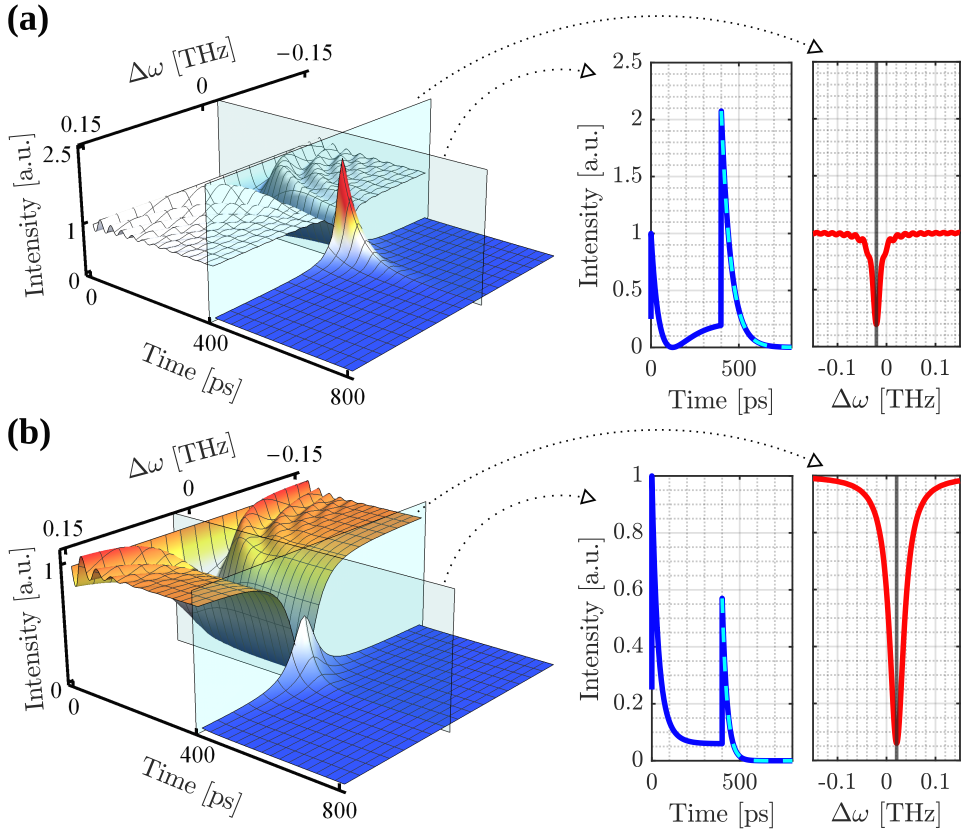

Figure 1.19: Time response of a MR characterized by a non-Hermitian backscattering when an asymmetric interferometric excitation [Eq. (1.106) satisfied] with a rectangular pulse shape ($\Delta t = 400$ ps) is used. The input time pulse of intensity 1 a.u. starts at time $t = 0$ and ends at $t = \Delta t$. In (a) and (b) the phase θ is equal to $+\pi/2$ and $-\pi/2$, respectively. The first column shows $|E_{out,R}|^2$ as a function of $\Delta\omega$ and time in a 3D plot. The second column shows the time response of the MR at the resonant frequency of the first or second supermode. Here, the dashed lines highlight the perfect exponential decay. The third column shows the spectral response of the MR at $t \simeq \Delta t$ (quasi-stationary regime). The MR parameters are $\Gamma = \gamma = 6.8$ GHz, $\beta_{tot,12} = 20.2$ GHz and $\beta_{tot,21} = (-20.2 + 9i)$ GHz. In panels (a) and (b), the black line shows $\Delta\omega$ equal to $-\tilde{\beta}$ and $\tilde{\beta} \simeq 20.7$ GHz, respectively. [103]

also reaches a value greater than 1 at the beginning of the discharge. The second supermode behaves differently. In particular, it is observed that for $\Delta\omega > 0$ (panel (b) of Fig. 1.19) the MR exhibits a time response typical of a single-mode MR in the under-coupling regime, see Fig. 1.16. In fact, this time the output intensity does not go to zero and at the beginning of the MR discharge the intensity does not reach 1. The different coupling regime of the two supermodes is due to two factors. First, we have that $\Gamma = \gamma$, so in the absence of a non-Hermitian backscattering the supermodes would be in the critical-coupling regime. Furthermore, we have that $\tilde{\gamma} \neq 0$, so one supermode will have less loss (over-coupling) and the other will have more loss (under-coupling). In the general case, one can use the eigenvalues of the system $\lambda_{1/2} = \omega_0 \mp \tilde{\beta} - i(\gamma \mp \tilde{\gamma} + \Gamma)$ to determine the coupling regime of the two supermodes. In fact, if $(\Gamma < \gamma - \tilde{\gamma})$ or $(\Gamma = \gamma - \tilde{\gamma})$ or $(\Gamma > \gamma - \tilde{\gamma})$, the first supermode ($\mathfrak{s}_1$) will be in under- or critical- or over-coupling, respectively. On the other hand, if $(\Gamma < \gamma + \tilde{\gamma})$ or $(\Gamma = \gamma + \tilde{\gamma})$ or $(\Gamma > \gamma + \tilde{\gamma})$ the second supermode ($\mathfrak{s}_2$) will be in under- or critical- or over-coupling, respectively. Note that the different coupling regime and Qs of the two supermodes are appreciated also in the discharging time. In fact, the first supermode has a faster decay time than the second supermode. Note that this is always true since $\tilde{\gamma} \geqslant 0$. However, it is possible to swap the spectral position of the supermodes by changing the phase of $\beta_{tot,12}$ and $\beta_{tot,21}$.

To show that the MR supermodes follow the same behavior as a single-mode MR, we enter the conditions for exciting a single supermode [Eq. (1.106), Eq. (1.107) and Eq. (1.108)] in Eq. (1.124), and get:

$$\begin{aligned} E_{out,R}[t] = \tfrac{\varepsilon_{in,L} e^{-i\omega t}}{i(\gamma+\Gamma\mp\tilde{\gamma})+\Delta\omega\pm\tilde{\beta}} \Big\{ \Theta[t] \Big(2i\Gamma e^{it(\Delta\omega\pm\tilde{\beta}+i(\gamma+\Gamma\mp\tilde{\gamma}))} \\ + i(\gamma - \Gamma \mp \tilde{\gamma}) + \Delta\omega \pm \tilde{\beta} \Big) \\ -\Theta[t-\Delta t] \Big(2i\Gamma e^{i(t-\Delta t)(\Delta\omega\pm\tilde{\beta}+i(\gamma+\Gamma\mp\tilde{\gamma}))} \\ + i(\gamma - \Gamma \mp \tilde{\gamma}) + \Delta\omega \pm \tilde{\beta} \Big) \Big\}. \end{aligned} \tag{1.127}$$

This formula is equivalent to the expression for the field transmitted by a bus waveguide coupled to a single-mode MR unaffected by BS and excited from one side [110, 103]. The only two differences are: the different position of the resonance $\Delta\omega = \mp\tilde{\beta}$ and the different rate of intrinsic losses $\gamma \to \gamma \mp \tilde{\gamma}$.

In the discharging, the outgoing intensity reduces to the product of a constant by an exponential decay function (see dashed cyan lines in Fig. 1.19):

$$|E_{out,R}[t]|^2 = e^{-2(\gamma+\Gamma\mp\tilde{\gamma})t} \frac{4\varepsilon_{in,L}^2 \Gamma^2 \left(1+e^{2\Delta t(\gamma+\Gamma\mp\tilde{\gamma})} - 2e^{\Delta t(\gamma+\Gamma\mp\tilde{\gamma})} \cos\left[\Delta\omega\pm\tilde{\beta}\right]\right)}{(\gamma+\Gamma\mp\tilde{\gamma})^2+(\Delta\omega\pm\tilde{\beta})^2}. \tag{1.128}$$

As in the Hermitian coupling case, the exponential decay is independent of $\Delta\omega$. Here, the time constant is $\tau_{ph} = \frac{1}{2(\gamma \mp \tilde{\gamma} + \Gamma)} = \frac{Q_{1/2}}{\omega_0}$. Note, $\tilde{\gamma}$ is subtracted in the case of the first supermode ($\Delta\omega = -\tilde{\beta}$) and added for the second one ($\Delta\omega = \tilde{\beta}$). From here we can calculate the two Qs of the MR:

$$Q_{1/2} = \frac{\omega_0 \mp \tilde{\beta}}{2(\gamma + \Gamma \mp \tilde{\gamma})} \simeq \frac{\omega_0}{2(\gamma + \Gamma \mp \tilde{\gamma})}. \tag{1.129}$$

Therefore, the simple fitting of the decay of the outgoing intensity allows the estimation of the Q as in the Hermitian case. However, in the case of Hermitian coupling, since $\tilde{\gamma} = 0$ and $\tilde{\beta} \ll \omega_0$, the Qs of the two supermodes are equal and independent of $\beta_{tot,12/21}$ (they depend only on γ and Γ). In the non-Hermitian case, we generally have $\tilde{\gamma} \neq 0$. Therefore, the two supermodes have different Qs. Note that γ contains also the losses due to the non-Hermitian BS, so reducing γ to $\gamma - |\tilde{\gamma}|$ does not mean that the supermode has lower losses than if the BS were zero, but it means that we remove most of the losses caused by the non-Hermitian BS. We can define the ultimate Q as the highest Q between those of the two supermodes.

In conclusion, using interferometric excitation, it is possible to measure the Q of a MR even when it is affected by BS. This is true not only in the steady state, via the spectral response, but also in the transient regime and thus via the time response of the MR.

1.5 Experimental Measurements

In this section, we describe the experimental setup we have built to perform measurements on different types of MRs. In particular, this setup is designed to simultaneously measure both the transmission and reflection of the device under test. In addition, it is possible to quickly switch from left to right excitation or to the interferometric excitation (simultaneous excitation from both directions).

Then, in Sec. 1.5.3 I will show some measurements made on integrated MRs. Here, both almost completely Hermitian and non-Hermitian BS will be observed. In addition, the new interferometric technique introduced in Sec. 1.3 will be used to transform a transmission doublet into a single Lorentzian centered on the real part of its eigenvalue and with FWHM equal to twice the absolute value of the imaginary part of the eigenvalue.

1.5.1 Experimental Setup

The experimental setup for the simultaneous measurement of transmission and reflection spectra is shown in Fig. 1.20. With this setup it is possible to measure in both single excitation and interferometric configurations [102]. The experimental setup is based on an interferometric scheme where we use both arms to realize the interferometric excitation or only one arm to obtain the spectral response of a single-side excitation.

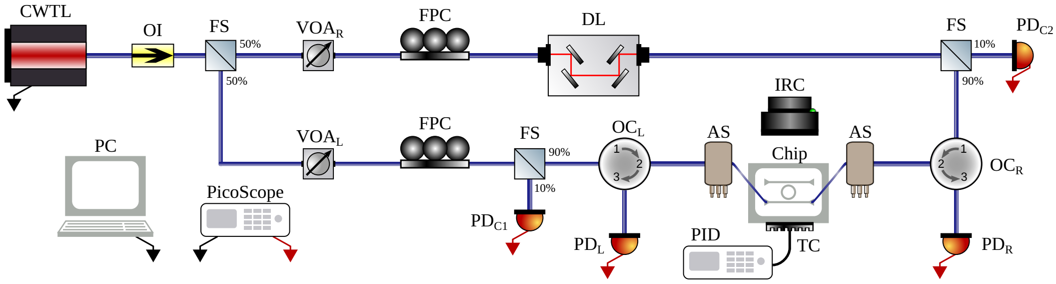

Figure 1.20: Scheme of the used experimental setup. It is composed by: a Continuous Wave Tunable Laser (CWTL) as light source, an Optical Isolator (OI) to protect the laser from the backscattered light, a 50/50 Fiber Splitter (FS) to separate the laser beam in two, two Variable Optical Attenuators (VOAs) to tune the light intensity, two Fiber Polarization Controllers (FPCs) to set the correct light polarization, a Delay Line (DL) to balance the optical length path of the two arms, two 10/90 Fiber Splitters (FSs) to measure the intensity in the two arms, two Optical Circulators (OCs) to excite and simultaneously measure the spectral responses, two Alignment Stages (ASs) and one Infrared Camera (IRC) to align the stripped optical fiber to the chip, one Temperature Controller (TC) and one Proportional–Integral–Derivative controller (PID) to control the chip temperature, four photodetectors (PDs) and one PC Oscilloscope (PicoScope) to measure the spectral responses and a Personal Computer (PC) to control all the instruments. [102]

The source is a Continuous Wave Tunable Laser (CWTL), namely Yenista TUNICS T-100S. This laser works in the third telecom window and more precisely its wavelength can range from 1475 nm to 1575 nm, with an accuracy of 1 pm. The output of the laser is fibered, can reach a maximum of about 8 mW and is linearly polarized. To control the laser, a MATLAB® [136] code was implemented that can scan the laser wavelength at different speeds. This program also commands the PC Oscilloscope (PicoScope), a PC oscilloscope, which is used to measure both the laser sync signal and the output voltages from the photodetectors (PDs). After the laser, a fiber Optical Isolator (OI) was inserted to protect the Continuous Wave Tunable Laser (CWTL) from any retroreflection which causes power instabilities or even laser failure. Then, the optical path is divided into two paths by using a 50/50 Fiber Splitter (FS). This allows exciting our sample from both sides (interferometric excitation). Two Variable Optical Attenuators (VOAs) controlled by the PC and a voltage generator are inserted on each of the two arms. The VOAs are used to control the optical power in the two paths and, in particular, to switch off one excitation direction (left or right). After the VOAs, a Fiber Polarization Controller (FPC) sets the correct polarization, in our case Tranverse Electric (TE), on the grating of the bus waveguide in the chip under consideration. In fact, most of the integrated structures presented in this thesis have been realized by using single mode WGs that only guide the TE polarization. After the fiber polarization controllers in one of the two arms, a Delay Line (DL) in air was inserted in order to compensate for the difference in optical length between the fibers on the two arms. Since the refractive index of the fiber has a different behavior as a function of wavelength than that of air (which remains almost constant), care was taken to keep the delay line as short as possible, about 5 cm. Then, to control the optical intensities in the two arms, two 90/10 fiber splitters are inserted, as shown in Fig. 1.20. On the 10% path, two indium gallium arsenide (InGaAs) photodetectors (PDs) with variable gain are used to monitor the light intensity. On the contrary, 90% of the signal is fiber coupled to an Optical Circulator (OC). The optical circulator is a three ports device that is designed to allow light to travel in only one direction. In particular, only the following paths are allowed: $1 \rightarrow 2$ and $2 \rightarrow 3$. Therefore the paths $2 \rightarrow 1$ and $3 \rightarrow 2$ are forbidden (they have a large isolation). In this scheme, the optical circulators are essential to measure the transmission and reflection spectra of the system simultaneously. They are also needed to be able to excite from both directions simultaneously and measure the spectral responses at the same time. Therefore, optical circulator port number 2 of the Optical Circulators (OCs) transmits the optical signal towards the device under test, while optical circulator port number 3 is coupled to an InGaAs variable gain PDs to measure the spectral responses of the device under test. The PDs are PDA10CS2 from Thorlabs, InGaAs switchable gain amplified detectors with a bandwidth of about 13 MHz operating in the $900 - 1700$ nm range. After the optical circulators there are the Alignment Stages (ASs) with angled supports needed to properly align the stripped optical fibers with the gratings of the integrated structures. The chip is placed on a copper block that can be heated or cooled by a Peltier cell, which is attached to a heat sink by thermal paste. The sample holder is attached with a thermally non-conductive material to a 4-axis stage to move the sample to the desired position. The temperature is controlled by a 10 kΩ thermistor in contact with the copper block, a constant current generator of about 500 µA, a Peltier cell and a Proportional–Integral–Derivative controller (PID). In this way, we are able to keep the chip temperature stable and thus have no drift in the resonance wavelengths. All the instruments, in particular the CWTL, the two VOAs and the PicoScope, are connected and programmable from a PC via MATLAB®. The PicoScope is connected to all PDs and the sync signal of the CWTL and is used to record the experimental measurements and spectra. There is also an Infrared Camera (IRC) to observe the structures on the chip and to ease the alignment of the fibers with the gratings.

In order to minimize the reflections due to the refractive index change at the transition between fiber, air and WG, we used glycerol as an index-matching material. This allowed us to reduce the spurious reflections by an additional order of magnitude and avoid strong Fabry-Pérot (FP) effects. Note that in this experimental setup it is very important to have very low reflections because we are not only interested in the transmission spectra but also in the reflection ones. Moreover, while it is easy to obtain equal transmissions, the couplings between the optical fibers and waveguides must be very similar to have the correct balance of reflections. In fact, the left reflection is affected twice by the left fiber grating coupling, while the right reflection is affected twice by the right fiber grating coupling. Instead, both transmissions are affected by both couplings. For this reason, the experimental setup was calibrated periodically. All fibers were cleaned, delay line was realigned, detectors were recalibrated, and stripped fibers were checked/cut again. All this was done to be sure of the symmetry of the experimental setup.

The reported spectral responses are normalized by the spectral transmission response of the gratings (Gaussian shape due to the coupling between a fiber and a grating).

1.5.2 Integrated photonic circuits/samples

The measurements reported in this section were performed on integrated photonic circuits fabricated by the IMEC/Europractice facility within the multi-project wafer program. The design of the MRs, whose experimental measurements I will report in this section, was carried out by other components of the Nanoscience Laboratory of the University of Trento. The integrated photonic circuit is realized in Silicon-on-Insulator (SOI). In particular, a single mode waveguide TE with a cross section of 450 nm $\times$ 220 nm was used. The WGs are realized in Si and surrounded by a cladding in SiO_2.

1.5.3 Results

The studied MRs are in the add-drop configuration (see Fig. 1.1 (c)) and have a radius of about 7 µm. In addition, the resonators have a gap width between the bus waveguide and the MR of about 250 nm or 300 nm and a coupling length (length of the part where the bus waveguide and the WG of the MR are parallel) of 0 µm or 3 µm (Tab. 1.1).

MR	coupling length [µm]	coupling distance [µm]	Figure
1	3	0.25	1.21
2	3	0.30	1.22
3	0	0.25	1.23
4	0	0.30	1.24

Table 1.1: Design characteristic of the four studied MRs.

In the following, I will present the measured spectral responses of the MRs listed in Tab. 1.1, see Fig. 1.21, Fig. 1.22, Fig. 1.23 and Fig. 1.24. These measurements are exploratory and are intended to present resonances that are characterized by different line shapes. To make the graphs clearer, only one of the two transmission spectra has been plotted. The transmission not shown is actually the same as the other in the region where the whole system was aligned and calibrated (1515–1540 nm). When a single Lorentzian was measured in more detail, the entire experimental setup was calibrated to a wavelength close to the resonance wavelength so that the correct transmission and reflection spectra were obtained.

From Figs. 1.21, 1.22, 1.23 and 1.24 it can be seen that the MRs in Tab. 1.1 are ordered from the MR having wider resonances (smaller Q) to the one with the split but single narrower resonances (larger Q). In all plots, the transmission out of resonance is not constant, but has oscillations. These are due to the spectral response of the input/output gratings and to the Fabry-Pérot formed by weak reflections between the input and the output gratings. At low and high wavelengths, both transmission and reflection spectra show more strain/noise, which can be attributed to several factors, including the grating band and its correction, the alignment and calibration of the polarization, and of the entire experimental setup, which was performed around 1525–1530 nm.

Another feature present in all 4 MRs is the increase in the FWHM of the resonances with increasing wavelength. This is due to the increase in γ_{tot} as a function of wavelength, which is most likely caused by the increase in coupling between the WGs and the MR. In fact, as the wavelength increases, the propagating mode in the WG is less confined and therefore the coupling between two adjacent WGs increases.

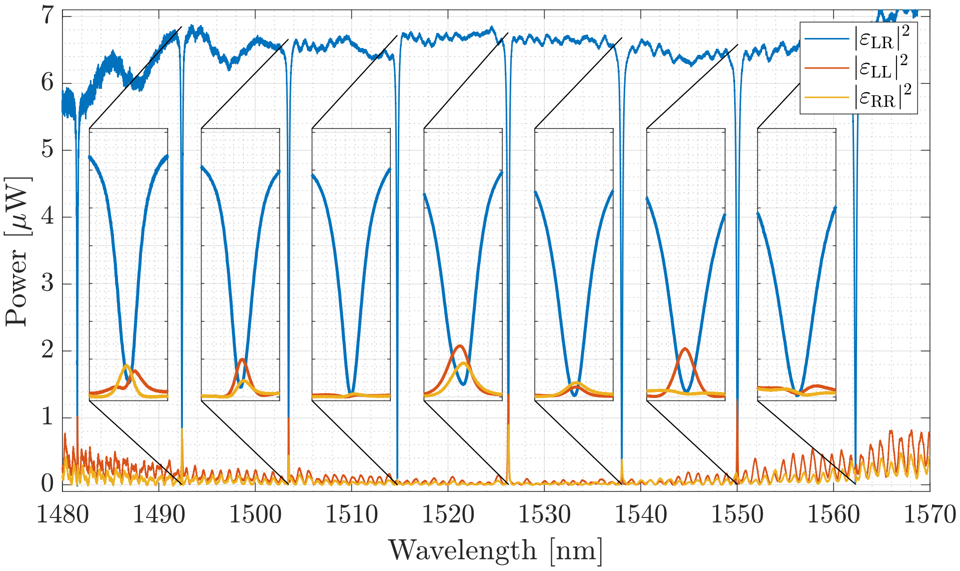

Figure 1.21: Spectral responses of the MR number 1 of Tab. 1.1, in the add-drop configuration. The MR coupling length is 3 μm and the gap between the WGs and the MR is 0.25 μm. The insets show a zoom of the resonances, the range of the ordinates is the same as in the main plot, instead, the range of the wavelengths is 0.4 nm. Each inset refers to the resonance located to its right.

In Fig. 1.21 no splitting of resonances is observed. However, at the same time, the reflections, which in the ideal case (without BS) should be zero, have peaks at the resonances. This means that even if the BS is not large enough to split the resonances, it is present and clearly visible in the reflections. Figure 1.21 shows that the resonances are almost all close to the critical-coupling regime, which is caused by the fact that the couplings between the MR and the bus and drop WGs are equal and the propagation losses within the MR are not large enough to move the MR to an under-coupling regime.

In Fig. 1.22 the coupling rates between the MR and the two WGs are smaller than in the previous graph. It can be observed that the resonances have a smaller FWHM. It is also observed that the resonance around 1493 nm has an asymmetric doublet. This is due to the fact that by increasing the Q of the MR, the BS effect becomes more and more visible.

Further decreasing the coupling rates between MR and WGs yields the spec-

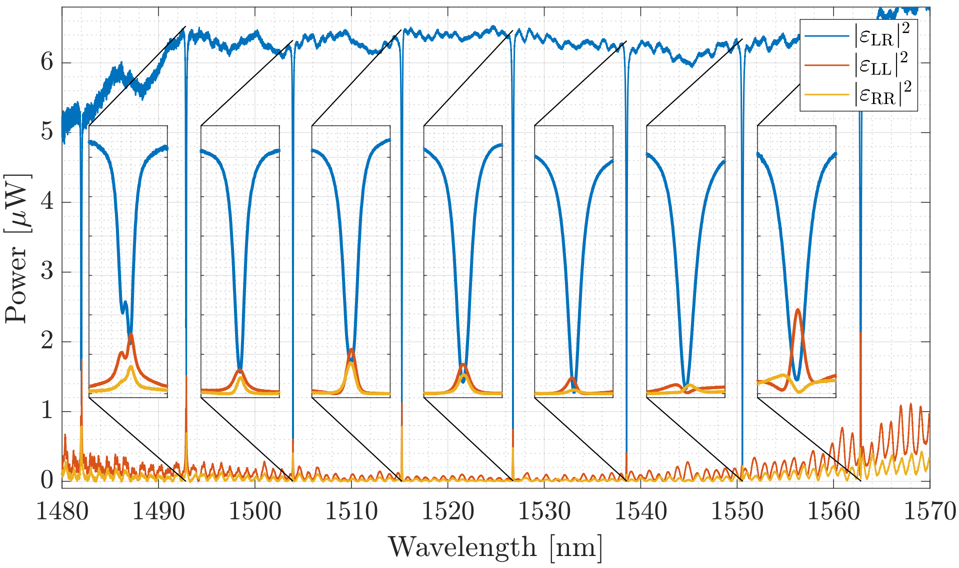

Figure 1.22: Spectral responses of the MR number 2 of Tab. 1.1, in the add-drop configuration. The MR coupling length is 3 µm and the gap between the WGs and the MR is 0.30 µm. The insets show a zoom of the resonances, the range of the ordinates is the same as in the main plot, instead, the range of the wavelengths is 0.4 nm. Each inset refers to the resonance located to its right.

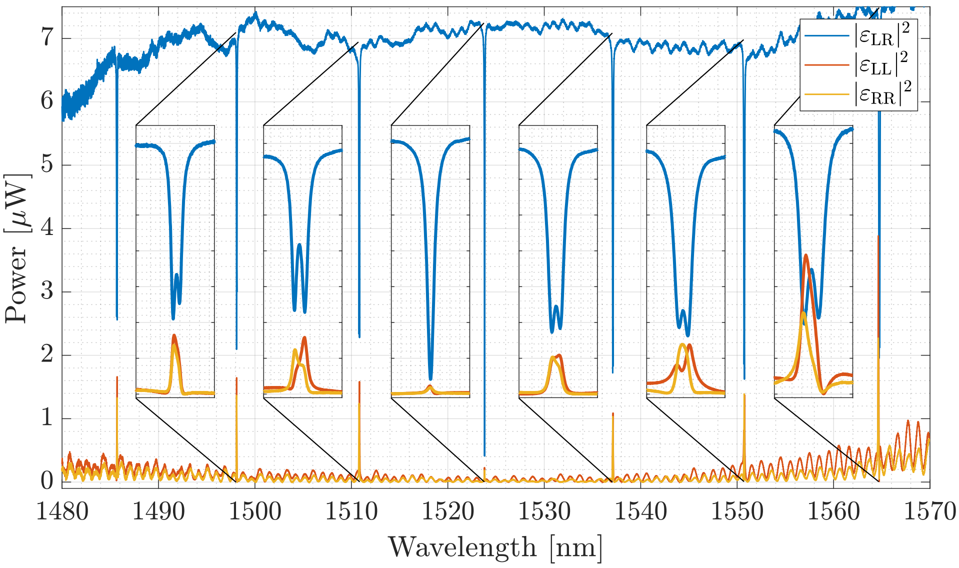

Figure 1.23: Spectral responses of the MR number 3 of Tab. 1.1, in the add-drop configuration. The MR coupling length is 0 µm and the gap between the WGs and the MR is 0.25 µm. The insets show a zoom of the resonances, the range of the ordinates is the same as in the main plot, instead, the range of the wavelengths is 0.4 nm. Each inset refers to the resonance located to its right.

tra in Fig. 1.23. Here all resonances except the one near 1525 nm are split, and in addition, one can see the presence of nearly symmetric resonances and asymmetric resonances. The symmetry or asymmetry of the resonances is given by the Hermiticity or non-Hermiticity of the BS.

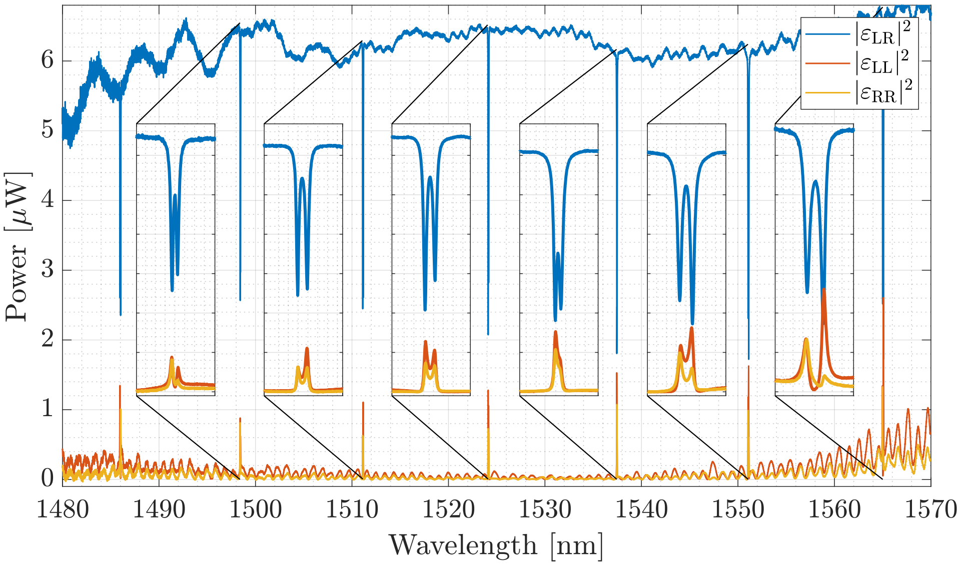

Figure 1.24: Spectral responses of the MR number 4 of Tab. 1.1, in the add-drop configuration. The MR coupling length is 0 µm and the gap between the WGs and the MR is 0.30 µm. The insets show a zoom of the resonances, the range of the ordinates is the same as in the main plot, instead, the range of the wavelengths is 0.4 nm. Each inset refers to the resonance located to its right.

The MR with zero coupling length and with a gap width equal to 0.30 µm, is the MR that ideally has the highest Q among the measured ones. Figure 1.24 shows that all the resonances of this MR exhibit either Hermitian or non-Hermitian splitting. In this graph, as in the others, it is clear that the BS is not constant throughout the spectrum, but each resonance is characterized by a different BS. This is because different wavelengths are affected differently by the surface-wall roughness and are therefore characterized by a different BS coefficient. Furthermore, each WG and thus each MR has its roughness, so it is not possible to derive a general trend of BS in WG as a function of wavelength.

In summary, we have observed that as the ideal Q increases, backscattering due to the surface roughness of the WGs becomes increasingly relevant and no longer negligible. This significantly limits the maximum Q achievable by silicon integrated MRs.

Let us now analyze two resonances in more detail. In particular, we analyze the resonance around 1525 nm for both 3rd and 4th MR, see Fig. 1.25 and Fig. 1.26.

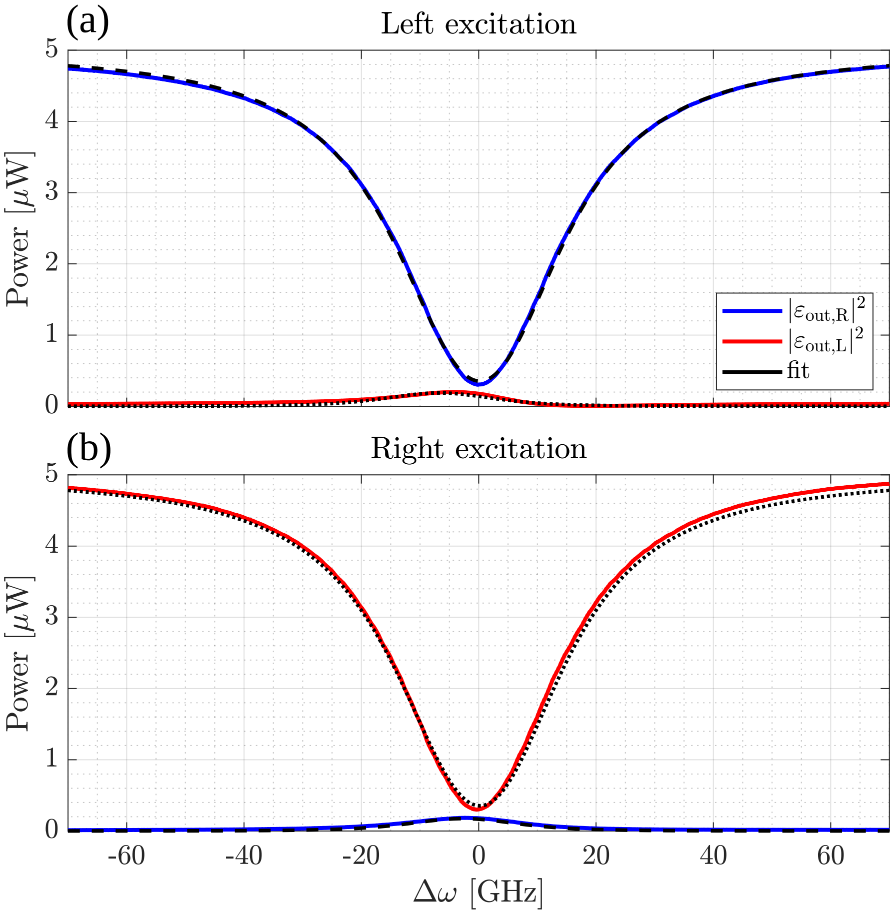

Figure 1.25: Spectral response around 1525 nm of the 3rd MR, see Tab. 1.1. (a) reports the spectral responses when the system is excited from left, and (b) when it is excited from right. The blue and red lines are the experimental data for the output intensities measured at the right and left ports, respectively. The dashed lines identify the fits made by the model obtained through the TCMT. The parameters of the fit are listed in Tab. 1.2.

Figure 1.25 shows the spectral responses of the 3rd MR. Here the resonance is not split, and the transmission spectra at the resonance have a dip with a minimum value of 0.3 µW, which is about 1/17 of the transmitted intensity out of the resonance. Note that this is the deepest transmission of this MR and also the only one that is not split. Moreover, the reflection spectra at resonance have a peak of only 0.2 µW, which is about 1/25 of the transmitted intensity out of resonance. This resonance is the one with the lowest BS of this MR. The spectral responses are well fit by the theoretical model of TCMT (Eq. (1.61) and Eq. (1.62)), the fit parameters are given in Tab. 1.2. Figure 1.25 shows that the two transmission spectra are equal. Since the dip in transmission is close to zero, the resonator is close to the critical-coupling configuration. More precisely, the MR is in the under-coupling regime. We can say this because the MR is in the add-drop configuration where the couplings between the WGs are equal, so γ is definitely greater than or at most equal to Γ. In fact, in this case, the parameter γ includes not only the propagation losses, but also the losses due to the coupling of the MR with the drop WG. The fact that the MR is in the under-coupling regime, is also shown in Tab. 1.2, where $\Gamma < \gamma$.

Parameter	Value
λ_0	$1524.61709(1)$ nm
ω_0	$1.23549157(1)$ PHz
γ	$9.54(1)$ GHz
Γ	$6.136(6)$ GHz
$\Re[\beta_{12}]$	$3.91(2)$ GHz
$\Im[\beta_{12}]$	$-0.71(3)$ GHz
$\Re[\beta_{21}]$	$-4.13(2)$ GHz
$\Im[\beta_{21}]$	$-0.15(3)$ GHz
h	$0.43(2) + 4.02(2)i$ GHz
n	$-0.11(2) - 0.28(2)i$ GHz

Table 1.2: Fit parameters for the resonance at $\lambda_0 \simeq 1525$ of the 3rd MR (Fig. 1.25).

Table 1.2 shows how the BS is smaller than the intrinsic and extrinsic decay rates and also turns out to be predominantly Hermitian, in fact, $|h| > |n|$. Since the BS is not very pronounced in this case, the Q computed directly from the spectrum is similar to those computed using the Eq. (1.111), $Q \simeq 4 \times 10^4$.

The resonance shown in Fig. 1.26 is completely different. Here the reflections are much more prominent and the resonance is clearly split. The spectra of Fig. 1.26 are related to the resonance near the wavelength of 1525 nm of the 4th MR in Tab. 1.1, which has a larger gap (0.30 μm) than the one lastly analyzed (0.25 μm). Again, the transmissions are equivalent for left and right excitation, while the reflections are slightly different; in fact, the spectrum in the reflection from the right has higher peaks. The doublets in transmission and reflection are not symmetric with respect to zero detuning, which means that the BS is non-Hermitian. We also observe that the transmission reaches a minimum at 30% of the maximum intensity and therefore there is never a complete constructive interference between the fields continuing in the bus waveguide or leaving the MR.

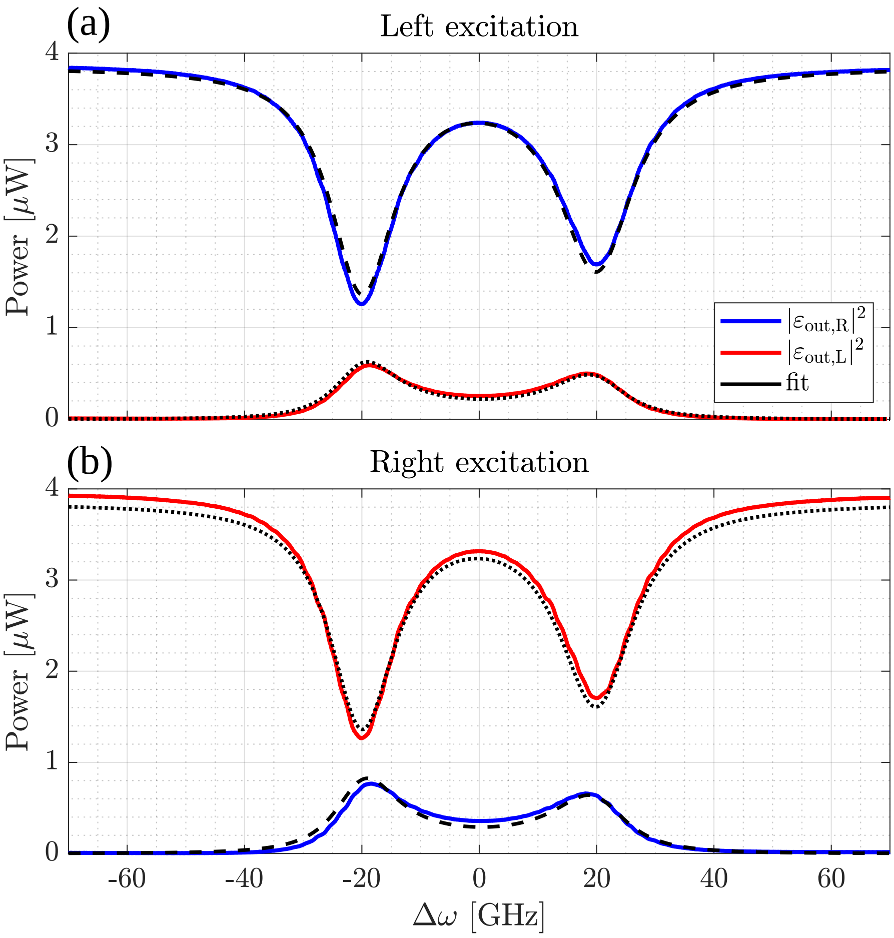

Figure 1.26: Spectral response around 1525 nm of the 4th MR, see Tab. 1.1. (a) reports the spectral responses when the system is excited from left, and (b) when it is excited from right. The blue and red lines are the experimental data for the output intensities measured at the right and left ports, respectively. The dashed lines identify the fits made by the model obtained through the TCMT. The parameters of the fit are listed in Tab. 1.3. [102]

Figure 1.26 shows that even at high BS the theoretical model reported in Sec. 1.2.1 fits well the experimental data. The parameters obtained from the fit are reported in Tab. 1.3. To achieve a greater accuracy in the parameters, a single set of parameters was used to fit the four spectra.

Parameter	Value
λ_0	$1524.94302(1)$ nm
ω_0	$1.235227507(8)$ PHz
γ	$4.56(1)$ GHz
Γ	$2.662(3)$ GHz
$\Re[\beta_{12}]$	$-19.72(2)$ GHz
$\Im[\beta_{12}]$	$-0.2(4)$ GHz
$\Re[\beta_{21}]$	$20.67(2)$ GHz
$\Im[\beta_{21}]$	$0.8(4)$ GHz
h	$-0.3(3) - 20.20(1)i$ GHz
n	$0.48(1) - 0.5(3)i$ GHz

Table 1.3: Fit parameters for the resonance at $\lambda_0 \simeq 1525$ of the 4th MR (Fig. 1.26).

Comparing Tab. 1.3 with Tab. 1.2 we see that the 4th MR has lower intrinsic and extrinsic decay rates as expected. In addition, the BS is much larger in this case and is also larger than both Γ and γ. Although the spectrum is asymmetric, it can be seen that the BS, in this case, is also mainly Hermitian $|h| > |n|$. This causes the MR to have little loss due to the BS ($|n|$ relatively small). The absolute value of the Hermitian part of the BS and of both BS coefficients are about 20 GHz, which causes the resonance to be characterized by two dips/peaks centered at $\Delta\omega \simeq \mp 20$ GHz, see Fig. 1.26. This results in a measured Q value of $\simeq 2.4 \times 10^4$ when using the FWHM of the entire resonance. Using Eq. (1.50), the values in Tab. 1.3 and neglecting the BS, we get $Q \simeq 8.55 \times 10^4$. Using our new definition, which includes the BS and differentiates the two supermodes of the MR [Eq. (1.111)], we get $Q_1 \simeq 9.18 \times 10^4$ and $Q_2 \simeq 8.01 \times 10^4$. This means that the spectral measurement of Q loses its meaning when a single-side excitation (non-interferometric) is used.

Interferometric excitation Since the interferometric excitation technique is based on coupling the light signal in both directions of propagation and having a constant and well-defined relative phase during the spectral measurement, we adjusted the delay line so that the two optical paths after the 50/50 fiber splitter are as equal as possible. In fact, if there is a change in the optical path equal to ΔL, then the relative phase between the two arms will be $\phi \simeq (2\pi\Delta L)/\lambda$. From this formula it is clear that if ΔL is not small enough, the phase will vary rapidly as a function of wavelength, making it impossible to make a spectral measurement in which the phase remains constant during the spectral measurement of a resonance. Since delay line is in air, we must also take into account the fact that the refractive indices of fiber and air do not vary in the same way as a function of wavelength. In fact, this means that the optical path difference ΔL varies as a function of wavelength, causing additional phase variations. To limit this phenomenon, we inserted a fiber segment of appropriate length to shorten the delay line in air as much as possible (5 cm). Since the spectrum of a resonance is about 0.3 nm wide, we were able to have a constant phase in the measurement window. However, this is not enough because since the interferometer is made of fiber, even fiber relaxation, a small change in temperature or airflow will cause the phase in one arm or the other to vary. In order to limit excessive variations in the relative phase between the two arms, we fixed the fibers to the table and made sure that there was as little air circulation as possible. Even with these arrangements, the phase varies over time, but it varies slowly enough to have a constant phase during the measurement of a single spectrum. Specifically, we measured a phase variation rate of $d\phi/dt \leqslant 0.1$ rad/s. Since we use a scan rate of the Continuous Wave Tunable Laser (CWTL) of 1 nm/s, and since the spectral window of interest is 0.3 nm wide, we have that the typical time to acquire a spectrum of a single Lorentzian is about 0.3 s. Consequently, the phase variation during a single scan is about 3×10^{-2} rad and therefore negligible. Using this setup, it is therefore possible to measure the spectral responses produced by the interferometric excitation for different ϕ phases, taking advantage of the fact that this phase varies randomly with time.

A much simpler and more accurate way to perform this type of measurement is to integrate the experimental setup within a chip using well-known and characterized blocks, such as integrated Multi-Mode Interferometers (MMIs), integrated Mach Zhender Interferometers (MZIs), and integrated phase shifters made by, for example, microheaters. In this way, both the intensities and the phases of the two arms of the MZI can be easily varied, and a constant phase can be obtained over almost the entire spectrum. Also, by deterministically varying both phase and amplitudes, the interferometric measurement would be much more accurate and faster.

In our case, the symmetric interferometric excitation is made possible by calibrating each part of the setup and estimating the coupling losses of the gratings, see Appendix B for more details.

To observe the variation of the spectra as a function of phase, 100 spectral measurements were made with a resolution of 0.1 pm. To allow sufficient randomness in the ϕ phases, a guard time of at least 1 s was used between different acquisitions. This is necessary because we cannot control the phase, and therefore we use its temporal variation, e.g. due to fiber temperature fluctuations, to measure spectra corresponding to different ϕ phases of the interferometric excitation.

Since it was not possible to control the phase ϕ value, to determine it we first measured the resonance at a single-side excitation as reported in Fig. 1.26. After fitting the four single-side excitation spectra, we used the obtained fit parameters, leaving only the relative phase between the two excitation fields (ϕ) as a free parameter. With this method, the error in the phase ϕ is 3×10^{-2} rad. Some measured spectra and the results obtained are given in Fig. 1.27 and Fig. 1.28.

The panels (a) and (b) of Fig. 1.27 report the doublet splitting as a function of the phase $\theta := \phi - (\arg[\beta_{\text{tot},21}/\beta_{\text{tot},12}]/2 + \pi/2)$, see Eq. (1.108). The doublet splitting is reported as a frequency detuning with respect to the MR fundamental angular frequency, i.e. $\delta\omega = \omega_{</>} - \omega_0$, where $\omega_<$ and $\omega_>$ are the measured angular frequencies of the two dip minima. In particular, $\omega_<$ refers to the lower angular frequency dip and $\omega_>$ to the higher angular frequency dip. Panels (a) and (b) show the variation of $\delta\omega$ as a function of θ for the right and left output field intensities, respectively. The magenta (purple) colored dots correspond to $\delta\omega = \omega_< - \omega_0$, while the black (gray) squares correspond to $\delta\omega = \omega_> - \omega_0$. The dashed magenta (purple) and dash-dotted black (gray) curves show the theoretical dependencies derived by Eq. (1.61) and Eq. (1.62). Note that the model developed in Sec. 1.2.1 and Sec. 1.3 reproduces the experimental data.

In Fig. 1.28 four examples of the measured interferometric excitation spectra are shown. The blue and red curves represent the experimental spectra relative to the right and left field intensities, respectively. The four panels (a), (b), (c) and (d) are characterized by $\theta = -0.27\pi$, 0.26π, -0.52π and 0.48π, respectively. Here we can see that the interferometric excitation gives very different responses as the relative phase of the two excitation fields varies. It is worth noticing that the experimental data is well fitted by the theoretical model. As predicted by theory (Sec. 1.3), when the phase $\theta = \mp\pi/2$, the interferometric excitation is able to merge the doublet into a single Lorentzian, see panels (c) and (d) of Fig. 1.28. Around these values of θ in Fig. 1.27 the points coincide with squares. Since the two phases are not perfectly $\mp\pi/2$ and since we have used a symmetric interferometric excitation even though $\sqrt{|\beta_{\text{tot},21}|/|\beta_{\text{tot},12}|}$ is not identically equal to 1 [see Eq. (1.106)], the spectra are not

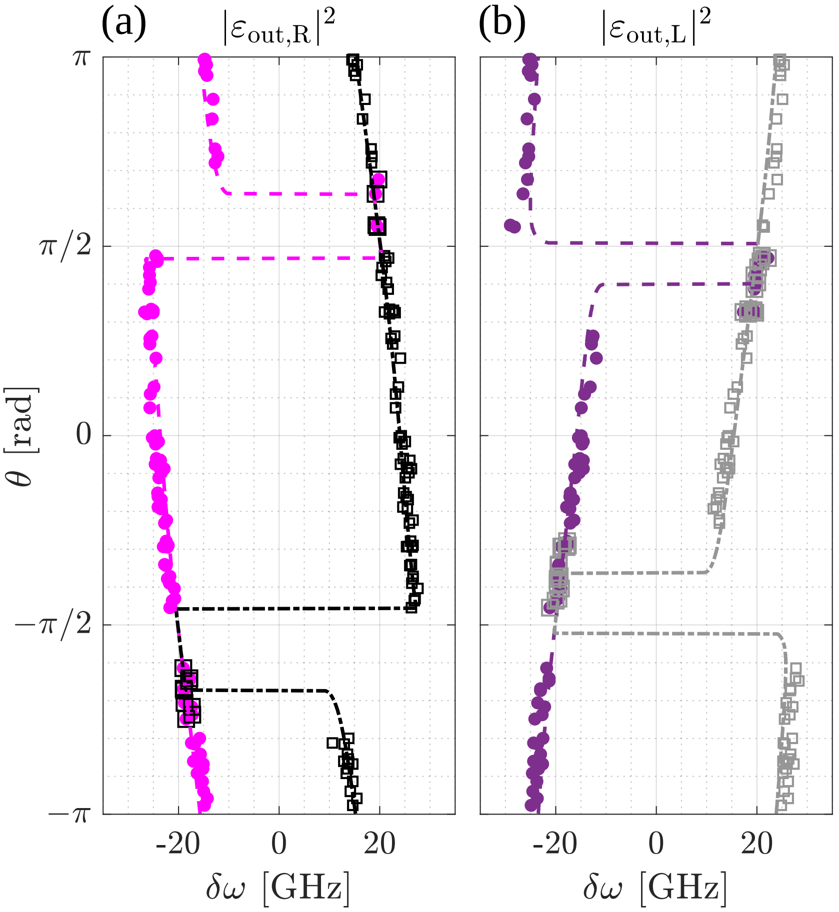

Figure 1.27: The position of the dips as a function of the phase $\theta := \phi - (\arg[\beta_{\mathrm{tot},21}/\beta_{\mathrm{tot},12}]/2 + \pi/2)$ for the right and left output intensities [panels (a) and (b)]. $\delta\omega = \omega_< - \omega_0$ and $\delta\omega = \omega_> - \omega_0$ are the angular frequency detuning for the dip with lower angular frequency ($\omega_<$) and the one with higher angular frequency ($\omega_>$). The experimental data are reported in magenta (purple) dots for $\delta\omega = \omega_< - \omega_0$ and in black (gray) square for $\delta\omega = \omega_> - \omega_0$. The theoretical curves are dashed magenta (purple) and dash-dotted black (gray) for $\omega_<$ and $\omega_>$, respectively. The data correspond to the symmetric interferometric excitation with a wavelength around 1525 nm of the 4th MR (Tab. 1.1). [102]

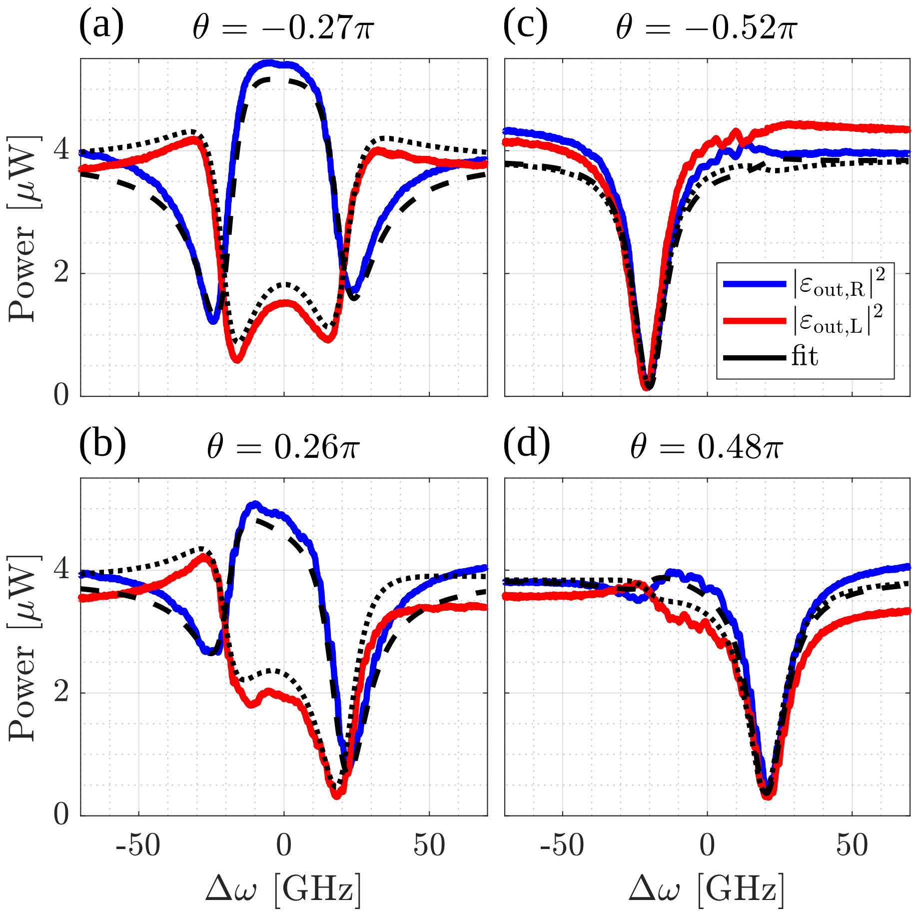

Figure 1.28: Response spectra of the 4th MR at the resonance of around 1525 nm for a symmetric interferometric excitation. Panels (a), (b), (c) and (c) correspond to the phases $\theta = -0.27\pi$, 0.26π, -0.52π and 0.48π. The blue and red curves represent the measured output field intensities at the right and left side, respectively. The black curves report the fit of the experimental data. [102]

perfectly Lorentzian. However, we can say that the spectral responses shown in panels (c) and (d) are hardly different from a Lorentzian one. We can therefore say that by using the interferometric excitation we are able to excite one of the two supermodes of the MR ($\mathfrak{s}_1$ or $\mathfrak{s}_2$). Using this method, we are then able to increase the Q of the MR, calculated using the spectral FWHM, from $Q \simeq 2.4 \times 10^4$ to $Q \simeq 9 \times 10^4$. It is important to note that now the extinction ratio of both dips is also increased with respect to the single-side excitation case. In fact, the first supermode [panel (c)] has the minimum of the dip reaching almost zero. Moreover, it becomes easy to measure both the real and imaginary parts of the eigenvalues λ_1 and λ_2. In fact, the position of the two Lorentzian dips, one in panel (c) and the other in panel (d), corresponds to the real part of the eigenvalues, while their FWHM corresponds to twice the absolute value of the imaginary part of the eigenvalues.

	Single Side Excitation [GHz]	Interferometric Exitation [GHz]
$\lvert\Re[\lambda_{1/2} - \omega_0]\rvert$	20.2 ± 0.3	21.0 ± 0.3
$\Im[\lambda_1]$	-6.73 ± 0.02	-6.8 ± 0.2
$\Im[\lambda_2]$	-7.71 ± 0.02	-7.51 ± 0.07

Table 1.4: Real and imaginary parts of the eigenvalues of the MR. The first column shows the values calculated by using the parameters obtained from the fit of the spectral responses of a single side excitation (Fig. 1.26). The second column shows the values estimated by using a simpler Lorentzian fit of the experimental data reported in panels (c) and (d) of Fig. 1.28. [102]

Table 1.4 shows the comparison between the real and imaginary parts of the eigenvalues derived by a full fit of all the single side spectra (Fig. 1.26) and by a simpler Lorentzian fit of the two merged doublet [panels (c) and (d) of Fig. 1.28]. We use the simple Lorentzian fit to determine the wavelength and FWHM of the resonances of the two supermodes. The two methods of eigenvalues calculation give compatible results. The difference in the values and the greater uncertainty in the estimation of $\Im[\lambda_{1/2}]$ is due to the use of a symmetric interferometric excitation with $\theta \neq \mp\pi/2$, which causes a small perturbation in the Lorentzian line shape.

In summary, we have also demonstrated experimentally that by using the interferometric excitation one can merge the doublet into a single Lorentzian line shape, thereby increasing the Q of the MR and also the extinction ratio. Moreover, by being able to excite a single supermode of the MR, one can measure, either directly from the spectrum or by performing a simple Lorentzian fit, both the real and imaginary parts of the eigenvalues of the system.

Chapter 2

Taiji Microresonator

This chapter discusses a particular MR called the Taiji Microresonator (TJMR). The TJMR consists of a simple MR with an embedded S-shaped waveguide [52, 137, 78, 77, 60, 138, 139, 140, 36, 141, 80, 47, 142, 143]. Its name comes from its special geometry, which resembles the Taiji symbol. The S-shaped WG creates an asymmetric coupling between the two counterpropagating modes inside the MR, and as a result a non-Hermitian coupling is obtained. Here it is shown that the TJMR is at an Exceptional Point (EP), which means that both eigenvalues and eigenvectors of the system coalesce [53, 31, 35, 36, 4, 105, 72, 144, 32]. Being on a EP, the TJMR has special features that can be exploited. The most important features of this structure are: the unidirectional reflector behavior [52], the possibility to break the transmission Lorentz reciprocity theorem when excited by a high power laser (nonlinear regime) [77, 78, 80], the unidirectional laser [36], the generation of tunable orbital angular momentum beams [145], and the sensitivity enhancement to a BS perturbation due to the EP features [47].

In Sec. 2.1 I will show the geometry of the TJMR and then I will describe it using the TCMT. Here we will observe the main characteristics of the TJMR in the linear regime (low laser power). Then, in the Sec. 2.2, the system is described using the TMM. A disturbing element found experimentally, the presence of a cavity FP created in the bus waveguide due to the presence of reflections at the waveguide ends, will also be introduced here. This phenomenon is very important when butt coupling is used and the ends of the bus waveguide are not accurately designed. In the following section (Sec. 2.3) the TJMR will also be analyzed in the nonlinear regime (high laser power) where we will demonstrate both theoretically and experimentally the breaking of the Lorentz reciprocity. Going back to the description of the TJMR via the TCMT, we will introduce the BS and demonstrate the enhanced sensitivity to a BS perturbation characteristic of the EPs (Sec. 2.4). We will also report experimental measurements of TJMRs characterized by different Qs and observe how the BS, mainly due to surface roughness, becomes increasingly relevant as Q increases. Finally, in Sec. 2.5 we will analyze the TJMR using the interferometric excitation both theoretically and experimentally.

Part of this chapter is derived from [78, 102, 77, 93, 52].

2.1 Design and Temporal Coupled Mode Theory model

The Taiji Microresonator (TJMR) is a particular MR characterized by an embedded S-shaped WG, see Fig. 2.1.

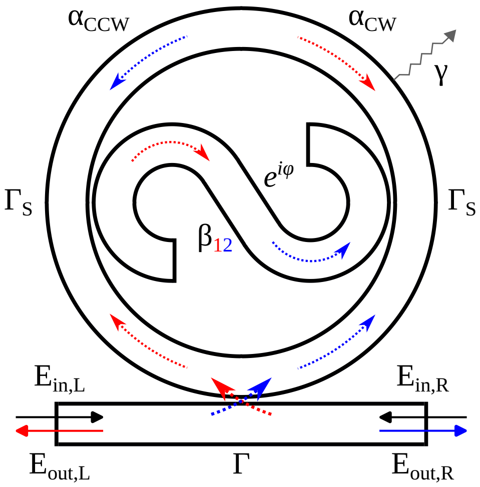

Figure 2.1: Sketch of the Taiji Microresonator (TJMR) in the all-pass configuration. γ and Γ are the intrinsic and the extrinsic damping rates. The indices R, L refer to left and right. E_{in} and E_{out} are the input and the output fields, respectively.

The S-shaped WG couples energy from the CW mode to the CCW mode ($\beta_{12} \neq 0$), but not vice versa ($\beta_{21} = 0$), thus creating an asymmetric coupling between the two counterpropagating modes. This means that the CCW mode will be dominant over the CW mode so the TJMR is a chiral MR [146, 53]. Note that the two counterpropagating modes, α_{CW} and α_{CCW}, suffer the same losses because they both suffer from the coupling between the MR and the S-shaped WG.

Using the TCMT, we can write the system of equations that describes the ideal

TJMR:

$$i\frac{d}{dt}\begin{pmatrix}\alpha_{CCW}\\ \alpha_{CW}\end{pmatrix} = \begin{pmatrix}\omega_0 - i\gamma_{tot} & -i\beta_{12}\\ 0 & \omega_0 - i\gamma_{tot}\end{pmatrix}\begin{pmatrix}\alpha_{CCW}\\ \alpha_{CW}\end{pmatrix} - \sqrt{2\Gamma}\begin{pmatrix}E_{in,L}\\ E_{in,R}\end{pmatrix}, \tag{2.1}$$

$$\begin{pmatrix}E_{out,R}\\ E_{out,L}\end{pmatrix} = \begin{pmatrix}E_{in,L}\\ E_{in,R}\end{pmatrix} + i\sqrt{2\Gamma}\begin{pmatrix}\alpha_{CCW}\\ \alpha_{CW}\end{pmatrix}, \tag{2.2}$$

where Γ is the extrinsic decay rate, $\gamma_{tot} = \gamma + \Gamma + 2\Gamma_S$ is the total loss rate, γ is the intrinsic decay rate due to absorption and scattering losses, Γ_S is the coupling rate between the MR and the S-shaped WG and β_{12} is the coupling rate from α_{CW} to α_{CCW}. In particular $\beta_{12} = 2e^{i\varphi}(\sqrt{2\Gamma_S})^2 = 4e^{i\varphi}\Gamma_S$ [93], where φ is the phase acquired by the field when it propagates through the S-shaped WG. In fact, β_{12} has to take into account that α_{CW} couples to the S-shaped WG twice in one round trip, and has to cross two coupling points (MR to S and S to MR) to enter the outer rim WG and transforms into the α_{CCW}.

From the Hamiltonian corresponding to TJMR,

$$H = \begin{pmatrix}\omega_0 - i\gamma_{tot} & -i\beta_{12}\\ 0 & \omega_0 - i\gamma_{tot}\end{pmatrix}, \tag{2.3}$$

we can immediately see the asymmetric coupling between the two counterpropagating modes (off-diagonal terms). Calculating the eigenvalues and eigenvectors of this Hamiltonian, we obtain

$$\lambda_1 = \lambda_2 = \omega_0 - i\gamma_{tot}, \qquad \nu_1 = \nu_2 = \begin{pmatrix}1\\ 0\end{pmatrix}. \tag{2.4}$$

Therefore not only the eigenvalues are degenerate, but also the eigenvectors coalesce, in fact the eigenvectors are equal to each other and therefore $| < \nu_1|\nu_2 > | = 1$. The coalescence of two or more eigenstates (eigenvalues and eigenvectors) is the necessary and sufficient condition for a system to be at an EP. Thus, we can say that the TJMR not only exhibits non-Hermitian coupling between its two counterpropagating modes, but is also at an EP.

Let us observe what it implies for the TJMR to be at an EP. We then solve the system of equations in Eq. (2.1) and Eq. (2.2) in the stationary regime by imposing:

$$E_{\mathrm{in,L}} := \varepsilon_{\mathrm{in,L}}\, e^{-i\omega t}\,, \qquad E_{\mathrm{in,R}} := \varepsilon_{\mathrm{in,R}}\, e^{i\phi}\, e^{-i\omega t}\,, \tag{2.5}$$

$$\alpha_{\mathrm{CCW}} := a_{\mathrm{CCW}}\, e^{-i\omega t}\,, \qquad \alpha_{\mathrm{CW}} := a_{\mathrm{CW}}\, e^{-i\omega t}\,, \tag{2.6}$$

$$E_{\mathrm{out,R}} := \varepsilon_{\mathrm{out,R}}\, e^{-i\omega t}\,, \qquad E_{\mathrm{out,L}} := \varepsilon_{\mathrm{out,L}}\, e^{-i\omega t}\,, \tag{2.7}$$

as in Sec. 1.1.2. This results in:

$$\varepsilon_{\mathrm{out,R}} = \left(1 - \frac{2\Gamma}{-i\Delta\omega + \gamma_{\mathrm{tot}}}\right)\varepsilon_{\mathrm{in,L}} + \left(\frac{2\Gamma\beta_{12}}{(-i\Delta\omega + \gamma_{\mathrm{tot}})^2}\right) e^{i\phi}\,\varepsilon_{\mathrm{in,R}}\,, \tag{2.8}$$

$$\varepsilon_{\mathrm{out,L}} = \left(1 - \frac{2\Gamma}{-i\Delta\omega + \gamma_{\mathrm{tot}}}\right) e^{i\phi}\,\varepsilon_{\mathrm{in,R}}\,, \tag{2.9}$$

$$a_{\mathrm{CCW}} = \frac{i\sqrt{2\Gamma}}{-i\Delta\omega + \gamma_{\mathrm{tot}}}\varepsilon_{\mathrm{in,L}} - \frac{i\sqrt{2\Gamma}\,\beta_{12}}{(-i\Delta\omega + \gamma_{\mathrm{tot}})^2} e^{i\phi}\,\varepsilon_{\mathrm{in,R}}\,, \tag{2.10}$$

$$a_{\mathrm{CW}} = \frac{i\sqrt{2\Gamma}}{-i\Delta\omega + \gamma_{\mathrm{tot}}} e^{i\phi}\,\varepsilon_{\mathrm{in,R}}\,, \tag{2.11}$$

where $\Delta\omega = \omega - \omega_0$ is the detuning angular frequency. Let us identify the field at the o output when the device is excited from the i input as $\varepsilon_{i\,o}$, where $i = \mathrm{L}, \mathrm{R}$ and $o = \mathrm{L}, \mathrm{R}$ (L stands for left and R stands for right). The intensities of the output fields when a single-side excitation is used are:

$$|\varepsilon_{\mathrm{LR}}|^2 = \left(1 - \frac{4(\gamma_{\mathrm{tot}} - \Gamma)\Gamma}{\Delta\omega^2 + \gamma_{\mathrm{tot}}^2}\right) |\varepsilon_{\mathrm{in,L}}|^2\,, \tag{2.12}$$

$$|\varepsilon_{\mathrm{RL}}|^2 = \left(1 - \frac{4(\gamma_{\mathrm{tot}} - \Gamma)\Gamma}{\Delta\omega^2 + \gamma_{\mathrm{tot}}^2}\right) |\varepsilon_{\mathrm{in,R}}|^2\,, \tag{2.13}$$

$$|\varepsilon_{\mathrm{LL}}|^2 = 0\,, \tag{2.14}$$

$$|\varepsilon_{\mathrm{RR}}|^2 = \frac{4\Gamma^2|\beta_{12}|^2}{(\Delta\omega^2 + \gamma_{\mathrm{tot}}^2)^2}|\varepsilon_{\mathrm{in,R}}|^2\,, \tag{2.15}$$

Consequently, one has:

$$T = \frac{|\varepsilon_{\mathrm{LR}}|^2}{|\varepsilon_{\mathrm{in,L}}|^2} = \frac{|\varepsilon_{\mathrm{RL}}|^2}{|\varepsilon_{\mathrm{in,R}}|^2} = 1 - \frac{4(\gamma_{\mathrm{tot}} - \Gamma)\Gamma}{\Delta\omega^2 + \gamma_{\mathrm{tot}}^2}\,, \tag{2.16}$$

$$R_{\mathrm{L}} = \frac{|\varepsilon_{\mathrm{LL}}|^2}{|\varepsilon_{\mathrm{in,L}}|^2} = 0\,, \tag{2.17}$$

$$R_{\mathrm{R}} = \frac{|\varepsilon_{\mathrm{RR}}|^2}{|\varepsilon_{\mathrm{in,R}}|^2} = \frac{4\Gamma^2|\beta_{12}|^2}{(\Delta\omega^2 + \gamma_{\mathrm{tot}}^2)^2} = \frac{4^3\Gamma^2\Gamma_S^2 e^{-2\Im[\varphi]}}{(\Delta\omega^2 + \gamma_{\mathrm{tot}}^2)^2}\,, \tag{2.18}$$

where T is the transmission intensity and R_L and R_R are the reflections intensities from left and right, respectively. It is evident that the transmissions are identical while the reflections are different, in fact $R_L = 0$ while $R_R \neq 0$. This means that at resonance the ideal TJMR behaves like a unidirectional reflector.

Note that the transmission spectrum is characterized by a Lorentzian dip centered at ω_0 (real part of the eigenvalues, $\Re[\lambda_{1/2}]$) and with a FWHM equal to $2\gamma_{tot}$ (the absolute value of twice the imaginary part of the eigenvalues, $|2\Im[\lambda_{1/2}]|$). Therefore, the transmission of an ideal TJMR is equivalent to the one of a MR characterized by the same Γ and γ_{tot} coefficients. In general, to be in the critical-coupling regime one must have $2\Gamma = \gamma_{tot}$, where γ_{tot} depends on Γ. For the TJMR this translates to $\Gamma = \gamma + 2\Gamma_S$. Consequently, the three coupling regimes, under-, critical-, and over-coupling, correspond to $\Gamma < \gamma + 2\Gamma_S$, $\Gamma = \gamma + 2\Gamma_S$, and $\Gamma > \gamma + 2\Gamma_S$, respectively.

The Q of the ideal TJMR can be calculated from the FWHM, which gives

$$Q = \frac{\omega_0}{2\gamma_{tot}} = \frac{\omega_0}{2(\gamma + \Gamma + 2\Gamma_S)} \,. \tag{2.19}$$

It is useful to note that the TJMR with the embedded S-shaped WG will always have more losses than a normal MR, and consequently, its Q will be lower. Note that if we impose the critical-coupling regime, $\Gamma = \gamma + 2\Gamma_S$, the reflectivity from the right side and at resonance becomes $R_R = \frac{4\Gamma_S^2 e^{-2\Im[\varphi]}}{(\gamma+2\Gamma_S)^2}$ and $Q = \frac{\omega_0}{4(\gamma+2\Gamma_S)}$. So, assuming that we keep $\gamma \neq 0$ constant and that we can vary Γ_S (and consequently Γ), there will be a maximum reflection ($\simeq e^{-2\Im[\varphi]}$) for Γ_S that tends to ∞. However, this means that the system is no longer a MR because Q goes to 0. This implies that to make the best use of the TJMR, one should not only aim for maximum reflection, but also, for example, for a large intensity difference within the TJMR between the left- and the right-excitation case (this concept will be seen in more detail in Sec. 2.3). Obviously, in the case of zero losses ($\gamma = 0$), we obtain a maximum reflection at the critical-coupling regime ($e^{-2\Im[\varphi]}$) that is independent of the value of $\Gamma = 2\Gamma_S$.

Let us now give an example of the spectral responses of a TJMR in the critical-coupling regime, see Fig. 2.2.

In Fig. 2.2 we observe, as expected, two identical transmissions and the unidirectional reflector behavior of the TJMR. Note also that by imposing $\Gamma = \gamma + 2\Gamma_S$ (critical coupling) the transmissions are zero at resonance. The transmission spectrum shows a dip with a Lorentzian line shape, instead the right reflection shows a peak with the shape corresponding to a squared Lorentzian, as can also be seen from Eq. 2.18.

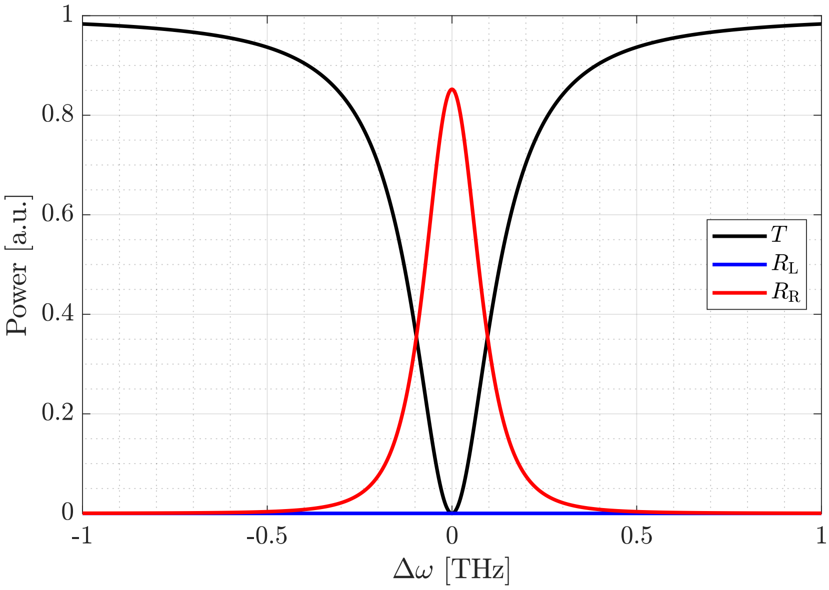

Figure 2.2: Theoretical spectral responses of a TJMR in the critical-coupling regime. The black curve shows the transmission spectrum, while the blue and red curves show the reflections from the left and right. The used coefficients are: $\gamma = 5$ GHz, $\Gamma_S = 30$, $\Gamma = \gamma + 2\Gamma_S = 65$ GHz and therefore $\gamma_{\mathrm{tot}} = 130$ GHz.

2.2 Transfer Matrix Method with Fabry Perot

In this section we want to include in the model of the TJMR also the reflections at the edges of the bus waveguide that create a Fabry-Pérot (FP) cavity of the same length as the bus waveguide. This will be necessary to best describe the experimental measurements made on some chips where the butt coupling method was used to couple light from the fiber to the sample. The most appropriate way to incorporate these new system features is to switch from the TCMT, as seen in the previous section, to the TMM.

In Fig. 2.3 the TJMR is schematized, and the black and red arrows and numbers are used to identify the direction and name of each electric field within the TJMR. In particular, the black arrows identify the E_n fields, where $n = -4, ..., 11$, and *forward* propagation direction. Instead, the red arrows identify the E_{nr} fields, which have opposite propagation directions. In this section we assume, without loss of generality, that the couplings between the different WGs are point-like. The TJMR has three different coupling points, one with the bus waveguide and two with the S-shaped WG, which we describe with the parameters (t_1, ik_1), (t_2, ik_2) and

(t_3, ik_3), respectively. The parameters t_j and k_j are the transmission and coupling coefficients, respectively. φ is the phase acquired by the field propagating in the S-shaped WG. In Fig. 2.3 there are also specified the parameters related to the terminations of the bus waveguide, i.e. $(t_L, \mp r_L)$ and $(t_R, \mp r_R)$, respectively for the left and right ends/facets. Again, the t parameters are the transmission coefficients between the two interfaces (air - WG), while the r parameters are the reflection coefficients, which have the sign $+$ or $-$ depending on whether the field is reflected inside or outside the WG. The change in sign is due to the fact that the field changes sign or not depending on whether it is reflected in the material with a lower or higher refractive index. This sign change results from Fresnel's laws.

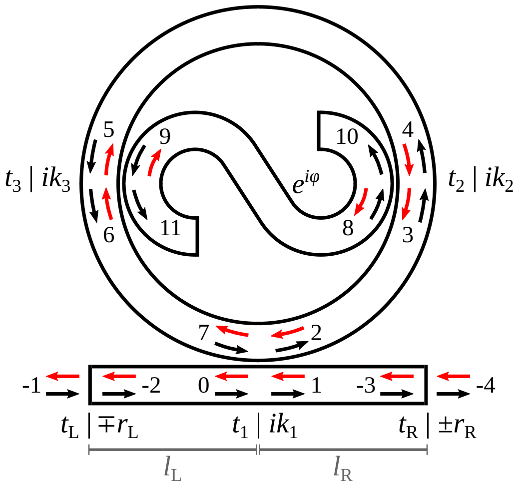

Figure 2.3: Sketches of the Taiji Microresonator (TJMR) in the all-pass configuration. The black arrows identify the E_n fields, where $n = -4, ..., 11$, and *forward* propagation direction. Instead, the red arrows identify the fields E_{nr}, which have opposite propagation directions. All the parameters are described in the text.

Before studying the whole system, which also includes the reflections of the ends of the bus waveguide, let us write the equations describing the TJMR:

$$
\begin{aligned}
E_1 &= t_1 E_0 + ik_1 E_7\,, & E_{0r} &= t_1 E_{1r} + ik_1 E_{2r}\,,\\
E_2 &= t_1 E_7 + ik_1 E_0\,, & E_{2r} &= \sigma_{23} e^{i\psi_{23}} E_{3r}\,,\\
E_3 &= \sigma_{23} e^{i\psi_{23}} E_2\,, & E_{3r} &= t_2 E_{4r}\,,\\
E_4 &= t_2 E_3 + ik_2 E_8\,, & E_{4r} &= \sigma_{45} e^{i\psi_{45}} E_{5r}\,,\\
E_5 &= \sigma_{45} e^{i\psi_{45}} E_4\,, & E_{5r} &= t_3 E_{6r}\,,\\
E_6 &= t_3 E_5 + ik_3 E_9\,, & E_{6r} &= \sigma_{67} e^{i\psi_{67}} E_{7r}\,,\\
E_7 &= \sigma_{67} e^{i\psi_{67}} E_6\,, & E_{7r} &= t_1 E_{2r} + ik_1 E_{1r}\,,\\
E_8 &= e^{i\varphi} E_{9r}\,, & E_{8r} &= ik_2 E_{4r}\,,\\
E_9 &= e^{i\varphi} E_{8r}\,, & E_{9r} &= ik_3 E_{6r}\,,\\
E_{10} &= t_2 E_8 + ik_2 E_3\,, & E_{11} &= t_3 E_9 + ik_3 E_5\,,\\
\psi_{jl} &:= \frac{2\pi}{\lambda} n_{\text{eff}} L_{jl}\,, & L &= L_{23} + L_{45} + L_{67}\,,\\
\sigma_{jl} &:= e^{-\alpha L_{jl}}\,, & L &:= 2\pi R\,,\\
\psi &= \frac{2\pi}{\lambda} n_{\text{eff}} L\,, & \sigma &:= e^{-\alpha L}\,.
\end{aligned}
\tag{2.20}
$$

The parameter L_{jl} identifies the WG length between the numbers j and l reported in Fig. 2.3. Here, n_{eff} is the WG effective refractive index, α is the propagation loss coefficient, L is the perimeter of the MR, and R is its radius. In the following, for simplicity, we assumed that all the coupling have no losses ($t_1^2 + k_1^2 = 1$, $t_2^2 + k_2^2 = 1$ and $t_3^2 + k_3^2 = 1$).

From (1.70) we derive:

$$
E_1 = \frac{t_1 - \sigma t_2 t_3 e^{i\psi}}{1 - \sigma t_1 t_2 t_3 e^{i\psi}} E_0 + \frac{2\sigma_{45}\sigma_{67}^2 k_1^2 k_2 k_3 t_3 e^{i(\psi_{45}+2\psi_{67}+\varphi)}}{(1 - \sigma t_1 t_2 t_3 e^{i\psi})^2} E_{1r}\,, \tag{2.21}
$$

$$
E_{0r} = \frac{t_1 - \sigma t_2 t_3 e^{i\psi}}{1 - \sigma t_1 t_2 t_3 e^{i\psi}} E_{1r}\,. \tag{2.22}
$$

From Eq. 2.21 and Eq. 2.22 the transmission and reflection amplitudes are derived

[52]:

$$t_{\text{taiji}} = t^{L}_{\text{taiji}} = t^{R}_{\text{taiji}} = \frac{t_1 - \sigma t_2 t_3 e^{i\psi}}{1 - \sigma t_1 t_2 t_3 e^{i\psi}}\,, \tag{2.23}$$

$$r^{L}_{\text{taiji}} = 0\,, \tag{2.24}$$

$$r^{R}_{\text{taiji}} = \frac{2\sigma_{45}\sigma^2_{67} k_1^2 k_2 k_3 t_3 e^{i(\psi_{45}+2\psi_{67}+\varphi)}}{(1 - \sigma t_1 t_2 t_3 e^{i\psi})^2}\,. \tag{2.25}$$

t^{L}_{taiji} and t^{R}_{taiji} are the transmission amplitudes for a left and right excitation, while r^{L}_{taiji} and r^{R}_{taiji} are the reflection amplitudes for light incident from left and right, respectively.

In the stationary regime, when the conditions $k_j \ll 1$, $t_j \simeq 1$, $\sigma \simeq 1$ (equivalent to $\gamma_{\text{tot}} \ll \omega_0$ or better $\gamma_{\text{tot}} \ll \tilde{f}$) are satisfied, this model is equivalent to the one used in Sec. 2.1. As seen in Ch. 1, to pass from the equations derived from TMM to those derived via TCMT, it is sufficient to use the following relations [93]:

$$t_1 \simeq 1 - \frac{\Gamma}{\tilde{f}}\,, \quad k_1 \simeq \sqrt{\frac{2\Gamma}{\tilde{f}}}\,, \tag{2.26}$$

$$t_2 \simeq 1 - \frac{\Gamma_S}{\tilde{f}}\,, \quad k_2 \simeq \sqrt{\frac{2\Gamma_S}{\tilde{f}}}\,, \tag{2.27}$$

$$t_3 \simeq 1 - \frac{\Gamma_S}{\tilde{f}}\,, \quad k_3 \simeq \sqrt{\frac{2\Gamma_S}{\tilde{f}}}\,, \tag{2.28}$$

$$\sigma \simeq 1 - \frac{\gamma}{\tilde{f}}\,, \quad g \simeq \sqrt{\frac{2\gamma}{\tilde{f}}}\,, \tag{2.29}$$

$$\sigma t_1 t_2 t_3 \simeq 1 - \frac{\gamma_{\text{tot}}}{\tilde{f}}\,, \tag{2.30}$$

$$\lambda_0 = \lambda_{\text{res}} = \frac{2\pi c}{\omega_0}\,, \quad \Re[\psi] = \frac{\Delta\omega}{\tilde{f}}\,, \tag{2.31}$$

$$\tilde{f} := \frac{c}{n_g L} = \frac{c\,\text{FSR}}{\lambda_0^2}\,, \quad \text{FSR} := \frac{\lambda_0^2}{n_g L}\,, \tag{2.32}$$

and expand for small couplings.

Now we want to add reflections at the ends of the bus waveguide. There are two ways to do this. The first is to include in the system of equations of the TJMR

(Eq. (2.20)) also the equations corresponding to the whole bus waveguide:

$$
\begin{aligned}
E_{-2} &= t_L E_{-1} + r_L E_{-2r}\,, & E_{-1r} &= t_L E_{-2r} - r_L E_{-1}\,,\\
E_0 &= \sigma_{-20} e^{i\psi_{-20}} E_{-2}\,, & E_{-2r} &= \sigma_{-20} e^{i\psi_{-20}} E_{0r}\,,\\
E_{-3} &= \sigma_{-31} e^{i\psi_{-31}} E_1\,, & E_{1r} &= \sigma_{-31} e^{i\psi_{-31}} E_{-3}\,,\\
E_{-4} &= t_R E_{-3} - r_R E_{-4r}\,, & E_{-3r} &= t_R E_{-4r} + r_R E_{-3}
\end{aligned}
$$

and then solve the complete system of equations once again with these new 8 equations as well. Another method is instead to take full advantage of the TMM technique, which consists of writing for each part of the system a transfer matrix that links the fields to the right of that sub-block with the fields to the left of it. In this way, it is sufficient to multiply the matrices in the correct order to obtain the transfer matrix for the whole system, without having to solve the entire system of equations. In the following, we will follow this path and explain the different steps in more detail.

First, using the definition of the scattering matrix $\mathbf{S}_{\text{taiji}}$ [107, 52]:

$$
\begin{pmatrix} E_{0r} \\ E_1 \end{pmatrix} = \mathbf{S}_{\text{taiji}} \begin{pmatrix} E_0 \\ E_{1r} \end{pmatrix} \tag{2.33}
$$

we obtain:

$$
\begin{aligned}
\mathbf{S}_{\text{taiji}} &= \begin{pmatrix} r^L_{\text{taiji}} & t^R_{\text{taiji}} \\ t^L_{\text{taiji}} & r^R_{\text{taiji}} \end{pmatrix} \\
&= \begin{pmatrix} 0 & \frac{t_1 - \sigma t_2 t_3 e^{i\psi}}{1 - \sigma t_1 t_2 t_3 e^{i\psi}} \\ \frac{t_1 - \sigma t_2 t_3 e^{i\psi}}{1 - \sigma t_1 t_2 t_3 e^{i\psi}} & \frac{2\sigma_{45}\sigma_{67}^2 k_1^2 k_2 k_3 t_3 e^{i(\psi_{45} + 2\psi_{67} + \varphi)}}{(1 - \sigma t_1 t_2 t_3 e^{i\psi})^2} \end{pmatrix}
\end{aligned} \tag{2.34}
$$

At this point we need to switch to the TJMR transfer matrix ($\mathbf{M}_{\text{taiji}}$), which connects the fields in this way:

$$
\begin{pmatrix} E_1 \\ E_{1r} \end{pmatrix} = \mathbf{M}_{taiji} \begin{pmatrix} E_0 \\ E_{0r} \end{pmatrix}\,. \tag{2.35}
$$

For this purpose, we introduce three general properties of matrices:

$$
\mathbf{A} = \begin{pmatrix} A_{11} & A_{12} \\ A_{21} & A_{22} \end{pmatrix}\,,
$$

$$\begin{pmatrix} x' \\ y' \end{pmatrix} = \begin{pmatrix} A_{11} & A_{12} \\ A_{21} & A_{22} \end{pmatrix} \begin{pmatrix} x \\ y \end{pmatrix} \Rightarrow \begin{pmatrix} y \\ x' \end{pmatrix} = \frac{1}{A_{22}} \begin{pmatrix} -A_{21} & 1 \\ \det[\mathbf{A}] & A_{12} \end{pmatrix} \begin{pmatrix} x \\ y' \end{pmatrix} \tag{2.36}$$

$$\begin{pmatrix} x' \\ y' \end{pmatrix} = \begin{pmatrix} A_{11} & A_{12} \\ A_{21} & A_{22} \end{pmatrix} \begin{pmatrix} x \\ y \end{pmatrix} \Rightarrow \begin{pmatrix} y \\ y' \end{pmatrix} = \frac{1}{A_{12}} \begin{pmatrix} -A_{11} & 1 \\ -\det[\mathbf{A}] & A_{22} \end{pmatrix} \begin{pmatrix} x \\ x' \end{pmatrix} \tag{2.37}$$

$$\begin{pmatrix} x' \\ y' \end{pmatrix} = \begin{pmatrix} A_{11} & A_{12} \\ A_{21} & A_{22} \end{pmatrix} \begin{pmatrix} x \\ y \end{pmatrix} \Rightarrow \begin{pmatrix} y' \\ y \end{pmatrix} = \frac{1}{A_{12}} \begin{pmatrix} -\det[\mathbf{A}] & A_{22} \\ -A_{11} & 1 \end{pmatrix} \begin{pmatrix} x \\ x' \end{pmatrix} \tag{2.38}$$

Using the property described in Eq. (2.38) we get:

$$\begin{aligned} \mathbf{M}_{\text{taiji}} &= \frac{1}{t^{R}_{\text{taiji}}} \begin{pmatrix} -\det\left[\mathbf{S}_{\text{taiji}}\right] & r^{R}_{\text{taiji}} \\ -r^{L}_{\text{taiji}} & 1 \end{pmatrix} \\ &= \frac{1}{t_{\text{taiji}}} \begin{pmatrix} t^{2}_{\text{taiji}} & r^{R}_{\text{taiji}} \\ 0 & 1 \end{pmatrix} . \end{aligned} \tag{2.39}$$

It is worth noting that the determinant of the transfer matrix of TJMR is one ($\det\left[\mathbf{M}_{taiji}\right] = 1$).

We now write the scattering matrix of the corresponding left facet of bus waveguide [107]:

$$\mathbf{S}_{\text{FL}} = \begin{pmatrix} -r_L & t_L \\ t_L & r_L \end{pmatrix} . \tag{2.40}$$

As a result, applying the property given in Eq. (2.38) yields the transfer matrix for the left facet:

$$\mathbf{M}_{\text{FL}} = \frac{1}{t_L} \begin{pmatrix} 1 & r_L \\ r_L & 1 \end{pmatrix} . \tag{2.41}$$

Here, we assumed $t_L^2 + r_L^2 = 1$ (energy conservation). Similarly, we can calculate the scattering matrix and the transfer matrix for the right-hand facet:

$$\mathbf{S}_{\text{FR}} = \begin{pmatrix} r_R & t_R \\ t_R & -r_R \end{pmatrix} \quad \Rightarrow \quad \mathbf{M}_{\text{FR}} = \frac{1}{t_R} \begin{pmatrix} 1 & -r_R \\ -r_R & 1 \end{pmatrix} . \tag{2.42}$$

We also write the scattering matrix and the transfer matrix for the field propagation in the left or right side of the bus waveguide [107]:

$$\mathbf{S}_{\text{P}j} = \begin{pmatrix} 0 & e^{i\Psi_j} \\ e^{i\Psi_j} & 0 \end{pmatrix} \quad \Rightarrow \quad \mathbf{M}_{\text{P}j} = \begin{pmatrix} e^{i\Psi_j} & 0 \\ 0 & e^{-i\Psi_j} \end{pmatrix} , \tag{2.43}$$

where $j = L, R$ identifies the parameters relative to the left or right side of the bus waveguide. $\Psi_j = ((2\pi/\lambda)n_{\mathrm{eff}} + i\alpha)l_j$ identifies the complex phase (including losses) that the field acquires when it passes through the part of bus waveguide that is to the left or right of the MR ($j = L, R$). Note that all the calculated transfer matrices have a determinant equal to 1.

In order to make the equations easier to understand, we use the following definitions:

$$E_{\mathrm{in},L} := E_{-1}\,, \qquad E_{\mathrm{out},R} := E_{-4}\,, \tag{2.44}$$

$$E_{\mathrm{out},L} := E_{-1r}\,, \qquad E_{\mathrm{in},R} := E_{-4r}\,. \tag{2.45}$$

At this point, we can calculate the transfer matrix of the entire system, which is defined as follows:

$$\begin{pmatrix} E_{\mathrm{out},R} \\ E_{\mathrm{in},R} \end{pmatrix} = \mathbf{M} \begin{pmatrix} E_{\mathrm{in},L} \\ E_{\mathrm{out},L} \end{pmatrix}\,. \tag{2.46}$$

by simply multiplying the transfer matrices [Eqs. (2.39), (2.41), (2.42) and (2.43)]:

$$\mathbf{M} = \mathbf{M}_{\mathrm{FR}}\mathbf{M}_{\mathrm{PR}}\mathbf{M}_{\mathrm{taiji}}\mathbf{M}_{\mathrm{PL}}\mathbf{M}_{\mathrm{FL}}\,. \tag{2.47}$$

$$\begin{aligned}\mathbf{M} &= e^{-i\tilde{\Psi}} \begin{pmatrix} \frac{r_L\left(-r_R + r_{\mathrm{taiji}}^R e^{2i\Psi_R}\right) + t_{\mathrm{taiji}}^2 e^{2i\tilde{\Psi}}}{t_L t_R t_{\mathrm{taiji}}} & \frac{-r_R + e^{2i\Psi_R}\left(r_{\mathrm{taiji}}^R + r_L e^{2i\Psi_L} t_{\mathrm{taiji}}^2\right)}{t_L t_R t_{\mathrm{taiji}}} \\ \frac{r_L\left(1 - r_R r_{\mathrm{taiji}}^R e^{2i\Psi_R}\right) - r_R t_{\mathrm{taiji}}^2 e^{2i\tilde{\Psi}}}{t_L t_R t_{\mathrm{taiji}}} & \frac{1 - r_R e^{2i\Psi_R}\left(r_{\mathrm{taiji}}^R + r_L e^{2i\Psi_L} t_{\mathrm{taiji}}^2\right)}{t_L t_R t_{\mathrm{taiji}}} \end{pmatrix} \\ &= \begin{pmatrix} M_{11} & M_{12} \\ M_{21} & M_{22} \end{pmatrix}\,,\end{aligned} \tag{2.48}$$

where $\tilde{\Psi} := \Psi_L + \Psi_R$. With Eq. (2.36) we can now switch from the transfer matrix to the scattering matrix:

$$\begin{aligned}\mathbf{S} &= \frac{1}{M_{22}} \begin{pmatrix} -M_{21} & 1 \\ \det[\mathbf{M}] & M_{12} \end{pmatrix} \\ &= \begin{pmatrix} -\frac{M_{21}}{M_{22}} & \frac{1}{M_{22}} \\ \frac{\det[\mathbf{M}]}{M_{22}} & \frac{M_{12}}{M_{22}} \end{pmatrix} \\ &= \begin{pmatrix} r_{\mathrm{tot}}^L & t_{\mathrm{tot}}^R \\ t_{\mathrm{tot}}^L & r_{\mathrm{tot}}^R \end{pmatrix}\end{aligned} \tag{2.49}$$

$$
\begin{aligned}
\mathbf{S} &= \begin{pmatrix} r^{L}_{tot} & t^{R}_{tot} \\ t^{L}_{tot} & r^{R}_{tot} \end{pmatrix} \\
&= \begin{pmatrix} \dfrac{-r_L\left(1-r_R r^{R}_{taiji} e^{2i\Psi_R}\right)+e^{2i\tilde{\Psi}} r_R t^{2}_{taiji}}{1-r_R e^{2i\Psi_R}\left(r^{R}_{taiji}+r_L e^{2i\Psi_L} t^{2}_{taiji}\right)} & \dfrac{e^{i\tilde{\Psi}} t_L t_R t_{taiji}}{1-r_R e^{2i\Psi_R}\left(r^{R}_{taiji}+r_L e^{2i\Psi_L} t^{2}_{taiji}\right)} \\ \dfrac{e^{i\tilde{\Psi}} t_L t_R t_{taiji}}{1-r_R e^{2i\Psi_R}\left(r^{R}_{taiji}+r_L e^{2i\Psi_L} t^{2}_{taiji}\right)} & -\dfrac{1}{r_R}+\dfrac{1}{r_R}\dfrac{1-r^{2}_{R}}{1-r_R e^{2i\Psi_R}\left(r^{R}_{taiji}+r_L e^{2i\Psi_L} t^{2}_{taiji}\right)} \end{pmatrix}
\end{aligned}
\tag{2.50}
$$

Here, r^{L}_{tot} and r^{R}_{tot} are the reflection amplitudes for the light incident from the left and the right end of the bus waveguide, respectively. Moreover, t^{L}_{tot} and t^{R}_{tot} are the transmission amplitudes when the system is excited from left or right.

It is worth noting that the two transmissions of the system are equal. Moreover, it is easy to prove that for r_L and r_R equal to zero (t_L and t_R equal to one) we obtain the expected spectral responses:

$$
t_{tot} = t^{R}_{tot} = t^{L}_{tot} \rightarrow t_{taiji} e^{i\tilde{\Psi}}\,, \tag{2.51}
$$

$$
r^{L}_{tot} \rightarrow 0\,, \tag{2.52}
$$

$$
r^{R}_{tot} \rightarrow r^{R}_{taiji} e^{2i\Psi_R}\,. \tag{2.53}
$$

In the diametrically opposite case, where we remove the TJMR ($t_1 = 0 \Rightarrow r^{R}_{taiji} = 0$ and $t_{taiji} = 1$) we get:

$$
t_{tot} = t^{R}_{tot} = t^{L}_{tot} \rightarrow \frac{t_L t_R e^{i\tilde{\Psi}}}{1 - r_L r_R e^{2i\tilde{\Psi}}}\,, \tag{2.54}
$$

$$
r^{L}_{tot} \rightarrow \frac{-r_L + r_R e^{2i\tilde{\Psi}}}{1 - r_L r_R e^{2i\tilde{\Psi}}}\,, \tag{2.55}
$$

$$
r^{R}_{tot} \rightarrow \frac{-r_R + r_L e^{2i\tilde{\Psi}}}{1 - r_L r_R e^{2i\tilde{\Psi}}}\,. \tag{2.56}
$$

As expected, these are the responses of a FP cavity with the typical periodic oscillations as a function of the frequency of the exciting field [107].

Equation (2.50) shows that the spectral responses of the whole system clearly show the characteristics of TJMR, but at the same time there are oscillations due to the FP cavity which cause special interferences, see Fig. 2.4 and Fig. 2.5.

Panels (a) and (b) of Fig. 2.4 show the theoretical spectra for a TJMR without and with the bus waveguide (Fabry-Pérot Oscillations (FPOs)), respectively. In Fig. 2.4 (a) the TJMR is in the critical coupling regime and has a right reflection that reaches about 0.7 a.u. at resonance, while the left reflection is always zero. It

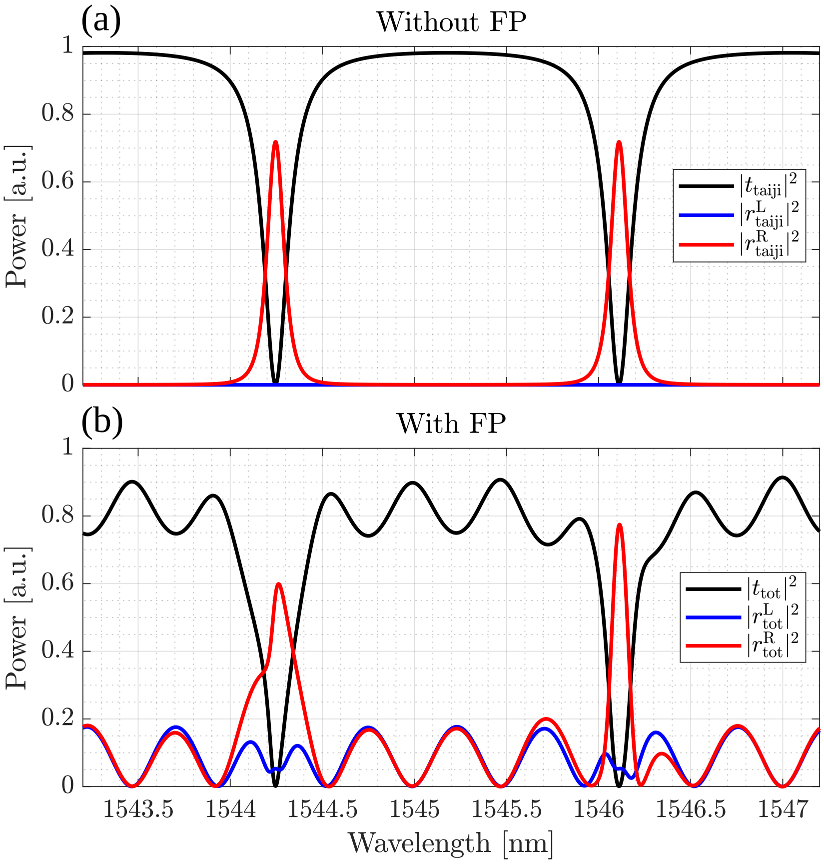

Figure 2.4: Panels (a) and (b) show the theoretical spectra of a TJMR without or with reflections at the ends of the bus waveguide. Here the TJMR is in the critical-coupling regime. The coefficients used are: $t_1 = 0.868$, $t_2 = t_3 = 0.945$, $n_{\text{eff}} = 1.58$, $\alpha \simeq 231/\text{m}$ (2 dB/cm), $L_{23} = L_{67} \simeq 206.3$ µm, $L_{45} \simeq 397.7$ µm, $L_{89} \simeq 391.1$ µm, $l_L = l_R = 750$ µm and $r_L = r_R = 0.23$. We used the effective refractive index of a silicon oxynitride (SiON) WG.

can be clearly seen that the TJMR at resonance is a unidirectional reflector. When the FP cavity (the bus waveguide) is added, wavelength-dependent oscillations are observed with a period equal to $\lambda^2/(2n_g(l_L + l_R))$, where λ is the wavelength of the incident field. The amplitude of the FPOs depends on the reflections of the ends of the bus waveguide, here we used $r_L = r_R = 0.23$. This value was found by fitting the spectral measurements, as reported in Sec. 2.3.1. It is worth noticing that in Fig. 2.4 (b) the oscillations also change the spectral shape of the resonance, both in transmission and in reflection. Moreover, the left reflection is no longer zero as in the ideal case, but has an oscillating wavelength response. Note also that since the TJMR is in the critical coupling regime ($t_{\text{taiji}} = 0$ at resonance), the left reflection at resonance is simply due to the reflection of the left facet and is, therefore, equal to $r_L^2 = 0.0529$. This can be quickly verified analytically using r_{tot}^L reported in Eq. (2.50). It is important to note that in this case, although the spectral responses are perturbed by the FPOs, at resonance the right-side reflection is always much larger than the left-side reflection, so the TJMR again behaves as a good unidirectional reflector.

Let us now decrease the coupling coefficients between the TJMR and the S-shaped WG and thus increase the transmission coefficients to $t_2 = t_3 = 0.99$, see Fig. 2.5. Figure 2.5 (a) shows that by increasing t_2 and t_3 the right reflection decreases, moreover we are now in the under-coupling regime and the transmission no longer reaches zero at resonance. Although the right reflection is small here, it reaches 0.1 a.u. at resonance, again the TJMR works as a unidirectional reflector.

Now let us look at the complete system, taking into account the reflections of the ends of the bus waveguide, see Fig. 2.5 (b). Again, all spectral responses are distorted by the FPOs. The transmissions may appear both narrower and wider than they would be, and even the minimum may occur at a different wavelength than the resonance one. The most important thing to note is that in the spectrum of the right reflection, due to interference from the FP cavity, the characteristic peak at the resonance may no longer be present, as observed in Fig. 2.5 (b) for the resonance around 1544.25 nm. In fact, the right reflection is even lower than the left reflection. This peculiar phenomenon is caused by the destructive interference between the field that passes through the S-shaped WG, is reflected, enters the bus waveguide, and then exits from the right side of the bus waveguide, and the field that is reflected outside the right facet of the bus waveguide. Indeed, by changing the resonance, we observe that the interference between these two waves varies, and we can also get a larger right reflection than in the ideal case (without FP). In fact, in the resonance at about 1546.1 nm, $|r_{tot}^R|^2$ exceeds the value of 0.3 a.u.. Therefore, in different FSRs the TJMR may or may not be a unidirectional reflector.

In conclusion, by using the TMM it is also possible to add in a simple way the reflections given by the ends of the bus waveguide. These reflections create a FP cavity inside the bus waveguide that causes distortions in the spectra of the TJMR and can also cause both a cancellation and an accentuation of the property of the TJMR to be a unidirectional reflector.

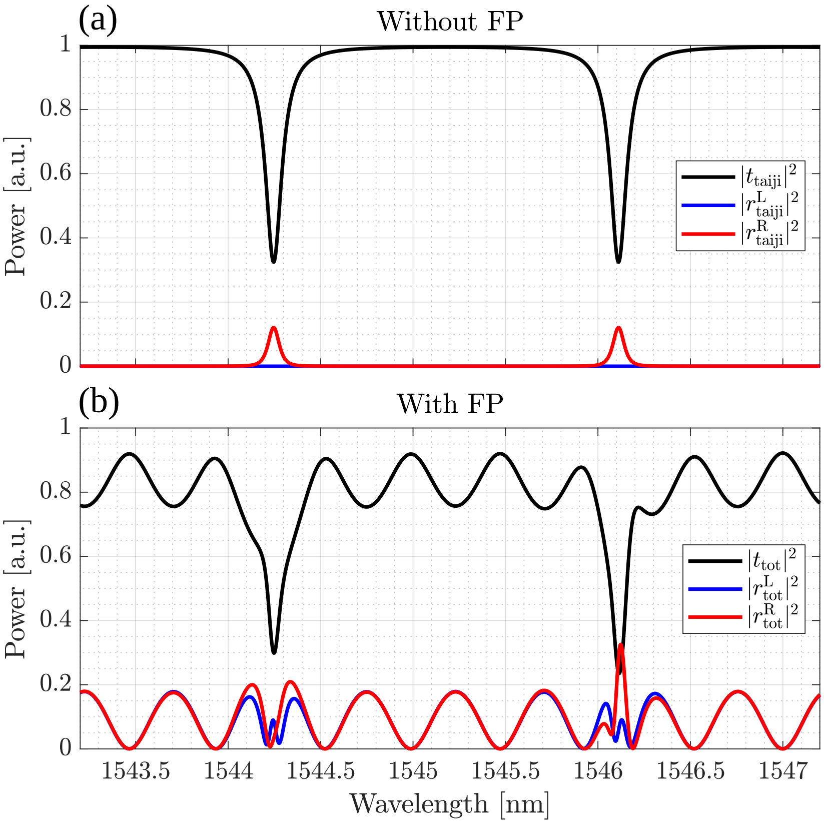

Figure 2.5: Panels (a) and (b) show the theoretical spectra of a TJMR without or with reflections at the ends of the bus waveguide. Here the TJMR is in the under-coupling regime. The coefficients used are: $t_1 = 0.868$, $t_2 = t_3 = 0.99$, $n_{\mathrm{eff}} = 1.58$, $\alpha \simeq 231$/m (2 dB/cm), $L_{23} = L_{67} \simeq 206.3$ μm, $L_{45} \simeq 397.7$ μm, $L_{89} \simeq 391.1$ μm, $l_L = l_R = 750$ μm and $r_L = r_R = 0.23$. We used the effective refractive index of a SiON WG.

2.3 Nonlinear breaking of Lorentz reciprocity theory and experimental measurements

In optics, nonreciprocal elements such as isolators and circulators [147, 148] are very important not only for being able to protect the source from back reflections, but also for their use in unidirectional lasers, high-speed optical communications and information processing systems [149, 150, 151]. Using nonmagnetic elements, it is not possible to break Lorentz's reciprocity while remaining in linear optics. In fact, Lorentz reciprocity is a fundamental property of fields propagating in a linear, nonmagnetic medium. Since this property is based on the linearity of the field equations, we can exploit material nonlinearities to overcome this limitation. Some devices use multiple cascaded coupled MRs or special configurations of resonators in the nonlinear regime to break the Lorentz reciprocity [152, 153, 154, 39, 155]. Other devices exploit the interaction between two fields [156, 157].

In this section, we will show that the TJMR, when used in the nonlinear regime, can also be used as an isolator. Unlike multiresonator systems, the TJMR does not require fine tuning of two or more resonant frequencies because it has the two degenerate modes CW and CCW.

Let us now explain how it works. First, in the nonlinear regime, the effective refractive index of the waveguide depends on the intensity of the light. In particular, there are three phenomena that characterize the variation of the refractive index in a normal waveguide: the Kerr effect, the Thermo Optic Effect (TOE) and the Two Photon Absorption (TPA) effects [Free Carrier Absorption (FCA) and Free Carrier Dispersion (FCD)] [128, 77, 78, 158, 159]. Here we will only describe the first two, because we will use an optical integrated circuit made of SiON waveguides, which around 1550 nm do not exhibit the TPA phenomenon. The Kerr effect is due to the nonlinear dependence of the polarization vector (**P**) on the field (**E**) [107, 160]:

$$\mathbf{P} = \varepsilon_0 \left(\chi^{(1)} \mathbf{E} + \chi^{(2)} \mathbf{E}^2 + \chi^{(3)} \mathbf{E}^3 \right) , \tag{2.57}$$

where $\varepsilon_0 = \frac{1}{\mu_0 c^2} \simeq 8.854187817 \times 10^{-12}$ F/m is the vacuum permittivity, $\chi^{(1)}$ is the linear susceptibility tensor and $\chi^{(2)}$ and $\chi^{(3)}$ are second and third order nonlinear susceptibilities. The a.c. Kerr effect [107, 161, 162] is due to the third order susceptibility ($\Re[\chi^{(3)}]$) and in first approximation influences the nonlinear refractive index (Δn) in this way:

$$\Delta n := n - n_0 \simeq \frac{3\chi^{(3)}}{8 n_0} |E_\omega|^2 =: n_K |E_\omega|^2 , \tag{2.58}$$

where E_ω is the electric field oscillating at a frequency of ω and n_K, usually denoted by n_2, is the nonlinear a.c. Kerr index. Thus, the a.c. Kerr effect causes the refractive index to vary linearly as a function of the intensity of the electric field.

The refractive index also depends on the temperature. Since some of the light lost from the WG is converted to heat, we have in a first approximation that Δn depends linearly on the optical intensity in the guide, i.e.

$$\Delta n = n_T I_{\text{thermal}} , \tag{2.59}$$

where n_T is the coefficient of the thermo-optic nonlinearity and I_{thermal} is the total electromagnetic intensity in the vicinity of the WG. This phenomenon is called Thermo Optic Effect (TOE) [107, 128, 78]. It should be noted that while the a.c. Kerr effect is a point effect, i.e. it causes the refractive index of the guide to change exactly where the field is located, the thermo optic effect, because it is due to the heating of the WG, is not a local effect. Moreover, the a.c. Kerr effect is an almost instantaneous phenomenon, whereas the thermo optic effect has much longer response times, around hundreds of nanoseconds. This is due to the fact that the thermo optic effect is driven by the temperature rise of the WG. In this section we will not study the time response in the nonlinear regime of TJMR, but will always work in a stationary regime, so without loss of generality we will always consider the two effects as instantaneous.

The nonlinear refractive index causes a change in the resonance wavelength of the MR, because $m\lambda_{\text{res}} = n_{eff}L$ ($m \in \mathbb{N}$). Consequently, the resonance wavelength also has a linear dependence on the power of the electric field inside the WG. We also emphasize that the MR with an enhancement factor higher than 1 (EF > 1) will have a higher refractive index change than the bus waveguide.

In a normal MR, which is symmetric, it is not possible to break Lorentz reciprocity simply by using this type of nonlinearity. In fact, the same optical intensity will be present in the MR for both left and right excitations, and consequently, the shift at resonance will be identical for both types of excitation. This is not the case for the TJMR; in fact, if one excites the TJMR from left, the field entering the S-shaped WG is diffused in the cladding by an appropriate design of the WG that prevents the back reflection of light. Whereas if it is excited from right, some of the light that couples into the S-shaped WG is coupled into the CCW mode of the microresonator, and as a result, there will be a higher optical intensity within the TJMR. Since there is a higher intensity, in the nonlinear regime, the resonance has a larger shift in the case of excitation from right than in the case of excitation from left, and consequently, the two transmission spectra will be different. Therefore, by using the TJMR in the nonlinear regime, one is able to break the Lorentz reciprocity.

In the following, starting from the experimental data in the linear regime and then moving to the nonlinear regime, we will demonstrate the breaking of Lorentz reciprocity in a TJMR. We will also discuss the interaction between the FP cavity due to facet reflections at the ends of the bus waveguide and the TJMR in both regimes. Simulations of the whole system in the linear and nonlinear regime will also be carried out to better explain this interaction.

Specifically, the structure of this section is as follows. In Sec. 2.3.1 I will present the experimental evidence for the different transmission and reflection behavior in the linear and nonlinear regimes. Then, in Sec. 2.3.2 I will present the numerical simulations that reproduce the experimental results.

2.3.1 Experiments

Experimental setup and photonic sample

In this subsection, we will study the system using a simplified experimental setup compared to the one described in Sec. 1.5.1. As the sketch of the experimental setup shows (Fig. 2.6), an Erbium Doped Fiber Amplifier (EDFA) is used to amplify the laser power to enter in the nonlinear regime of the TJMR. The setup consists of a CWTL (Yenista OPTICS, TUNICS-T100S) that operates from 1490 nm to 1640 nm, followed by a fiber coupled EDFA (IPG photonics) that can amplify the signal up to 5 W. To avoid damage from retroreflection, the EDFA is followed by a Optical Isolator (OI). A Fiber Polarization Controller (FPC) is then used to vary the polarization of the light within the fiber so that the correct polarization is obtained at the input to the chip. Next, one Optical Circulator (OC) and two PDs (Thorlabs, PDA20CS2) are used to simultaneously measure the transmission and reflection spectra ($\mathrm{PD_T}$ and $\mathrm{PD_R}$). At output number 2 of the optical circulator, an Alignment Stage (AS) is used to align a tapered lensed fiber to the waveguide present on the sample. We use the butt coupling method to input the signal in the chip. Butt coupling is also used to collect the transmitted light. As in the setup described in Sec. 1.5.1, the PDs are read by an oscilloscope (PicoScope 4000 series) interfaced to a PC.

It is not possible to quickly change the excitation direction of the system in this setup. In order to do this, and to avoid problems with changes in propagation loss that could be caused by changing fibers in the connectors (dust), we decided that to vary the excitation direction we would simply rotate the sample by 180°.

Given this rotation of the sample, we define the *forward* excitation as the one that couples light via the bus waveguide in the CCW mode of the TJMR [path with blue arrows in Fig. 2.6 (a)]. The *reverse* excitation is the opposite, which couples light via the bus waveguide to the CW mode of the TJMR, which then couples to the CCW mode via the S-shaped WG [path with red arrows in Fig. 2.6 (a)]. So far we have referred to the *forward* and *reverse* excitation as left and right excitation. Thus, neglecting the facet reflections of the bus waveguide, in the *forward* excitation we

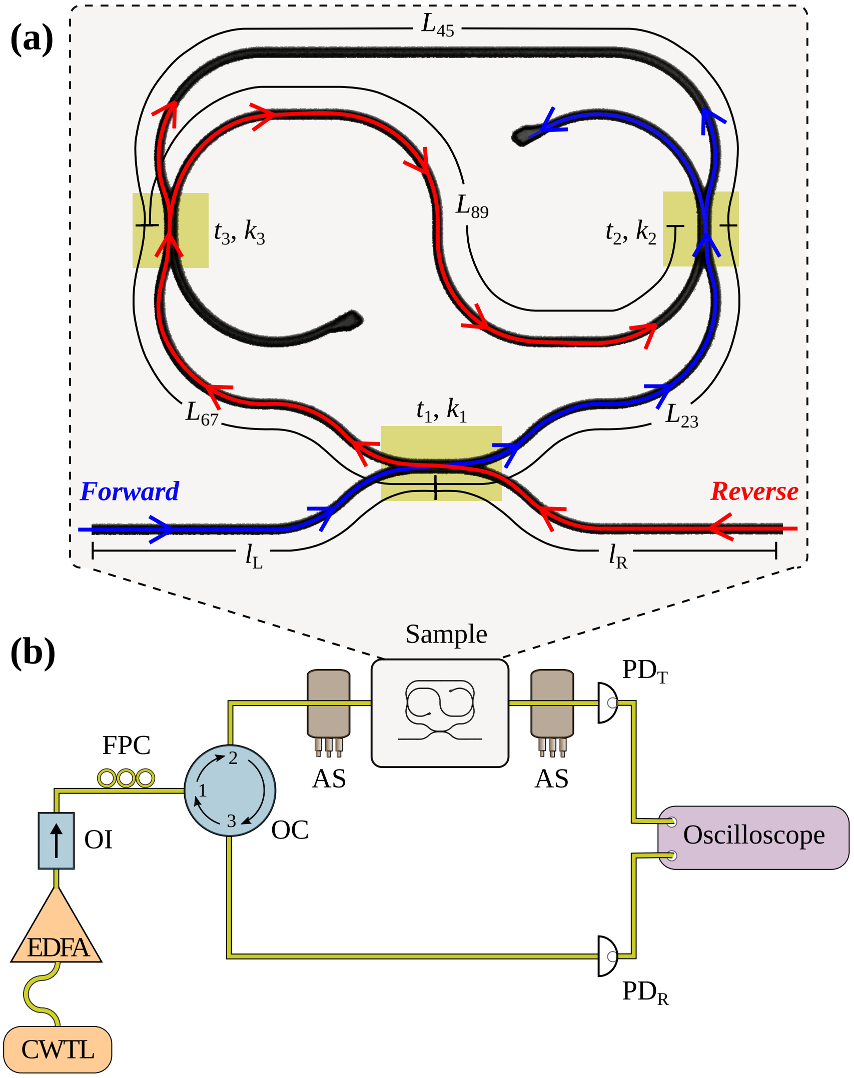

Figure 2.6: In panel (a) is reported the design of the TJMR. In panel (a) the meaning of *forward* (blue arrows) and *reverse* (red arrows) excitation is shown. The yellow regions highlight the three directional couplers. In (b) a sketch of the experimental setup is shown. The instrumentation used is an Continuous Wave Tunable Laser (CWTL), an Erbium Doped Fiber Amplifier (EDFA), an Optical Isolator (OI), a Fiber Polarization Controller (FPC) an Optical Circulator (OC), two Alignment Stages (ASs), two photodetectors (PDs) and an oscilloscope. [78]

will have a zero reflection, while in the *reverse* excitation we will have a non-zero reflection at resonance. In the *reverse* excitation, there will be more energy inside the TJMR, given the fact that the light coupled to the S-shaped waveguide is coupled back to the microresonator. The structure in Fig. 2.6 (a) is the design geometry of the TJMR that we measured. Here one can see that the terminations of the S-shaped WG have been designed to minimize retroreflections.

The bus waveguide/TJMR device was made of channel waveguides in SiON with a cross section of 1.2 μm × 0.57 μm. Consequently, the WGs guide only the first mode for each polarization. Here we will use only the Tranverse Magnetic (TM) polarization. Below the waveguide core is a 5 μm layer of SiO_2 grown on a standard 150 mm Si wafer. Whereas, above the WGs a double stack of 410 nm borophosphosilicate (BPSG) glass and a 2 μm thick Plasma-Enhanced Chemical Vapor Deposition (PECVD) silicon oxide (SiO_x) layer is deposited. The TJMR is composed of a microresonator with an embedded S-shaped WG as reported in Fig. 2.6 (a). Here, the used bending radius is 25 μm. The coupling gaps and lengths of the three directional couplers are 0.86 μm and 18.81 μm for the bus waveguide and 0.8 and 10.28 μm for the two couplers with the S-shaped WG. The lengths of the different parts of the TJMR are $L_{23} = L_{67} \simeq 206.26$ μm, $L_{45} \simeq 397.71$ μm and $L_{89} \simeq 391.12$ μm, as a result, the total perimeter of the TJMR is $L = L_{23} + L_{45} + L_{67} \simeq 810.24$ μm, see Fig. 2.6 (a). The ends of the bus waveguide are polished. The two lengths identifying the position of the TJMR are l_L on the left and l_R on the right, respectively. Below we will present measurements made on two TJMRs with the same characteristics but characterized by a different position with respect to the center of the bus waveguide. In particular, in both cases we have $l_L \simeq 0.431$ mm, while we have two different l_R: 5.52 mm and 1.062 mm. More details about the device and the chip are reported in [52, 78].

Linear regime

Here I present the experimental results in the linear (low power) regime for the system composed of bus waveguide and TJMR. In Fig. 2.7 the spectral responses of two TJMR with the same characteristics are shown, the only difference is the length l_R of the right side of the bus waveguide. In fact in panel (a) $l_R \simeq 5.52$ mm while in panel (b) $l_R \simeq 1.062$ mm. In both cases, the length of the left part is $l_L \simeq 0.431$ mm. In Fig. 2.7, only one of the two transmission spectra is reported because the other was, as expected, equivalent. To see what the different parameters correspond to, we refer to Fig. 2.6 (a) or Fig. 2.3.

In Fig. 2.7 (a), the presence of the Fabry-Pérot (FP) oscillations is easily observed due to the nonzero reflections of the facets of the bus waveguide, which create a FP cavity. This leads to the presence of a non-zero reflection even in the *forward* excitation (R_f, blue curve), as discussed in Sec. 2.2. Figure 2.7 shows that for a sufficiently long bus waveguide length [panel (a)], the FP oscillations have a wavelength period so short that there is always more than one complete oscillation in the resonance band. This causes the interference between the reflected field by the TJMR and that reflected by the bus waveguide facets to change rapidly as a function of wavelength, and thus both destructive and constructive interferences are observed within the same resonance. This is observed in panel (a) of Fig. 2.7 and causes a reflection in *reverse* (R_r) at resonance larger than the reflection in *forward* (R_f). Note also that outside resonance the two reflections have similar values, i.e. the *forward* and *reverse* couplings between the fiber and the bus waveguide are nearly equal, as are the reflections of the two facets $r_L \simeq r_R$. Thus, for long enough waveguides (in this case about 6 mm), the spectral responses are affected by the FP oscillations, but overall the system still behaves as a unidirectional reflector.

On the other hand, if we shorten the bus waveguide, the period of the FP oscillations increases and thus we get a more constant interference between the two cavities (TJMR and FP) within the same resonance. This allows us to distinguish different cases with different behaviors in reflection. In transmission, a Lorentzian line shape deformation is observed, but no particular phenomena are observed. Panels (b1), (b2) and (b3) show zooms of the experimental spectra corresponding to $l_R \simeq 1.062$ mm. Let us focus on the two reflections R_r and R_f. In the previous case, as well as in the ideal case, the reflection relative to *reverse* excitation is greater than the reflection in *forward* for every resonance in the spectrum (for all FSRs). However, in panel (b) it can be seen that different resonances show different behaviors in reflection. In particular, we consider the three cases shown in panels (b1), (b2) and (b3). These cases differ in the spectral shape of the reflections and, therefore, in a different interference between the reflection of TJMR and that of bus waveguide. In (b1) we observe that R_r is larger than R_f. We will call this case *constructive*-like (C) reflection lineshape. Here, constructive interference causes R_r to present a peak at resonance, and thus the system behaves like a typical TJMR. In (b2), on the other hand, the peak present in R_r has a different shape; it is a sharp peak with a height similar to that of FP oscillations. For this reason we will call this case *Fano*-like (F). The last case [panel (b3)] is the most peculiar. Here the reflection R_r shows a spectral

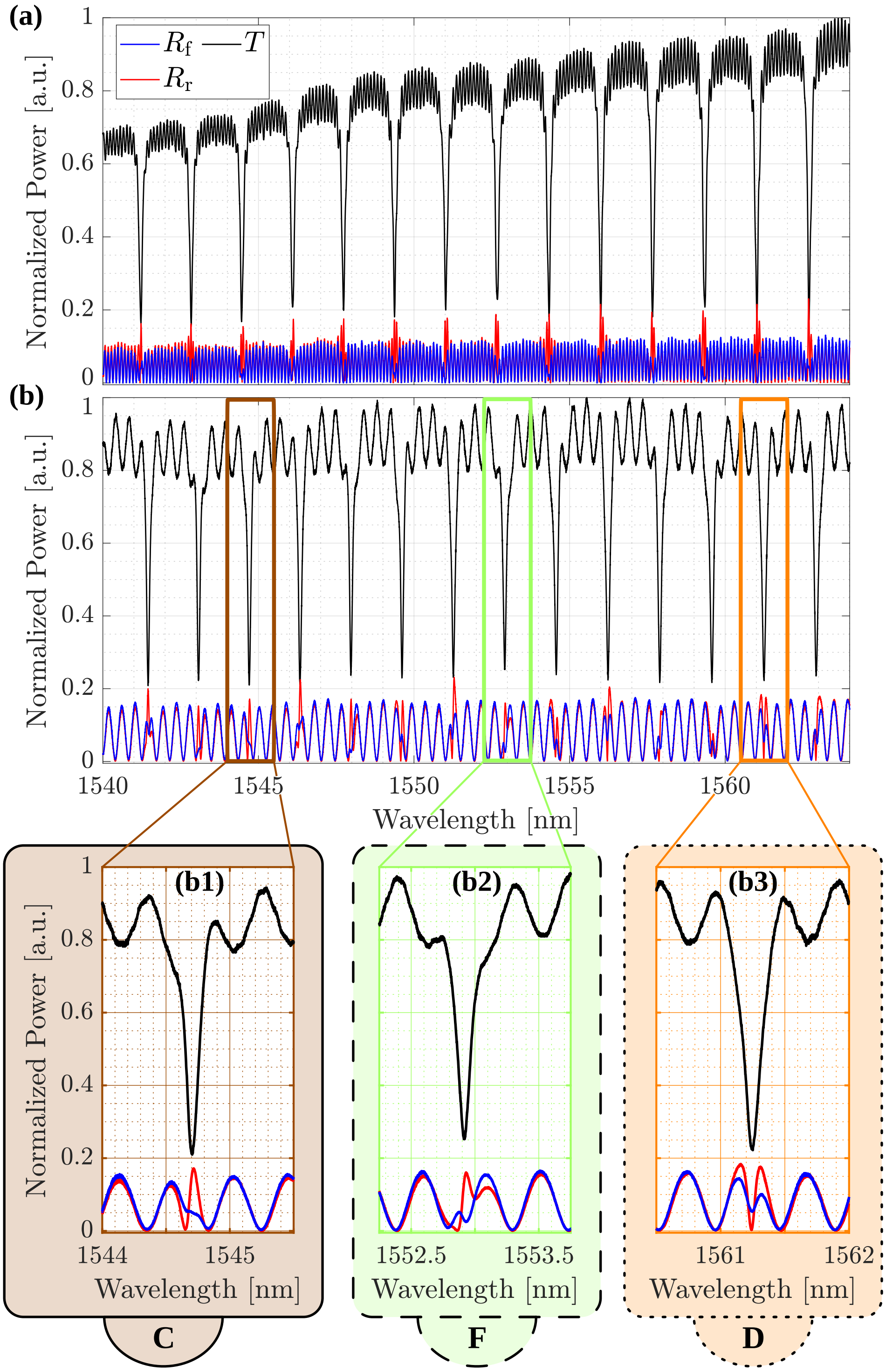

Figure 2.7: Experimental power spectra of a bus waveguide/TJMR system. Black lines report the transmission data, instead the blue and the red ones show the reflection for a *forward* and a *reverse* excitation, respectively. In all the panels $\mathfrak{l}_\mathrm{L} \simeq 0.431$ mm. In panel (a) $\mathfrak{l}_\mathrm{R} \simeq 5.52$ mm instead in (b) $\mathfrak{l}_\mathrm{R} \simeq 1.062$ mm. The zooms reported in (b1), (b2) and (b3) highlight three different interference cases characterized by *constructive*-like (C), *Fano*-like (F) and *destructive*-like (D) line shapes, respectively. [78]

dip at resonance that reaches approximately zero, and also R_r is smaller than the reflection in *forward* (R_f). This strange behavior is due to destructive interference between the *reverse* reflection of the TJMR and that of the FP cavity. We will call this case *destructive*-like (D). In the *destructive*-like case, the unidirectional behavior of the TJMR is drastically reduced or even eliminated or reversed. Consequently, in the case reported in panel (b) of Fig. 2.7, the system behaves as a unidirectional reflector device only for some resonance frequencies.

Nonlinear regime

Let us now analyze the sample with $l_R \simeq 1.062$ mm in the nonlinear regime. Here we show the change of the transmission spectra obtained by scanning from low to high wavelengths as a function of the coupled power within the bus waveguide, see Fig. 2.8 and Fig. 2.9. In the nonlinear regime, it was not possible to measure the reflection spectra because the optical circulator has a low damage threshold power.

We first describe the behavior followed by the *constructive*-like resonance in Fig. 2.7 (b1), the nonlinear measurements are shown in Fig. 2.8. Panels (a) and (b) of Fig. 2.8 show the trend of the transmission spectra as a function of power in the case of *forward* excitation and *reverse* excitation, respectively. In both cases, as the power increases, the resonance shifts to longer wavelengths (redshift), and even at higher powers it can be seen that the resonance deforms, taking on the characteristic triangular shape of the spectrum of a high-power resonance [163, 164, 165, 166]. This redshift is mainly caused by the Thermo Optic Effect (TOE), which for SiON amounts to $n_T \simeq 2 \times 10^{-13}$ cm^2/W much larger than the nonlinear Kerr index $n_K \simeq 8 \times 10^{-16}$ cm^2/W. It is worth noting that $n_T > 0$, in fact, we observe an increase in wavelength as the power increases. Comparing panels (a) and (b) of Fig. 2.8, it is clear that at high powers the resonance in the *reverse* configuration is more redshifted compared to the *forward* one. For example, at 0.65 W there is a window of about 0.17 nm between 1545.1 nm and 1545.27 nm in which the *reverse* transmission is low (< 0.3 a.u.) while the *forward* transmission is high ($\gtrsim 0.8$ a.u.). Therefore, we have shown experimentally that by using a TJMR in the nonlinear regime it is possible to break Lorentz reciprocity. As explained earlier, the breaking of Lorentz reciprocity is due to the different energy inside the TJMR when it is excited in the *forward* or *reverse* direction. In fact, in the second case we have that the light intensity of the CW mode is the same as that of the CCW mode when the TJMR is excited in the *forward* configuration, and in addition the energy in the

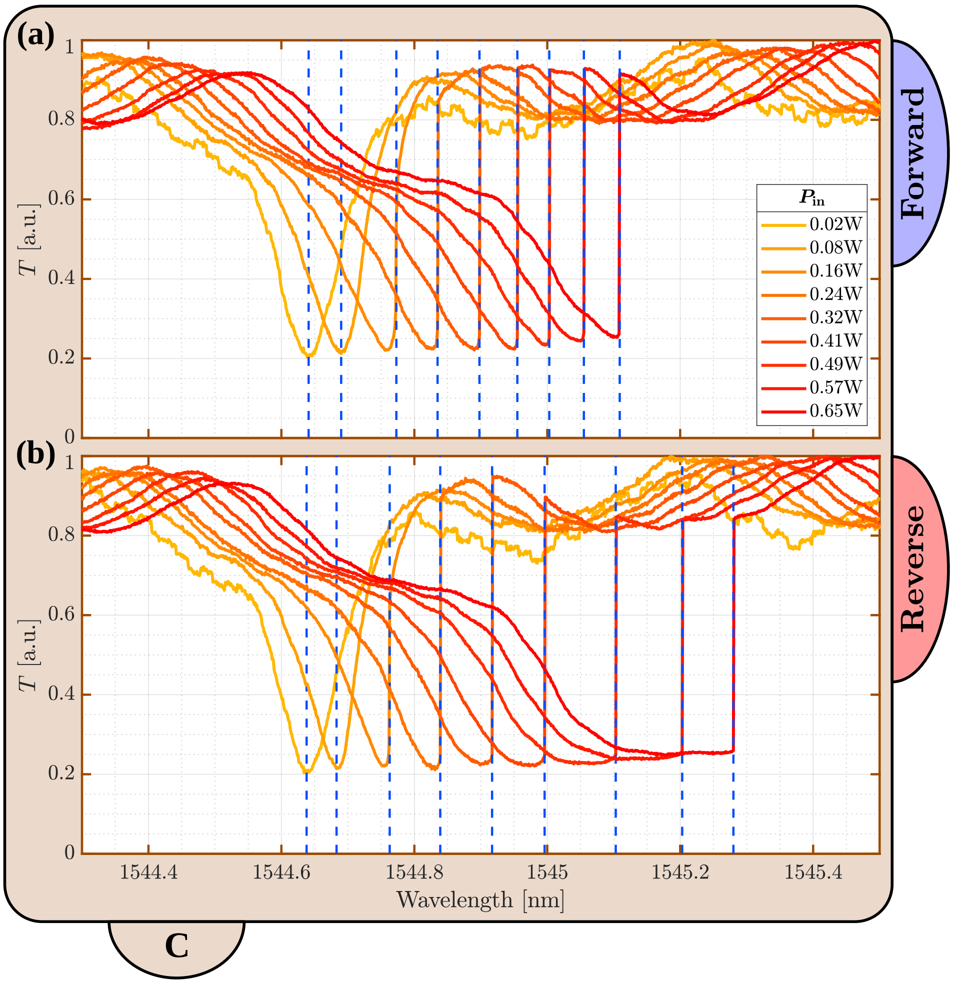

Figure 2.8: Normalized transmission spectra of upward wavelength ramps for different input powers, for a bus waveguide/TJMR system exhibiting a *constructive*-like (C) line shape in the linear regime. Panels (a) and (b) show the experimental data for a *forward* and *reverse* configuration, respectively. The resonant wavelengths for different powers are indicated by the blue dashed lines. For low input power, the resonant wavelength is considered to be the minimum of the Lorentzian dips, while for high input power, the resonant wavelength is considered to be the wavelength at which the transmission jump occurs. [78]

CCW mode (in *reverse*) is also different from zero. However, the FP cavity can create special situations due to interference within the TJMR, see Fig. 2.9. Before going on to describe the three different cases observed experimentally, let us make two more considerations about the graphs shown in Fig. 2.8. It is indeed worth noting that the fringes of the FP cavity also show a redshift with increasing power, but these redshifts are almost equivalent in the two excitation directions and are also smaller than that observed for the resonance. These shifts are simply due to the heating of the bus waveguide and are smaller than that found for the resonance of the TJMR, because the TJMR has a larger EF ($\simeq 9$) than that of the FP cavity. Due to the presence of the FP oscillations, we will identify the position of the resonance (λ^{res}) at different energies in this way. At low powers, that is, when the characteristic sharp jump of the signal (triangular shape) cannot be observed, we use the wavelength corresponding to the minimum of the transmission dip, while at high powers we use the wavelength at which the sharp increase in transmission occurs, see blue dashed lines in Fig. 2.8. This transmission jump is due to the fact that the power inside the microresonator is no longer sufficient to shift the resonance further, and thus the wavelength of the laser overtakes the "hot" resonance of the TJMR, and thus the TJMR cools down quickly.

Let us now describe three characteristic cases. To quantify the region where Lorentz reciprocity is broken, we compute the difference $\Delta\lambda_{\mathrm{r}}[\mathrm{P}] - \Delta\lambda_{\mathrm{f}}[\mathrm{P}]$ between the relative shift of λ^{res} for the *reverse* configuration $\Delta\lambda_{\mathrm{r}}[\mathrm{P}] := \lambda_{\mathrm{r}}^{\mathrm{res}}[\mathrm{P}] - \lambda_{\mathrm{r}}^{\mathrm{res}}[\mathrm{P} \simeq 0]$ and for the *forward* configuration $\Delta\lambda_{\mathrm{f}}[\mathrm{P}] := \lambda_{\mathrm{f}}^{\mathrm{res}}[\mathrm{P}] - \lambda_{\mathrm{f}}^{\mathrm{res}}[\mathrm{P} \simeq 0]$. Figure 2.9 (a) shows $\Delta\lambda_{\mathrm{r}}[\mathrm{P}] - \Delta\lambda_{\mathrm{f}}[\mathrm{P}]$ as a function of power for the three different cases, *constructive*-like, *Fano*-like, and *destructive*-like, identified by the colors brown, green, and orange, respectively. These three cases correspond to those reported in the linear regime in Fig. 2.7, panel (b1), (b2) and (b3), respectively. The transmission spectra for the *forward* and *reverse* configurations at a coupled power in bus waveguide of about 0.65 W are shown in panels (a1), (a2) and (a3) of Fig. 2.9. In blue is the *forward* spectrum and in red is the *reverse* spectrum.

In the *constructive*-like case (brown symbols) $\Delta\lambda_{\mathrm{r}}[\mathrm{P}] - \Delta\lambda_{\mathrm{f}}[\mathrm{P}]$ is positive and reaches the value of about 0.17 nm at 0.65 W, see panels (a) and (a1) of Fig. 2.9. Therefore, in the *constructive*-like case, as seen in Fig. 2.8 in the *reverse* configuration the energy inside the TJMR is higher than the one in the *forward*. Even in the *destructive*-like case (orange symbols) $\Delta\lambda_{\mathrm{r}}[\mathrm{P}] - \Delta\lambda_{\mathrm{f}}[\mathrm{P}]$ is positive, but small compared to the previous case, see panels (a) and (a3) of Fig. 2.9. Instead, in the *Fano*-like case (green symbols) $\Delta\lambda_{\mathrm{r}}[\mathrm{P}] - \Delta\lambda_{\mathrm{f}}[\mathrm{P}]$ is small but negative at high powers, see panels (a)

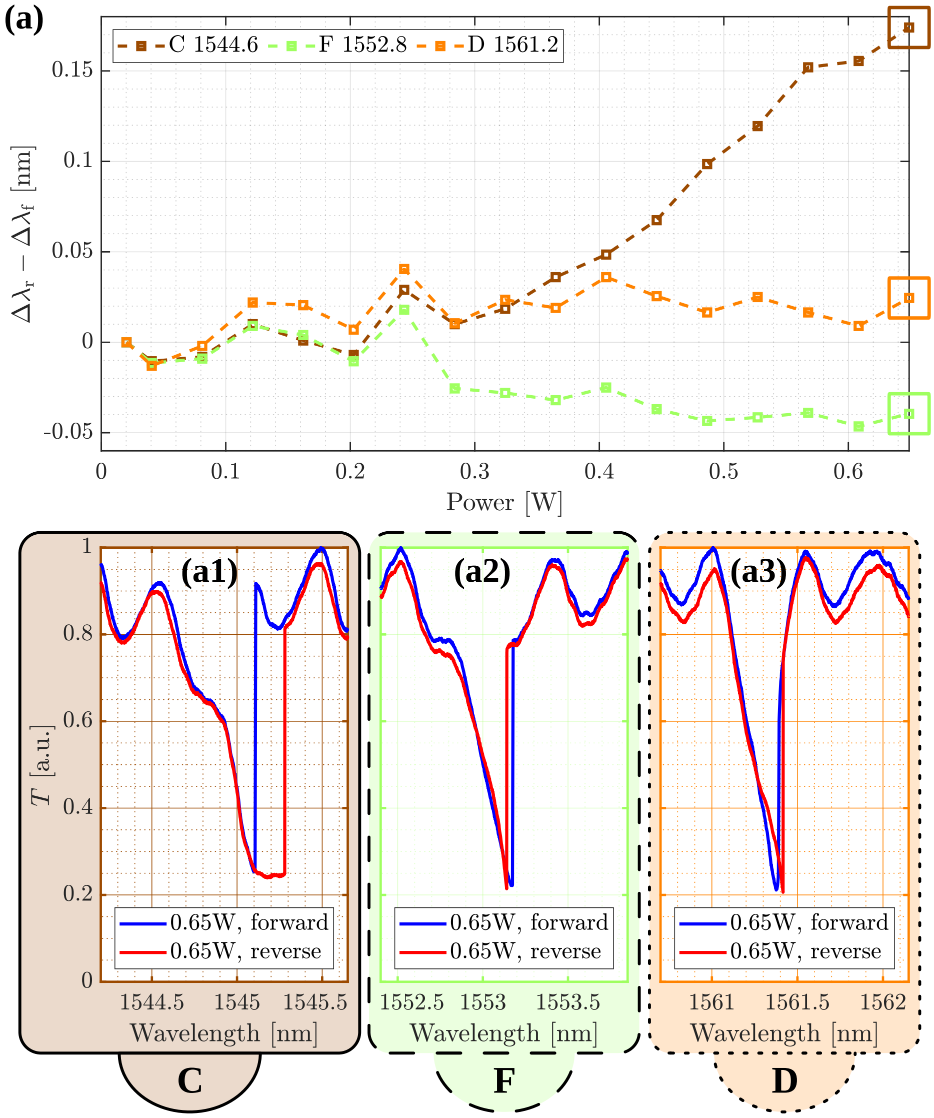

Figure 2.9: Panel (a) shows the difference between the resonant shift in the *reverse* and *forward* configurations as a function of the input power for the three cases described in Fig. 2.7. The brown, green and orange colors highlight the *constructive*-like (C), *Fano*-like (F) and *destructive*-like (D) cases seen in the linear regime. Panels (a1)-(a3) show the experimental results of the normalized transmission spectra at $P_{in} \simeq 0.65$ W for the *forward* (blue lines) and *reverse* (red lines) configurations and for the three interference cases. The wavelength scans were performed starting from shorter wavelengths to longer wavelengths. [78]

and (a2) of Fig. 2.9. This means that because of the interference with the FP cavity modes, the behavior of the TJMR changes which causes an increased energy inside the TJMR in the *forward* excitation.

2.3.2 Theoretical simulations

Simulation Model

The theoretical simulations of the bus waveguide/TJMR system are based on the equations derived in Sec. 2.2 by using the TMM. However, in the nonlinear regime we will consider not only the variation of the effective refractive index of the WG as a function of wavelength, but also its dependence on the optical power in the WGs.

In the case of a local Kerr nonlinearity when two counterpropagating fields are present the refractive index shift is proportional to $|E_{CW}+E_{CCW}|^2(E_{CW}+E_{CCW})$ [77, 78, 167], where E_{CW} and E_{CCW} are the electric fields with the propagation direction CW and CCW, respectively. Expanding the squared modulus gives:

$$\begin{aligned}
&|E_{CW}+E_{CCW}|^2(E_{CW}+E_{CCW}) = \\
=&(|E_{CW}|^2+|E_{CCW}|^2+E^*_{CW}E_{CCW}+E_{CW}E^*_{CCW})(E_{CW}+E_{CCW}) = \\
=&(|E_{CW}|^2+2|E_{CCW}|^2)E_{CW}+(2|E_{CW}|^2+|E_{CCW}|^2)E_{CCW}+E^*_{CW}E^2_{CCW}+E^2_{CW}E^*_{CCW} \\
\simeq&(|E_{CW}|^2+2|E_{CCW}|^2)E_{CW}+(|E_{CCW}|^2+2|E_{CW}|^2)E_{CCW}\,, \qquad (2.60)
\end{aligned}$$

where the two terms $E^*_{CW}E^2_{CCW}$ and $E^2_{CW}E^*_{CCW}$ are neglected because they oscillate rapidly and average to zero in the rotating wave approximation. Note that there is a factor 2 for the Kerr shift due to counterpropagating waves [77, 167]. In the case of thermo optic nonlinearity, however, this factor of 2 is reduced to 1 because this phenomenon is not local [77, 167]. In the nonlinear regime, we will therefore use the following formula for the effective refractive index of the WG [77, 78]:

$$n_{eff} = n_L + n_T I_{thermal} + n_K(|E_{CCW/CW}|^2 + 2|E_{CW/CCW}|^2)\,, \qquad (2.61)$$

where n_L is the effective refractive index in the linear regime, n_T is the coefficient of the thermo optic nonlinearity, $n_K \simeq 8\times10^{-16}$ cm^2/W $\ll n_T$ is the a.c. Kerr nonlinear index and $I_{thermal}$ is the total light intensity for the three different regions: microresonator, S-shaped WG and bus waveguide. In the simulations, we used the relation $n_T \propto 1-e^{-\alpha L}$, which relates the Thermo Optic (TO) nonlinear coefficient to the propagation losses α (L is the microresonator perimeter). By comparing the experimental results with the simulated ones, we estimated n_T, see Fig. 2.10.

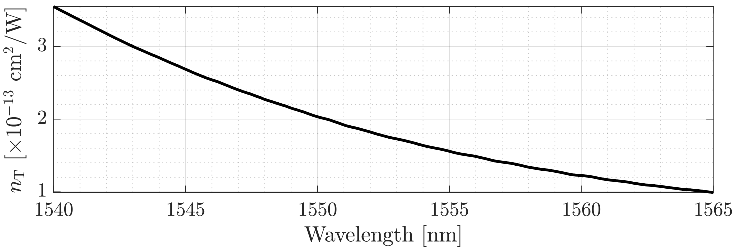

Figure 2.10: Thermo Optic (TO) nonlinear coefficient as a function of the wavelength, estimated by comparing experimental and simulated spectra. [78]

To derive the transmission, reflection, and internal energy spectra, we evolved the system of equations starting at low wavelengths and increasing the wavelength in small steps. In addition, for each value of the wavelength, we evolved the system to convergence. This was necessary because the refractive index depends on the internal fields of the system, which in turn depend on the refractive index.

Taiji microresonator internal energy calculation

In the nonlinear regime, it is important to calculate the intensities within the system in the correct way to obtain the correct value of the refractive index. In particular, it is necessary to calculate the internal energy in the three regions: microresonator, S-shaped WG and bus waveguide. Since the procedure is equivalent, we will only explain here how we calculated the internal energy of the MR. First, we need to calculate the CW and CCW fields for each point inside the MR. To do this, we can take advantage of the fact that along the wave propagation direction (z) and between two coupling regions, we can write the electric field as $E[z] = E[z_0]e^{i(\frac{2\pi}{\lambda}n_{\text{eff}}+i\alpha)(z-z_0)}$, where z_0 is the starting position and z is the coordinate along the WG. Then, using the equations derived from the TMM (see Sec. 2.2), we compute all the CW (E_{CW}) and CCW (E_{CCW}) fields. At this point, the internal energy is easily determined by calculating the integral of $|E_{CW} + E_{CCW}|^2$ along the entire MR.

Parameters of the simulation

From the design of TJMR we have: $L_{23} = L_{67} \simeq 206.26$ µm, $L_{45} \simeq 397.71$ µm and $L_{89} \simeq 391.12$ µm, so $L = L_{23} + L_{45} + L_{67} \simeq 810.24$ µm.

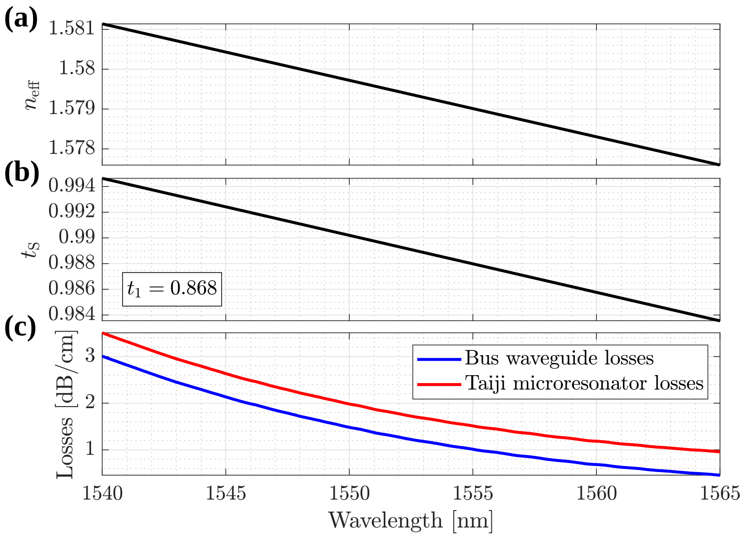

Figure 2.11: Parameters used in the theoretical simulation as a function of wavelength. Panels (a) and (b) show the spectral dependence of the effective refractive index (n_{eff}) and the transmission coefficients of the coupling between MR and S-shaped WG ($t_2 = t_3 = t_S$). (c) shows the propagation losses within bus waveguide and TJMR as a function of wavelength in blue and red, respectively. [78]

The effective refractive index (n_{eff}) was extrapolated from that reported in [52] and a variation was applied to it to match the simulated TJMR resonances with the experimental ones. In Fig. 2.11 (a) the obtained n_{eff} is reported as a function of wavelength. The bus waveguide length $l_L \simeq 0.431$ mm was obtained from the design, while the bus waveguide length $l_L \simeq 1.062$ mm and the reflection coefficients $r_L = r_R \simeq 0.23$ were extrapolated from the experimentally measured FP oscillations. In the simulations, we assumed that the three couplings are lossless, i.e. $t^2 + k^2 = 1$. The spectral dependence of the transmission coefficients $t_2 = t_3 = t_S$, losses and $t_1 = 0.868$ were estimated by measuring the transmission, reflection and propagation loss spectra. The obtained parameters are shown in panels (b) and (c) of Fig. 2.11. Fitting the experimental spectra in the linear regime and in the nonlinear regime, we observed that the propagation losses within the TJMR are higher than those due to the bus waveguide, see Fig. 2.11 (c). This difference is easily explained by the additional losses that light encounters in the TJMR due to the presence of bends.

Linear regime

In this subsection we will study the bus waveguide/TJMR system using simulations and investigate the different types of interference between the TJMR and the FP cavity. The length $l_L \simeq 0.431$ mm of the bus waveguide and all parameters of the TJMR will be kept constant, and we vary l_R.

Since we are interested in understanding the interaction between the TJMR and the FP cavity, we calculated the reflections in three cases: for the *reverse* excitation R_r, for the *forward* one R_f and for the situation where the TJMR is removed ($t_1 = 1$) and only the FP cavity remains R_{FP}. Panels (a) and (b1) Fig. 2.12 show the wavelength vs l_R maps of $R_r - R_f$ and of $R_r - R_{FP}$, respectively. A 2 μm-range of l_R around $l_R = 5.524$ mm [panel (a)] and $l_R = 1.062$ mm [panel (b1)] is mapped. Since the intensity inside the TJMR is also affected by the interferences with the FP cavity, in panel (b2) of Fig. 2.12 we report the λ vs l_R map of the difference between the intensity inside the TJMR in the *reverse* configuration (I_r) and that in the *forward* configuration (I_f). This map is only reported for $l_R \simeq 1.062$ mm. In all three maps, vertical lines can be seen; these correspond to the resonance wavelengths of the TJMR. Recall that all simulations also take into account the variation of various parameters (such as n_{eff}, t_S and the propagation losses) as a function of wavelength, as described above.

In agreement with the experimental measurements [Fig. 2.7 (a)], for long bus waveguide ($l_R \simeq 5.524$ mm) the system behaves as a unidirectional reflector ($R_r - R_f > 0$), see Fig. 2.12 (a). In addition, from the simulations with $l_R \simeq 1.062$ mm [Fig. 2.7 (b)], we are able to find all the cases that we found experimentally. These cases are marked by rectangles in panels (b1) and (b2). Furthermore, in panels (b3), (b4)-(b5) and (b6), the transmission and reflection spectra for the cases marked by the rectangles are given, respectively, for $l_R = 1.0620$ mm (top) and $l_R = 1.0624$ mm (bottom). In particular, (b3) reports two *destructive*-like (D) cases, (b4) and (b5) two *constructive*-like (C) cases, and (b6) two *Fano*-like (F) cases. The plus or minus sign inside the graphs describes a positive or negative difference between I_r and I_f.

We start with the *destructive*-like case [dotted rectangles in Fig. 2.7 (b1)-(b2) and lineshapes in Fig. 2.7 (b3)]. Here we have that the reflection in *reverse* has a dip at resonance. This is due to the destructive interference between the light reflected at the input facet (magenta arrows) and the light entering the bus waveguide, coupling to the CW mode (red arrows), which in turn couples to the CCW mode through the S-shaped WG (blue arrows), goes back to the bus waveguide, and exits the

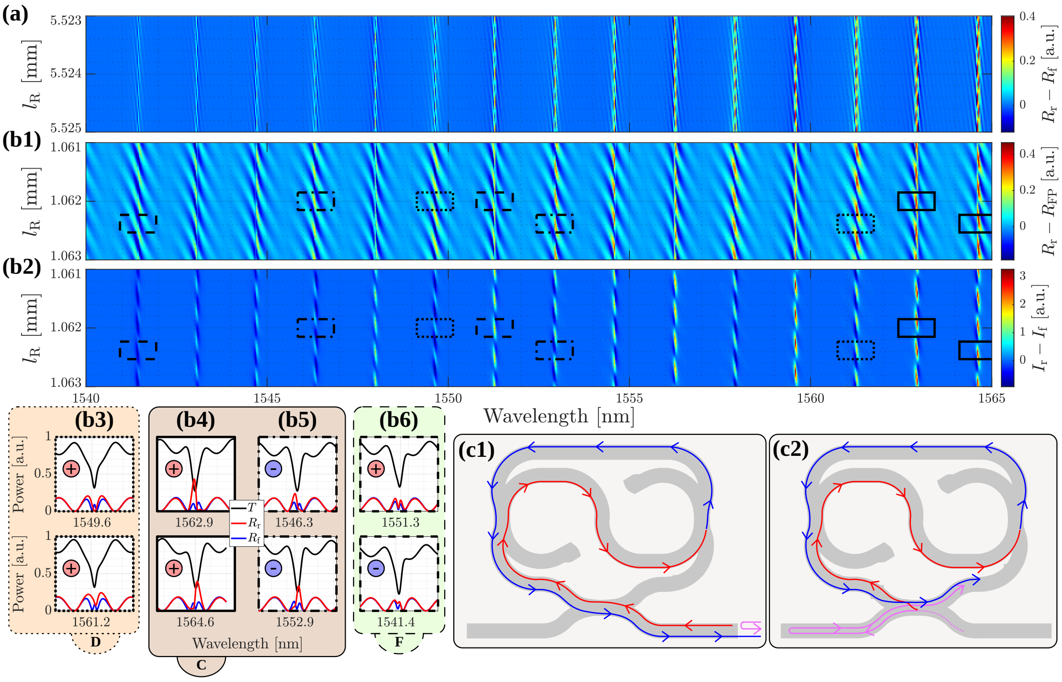

Figure 2.12: Panel (a) shows the wavelength vs l_R map of the difference between the reflection in *reverse* and *forward*, for $l_R \simeq 5.524$ mm, i.e. $R_r - R_f$. Panel (b1) shows the simulated wavelength vs l_R map of the difference between the reflected intensities for the *reverse* and the FP oscillations (without the TJMR), namely, $R_r - R_{FP}$. Panel (b2) shows the map of the difference between the intensity inside the TJMR in the *reverse* (I_r) and *forward* (I_f) configurations as a function of the wavelength and $l_R \simeq 1.062$ mm. In panels (b3), (b4)-(b5) and (b6) are plotted the transmission and reflection spectra for $l_R = 1.0620$ mm (top) and $l_R = 1.0624$ mm (bottom) for the *destructive*-like (D), *constructive*-like (C) and *Fano*-like (F) cases. The different line-style of the rectangles connects these graphs with the maps (b1) and (b2). The + and - signs inside the graphs indicate when $I_r - I_f > 0$ and $I_r - I_f < 0$, respectively. Panels (c1) and (c2) show the interference diagrams. The red and blue arrows label the CW and the CCW modes, respectively. $l_L \simeq 0.431$ mm is constant in all the panels. Here the bus waveguide/TJMR system is in the linear regime. [78]

right facet, as shown in panel (c1) of Fig. 2.7. Thus, the condition of destructive interference between these two waves can be written as follows:

$$\frac{2\pi}{\lambda} n_{\mathrm{eff}}(2l_R + 2L_{67} + L_{89} + L_{45}) + 2\pi = \pi + \pi + 2\pi m_{I1}\,, \quad m_{I1} \in \mathbb{Z}\,. \tag{2.62}$$

In other words, the phase difference between the path followed by the field reflected by the TJMR and the path followed by the light reflected by the input facet must be an odd multiple of π. Therefore, m_{I1} must satisfy:

$$m_{I1} = \frac{n_{\mathrm{eff}}(2l_R + 2L_{67} + L_{89} + L_{45})}{\lambda}\,. \tag{2.63}$$

This condition is met in (b3, top) where the *reverse* reflection goes to zero at resonance. Also in (b3, bottom) the dip in the *reverse* reflection is observed, but in this case the small variation in the length of the bus waveguide causes the perturbation to be slightly different, in fact, the dip does not reach zero. It is worth noting from the map in Fig. 2.12 (b2) (dotted rectangles) that the electromagnetic intensity within the TJMR results higher in the *reverse* case than in the *forward* case. In fact, destructive interference in reflection does not mean that there is the same kind of interference inside the TJMR. To understand this, we need to introduce two new interference diagrams. Let us consider the FP cavity. It has constructive interference at the output of the input facet if the following relation is satisfied:

$$\frac{2\pi}{\lambda} n_{\mathrm{eff}}(2l_R + 2l_L) = \pi + 2\pi m_{\mathrm{FPCR}}\,, \quad m_{\mathrm{FPCR}} \in \mathbb{Z}\,. \tag{2.64}$$

The interference between two other fields must be taken into account, see panel (c2). This is the constructive interference within the TJMR between the CW field (red arrows) that transforms into the CCW mode (blue arrows) and then returns to the coupling region and from the field that continues into the bus waveguide, is reflected back to the left facet, returns to the coupling region with the TJMR and then couples with the latter (magenta arrows). This constructive interference occurs when:

$$\frac{2\pi}{\lambda} n_{\mathrm{eff}} 2l_L + \frac{\pi}{2} = \frac{\pi}{2} + \frac{2\pi}{\lambda} n_{\mathrm{eff}}(2L_{67} + L_{89} + L_{45}) + \pi + 2\pi m_{I2}\,, \quad m_{I2} \in \mathbb{Z}\,. \tag{2.65}$$

It is worth to note that the three numbers m_{FPCR}, m_{I1} and m_{I2} are actually related:

$$m_{\mathrm{FPCR}} = m_{I1} + m_{I2}\,. \tag{2.66}$$

Therefore, if m_{FPCR} and m_{I1} are integers, then m_{I2} will also be integer. In other words, if the FP oscillations have a reflection peak and the whole system has a reflection dip, then there will be constructive interference within the TJMR and consequently $I_r - I_f > 0$.

This model also explains the *constructive*-like case. The solid and dashed-dotted rectangles in the panels (b1) and (b2) of Fig. 2.12 highlight some regions where the *constructive*-like shape is present. Using also the spectra corresponding to the four rectangles given in panels (b4) and (b5), it is observed that here the structure behaves as a unidirectional reflector. In fact, the reflection in *reverse* is higher than that in *forward*. Using the map in panel (b2), it can be seen that the cases reported in (b4) are characterized by higher energy within the TJMR in the *reverse* configuration (+ sign), while those in (b5) exhibit higher internal energy in the *forward* excitation (− sign). The resonances in (b5) have shorter wavelengths than those in (b4), so the larger propagation losses observed at shorter wavelengths (Fig. 2.11 (c)) and the unbalance of the two lengths $l_R > l_L$ cause the discrepancy between the internal energies found in these cases.

The simulations performed also report *Fano*-like situations, see the dashed rectangles in panels (b1) and (b2) and the transmission and reflection spectra in panel (b6) of Fig. 2.12. Here we are in an intermediate case between *constructive*-like and *destructive*-like, and moreover, the internal energy at the TJMR in *reverse* can be both higher and lower than that in *forward*.

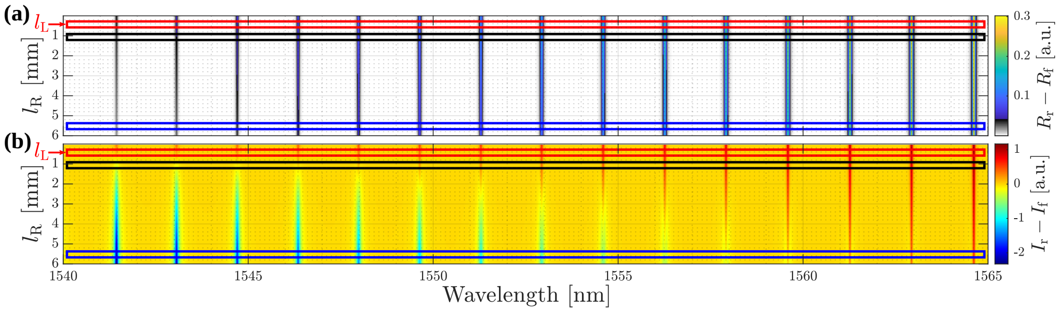

Figure 2.13: Panels (a) and (b) show the wavelength vs l_R maps of $R_r - R_f$ and $I_r - I_f$, respectively. In these maps, the facet reflections of the bus waveguide are considered equal to zero ($r_{L/R} = 0$) and $l_L \simeq 0.431$ mm is constant. The red, black, and blue rectangles highlight the regions where $l_R = l_L = 0.431$ mm, $l_R = 1.062$ mm and $l_R = 5.52$ mm, respectively. Here the bus waveguide/TJMR system is in the linear regime. [78]

We have seen that due to the interference of the FP cavity, the TJMR can lose its property of being a unidirectional reflector. Let us now simulate the case where the reflections of both ends of bus waveguide are zero ($r_L = r_R = 0$), see Fig. 2.13.

Panel (a) shows the map of the difference between the reflections ($R_r - R_f$) as a function of the wavelength and the length of the right side of the bus waveguide (l_R). Also in this figure, $l_L = 0.431$ mm is kept constant. Note that here the reflection R_r is always higher than in *forward*, because in the absence of the facet reflections $R_f = 0$. Note also that we do not observe any oscillations in the map, which confirms that the oscillations are caused by the FP cavity. It is worth noting that the reflection R_r decreases with decreasing wavelength and increasing length l_R. This is due to propagation losses, which are largest at 1540 nm and decrease monotonically with increasing wavelength. Also, by increasing the length l_R, due to propagation losses, less light is coupled to the CW mode and consequently less energy is transferred from the CW mode to the CCW mode. To observe this phenomenon more closely, in panel (b) of Fig. 2.13 we show the λ vs l_R map of $I_r - I_f$. In Fig. 2.13 the red, black and blue colored rectangles identify the regions where $l_R = l_L = 0.431$ mm, $l_R \simeq 1.062$ mm and $l_R \simeq 5.52$ mm, respectively. Because of the wavelength dependence of the propagation losses we have that for any fixed l_R the difference $I_r - I_f$ decreases with decreasing wavelength, see Fig. 2.13 (b). Moreover, by increasing the length l_R the TJMR is no longer centered between the two facets of the bus waveguide, so due to propagation losses less energy is coupled within the TJMR in the *reverse* case than in the *forward* case. This causes that, especially at low wavelengths, where the losses are higher, the effect of the S-shaped WG is not sufficient to counteract the lower energy coupled to the TJMR, and therefore regions where $I_r - I_f < 0$ are observed. On the other hand, when $l_R = l_L$, the optical intensity within the TJMR is always higher in the *reverse* configuration ($I_r - I_f > 0$).

In summary, we have observed that, depending on the interaction between the FP cavity and the TJMR, we can have that the TJMR behaves as a unidirectional reflector or not, and the internal energy in the *reverse* case can be both higher and lower than in the *forward* one. Thus, by simply changing the free spectral range (resonance), different cases can be studied. In addition, we found that the total length of the waveguide and the position of the TJMR with respect to the two ends of the bus waveguide are also very important.

Nonlinear regime

Let us now simulate the bus waveguide/TJMR system in the nonlinear regime. Panels (a) and (b) of Fig. 2.14 show the transmission spectra and the internal intensity spectra of TJMR as a function of the input power P_{in}, when a wavelength scan from low to high values is performed. Here, by P_{in} we mean the input coupled optical power within the bus waveguide. In panels (a), (b), (c) and (d1) $l_R = 1.0624$ mm, while in (d2) $l_R = 1.0620$ mm. In panels (a1), (b1) and (c1) we use *reverse* excitation, while in (a2), (b2) and (c2) we use *forward* excitation. Let us focus on panels (a) and (b). As expected, by increasing P_{in} the resonances shift to higher wavelengths proportionally to the internal intensity of the TJMR. The positive shift is consistent with the fact that the nonlinear coefficients of the material used are positive. Note that the dominant nonlinear coefficient here is the one associated with thermo optic effect ($n_T \gg n_K$). The FP fringes also show a redshift, but it is smaller than that of the resonances. This difference is due to the different energies within the TJMR and the bus waveguide, in fact, the TJMR is characterized by a Enhancement Factor (EF) of about 9. Note also that because of the higher losses at shorter wavelengths and the assumed $n_T \propto 1 - e^{-\alpha L}$ relationship, a higher redshift of the resonances is observed at shorter wavelengths, even though the intensity inside the TJMR is higher at longer wavelengths. The *destructive*-like, *constructive*-like and *Fano*-like cases reported for the linear regime in panels (b3), (b4)-(b5) and (b6) of Fig. 2.12 (bottom panels, $l_R = 1.0624$ mm) are highlighted by the rectangles in the nonlinear maps in Fig. 2.14. Specifically, the dashed rectangles mark the *Fano*-like case (F-), the dash-dotted/solid rectangles mark the *constructive*-like cases (C-/C+), and the dotted rectangles mark the *destructive*-like cases (D+). The signs $+$ and $-$ indicate that for the linear case this resonance has $I_r - I_f > 0$ and $I_r - I_f < 0$, respectively. Panels (c1) and (c2) of Fig. 2.14 correspond to the *constructive*-like C- case and they are the theoretical analog of the experimental data reported in panels (b) and (a) of Fig. 2.8. From these transmission spectra taken at different powers, scanning from a shorter to a longer wavelength, it is observed that at high powers the redshift is higher in the *reverse* (c1) configuration than in the *forward* (c2) configuration. Thus, even theoretically, we have reported Lorentz reciprocity breaking using a TJMR in the nonlinear regime. From panels (c1) and (c2) it can be seen that, due to the interference of the FP fringes, the difference between the nonlinear redshifts of the resonances for the *reverse* and *forward* configurations does not show a linear trend. Fig. 2.14 (d1) shows the difference $\Delta\lambda_r - \Delta\lambda_f$ obtained from the maps in panels (a1) and (a2) for the four resonances highlighted by the rectangles. Specifically, the dotted, dash-dotted/solid, and dashed lines correspond to the *destructive*-like (D+), *constructive*-like (C-/C+), and *Fano*-like (F-) cases, respectively. As observed experimentally, the different cases show different trends of $\Delta\lambda_r - \Delta\lambda_f$ as a function of the power P_{in}. In the *destructive*-like case, a positive value of $\Delta\lambda_r - \Delta\lambda_f$ slightly larger than zero is observed, both in the theoretical simulation [labeled D+ in Fig. 2.14 (d1)] as well as in the experimental measurement (labeled D in Fig. 2.9). The same agreement also occurs between the theoretical C- and the experimental C case, where $\Delta\lambda_r - \Delta\lambda_f$ is always positive and reaches a high value of 0.07 nm and 0.17 nm, respectively. The *Fano*-like case also shows good agreement between theory (F-) and experiment (F), in fact in both cases $\Delta\lambda_r - \Delta\lambda_f$ has negative values.

However, there is no clear relationship between $I_r - I_f$ in the linear regime and $\Delta\lambda_r - \Delta\lambda_f$ in the nonlinear regime. In fact, in the *constructive*-like case, the $\Delta\lambda_r - \Delta\lambda_f$ vs P_{in} curve shows both a positive slope for the C- case (where $I_r - I_f < 0$ in the linear regime), and an almost zero slope in the C+ case (where $I_r - I_f > 0$ in the linear regime). The absence of a direct correlation between the trend of $\Delta\lambda_r - \Delta\lambda_f$ as a function of P_{in} and the value of $I_r - I_f$ in the linear regime is even more evident in Fig. 2.14 (d2). Here, the trends correspond to nonlinear simulations performed on the resonances reported at the top of panels (b3)-(b6) of Fig. 2.12, where $l_R = 1.0620$ mm. Here, D+, C- and F+ have a negative $\Delta\lambda_r - \Delta\lambda_f$ value at high P_{in} instead C+ has always a positive $\Delta\lambda_r - \Delta\lambda_f$ as a function of P_{in}. These behaviors do not match with those observed in panel (d1). Therefore, depending on their spectral position and on the length l_R, the resonances of the TJMR show a different $\Delta\lambda_r - \Delta\lambda_f$ shift which we attribute to the interplay between the FP and the asymmetric losses ($l_L \neq l_R$) in the bus waveguide.

In Fig. 2.15 we analyze the interplay between the FP and the asymmetric losses ($l_L \neq l_R$) in the bus waveguide by plotting the trends of $\Delta\lambda_r - \Delta\lambda_f$ as a function of P_{in} in different configurations. In panels (a1) and (a2) we have removed the facet reflections ($r_L = r_R = 0$, no FP fringes), while in (b) and (c) we have $r_L = r_R = 0.23$ and $r_L = r_R = 0.1$, respectively. Furthermore, in (a1) $l_R = 1.0624$ mm $> l_L = 0.431$ mm, while in the other panels $l_R = l_L = 0.431$ mm.

In the simulations without FP [panels (a1) and (a2)], a linear trend of $\Delta\lambda_r - \Delta\lambda_f$ as a function of P_{in} is observed. The different slopes are due to the different propagation losses, in fact, the resonance at 1541.4 nm, with larger losses, has a smaller slope, while the resonance at 1564.6 nm, with smaller losses, has the maximum slope. It is important to note that in the asymmetric case [$l_R > l_L$, panel (a1)] the resonance with higher losses has a negative slope. This is due to the fact that, since the TJMR is asymmetrically positioned with respect to the facets of the bus waveguide, the two configurations *forward* and *reverse* excite the TJMR with different intensities. In particular, in (a1) we have that the TJMR is more excited in the *forward* configuration, but nevertheless, only for high loss values this asymmetry succeeds in winning

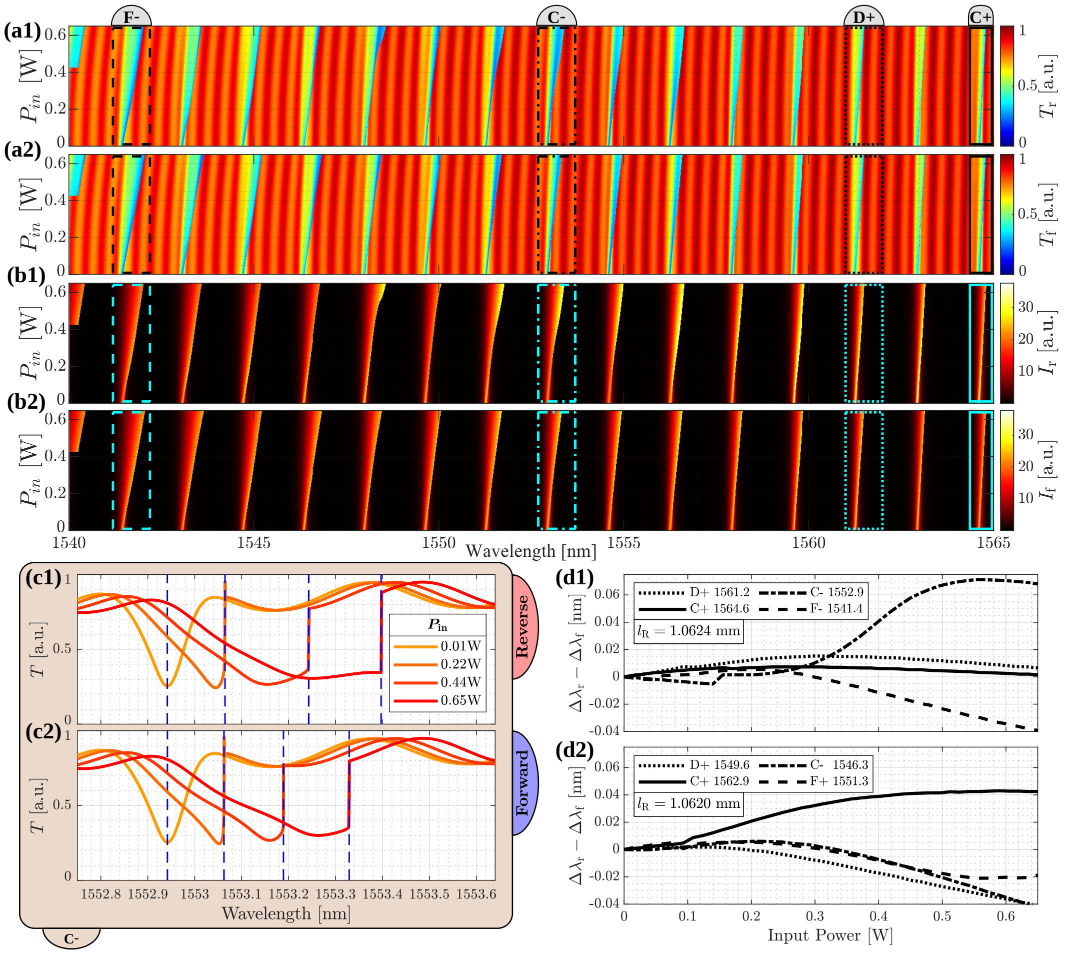

Figure 2.14: Panels (a1) and (a2) show the spectral transmission (T_r and T_f) map as a function of the input power (P_{in}) for the *reverse* and *forward* configurations, respectively. Panels (b1) and (b2) show the spectral internal intensity of the TJMR (I_r and I_f) map as a function of the input power (P_{in}) for the *reverse* and *forward* configurations, respectively. Panels (c1) and (c2) are the spectral transmission for the C- case, i.e. *constructive*-like shape where $I_r - I_f < 0$ in the linear regime, for different input powers and for the *reverse* and *forward* excitation, respectively. An upward wavelength ramp is used in all these panels. Panel (d1) shows the difference between the resonances shift in the *reverse* and *forward* configurations, $\Delta\lambda_r - \Delta\lambda_f$, as a function of P_{in}. For (a1), (a2), (b1), (b3), (c1), (c2) and (d1) the right bus waveguide length is $l_R = 1.0624$ mm. Panel (d2) reports $\Delta\lambda_r - \Delta\lambda_f$ vs P_{in} for $l_R = 1.0620$ mm. The dashed, dotted-dashed, dotted and solid rectangles allow relating the maps (a1)-(a2) and (b1)-(b2) to the graph in panel (d1). The letters D, C and F denote, in the linear regime, the *destructive*-like, *constructive*-like and *Fano*-like cases, respectively. The + and - signs highlight when $I_r - I_f > 0$ and $I_r - I_f < 0$ in the linear regime, respectively. Here the bus waveguide/TJMR system is in the nonlinear regime. [78]

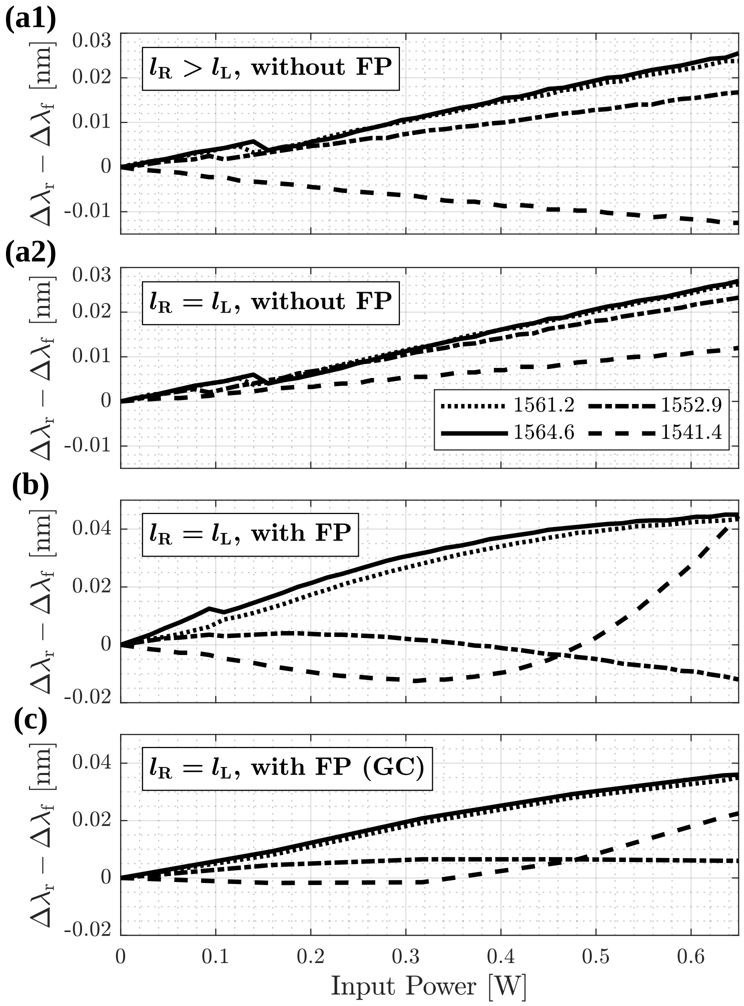

Figure 2.15: Difference between the shift of the resonance of TJMR in the *reverse* configuration versus that in the *forward* configuration ($\Delta\lambda_r - \Delta\lambda_f$) as a function of the input power (P_{in}). Panels (a1) and (a2) are characterized by $r_{L/R} = 0$ (no FP cavity). Panels (b) and (c) have the reflection coefficients of the bus waveguide corresponding to a butt-coupling ($r_{L/R} = 0.23$) and a grating coupling (GC, $r_{L/R} = 0.1$), respectively. In panel (a1) $l_R = 1.0624$ mm $> l_L = 0.431$ mm instead in panels (a2), (b) and (c) $l_R = l_L = 0.431$ mm. [78]

over the energy recirculation given by the S-shaped WG. If $l_R = l_L$ and $r_L = r_R = 0$ [Fig. 2.15 (a2)], the slopes of $\Delta\lambda_r - \Delta\lambda_f$ vs P_{in} are always positive, and thus the TJMR always succeeds in breaking Lorentz reciprocity in the nonlinear regime.

Considering the FP cavity in the symmetric configuration [$l_R = l_L$, Fig. 2.15 (b)], nonlinear trends are observed due to the different perturbations found at different powers. Cases are also observed where the slope of the curve changes its sign with increasing power, as for the frequencies 1541.4 nm and 1552.9 nm (dashed and dotted lines). Figure 2.15 (b) shows that even with $l_R = l_L$ the FP cavity interference can cause a negative $\Delta\lambda_r - \Delta\lambda_f$ shift. By comparing Fig. 2.14 (d1) and Fig. 2.15 (a1) (with and without FP, $l_R = 1.0624$ mm $> l_L = 0.431$ mm), it is worth noticing that the presence of the FP cavity is able to increase the maximum width of the window in which reciprocity breaking occurs, in fact in Fig. 2.14 (d1) $\max[\Delta\lambda_r - \Delta\lambda_f] \simeq 0.07$ nm while in Fig. 2.15 (a1) $\max[\Delta\lambda_r - \Delta\lambda_f] < 0.03$ nm.

It is worth noticing that since we are using a fiber-to-chip coupling realized by simple butt coupling, the facet reflections are quite high $r^2_{L/R} \simeq 0.053$. This reflection can be decreased by several techniques, such as using a matched index resin [168], inverse tapering of the bus waveguide [169, 170], or grating couplers [171]. Since we had a silicon sample with grating couplers, we estimated the reflections of the bus waveguide in this much better performing case and obtained $r^2_{L/R} \simeq 0.01$. Rerunning the simulations with this new value, which is five times lower than that measured in butt coupling, we obtained panel (c) in Fig. 2.15. Note that even with a reflection equal to 1%, we observe nonlinear trends of $\Delta\lambda_r - \Delta\lambda_f$ vs P_{in} due to the presence of the cavity FP.

2.4 Backscattering and Exceptional Point

In Sec. 1.5.3 we observed that an integrated MR in silicon (Si) with a sufficiently high Q ($Q \gtrsim 5 \times 10^4$) exhibits backscattering (BS) due to the surface roughness, which cannot be neglected. In fact, in these cases, the BS is high enough to cause resonance splitting.

Therefore, in this section, we will study a TJMR with non-zero BS. For simplicity, we will ignore the effects caused by the FP cavity and analyze the system using the TCMT. In Sec. 2.4.1 we will introduce the BS inside the TJMR and present the experimental measurements obtained on the TJMR integrated on a Si chip. Then in Sec. 2.4.2 we will analyze in more detail how the TJMR ideally located at an Exceptional Point (EP) behaves as a function of a Hermitian perturbation of the BS coefficients.

2.4.1 Theory and Experimental Measurements

Similar to what was done in Sec. 1.2.1, we introduce into the system of equations Eq. 2.1 a new term describing the coupling between the two modes CW and CCW:

$$K_{BS}\begin{pmatrix}\alpha_{CCW}\\ \alpha_{CW}\end{pmatrix} := \begin{pmatrix}0 & -i\beta_{BS,12}\\ -i\beta_{BS,21} & 0\end{pmatrix}\begin{pmatrix}\alpha_{CCW}\\ \alpha_{CW}\end{pmatrix}, \tag{2.67}$$

Consequently, the Hamiltonian of the TJMR [Eq. (2.3)] turns into:

$$H = \begin{pmatrix}\omega_0 - i\gamma_{tot} & -i\left(\beta_{12}+\beta_{BS,12}\right)\\ -i\beta_{BS,21} & \omega_0 - i\gamma_{tot}\end{pmatrix}. \tag{2.68}$$

As a result, the eigenvalues of the system are no longer degenerate:

$$\lambda_{1/2} = \omega_0 \pm i\sqrt{\left(\beta_{12}+\beta_{BS,12}\right)\,\beta_{BS,21}} - i\gamma_{tot} \;\Rightarrow\; \lambda_1 \neq \lambda_2\,, \tag{2.69}$$

and the eigenvectors are no longer equal:

$$\begin{aligned} v_{1/2} &= \frac{1}{\sqrt{|\beta_{12}+\beta_{BS,12}|/|\beta_{BS,21}|+1}}\begin{pmatrix}\mp\sqrt{\frac{\beta_{12}+\beta_{BS,12}}{\beta_{BS,21}}}\\ 1\end{pmatrix} \\ \Rightarrow <v_1|v_2> &= \frac{1-|\beta_{12}+\beta_{BS,12}|/|\beta_{BS,21}|}{1+|\beta_{12}+\beta_{BS,12}|/|\beta_{BS,21}|}\,. \end{aligned} \tag{2.70}$$

This results in the appearance of a doublet in the transmission spectrum and a non-zero reflection in the excitation from the left (*forward*).

We now define the new total coupling coefficients between the two counter-propagating modes of TJMR. These include both the couplings given by the geometry of the structure ($\beta_{12} \neq 0$ and $\beta_{21} = 0$) and the BS coefficients ($\beta_{BS,12}$ and $\beta_{BS,21}$):

$$\beta_{tot,12} := \beta_{12} + \beta_{BS,12}\,, \qquad \beta_{tot,21} := \beta_{21} + \beta_{BS,21} = \beta_{BS,21}\,. \tag{2.71}$$

When the perturbation given by the BS is small, $|\beta_{12}| \gg |\beta_{BS,12}|$ and $|\beta_{12}| \gg |\beta_{BS,21}|$, hence $|\beta_{tot,12}| \gg |\beta_{tot,21}|$. Note that all β coefficients are generally complex, and therefore β_{12} and $\beta_{BS,12}$ can also have a different (even opposite) argument (phase).

With these new definitions, we rewrite the equations of TJMR:

$$i\frac{d}{dt}\begin{pmatrix}\alpha_{CCW}\\ \alpha_{CW}\end{pmatrix}=\begin{pmatrix}\omega_0-i\gamma_{tot} & -i\beta_{tot,12}\\ -i\beta_{tot,21} & \omega_0-i\gamma_{tot}\end{pmatrix}\begin{pmatrix}\alpha_{CCW}\\ \alpha_{CW}\end{pmatrix}-\sqrt{2\Gamma}\begin{pmatrix}E_{in,L}\\ E_{in,R}\end{pmatrix}, \tag{2.72}$$

$$\begin{pmatrix}E_{out,R}\\ E_{out,L}\end{pmatrix}=\begin{pmatrix}E_{in,L}\\ E_{in,R}\end{pmatrix}+i\sqrt{2\Gamma}\begin{pmatrix}\alpha_{CCW}\\ \alpha_{CW}\end{pmatrix}. \tag{2.73}$$

Note that these equations are identical to those in Eq. (1.59) and Eq. (1.60) except for the change of the variables $\beta_{BS,12}\rightarrow\beta_{tot,12}$ and $\beta_{BS,21}\rightarrow\beta_{tot,21}$. So the solution of this system of equations in the steady state is:

$$\begin{aligned}\varepsilon_{out,R}=&\left(1-\frac{2\Gamma\left(-i\Delta\omega+\gamma_{tot}\right)}{\left(-i\Delta\omega+\gamma_{tot}\right)^2-\beta_{tot,12}\beta_{tot,21}}\right)\varepsilon_{in,L}\\ &+\left(\frac{2\Gamma\beta_{tot,12}}{\left(-i\Delta\omega+\gamma_{tot}\right)^2-\beta_{tot,12}\beta_{tot,21}}\right)e^{i\phi}\,\varepsilon_{in,R},\end{aligned} \tag{2.74}$$

$$\begin{aligned}\varepsilon_{out,L}=&\left(1-\frac{2\Gamma\left(-i\Delta\omega+\gamma_{tot}\right)}{\left(-i\Delta\omega+\gamma_{tot}\right)^2-\beta_{tot,12}\beta_{tot,21}}\right)e^{i\phi}\,\varepsilon_{in,R}\\ &+\left(\frac{2\Gamma\beta_{tot,21}}{\left(-i\Delta\omega+\gamma_{tot}\right)^2-\beta_{tot,12}\beta_{tot,21}}\right)\varepsilon_{in,L},\end{aligned} \tag{2.75}$$

$$a_{CCW}=\frac{\sqrt{2\Gamma}(\Delta\omega+i\gamma_{tot})}{(-i\Delta\omega+\gamma_{tot})^2-\beta_{tot,12}\beta_{tot,21}}\varepsilon_{in,L} \tag{2.76}$$

$$-\frac{i\sqrt{2\Gamma}\,\beta_{tot,12}}{(-i\Delta\omega+\gamma_{tot})^2-\beta_{tot,12}\beta_{tot,21}}e^{i\phi}\,\varepsilon_{in,R}, \tag{2.77}$$

$$a_{CW}=\frac{\sqrt{2\Gamma}(\Delta\omega+i\gamma_{tot})}{(-i\Delta\omega+\gamma_{tot})^2-\beta_{tot,12}\beta_{tot,21}}e^{i\phi}\,\varepsilon_{in,R} \tag{2.78}$$

$$-\frac{i\sqrt{2\Gamma}\,\beta_{tot,21}}{(-i\Delta\omega+\gamma_{tot})^2-\beta_{tot,12}\beta_{tot,21}}\varepsilon_{in,L}, \tag{2.79}$$

where we assumed the conditions given in Eq. (2.5), Eq. (2.6), and Eq. (2.7).

Integrated sample and TJMR design

We have designed four TJMRs based on silicon waveguides. The channel WGs have a cross section of 450 nm × 220 nm and are surrounded by a cladding in SiO_2. In the spectral range where we will use them (1475 nm-1575 nm) the WGs guide only the first TE mode. The designed TJMRs were fabricated in a run at the IMEC/Europractice facility within the multi-project wafer program (the design of the whole chip is shown in Fig. A.1 of Appendix A). To design the TJMRs, we assumed propagation losses of 2 dB/cm and no BS. In addition, all couplings were designed to work best at about 1550 nm. The four TJMRs were designed to have different Qs while still remaining in the critical-coupling regime. In addition, the TJMR with the lower Q is designed to have a very high right (*reverse*) reflection.

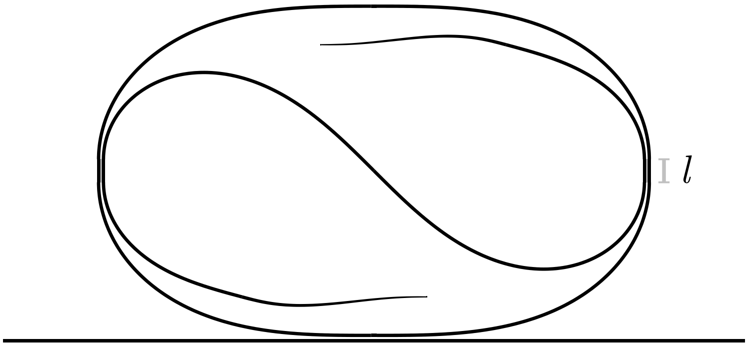

Figure 2.16: Our design of the Taiji Microresonator (TJMR) in the all-pass configuration.

As shown in Fig. 2.16, we decided to use a different geometry than the one shown in Fig. 2.6 (a). In fact, to minimize BS, we decided to use Euler curves [172, 173, 174] with minimum radii of curvature of 15 µm and 10 µm, which is smoother than a constant radius curve. Specifically, the MR consists of four 90° Euler curves with minimum radii of curvature of 15 µm, connected by straight WGs. Therefore, the perimeter of the TJMR is about $L \simeq 196.22$ µm. Starting from the center of the TJMR and proceeding symmetrically, the S-shaped WG is formed by two 135° Euler curves with a minimum radius of curvature of 10 µm, two straight sections of about $l = 3.106$ µm, two more 75° Euler curves with a minimum radius of curvature of 10 µm, and two terminations. The terminations of the S-shaped WG are adiabatically tapered so that the field passes into the SiO_2 without retroreflection. They behaves as perfect loss points. The gap widths between the bus waveguide and the TJMR for the four devices are $\text{gap}_{\text{TB}} = [241, 415, 472, 433]$ nm, while those between the TJMR and the S-shaped WG are $\text{gap}_{\text{TS}} = [210, 410, 550, 440]$ nm. To couple the light from the fiber to the sample, we used the grating at the ends of the bus waveguide.

To measure these devices, we used the experimental setup described in Sec. 1.5.1. Again, to minimize edge reflections from the bus waveguide, we used glycerol to match the refractive indices.

Results

The spectral measurements of the four TJMRs around 1530 nm ($\omega \simeq 2\pi\cdot196\,\text{THz}$) are shown in Fig. 2.17. The blue lines show the experimental data corresponding to the right output intensity, while the red lines are the data at the left output port. Panel (a) shows the transmission spectra (blue lines) and reflection spectra (red lines) corresponding to the left (*forward*) excitation. Panel (b) shows the transmission (red lines) and reflection (blue lines) spectra corresponding to the excitation from the right (*reverse*). With the numbers 1, 2, 3, 4 we identify the four different MRs with different Qs. The dashed and dotted black lines show the theoretical fit performed simultaneously on the four available spectra (two transmissions and two reflections) using Eq. (2.74) and Eq. (2.75). To derive the fit parameters, we used the particle swarm optimization (PSWO) [175]. Particle swarm optimization is a computational technique inspired by the behavior of bird flocks or fish schools, where a group of particles iteratively searches for the optimal solution in a given problem space by adjusting their positions and velocities based on their own experience and the knowledge of the swarm [176, 177, 178]. For all four TJMRs, the fits describe the experimental data well. Here, the coefficients of the BS are necessary to obtain a good agreement between theory and experiment.

Panels (a1) and (b1) of Fig. 2.17 show that the TJMR with the lowest Q behaves like an ideal TJMR. In fact, the reflection from the left is almost zero, while the reflection from the right has a peak at resonance with a height greater than 80% of the maximum transmission. However, by increasing the Q of the TJMR, the unidirectional reflectivity of the device disappears due to the predominance of BS caused by the roughness of the WGs walls. In fact, it is observed that as the Q increases, the resonance splitting becomes more and more evident and the reflections become similar to each other. From the spectral responses of these four types of TJMRs, we have observed that the resonance doublet created can be balanced in some few cases [the two sub-dips have the same ER, for example panels (a3) and (b3)] or unbalanced in other cases, as in panels (a2), (b2), (a4) and (b4). In Fig. 2.17 we also report the Q_{max} of the four TJMRs. We consider the Q_{max} as the maximum Q among those of the two supermodes of the system. In particular, from Eq. (1.111) we have

$$Q_{\text{max}} = \frac{\omega_0}{2(\gamma_{\text{tot}} - \tilde{\gamma})}, \tag{2.80}$$

where $\tilde{\gamma} := \sqrt{|\beta_{\text{tot},12}\beta_{\text{tot},21}|}\cos\left[\arg\left[\beta_{\text{tot},12}\beta_{\text{tot},21}\right]/2\right]$ is always positive. In this

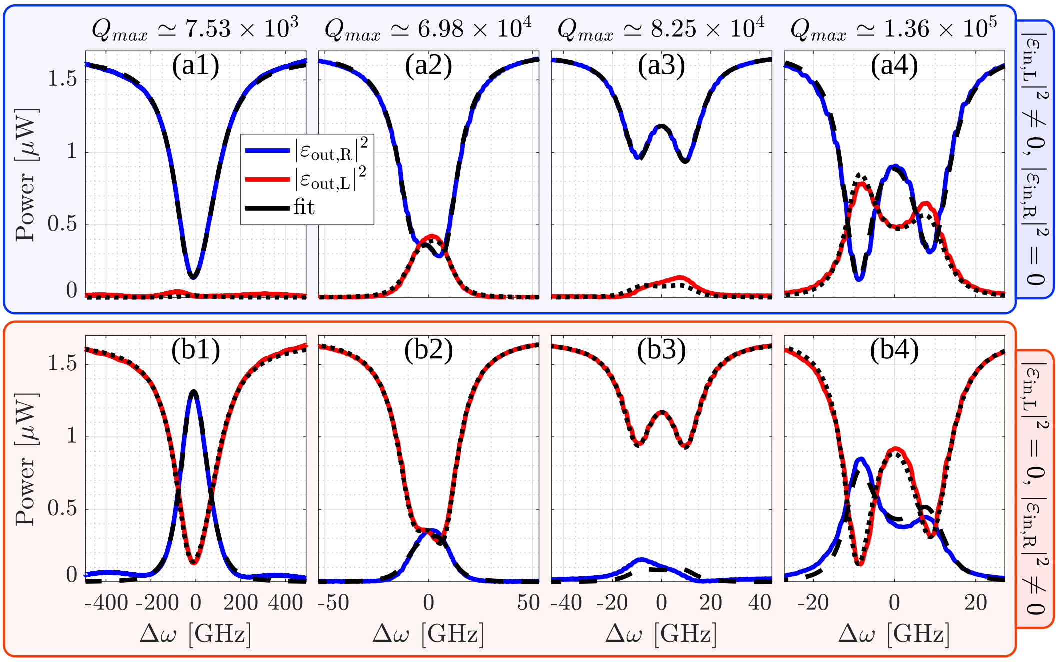

Figure 2.17: Experimental spectra of the four TJMRs. In panel (a) the spectra corresponding to the excitation from the left (*forward*) are plotted, while in (b) those corresponding to the excitation from the right (*reverse*) are plotted. In blue and red are the measured output responses on the right and left, respectively. The black curves show the fits of the experimental data. The four reported resonances have a resonant angular frequency of $\omega_0 \simeq 2\pi \cdot 196$ THz. The gaps of the four TJMRs are $\text{gap}_{\text{TB}} = [241, 415, 472, 433]$ nm and $\text{gap}_{\text{TS}} = [210, 410, 550, 440]$ nm. [47]

definition of Q, almost all influence of BS is removed by $\tilde{\gamma}$. Therefore, by using this new definition, it is possible to compare different types of resonators in the presence of BS. We also saw in Sec. 1.3 that by using interferometric excitation it is possible to transform a doublet into a single Lorentzian with this Q. Thus, Figure 2.17 shows that if the TJMR has a low Q_{max} then the BS is negligible and the device behaves ideally, while if the TJMR has a high Q_{max} then the BS becomes dominant.

To study these four TJMRs in more detail, and to do some statistics on the parameters describing these TJMRs, we decided to fit 9 different resonances from 5 different spectra of the four TJMRs (a total of 180 resonances). In Fig. 2.18 we report the results of the fits of the experimental measurements made on the four TJMRs as a function of Q_{max}. In particular, panel (a) reports $\gamma_{\text{tot}} - \Gamma$ with blue dots, (b) reports the extrinsic coefficient Γ with blue circles, and (c) and (d) instead report the absolute value of the two BS coefficients, $|\beta_{\text{tot},12}|$ and $|\beta_{\text{tot},21}|$, with red squares and magenta triangles, respectively. Panels (a) and (b) of Fig. 2.18 show

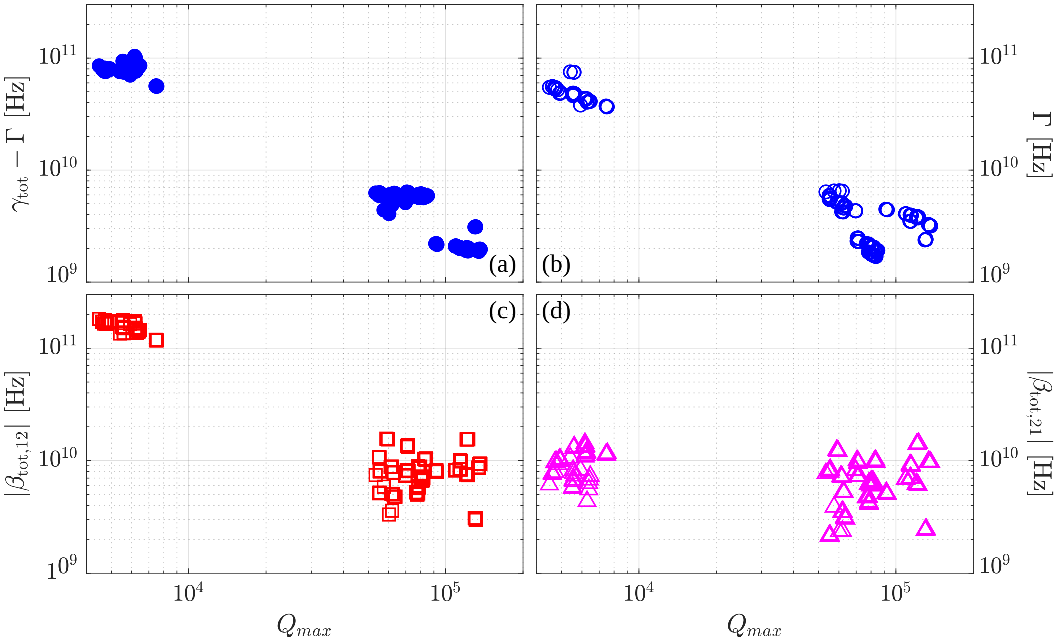

Figure 2.18: TJMR parameters obtained by fitting 5 measured spectra, each with 9 different resonances, for each of the 4 TJMRs (180 resonance dips/peaks). These parameters are plotted as a function of $Q_{\rm max}$, see Eq. (2.80). (a) reports the values of $\gamma_{\rm tot}-\Gamma$, (b) those of the extrinsic coefficient Γ, (c) and (d) those of the absolute values of the two BS coefficients, $|\beta_{\rm tot,12}|$ and $|\beta_{\rm tot,21}|$, respectively. [47]

that, as expected and by design, increasing $Q_{\rm max}$ decreases both $\gamma_{\rm tot}-\Gamma$ and Γ. From panels (a) and (b) of Fig. 2.18 it is observed that $|\beta_{\rm tot,12}| \gg |\beta_{\rm tot,21}|$ only for low values of $Q_{\rm max}$ ($Q_{\rm max} \lesssim 10^4$), while when $Q_{\rm max} \gtrsim 5\times10^4$ the two absolute values are comparable ($|\beta_{\rm tot,12}| \simeq |\beta_{\rm tot,21}|$) and so the device no longer behaves as an ideal TJMR. For $Q_{\rm max} \gtrsim 5\times10^4$, the two absolute values of the two BS coefficients always have a value between 2 GHz and 20 GHz. It is also worth noting that $|\beta_{\rm tot,21}|$ remains within this range for all resonances of all four TJMRs. Since the four TJMRs are characterized by different directional couplers (different gap widths), we can conclude that the observed BS does not depend on the gaps of the coupling regions, but only on the surface roughness of the walls of the WGs and the radii of curvature of the WGs. In conclusion, Fig. 2.18 shows that a MR similar to the studied TJMRs will have a BS between 2 GHz and 20 GHz. This is a relevant parameter when designing TJMRs or MRs. The Tab. 2.1 shows how the four TJMRs, which by design have different coupling gap widths, consequently have different coupling parameters. In particular, Tab. 2.1 show that as the gap width between the TJMR and the bus waveguide increases, the coupling rate Γ decreases as expected.

$\mathrm{gap}_{\mathrm{TB}}$ [nm]	$\mathrm{gap}_{\mathrm{TS}}$ [nm]	Γ [GHz]	$\gamma_{\mathrm{tot}} - \Gamma$ [GHz]	$\lvert\beta_{\mathrm{tot},12}\rvert$ [GHz]	$\lvert\beta_{\mathrm{tot},21}\rvert$ [GHz]	$Q_{\max}$ $\times 10^3$
241	210	48 ± 1	80 ± 2	155 ± 3	9.5 ± 0.4	5.8 ± 0.1
415	410	5.2 ± 0.1	5.77 ± 0.08	8.0 ± 0.5	6.4 ± 0.5	60.2 ± 0.7
433	440	3.60 ± 0.09	2.13 ± 0.05	8.7 ± 0.5	7.8 ± 0.5	119 ± 2
472	550	2.04 ± 0.04	5.94 ± 0.03	7.3 ± 0.5	6.2 ± 0.4	78.4 ± 0.7

Table 2.1: Table showing the design widths of the gaps and TCMT parameters obtained by fitting the measured experimental spectra. The values corresponding to four different TJMRs are shown. By design, the propagation losses are 2 dB/cm, the perimeter of the TJMRs is $L \simeq 196$ µm, the effective refractive index of the waveguide is $n_{\mathrm{eff}} \simeq 2.36$ and its group index is $n_g \simeq 4.29$.

2.4.2 Exceptional Point Behavior

As we demonstrated in Sec. 2.1, the TJMR is at an Exceptional Point (EP). In this subsection, we will see how a device operating at an EP behaves as a function of a perturbation of the BS coefficient. Finally, we will make a comparison between a MR working at a DP and the TJMR working at an EP.

We begin by describing the variation of the eigenvalues of the TJMR as a function of a perturbation of the BS coefficients. This perturbation can be thought as the value we want to obtain from an experimental measurement. To understand the trend, we rewrite here the eigenvalues of the system [Eq. 2.69]:

$$\lambda_{1/2} = \omega_0 \pm i\sqrt{(\beta_{12} + \beta_{BS,12})\ \beta_{BS,21}} - i\gamma_{\mathrm{tot}}\,, \tag{2.81}$$

where $\beta_{BS,12}$ e $\beta_{BS,21}$ can be seen as perturbations of the ideal TJMR. These perturbations can be caused by surface wall roughness, but also by any molecules/substances in the waveguide cladding. For simplicity, we assume a Hermitian perturbation, i.e. $\delta\beta := \beta_{BS,12} = -\beta^*_{BS,21}$. Consequently, the eigenvalues transform to:

$$\lambda_{1/2} = \omega_0 \pm i\sqrt{-(\beta_{12} + \delta\beta)\ \delta\beta^*} - i\gamma_{\mathrm{tot}}\,. \tag{2.82}$$

In both the formulas given in Eq. (2.81) and Eq. (2.82) it is evident that for small perturbations ($\delta\beta \ll \beta_{12}$) the eigenvalues have a square root behavior as a function of perturbation. This is different from what was observed for the MR (DP), in which case there was a linear dependence. In fact, this square-root behavior is characteristic of EPs, and we will see that it allows enhanced sensing compared to that of a DP system.

Before comparing the linear and square-root trends of the DPs and EPs, let us analyze in more detail the variation of the eigenvalues as a function of the Hermitian perturbation $\delta\beta$. Assuming that we are ideally able to directly measure both the real and imaginary parts of the eigenvalues, we analyze the sensing performance of the TJMR. In Fig. 2.19 (a) and (b) the real parts ($\Re[\lambda]$) and imaginary parts ($\Im[\lambda]$) of the two eigenvalues divided by $|\beta_{12}|$ are shown as a function of $\Re[\delta\beta/\beta_{12}]$ and $\Im[\delta\beta/\beta_{12}]$. All parameters are normalized by β_{12} to make general graphs. In Fig. 2.19, the red surfaces describe the values of the first eigenvalue (λ_1), while the blue ones report the values of the second eigenvalue (λ_2). These surfaces are called Riemann sheets [41, 3, 104, 4, 105, 106]. The panel (a) of Fig. 2.19 shows that the real parts of the two eigenvalues are equal when $\Im[\delta\beta/\beta_{12}] = 0$ and $-1 \leqslant \Re[\delta\beta/\beta_{12}] \leqslant 0$. Moreover, Fig. 2.19 (b) shows that the imaginary parts of the eigenvalues are equal when $\Im[\delta\beta/\beta_{12}] = 0$ and $\Re[\delta\beta/\beta_{12}] \leqslant -1 \vee \Re[\delta\beta/\beta_{12}] \geqslant 0$. In addition, panel (c) of Fig. 2.19 shows the inner product of the two eigenvectors ($| < \nu_1|\nu_2 > |$) which results equal to 1 only at $(0, 0)$ and at $(-1, 0)$. As a result, the TJMR is at an EP both when there is no perturbation, at $(0, 0)$, and when there is a perturbation $\delta\beta$ that can reach the point $(-1, 0)$. Note that these two EPs have two opposite chiralities, in $(0, 0)$ the α_{CCW} mode is dominant, while in $(-1, 0)$ it is α_{CW}. From Fig. 2.19 we can also see that only the Riemann surfaces of the two real parts of the two eigenvalues intersect [panel (a)], while those of the imaginary parts [panel (b)] do not. This is due to the fact that $\tilde{\beta} = \sqrt{|(\beta_{12} + \delta\beta)\,\delta\beta^*|}\,\sin\left[\arg\left[-(\beta_{12} + \delta\beta)\,\delta\beta^*\right]/2\right]$ changes sign when $\Im[\delta\beta/\beta_{12}]$ does, while $\tilde{\gamma} = \sqrt{|(\beta_{12} + \delta\beta)\,\delta\beta^*|}\,\cos\left[\arg\left[-(\beta_{12} + \delta\beta)\,\delta\beta^*\right]/2\right]$ is always positive. In addition, we can observe that by imposing $\Re[\delta\beta/\beta_{12}] = -1/2$ and varying only the imaginary part of the perturbation ($\Im[\delta\beta/\beta_{12}]$), we have a linear dependence of the real splitting as a function of this parameter (as in the case of a DP). On the other hand, if we fix $\Im[\delta\beta/\beta_{12}] = 0$ and $\Re[\delta\beta/\beta_{12}] \geqslant 0$, then we have the characteristic square root dependence of the real splitting of the eigenvalues, while the imaginary splitting is always zero.

As discussed in Sec. 2.1, $\beta_{12} = 4e^{i\varphi}\Gamma_S$, where φ is the phase acquired by the field as it passes through the S-shaped WG. Therefore, by varying the phase φ, for example by a microheater on the S-shaped WG, it is possible to vary the eigenvalues of the system along a circular-like path around the EP in $(0, 0)$. This encircling of the EP follows the Riemann sheets reported in panels (a) and (b) of Fig. 2.19. In this way, it is possible to change the sensitivity of TJMR to get maximum splitting of the real part of the eigenvalues and thus maximum splitting in the transmission spectrum. In fact, by aligning β_{12} with $\delta\beta$, we have that $\Im[\delta\beta/\beta_{12}] = 0$ and $\Re[\delta\beta/\beta_{12}] \geqslant 0$

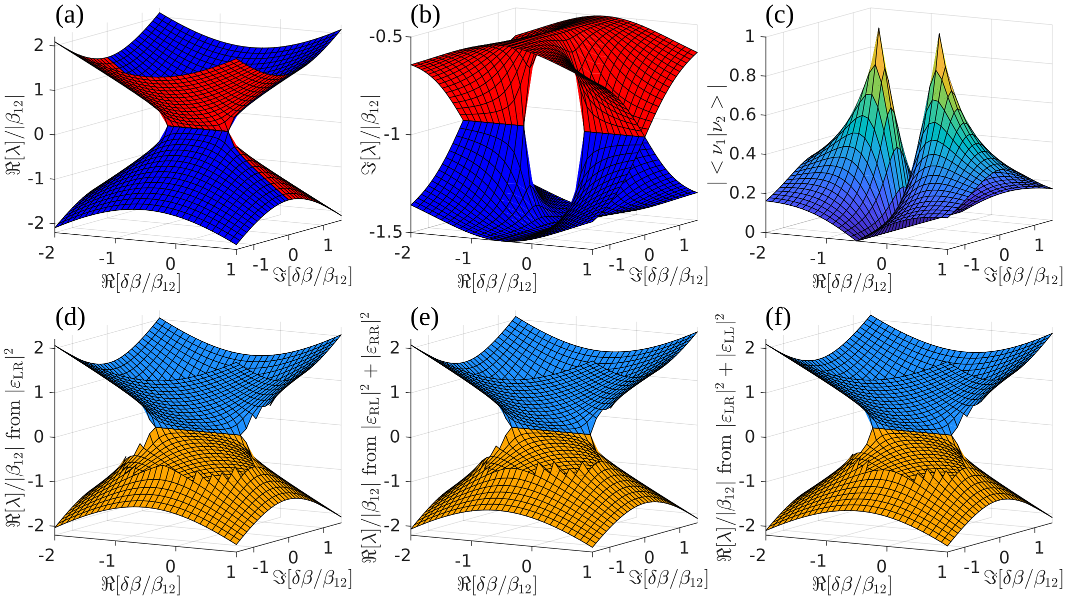

Figure 2.19: Normalized Riemann sheets for the TJMR as a function of the real $\Re[\delta\beta/\beta_{12}]$ and the imaginary $\Im[\delta\beta/\beta_{12}]$ part of the Hermitian BS perturbation ($\delta\beta$). All the quantities are normalized to β_{12} to make the graphs independent of this parameter. Panels (a) and (b) report the real $\Re[\lambda]$ and the imaginary $\Im[\lambda]$ parts of the eigenvalues. In $\Re[\lambda]$ the resonance angular frequency ω_0 is removed. The red Riemann surfaces correspond to the first eigenvalue λ_1, instead the blue ones to the second eigenvalue λ_2. Panel (c) shows the absolute value of the inner product between the two eigenvectors of the system as a function of $\Re[\delta\beta/\beta_{12}]$ and $\Im[\delta\beta/\beta_{12}]$. Panels (d), (e) and (f) show the dips position evaluated through the spectra of $|\varepsilon_{LR}|^2$, $|\varepsilon_{RL}|^2+|\varepsilon_{RR}|^2$ and $|\varepsilon_{LR}|^2+|\varepsilon_{LL}|^2$, respectively. In orange the position of the dip with lower angular frequency and in Dodger blue the position of the dip with higher angular frequency. The holes in panels (d), (e), and (f) are due to the inability to recognize two peaks. Here, we use $\gamma=\Gamma=\Gamma_S=1/4$ a.u. ($\beta_{12}=1$ a.u. and $\gamma_{tot}=1$ a.u.).

and consequently we get the maximum difference between the real parts of the two eigenvalues, $\Re[\lambda_2]-\Re[\lambda_1]$, which will follow a square root trend as a function of the perturbation. Note that by encircling the EP here we do not mean a dynamic encircling of the EP as in [41, 105]. In fact, since the TJMR is a resonant cavity, its memory (in the linear regime) lasts only for the lifetime of the cavity, which in our case is very short, of the order of 10 ps. This means that by exciting the system from a single side with a continuous and coherent source and slowly varying the phase, we are not able to perform dynamic encircling of the EP. However, through this feature one can think of a way to study the encircling of the EP by studying a MR like TJMR instead of using other devices as in [41, 105, 37, 40, 179, 180, 181, 182, 76, 183, 184, 185].

Experimentally, it is not possible to directly measure the eigenvalues of the system with a single-side excitation. To estimate the real part $\Re[\lambda]$ of the eigenvalues using the spectral response of the system (i.e. the actual observable of the system), it is common to calculate the spectral position of the two minima of the spectral doublet (two dips). Figure 2.19 (d) shows the Riemann surfaces computed from the transmission spectra of the TJMR characterized by the Hermitian BS perturbation ($\delta\beta$). The orange and Dodger blue colors correspond to the positions of the two different dips. Note that in panels (d), (e) and (f) of Fig. 2.19, in some regions it is not possible to identify two distinct spectral dips, causing a cancellation of the TJMR sensitivity (holes in the 3D plots). Thus, as also observed in the case of MR (Fig. 1.9), using the spectral response in single excitation does not give the eigenvalues of the system without a multiparametric fit, but only an estimate of them. Moreover, in some regions, especially for small perturbations $\delta\beta$, both TJMR and MR do not show any clear splitting, which cancels out the sensitivity. To slightly reduce the region of insensitivity of the TJMR, one can use the sum of the transmission intensities with the reflection intensities ($|\varepsilon_{RL}|^2+|\varepsilon_{RR}|^2$ and $|\varepsilon_{LR}|^2+|\varepsilon_{LL}|^2$). The sum of these spectra is easily obtained by using the spectra obtained with two different calibrated detectors placed in transmission and reflection. The Riemann surfaces corresponding to the two different sums are shown in panels (e) and (f) of Fig. 2.19. Since, by varying the phase φ, it is possible to maximize the splitting by rotating around the EP that lies in $(0,0)$, we can fix $\Im[\delta\beta/\beta_{12}] = 0$ and see in more detail the splitting trends as a function of $\Re[\delta\beta/\beta_{12}]$. These trends are shown in Fig. 2.20.

First, we observe the square root dependence of the eigenvalues splitting as a function of the perturbation ($\Re[\Delta\lambda]/|\beta_{12}|$ vs $\Re[\delta\beta/\beta_{12}]$), magenta line in Fig. 2.20. In the range between -1 and 0 the eigenvalues change only their imaginary part, and therefore $\Re[\Delta\lambda]$ is zero. However, since we can rotate around the EP varying the phase φ, the region of interest is where $\Re[\delta\beta/\beta_{12}] \geqslant 0$. The gray line in Fig. 2.20 shows the splitting calculated from the transmission spectrum ($|\varepsilon_{LR}|^2$). Note that the splitting is zero when $-1.288 \lesssim \Re[\delta\beta/\beta_{12}] \lesssim 0.288$, after which the splitting increases as a square root that tends to the splitting of the eigenvalues (magenta line). The region of insensitivity (i.e. zero values in the splitting) is related to the width of the two dips due to the total losses of the system. To reduce this region, the transmission spectral response can be summed with the reflection spectral response; in this way, the regions where the system has higher losses are emphasized by dips in the spectrum, which will be closely related to the eigenvalues of the system. The dash-dotted orange line corresponds to $|\varepsilon_{RL}|^2 + |\varepsilon_{RR}|^2$, while the dashed black line corresponds to $|\varepsilon_{LR}|^2 + |\varepsilon_{LL}|^2$. By using $|\varepsilon_{RL}|^2 + |\varepsilon_{RR}|^2$ one can reduce the region of insensitivity, in fact now the splitting for $\Re[\delta\beta/\beta_{12}] \gtrsim$

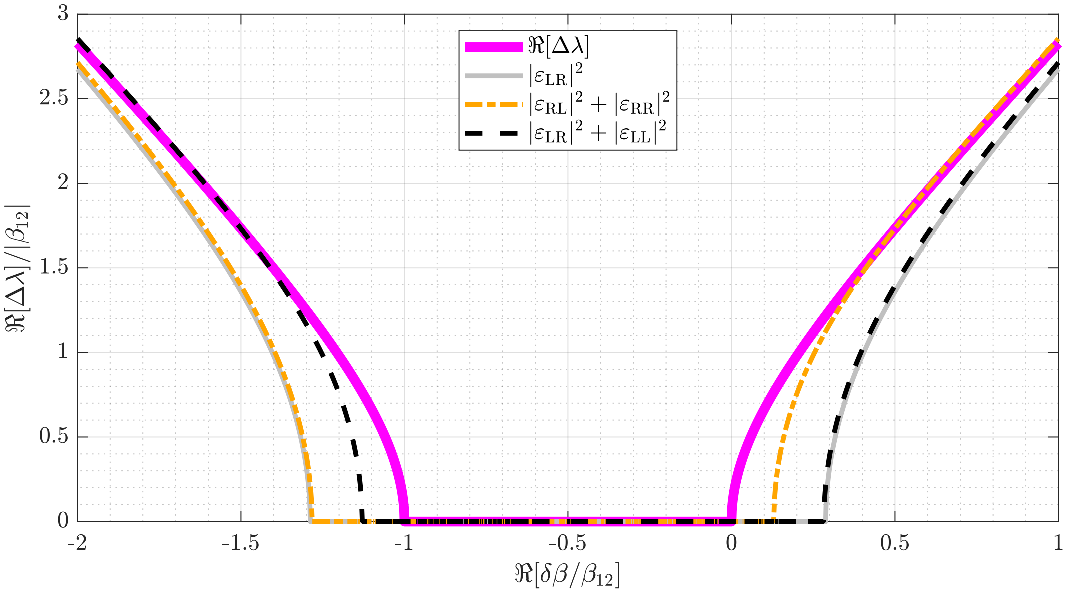

Figure 2.20: Eigenvalues splitting of a TJMR as a function of the $\Re[\delta\beta/\beta_{12}]$. The magenta, gray, orange and black lines represent the splitting of the eigenvalues, of the doublets observed in the transmission spectra, the one observed in the $|\varepsilon_{\rm RL}|^2+|\varepsilon_{\rm RR}|^2$ spectra and the one observed in the $|\varepsilon_{\rm LR}|^2+|\varepsilon_{\rm LL}|^2$, respectively. Here, we use $\gamma=\Gamma=\Gamma_S=1/4$ a.u. ($\beta_{12}=1$ a.u. and $\gamma_{\rm tot}=1$ a.u.).

0.129 is greater than zero. Note that when $\Im[\delta\beta/\beta_{12}]=0$ and $\Re[\delta\beta/\beta_{12}]=-1$ it is like having the TJMR with the S-shaped WG turned in the other direction. Therefore for values of $\Re[\delta\beta/\beta_{12}]\lesssim -1$ the splitting corresponding to $|\varepsilon_{\rm LR}|^2+|\varepsilon_{\rm LL}|^2$ is more efficient. In conclusion, it is not possible to reconstruct the perfect square root behavior of the eigenvalue splitting from the spectral responses without performing multiparameter fits. However, by using the spectrum of $|\varepsilon_{\rm RL}|^2+|\varepsilon_{\rm RR}|^2$, it is possible to minimize the region of insensitivity of the TJMR and to obtain, at smaller perturbations, a good match between the two splittings (dash-dotted orange and magenta lines in Fig. 2.20).

2.5 Interferometric Excitation

In this section, we analyze both theoretically and experimentally how an ideal/semi-ideal TJMR responds to symmetric interferometric excitation. The formulas used are the same as in Eq. 2.74, Eq. 2.75 and $\theta := \phi - \left(\frac{\arg[\beta_{\rm tot,21}/\beta_{\rm tot,12}]}{2}+\frac{\pi}{2}\right)$ from Eq. (1.108).

Figure 2.21 shows the spectra of the output intensities for a TJMR for single-side excitation, panels (a1) and (a2), and interferometric excitation, panels (b1)-(b2) and (c1)-(c4). In Fig. 2.21, the blue and red lines identify the spectral response of the TJMR at the right and left output, respectively. Panel (a1) corresponds to the excitation from left, while (a2) corresponds to the excitation from right. Panels (a1) and (a2) highlight the unidirectional reflector behavior of the TJMR.

Looking at the spectral responses corresponding to the interferometric excitation [panels (b1)-(b2) and (c1)-(c4)], it is clear that $|\varepsilon_{\mathrm{out,L}}|^2$ is independent of the angle θ and, thus, of the phase relationship between the input fields. Instead, $|\varepsilon_{\mathrm{out,R}}|^2$ varies as a function of θ. This is due to the fact that the TJMR working at an EP has different from zero only one of the two couplings between its counterpropagating modes ($\beta_{12} \neq 0$ and $\beta_{21} = 0$). Therefore, in the left output, no interference is established since there is no reflection of the system. Thus, the spectral response is characterized by a Loerentzian dip centered at the resonant angular frequency ($\Delta\omega = 0$). In fact, panels (c1)-(c4) report in red the spectral response of $|\varepsilon_{\mathrm{out,L}}|^2$ for different values of θ. This is identical to the transmission in the single-side excitation [red curve in panel (a2)]. The non-zero reflection in the right port instead causes that $|\varepsilon_{\mathrm{out,R}}|^2$ is characterized by interference between reflection and transmission and thus its spectrum changes as a function of angle θ, see Fig. 2.21 (b1) and blue lines in panels (c1)-(c4).

Note that here we used a symmetric interferometric excitation ($|\varepsilon_{\mathrm{in,R}}|^2 = |\varepsilon_{\mathrm{in,L}}|^2$) even though the system is non-Hermitian ($\beta_{12} \neq 0$ and $\beta_{21} = 0$). Actually, to derive the eigenvalues of the system, as we saw in Sec. 1.3 [Eq. 1.106], we would need an asymmetric interferometric excitation, which in this case would correspond to a single-side excitation from left. In fact, the TJMR has a single eigenvalue, and already from the single-side excitation transmission we can derive $\Re\left[\lambda_{1/2}\right]$, which is equal to ω_0 (the position of the dip center), and $\Im\left[\lambda_{1/2}\right] = -\gamma_{\mathrm{tot}}$, which corresponds to minus half the FWHM of the Lorentzian dip.

To demonstrate the validity of the formulas for the interferometric excitation also for TJMR, we experimentally measured the spectral responses of a TJMR with this type of excitation, see Fig. 2.22. Here, we used the TJMR with lower Q among those described in Sec. 2.4.1. We analyzed the resonance with $\omega_0 \simeq 2\pi \cdot 194.430$ THz. We used the experimental setup described in Sec. 1.5.1 and followed a similar procedure to the one described in Sec. 1.5.3 to measure the spectral responses of the MR.

First, we measured the spectra in the single-side excitation, see panels (a1) and (a2) of Fig. 2.22. Here, it can be seen that the TJMR behaves as a unidirectional reflector as in Fig. 2.21. By fitting these four spectra simultaneously, we obtained the

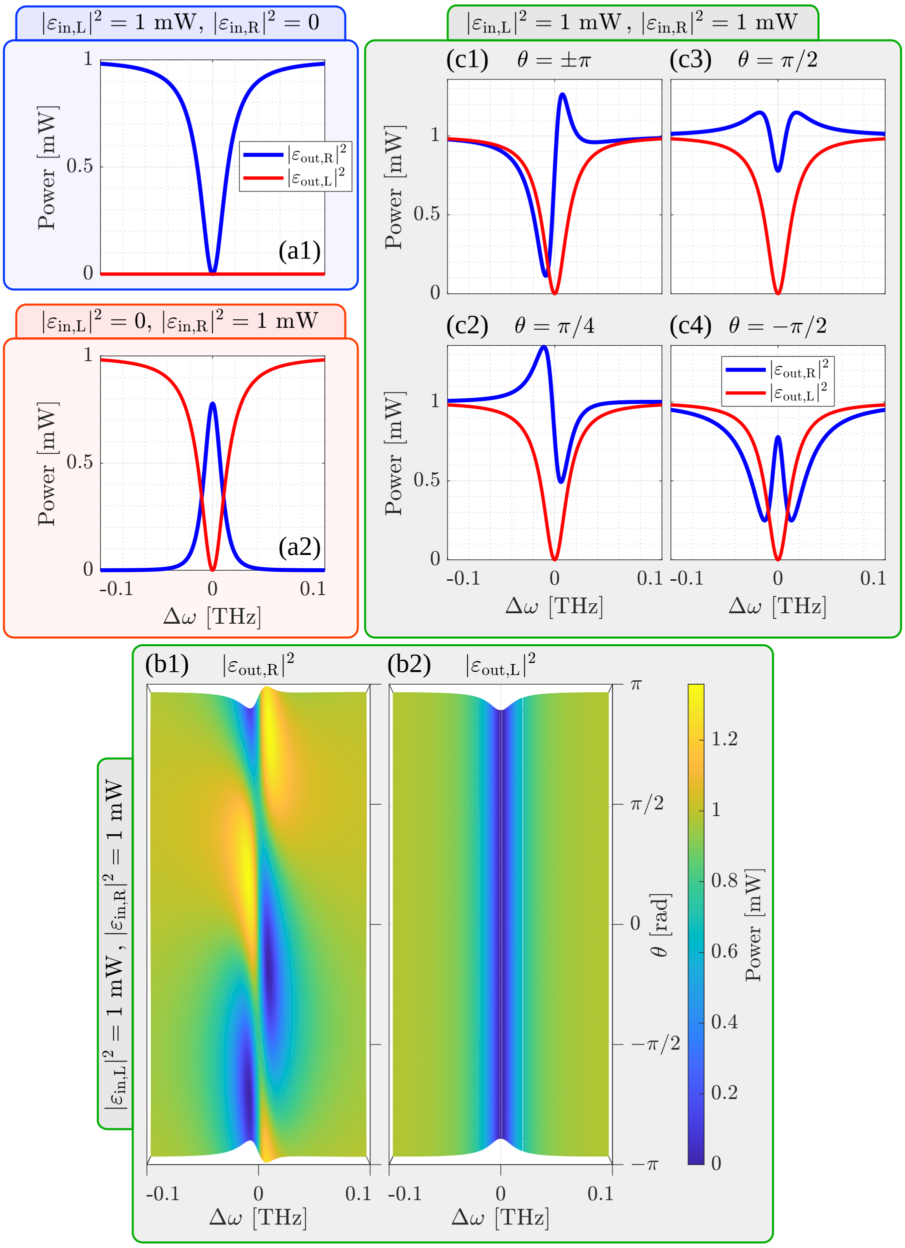

Figure 2.21: Spectral responses for a TJMR. Panels (a1) and (a2) report the transmission and reflection spectra for an excitation from the left and right input sides, respectively. Maps (b1) and (b2) show, respectively, the right and left output field intensities as a function of θ and $\Delta\omega$ for a symmetric interferometric excitation ($|\varepsilon_{\mathrm{in,L}}|^2 = |\varepsilon_{\mathrm{in,R}}|^2$). (c1)-(c4) show the output field intensity spectrum for fixed values of $\theta = \{\pm\pi, \pi/4, \pi/2, -\pi/2\}$. The blue and red curves correspond to the right and the left output field intensities, respectively. The used coefficients are: $\Gamma = \gamma + 2\Gamma_S = \gamma_{\mathrm{tot}} - \Gamma = 6.8$ GHz, $\beta_{12} = 12$ GHz, $\beta_{21} = 0$ and $\omega_0 = 2\pi \cdot 193$ THz. [102]

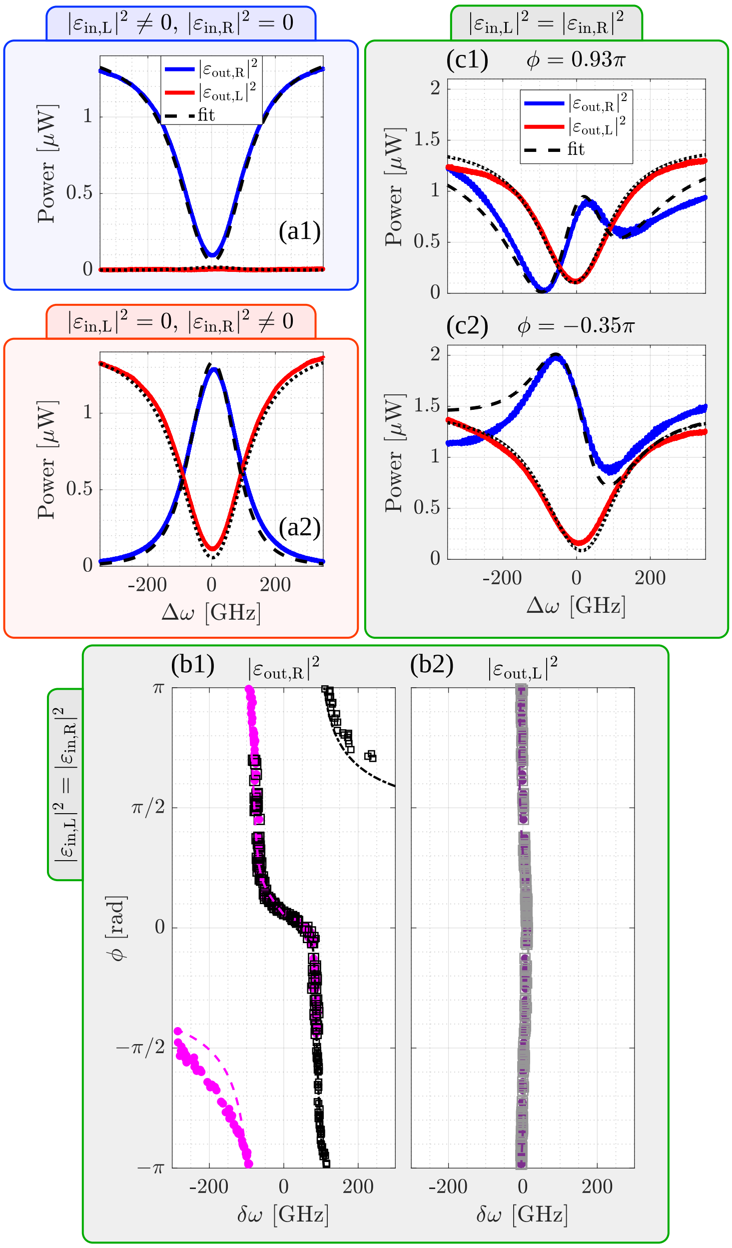

Figure 2.22: Experimental results for a TJMR. Here are reported response spectra of a TJMR for both single-side excitation and a symmetric interferometric excitation. The blue and red curves represent the measured output field intensity at the right and left sides, respectively. The black curves report the fit of the experimental data. Panels (a1) and (a2) report the transmission and reflection spectra for an excitation from the left and right input sides, respectively. Panels (b1) and (b2) show the dips position as a function of the phase ϕ between the two input fields for the right and left output intensities, respectively. $\delta\omega = \omega_< - \omega_0$ and $\delta\omega = \omega_> - \omega_0$ are the angular frequency detuning for the dip with lower angular frequency ($\omega_<$) and the one with higher angular frequency ($\omega_>$). The experimental data are reported in magenta (purple) dots for $\delta\omega = \omega_< - \omega_0$ and in black (gray) squares for $\delta\omega = \omega_> - \omega_0$. The theoretical curves are dashed magenta (purple) and dash-dotted black (gray) for $\omega_<$ and $\omega_>$, respectively. Panels (c1) and (c2) show two examples of spectral responses for an interferometric excitation with a phase $\phi = 0.93\pi$ and -0.35π, respectively. From the fit we obtain the following coefficients: $\Gamma = (75.1 \pm 0.1)$ GHz, $\gamma_{\mathrm{tot}} - \Gamma = \gamma + \Gamma_S = (42.6 \pm 0.1)$ GHz, $\beta_{\mathrm{tot},12} = [(-90.8 \pm 0.1) - i(24.17 \pm 0.03)]$ GHz, $\beta_{\mathrm{tot},21} = [(8.7 \pm 0.1) - i(7.30 \pm 0.09)]$ GHz. [102]

following parameters: $\omega_0 \simeq 2\pi \cdot 194.430$ THz, $\gamma_{\text{tot}} - \Gamma = \gamma + 2\Gamma_S = (42.6 \pm 0.1)$ GHz, $\Gamma = (75.1 \pm 0.1)$ GHz, $\beta_{\text{tot},12} = [(-90.8 \pm 0.1) - i(24.17 \pm 0.03)]$ GHz and $\beta_{\text{tot},21} = [(8.7 \pm 0.1) - i(7.30 \pm 0.09)]$ GHz. Note that the experimental data shown in blue and red are well described by the obtained fits (black lines). At this point, using a symmetric interferometric excitation ($|\varepsilon_{\text{in},R}|^2 = |\varepsilon_{\text{in},L}|^2$), we measured the spectra as the relative phase between the two input fields, ϕ, changed. Two examples of spectral responses related to interferometric excitation, when ϕ is about 0.93π and -0.35π, are given in panels (c1) and (c2), respectively. Again, although with less precision, the theoretical fits accurately describe the experimental data. It is also important to note that even experimentally it is observed that the spectrum of $|\varepsilon_{\text{out},L}|^2$ remains almost constant as a function of phase ϕ, while that of $|\varepsilon_{\text{out},R}|^2$ varies considerably. To emphasize this fact, in (b1) and (b2) the positions of the minor detuning dips (magenta and purple dots) and the major detuning dips (black and gray squares) are shown as a function of the phase ϕ obtained from the spectra of $|\varepsilon_{\text{out},R}|^2$ and $|\varepsilon_{\text{out},L}|^2$, respectively. The dashed curves represent the theoretical trend derived using the parameters fitted from the single-side excitation spectra. Fig. 2.22 (b2) shows that there is only a dip in the spectral response on the left, which shifts only imperceptibly from ω_0 as ϕ changes. The small oscillation is given by the non-ideality of the TJMR. In fact, because of the BS, the coefficient $\beta_{\text{tot},21}$, although $|\beta_{\text{tot},21}| \ll |\beta_{\text{tot},12}|$, is different from zero ($\beta_{\text{tot},21} = [(8.7 \pm 0.1) - i(7.30 \pm 0.09)]$ GHz). In Fig. 2.22 (b1) it is observed that the position of the dips varies as a function of ϕ, as also found in Fig. 2.21. Note the agreement with the theoretical predictions.

Chapter 3

Infinity-Loop Microresonator

In the literature, there are many applications for systems operating at an EP, but still, there are few integrated structures that have this particular coalescence of their eigenvalues and eigenvectors [3, 4, 5, 36, 44]. In Ch. 2 we presented the TJMR, which is an example of an integrated structure that is at an EP.

In this chapter, we will present a new structure that we call Infinity-Loop Microresonator (ILMR) [93]. The ILMR consists of an infinity-shaped WG coupled twice with a bus waveguide. In Sec. 3.1 we will model this structure with the TCMT and show that the ILMR works at an EP. We will show that the ILMR always remains at an EP even if the two couplings with the bus waveguide are changed symmetrically or asymmetrically. In addition, we will give examples of spectral responses in which we will show how this device can have completely different responses simply by changing the couplings with the bus waveguide It could become either a unidirectional reflector or it can have identical reflections. In Sec. 3.2, we will add the BS to the model of the ILMR described by the TCMT. In this section, the Riemann sheets are also shown and the ILMR is analyzed for its sensing characteristics. In Sec. 3.4, the ILMR is modeled by the TMM, and two other ways to construct a structure with the same properties as the ILMR are reported. Finally, Sec. 3.5 reports experimental results on four different ILMRs that we have designed and measured. Specifically, the spectral responses of four ILMRs will be reported, one of which has a symmetric structure, while the other three have two asymmetric bus waveguide couplings.

This chapter is based on the work reported in [93].

3.1 Design and Temporal Coupled Mode Theory model

The ILMR is a microresonator formed by an infinity-shaped WG coupled to the bus waveguide in each of its two lobes, see Fig. 3.1. To create the infinity-shaped WG, we need a crossing that connects the two lobes of the infinity WG. We will consider the crossing ideal, i.e. the optical mode can only pass through it in a straight line and no excitation of the modes in the crossed WG is possible (zero insertion loss and zero crosstalk). We assume that all WGs are single mode.

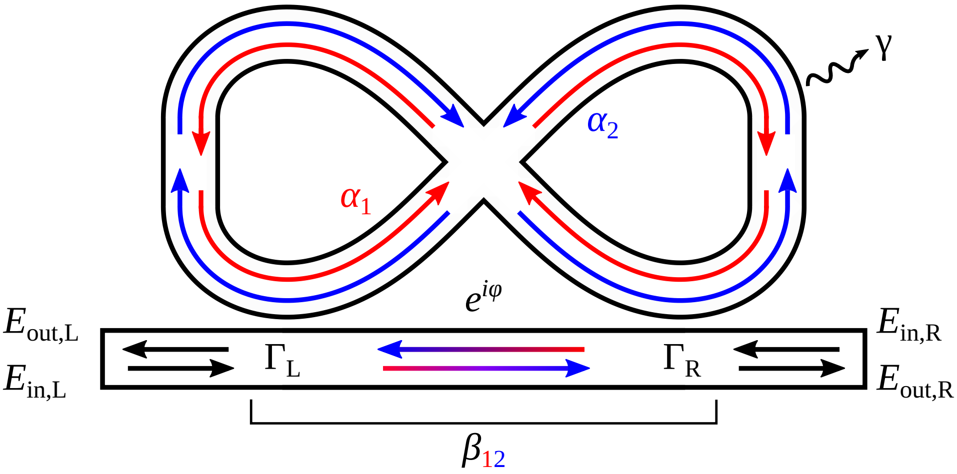

Figure 3.1: Sketch of the Infinity-Loop Microresonator (ILMR). γ and Γ are the intrinsic and the extrinsic damping rate. The index R, L refer to left and right. E_{in} and E_{out} are the input and the output fields, respectively. All the parameters are described in the text. [93]

As can be seen from the sketch in Fig. 3.1, the characteristic parameters of the system, in addition to the angular frequency of resonance (ω_0), are the intrinsic loss rate γ, the two coupling rates Γ_L and Γ_R (for the left and the right coupling with the bus waveguide), the phase φ acquired by the field propagating in the bus waveguide between the two coupling regions of the two lobes, and the total loss rate ($\gamma_{tot} = \gamma + \Gamma_L + \Gamma_R$).

Like the MR or TJMR, the ILMR supports two counterpropagating modes, α_1 and α_2, see Fig. 3.1. The first mode, α_1, rotates in the CCW direction in the left lobe and in the CW direction in the right lobe. In addition, α_1, when near one of the two coupling regions with the bus waveguide, is always directed toward the center of the ILMR, i.e., toward the crossing (Fig. 3.1). The second mode, α_2, is counterpropagating to α_1, and thus near the couplings with the bus waveguide is always directed to the borders of the structure, see Fig. 3.1. Consequently, the two modes interact differently with the bus waveguide. In fact, we notice that no matter which direction the system is excited from (left or right excitation), the first excited mode is always α_1, while the second is α_2. More importantly, the α_1 mode is the only one that can exchange energy with α_2 through the bus waveguide. In fact, when α_1 couples to the bus waveguide, it propagates toward the other coupling region and excites α_2. This does not happen for α_2. In fact, when it couples to the bus waveguide it always propagates directly to one of the two outputs of the bus waveguide and, consequently, does not transfer energy to α_1. These considerations can be simplified by saying that the coupling coefficient from α_1 to α_2 is non-zero ($\beta_{12} \neq 0$), while that from α_2 to α_1 is zero ($\beta_{21} = 0$). Thus, by these simple considerations, we can already say that the ILMR is at an EP.

To more rigorously demonstrate that the ILMR is at an EP, we model the system using the TCMT and calculate the eigenvalues and eigenvectors of the ILMR. Here we will describe an ideal ILMR, i.e. neglecting the presence of BS due to waveguide surface-wall roughness, which would cause coupling between the two modes of the ILMR. Furthermore, we will study the system in the linear regime, i.e. at low input optical intensities ($|E_{in}|^2 \ll 1$ mW), and in order to use the TCMT we will assume $\gamma_{tot} \ll \omega_0$. The TCMT equations that govern the ILMR are:

$$\begin{aligned} i\frac{d}{dt}\begin{pmatrix}\alpha_2\\ \alpha_1\end{pmatrix} &= \begin{pmatrix}\omega_0 - i\gamma_{tot} & -i\beta_{12}\\ 0 & \omega_0 - i\gamma_{tot}\end{pmatrix}\begin{pmatrix}\alpha_2\\ \alpha_1\end{pmatrix} \\ &- \begin{pmatrix}\sqrt{2\Gamma_R}e^{i\varphi} & \sqrt{2\Gamma_L}e^{i\varphi}\\ \sqrt{2\Gamma_L} & \sqrt{2\Gamma_R}\end{pmatrix}\begin{pmatrix}E_{in,L}\\ E_{in,R}\end{pmatrix}, \end{aligned} \tag{3.1}$$

where the coupling coefficient from α_1 to α_2 can be written as a function of the coupling rates with the bus waveguide, $\beta_{12} = 4e^{i\varphi}\sqrt{\Gamma_L\Gamma_R}$. In addition, $E_{in,L}$ and $E_{in,R}$ are the left and right input electric fields, respectively. The subscripts L and R are used to refer to the left and right sides in Fig. 3.1. The Hamiltonian of the ILMR is thus:

$$H_{ILMR} = \begin{pmatrix}\omega_0 - i\gamma_{tot} & -i\beta_{12}\\ 0 & \omega_0 - i\gamma_{tot}\end{pmatrix}. \tag{3.2}$$

This Hamiltonian is non-Hermitian ($H_{ILMR} \neq H^{\dagger}_{ILMR}$) and is equivalent to that of the TJMR at an EP (ideal TJMR), see Eq. (2.3). Therefore the eigenvalues and eigenvectors of the ILMR are:

$$\lambda_1 = \lambda_2 = \omega_0 - i\gamma_{tot}\,, \qquad \nu_1 = \nu_2 = \begin{pmatrix} 1 \\ 0 \end{pmatrix}. \tag{3.3}$$

Note that both eigenvalues and eigenvectors coalesce, so we have demonstrated that the ILMR is at an EP. Note also that this is true for any value of the couplings Γ_L and Γ_R, it suffices that both are different from zero [EP $\iff$ ($\Gamma_L \neq 0$ & $\Gamma_R \neq 0$)]. It is worth noting that both α_1 and α_2 modes are excited by both input fields ($E_{in,L}$ and $E_{in,R}$), see Eq. (3.1).

To obtain the spectral responses of the ILMR, it is necessary to relate the output electric fields ($E_{out,R}$,$E_{out,L}$) to the input electric fields ($E_{in,L}$,$E_{in,R}$) and to the internal modes of the ILMR (α_2,α_1). These relations are:

$$\begin{pmatrix} E_{out,R} \\ E_{out,L} \end{pmatrix} = e^{i\varphi} \begin{pmatrix} E_{in,L} \\ E_{in,R} \end{pmatrix} + i \begin{pmatrix} \sqrt{2\Gamma_R} & \sqrt{2\Gamma_L} e^{i\varphi} \\ \sqrt{2\Gamma_L} & \sqrt{2\Gamma_R} e^{i\varphi} \end{pmatrix} \begin{pmatrix} \alpha_2 \\ \alpha_1 \end{pmatrix}. \tag{3.4}$$

Note that in the ILMR system, unlike the case of the MR and that of the TJMR, both $E_{out,R}$ and $E_{out,L}$ depend on both α_1 and α_2 modes, see Eq. (1.31), Eq. (2.2) and Eq. (3.4) for comparison. Solving Eq. (3.1) and Eq. (3.4) in the steady state and assuming

$$E_{in,L} := \varepsilon_{in,L}\, e^{-i\omega t}\,, \qquad E_{in,R} := \varepsilon_{in,R}\, e^{i\phi}\, e^{-i\omega t}\,, \tag{3.5}$$

$$\alpha_2 := a_2\, e^{-i\omega t}\,, \qquad \alpha_1 := a_1\, e^{-i\omega t}\,, \tag{3.6}$$

$$E_{out,R} := \varepsilon_{out,R}\, e^{-i\omega t}\,, \qquad E_{out,L} := \varepsilon_{out,L}\, e^{-i\omega t}\,, \tag{3.7}$$

we obtain:

$$\begin{aligned} \varepsilon_{out,R} = & e^{i\varphi} \left(1 - \frac{2\,(\Gamma_L + \Gamma_R)}{-i\Delta\omega + \gamma_{tot}} + \frac{8\Gamma_L\Gamma_R}{(-i\Delta\omega + \gamma_{tot})^2} \right) \varepsilon_{in,L} \\ & - \frac{4e^{i\varphi}\sqrt{\Gamma_L\Gamma_R}}{-i\Delta\omega + \gamma_{tot}} \left(1 - \frac{2\Gamma_R}{-i\Delta\omega + \gamma_{tot}} \right) e^{i\phi}\,\varepsilon_{in,R}\,, \end{aligned} \tag{3.8}$$

$$\begin{aligned} \varepsilon_{out,L} = & e^{i\varphi} \left(1 - \frac{2\,(\Gamma_L + \Gamma_R)}{-i\Delta\omega + \gamma_{tot}} + \frac{8\Gamma_L\Gamma_R}{(-i\Delta\omega + \gamma_{tot})^2} \right) e^{i\phi}\,\varepsilon_{in,R} \\ & - \frac{4e^{i\varphi}\sqrt{\Gamma_L\Gamma_R}}{-i\Delta\omega + \gamma_{tot}} \left(1 - \frac{2\Gamma_L}{-i\Delta\omega + \gamma_{tot}} \right) \varepsilon_{in,L}\,, \end{aligned} \tag{3.9}$$

$$
\begin{aligned}
a_2 = & \frac{i\sqrt{2\Gamma_R}e^{i\varphi}}{-i\Delta\omega + \gamma_{\text{tot}}}\left(1 - \frac{4\Gamma_L}{-i\Delta\omega + \gamma_{\text{tot}}}\right)\varepsilon_{\text{in,L}} \\
& + \frac{i\sqrt{2\Gamma_L}e^{i\varphi}}{-i\Delta\omega + \gamma_{\text{tot}}}\left(1 - \frac{4\Gamma_R}{-i\Delta\omega + \gamma_{\text{tot}}}\right)e^{i\phi}\,\varepsilon_{\text{in,R}}\,, \qquad (3.10)\\
a_1 = & \frac{i\sqrt{2\Gamma_L}}{-i\Delta\omega + \gamma_{\text{tot}}}\varepsilon_{\text{in,L}} + \frac{i\sqrt{2\Gamma_R}}{-i\Delta\omega + \gamma_{\text{tot}}}e^{i\phi}\,\varepsilon_{\text{in,R}}\,. \qquad (3.11)
\end{aligned}
$$

Note that here, in addition to the terms also present in the case of TJMR [Eq. (2.8), (2.9), (2.10), and (2.11)], we have additional terms. We will see that these completely change the transmission and reflection spectra. Equation (3.8), Eq. (3.9), Eq. (3.10) and Eq. (3.11) can be used either for an interferometric excitation [102], where the system is excited by both input ports of the bus waveguide with two coherent fields with relative phase ϕ, or for a single-side excitation. In fact, in the case of single-side excitation, it is sufficient to set one of the two amplitudes of the input fields equal to zero. It is worth noting that if the ILMR is ideal (no BS), then the spectral shape of the intensity of the output fields will be independent of the value of the phase φ that the field acquires as it propagates in the bus waveguide between the two coupling regions. In fact, in Eq. (3.8) and Eq. (3.9) the term $e^{i\varphi}$ can be collected. This means that one can vary the phase of the parameter $\beta_{12} = 4e^{i\varphi}\sqrt{\Gamma_L\Gamma_R}$ without changing the spectral response of the ideal ILMR.

Let us now look at some examples of spectral responses of the ILMR for single-side excitation. In Fig. 3.2 the spectral responses corresponding to four ILMRs are given. In particular, in (a) the ILMR is symmetric $\Gamma_L = \Gamma_R$, while in (b), (c) and (d) the ILMRs are asymmetric $\Gamma_L \neq \Gamma_R$. The parameters used to generate Fig. 3.2 are given in Tab. 3.1. These parameters were obtained through simulations of the couplings during the design of the ILMRs. More details about the design parameters can be found in Sec. 3.5 and especially in Tab. 3.2. As in Ch. 2, we identify the field at the o output when the device is excited from the i input as $\varepsilon_{i\,o}$, where $i = L, R$ and $o = L, R$ (L stands for Left and R stands for Right).

Figure 3.2 (a) reports counterintuitive spectral responses for a structure without BS that is at an EP. In fact, unlike what we observed for the TJMR, here the reflections are equal and all four spectra show a doublet (two dips/peaks), even though the eigenvalues and eigenvectors of the system coalesce. This splitting is not induced by the presence of the BS, but by the interference established in the bus waveguide between the field continuing in the bus waveguide and that coming from the two modes α_1 and α_2. Since the structure is symmetric, it is observed that both transmissions and reflections of the ILMR are equal, see Figure 3.2 (a). By changing the

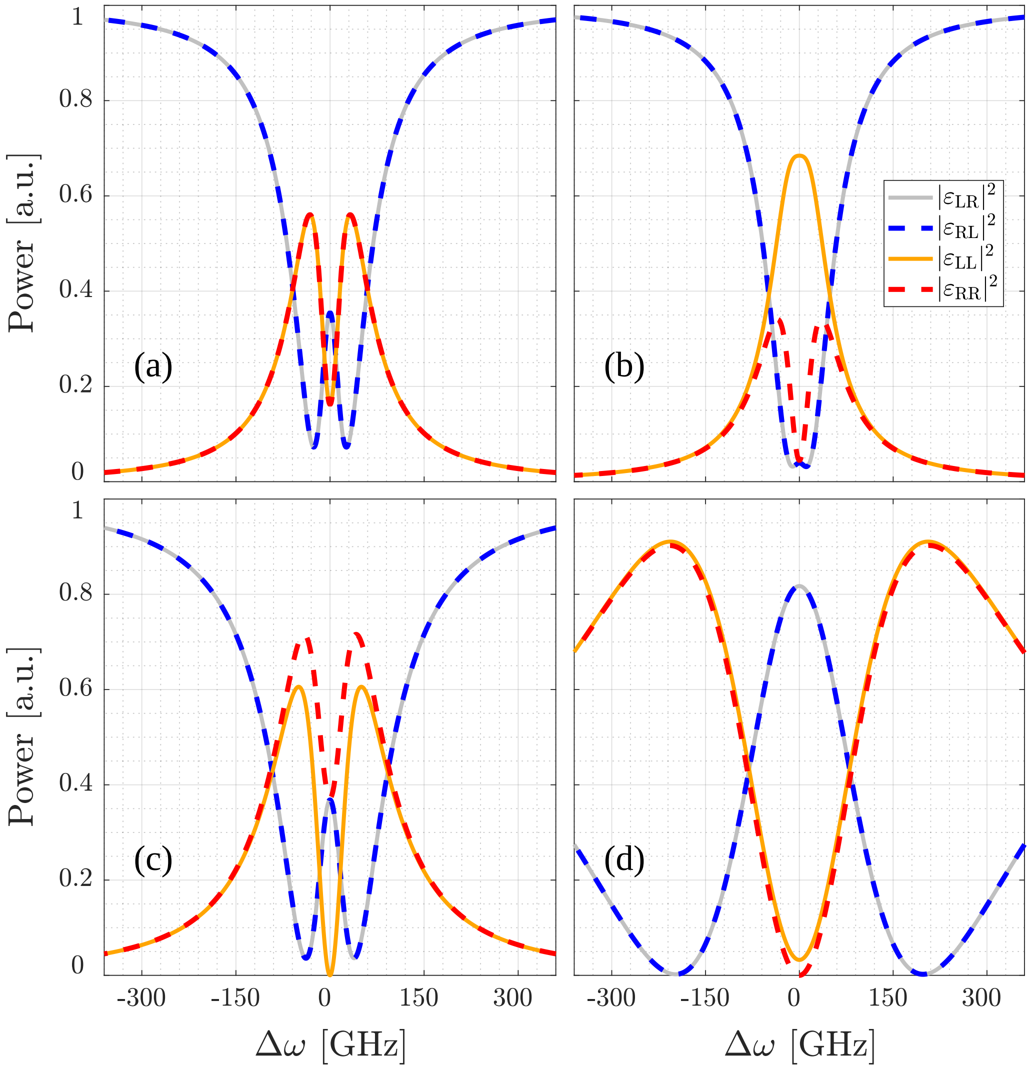

Figure 3.2: Spectral responses of the four different ILMRs whose parameters are given in Tab. 3.1. In (a) the ILMR is symmetric ($\Gamma_\mathrm{L} = \Gamma_\mathrm{R}$), while in (b), (c) and (d) the ILMR is asymmetric ($\Gamma_\mathrm{L} \neq \Gamma_\mathrm{R}$). Solid lines show transmission spectra in gray and reflection spectra in orange when the system is excited from left. The dashed lines show transmission spectra in blue and reflection spectra in red when the system is excited from right. [93]

	Γ_L [GHz]	Γ_R [GHz]	γ_{tot} [GHz]
Fig. 3.2 (a) & Fig. 3.3 (a)	12.6	12.6	35
Fig. 3.2 (b) & Fig. 3.3 (b)	5.1	21.6	36.5
Fig. 3.2 (c) & Fig. 3.3 (c)	25	15.2	50
Fig. 3.2 (d) & Fig. 3.3 (d)	94.1	104	207.9

Table 3.1: Parameters used in Fig. 3.2 and in Fig. 3.3. [93]

couplings Γ_L and Γ_R a zoo of spectral shapes can be obtained. For example, in Figure 3.2 (b) we observe that the transmissions and also the reflection on the left have a quasi-single dip/peak, instead, the reflection on the right has two peaks. We also notice that the transmission spectra reach almost zero at resonance ($\Delta\omega = 0$). Here the reflections at resonance are very different, their ratio is about $|\varepsilon_{LL}|^2/|\varepsilon_{RR}|^2 \simeq 15$ and therefore the ILMR can also be used as a unidirectional reflector. By asymmetrically changing the parameters Γ_L and Γ_R it is also possible to get the reflection $|\varepsilon_{LL}|^2$ equal to zero at resonance, see panel (c) of Fig. 3.2. This condition is easily obtained from Eq. (3.9) by imposing $|\varepsilon_{in,R}|^2 = 0$ and $|\varepsilon_{out,L}|^2 = 0$ at $\Delta\omega = 0$. The condition to get $|\varepsilon_{LL}|^2 = 0$ at resonance is then: $2\Gamma_L = \gamma_{tot}$ and then $\Gamma_L = \Gamma_R + \gamma$. In Fig. 3.2 (c), in addition to $|\varepsilon_{LL}|^2 = 0$ at resonance, it is observed that all four spectra show splitting. As reported in Fig. 3.2 (d), by increasing Γ_L and Γ_R it is also possible to obtain a peak in transmission and a dip in reflection, both centered at $\Delta\omega = 0$. Here, because of this behavior, it almost seems as if the reflection spectra have been swapped with the transmission spectra. Again, all these different spectra are obtained by staying at an EP.

In order to observe what happens to the fields inside the ILMR in these four cases, we have reported in Fig. 3.3 the spectra of the square of the absolute values of the two modes a_1 and a_2 multiplied by $\tilde{f} := c/(n_g L)$, where in this case L is the length of the infinity-shaped WG. Here we have multiplied $|a_1|^2$ and $|a_2|^2$ by $\tilde{f}$ to get the Enhancement Factor (EF) multiplied by the input optical power $|\varepsilon_{in}|^2 = 1$ a.u.. In the following, we refer to the ILMR mode number j exited from i as $a_{i,j}$, where $i = L, R$ and $j = 1, 2$ (L stands for left and R for right). Figure 3.3 shows that the spectrum of $|a_{i,1}|^2$ always has a single Lorentzian peak centered at $\Delta\omega = 0$. This can be easily verified by Eq. (3.11) and is due to the fact that the α_2 mode cannot transfer energy to the α_1 mode. On the other hand, the spectra of $|a_{i,2}|^2$ are very different from each other; in fact, they can be characterized by either two peaks or

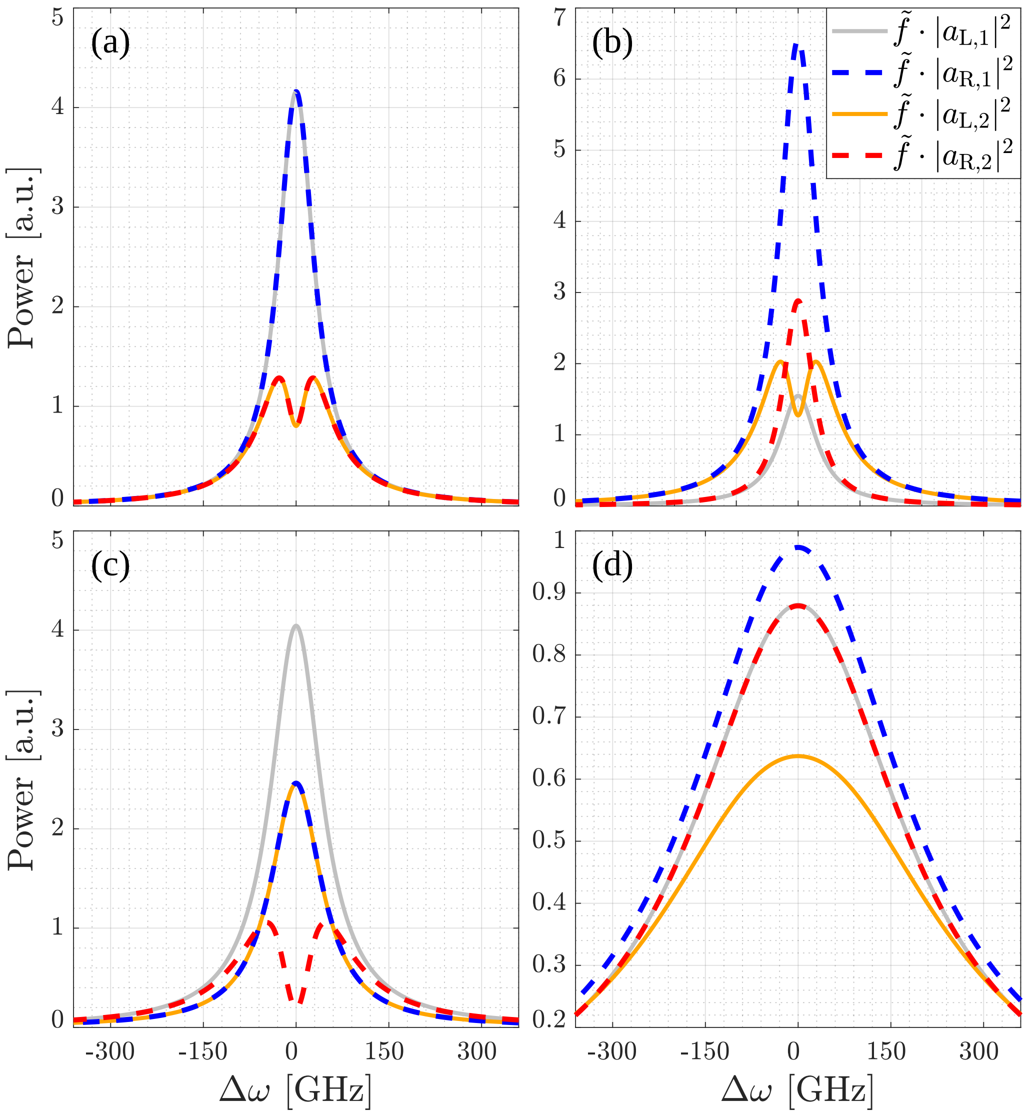

Figure 3.3: Enhancement Factor (EF) of the two modes of the ILMR α_1 and α_2 as a function of the detuning $\Delta\omega$. Here are the four cases corresponding to the coefficients in Tab. 3.1. In (a) the ILMR is symmetric ($\Gamma_L = \Gamma_R$), while in (b), (c) and (d) the ILMR is asymmetric ($\Gamma_L \neq \Gamma_R$). $a_{i,j}$ corresponds to the ILMR mode number j exited from i, where $i = L, R$ and $j = 1, 2$ (L stands for left and R for right). The solid lines show the cases where the system is excited from left. The dotted lines show the cases where the system is excited from right. Gray and blue lines refer to $|a_1|^2$, while orange and red lines refer to $|a_2|^2$.

a single peak. In Fig. 3.3 (a) we have that $|a_{L,2}|^2$ and $|a_{R,2}|^2$ are equal and have a doublet. In Fig. 3.3 (b) $|a_{L,2}|^2$ shows a doublet while $|a_{R,2}|^2$ has only one peak. A special case is given in panel (c), where the condition we set earlier $\gamma_{tot} = 2\Gamma_L$ makes $|a_{L,2}|^2 = |a_{R,1}|^2$ and its spectral peak is Lorentzian. In Fig. 3.3 (c) $|a_{R,2}|^2$ instead shows an evident doublet. Figure 3.3 (d) shows that by increasing the two couplings Γ_L and Γ_R the EF decreases.

Figure 3.2 (a) and Fig. 3.3 (a) show that although the spectral responses are symmetrical, the ILMR is chiral because $|a_{i,1}|^2 > |a_{i,2}|^2$.

It is worth noting that in panel (a) the sum $|a_{L,1}|^2 + |a_{L,2}|^2$ (solid lines) is equal to $|a_{R,1}|^2 + |a_{R,2}|^2$ (dashed lines), while this is not the case in the other panels. In fact, in Fig. 3.3 (b) and in Fig. 3.3 (d) $|a_{L,1}|^2 + |a_{L,2}|^2 < |a_{R,1}|^2 + |a_{R,2}|^2$, while in Fig. 3.3 (c) $|a_{L,1}|^2 + |a_{L,2}|^2 > |a_{R,1}|^2 + |a_{R,2}|^2$. This can be very useful to break Lorentz reciprocity by going into the nonlinear regime, equivalent to what we did with the TJMR in Sec. 2.3.

3.2 Backscattering, Riemann Sheets and Sensing

To describe a real ILMR, we must take into account that the WGs have a surface-wall roughness that causes BS. As the Q of a MR increases, the BS becomes increasingly relevant and cannot be neglected (Sec. 2.4.1). In this section we will add the BS to the TCMT model of the ILMR and see how the ILMR responds to a Hermitian $\delta\beta$ perturbation of the BS coefficients.

To incorporate the BS we need to add the following coupling matrix to the Hamiltonian of the system:

$$K_{BS} := \begin{pmatrix} 0 & -i\beta_{BS,12} \\ -i\beta_{BS,21} & 0 \end{pmatrix} . \tag{3.12}$$

Thus, the Hamiltonian of the system [Eq. (3.2)] becomes:

$$H = \begin{pmatrix} \omega_0 - i\gamma_{tot} & -i\,(\beta_{12} + \beta_{BS,12}) \\ -i\beta_{BS,21} & \omega_0 - i\gamma_{tot} \end{pmatrix} . \tag{3.13}$$

Thus, the eigenvalues and eigenvectors of the system are:

$$\lambda_{1/2} = \omega_0 \pm i\sqrt{(\beta_{12} + \beta_{BS,12})\ \beta_{BS,21}} - i\gamma_{tot} \ \Rightarrow\ \lambda_1 \neq \lambda_2 \,, \tag{3.14}$$

$$
\begin{aligned}
\nu_{1/2} &= \frac{1}{\sqrt{|\beta_{12}+\beta_{\mathrm{BS},12}|/|\beta_{\mathrm{BS},21}|+1}} \begin{pmatrix} \mp\sqrt{\frac{\beta_{12}+\beta_{\mathrm{BS},12}}{\beta_{\mathrm{BS},21}}} \\ 1 \end{pmatrix} \\
\Rightarrow < \nu_1|\nu_2 > &= \frac{1-|\beta_{12}+\beta_{\mathrm{BS},12}|/|\beta_{\mathrm{BS},21}|}{1+|\beta_{12}+\beta_{\mathrm{BS},12}|/|\beta_{\mathrm{BS},21}|}\,.
\end{aligned}
\tag{3.15}
$$

Note that now the eigenvalues and eigenvectors for $\beta_{\mathrm{BS},21} \neq 0$ do not coalesce. Note also that this Hamiltonian, and thus its eigenvalues and eigenvectors, is equivalent to that of the TJMR with BS, reported in Eq. (2.68). Note, however, that the coefficients β_{12} and γ_{tot} are different for the two devices.

The system of equations linking the modes of the ILMR and the input and output fields [Eq. (3.1) and Eq. (3.4)] turns into:

$$
\begin{aligned}
i\frac{d}{dt}\begin{pmatrix}\alpha_2\\ \alpha_1\end{pmatrix} &= \begin{pmatrix}\omega_0 - i\gamma_{\mathrm{tot}} & -i\left(\beta_{12}+\beta_{\mathrm{BS},12}\right)\\ -i\beta_{\mathrm{BS},21} & \omega_0 - i\gamma_{\mathrm{tot}}\end{pmatrix}\begin{pmatrix}\alpha_2\\ \alpha_1\end{pmatrix} \\
&\quad - \begin{pmatrix}\sqrt{2\Gamma_R}e^{i\varphi} & \sqrt{2\Gamma_L}e^{i\varphi}\\ \sqrt{2\Gamma_L} & \sqrt{2\Gamma_R}\end{pmatrix}\begin{pmatrix}E_{\mathrm{in},L}\\ E_{\mathrm{in},R}\end{pmatrix},
\end{aligned}
\tag{3.16}
$$

$$
\begin{pmatrix}E_{\mathrm{out},R}\\ E_{\mathrm{out},L}\end{pmatrix} = e^{i\varphi}\begin{pmatrix}E_{\mathrm{in},L}\\ E_{\mathrm{in},R}\end{pmatrix} + i\begin{pmatrix}\sqrt{2\Gamma_R} & \sqrt{2\Gamma_L}e^{i\varphi}\\ \sqrt{2\Gamma_L} & \sqrt{2\Gamma_R}e^{i\varphi}\end{pmatrix}\begin{pmatrix}\alpha_2\\ \alpha_1\end{pmatrix}. \tag{3.17}
$$

In the stationary regime, the solutions of this system are:

$$
\begin{aligned}
\varepsilon_{\mathrm{out},R} = \varepsilon_{\mathrm{in},L}e^{i\varphi}\Bigg[1 &- \frac{2\Gamma_R\left(-i\Delta\omega+\gamma_{\mathrm{tot}}\right)+2\Gamma_L\left(-i\Delta\omega+\gamma_{\mathrm{tot}}-4\Gamma_R\right)}{\left(-i\Delta\omega+\gamma_{\mathrm{tot}}\right)^2-\left(\beta_{\mathrm{BS},12}+4e^{i\varphi}\sqrt{\Gamma_L\Gamma_R}\right)\beta_{\mathrm{BS},21}} + \\
&+ \frac{2\sqrt{\Gamma_L\Gamma_R}\left(e^{-i\varphi}\beta_{\mathrm{BS},12}+e^{i\varphi}\beta_{\mathrm{BS},21}\right)}{\left(-i\Delta\omega+\gamma_{\mathrm{tot}}\right)^2-\left(\beta_{\mathrm{BS},12}+4e^{i\varphi}\sqrt{\Gamma_L\Gamma_R}\right)\beta_{\mathrm{BS},21}}\Bigg] \\
+ \varepsilon_{\mathrm{in},R}e^{i\phi}e^{i\varphi}\Bigg[&- \frac{4\sqrt{\Gamma_L\Gamma_R}\left(-i\Delta\omega+\gamma_{\mathrm{tot}}-2\Gamma_R\right)}{\left(-i\Delta\omega+\gamma_{\mathrm{tot}}\right)^2-\left(\beta_{\mathrm{BS},12}+4e^{i\varphi}\sqrt{\Gamma_L\Gamma_R}\right)\beta_{\mathrm{BS},21}} \\
&+ \frac{2e^{i\varphi}\Gamma_L\beta_{\mathrm{BS},21}+2e^{-i\varphi}\Gamma_R\beta_{\mathrm{BS},12}}{\left(-i\Delta\omega+\gamma_{\mathrm{tot}}\right)^2-\left(\beta_{\mathrm{BS},12}+4e^{i\varphi}\sqrt{\Gamma_L\Gamma_R}\right)\beta_{\mathrm{BS},21}}\Bigg]
\end{aligned}
\tag{3.18}
$$

$$\begin{aligned}\varepsilon_{\mathrm{out,L}} = \varepsilon_{\mathrm{in,R}} e^{i\phi} e^{i\varphi} \Bigg[1 &- \frac{2\Gamma_R\left(-i\Delta\omega+\gamma_{\mathrm{tot}}\right)+2\Gamma_L\left(-i\Delta\omega+\gamma_{\mathrm{tot}}-4\Gamma_R\right)}{\left(-i\Delta\omega+\gamma_{\mathrm{tot}}\right)^2-\left(\beta_{\mathrm{BS},12}+4e^{i\varphi}\sqrt{\Gamma_L\Gamma_R}\right)\beta_{\mathrm{BS},21}} + \\ &+ \frac{2\sqrt{\Gamma_L\Gamma_R}\left(e^{-i\varphi}\beta_{\mathrm{BS},12}+e^{i\varphi}\beta_{\mathrm{BS},21}\right)}{\left(-i\Delta\omega+\gamma_{\mathrm{tot}}\right)^2-\left(\beta_{\mathrm{BS},12}+4e^{i\varphi}\sqrt{\Gamma_L\Gamma_R}\right)\beta_{\mathrm{BS},21}} \Bigg] \\ + \varepsilon_{\mathrm{in,L}} e^{i\varphi} \Bigg[&- \frac{4\sqrt{\Gamma_L\Gamma_R}\left(-i\Delta\omega+\gamma_{\mathrm{tot}}-2\Gamma_L\right)}{\left(-i\Delta\omega+\gamma_{\mathrm{tot}}\right)^2-\left(\beta_{\mathrm{BS},12}+4e^{i\varphi}\sqrt{\Gamma_L\Gamma_R}\right)\beta_{\mathrm{BS},21}} \\ &+ \frac{2e^{-i\varphi}\Gamma_L\beta_{\mathrm{BS},12}+2e^{i\varphi}\Gamma_R\beta_{\mathrm{BS},21}}{\left(-i\Delta\omega+\gamma_{\mathrm{tot}}\right)^2-\left(\beta_{\mathrm{BS},12}+4e^{i\varphi}\sqrt{\Gamma_L\Gamma_R}\right)\beta_{\mathrm{BS},21}} \Bigg] \end{aligned} \tag{3.19}$$

We will use these equations to fit the experimental data reported in Sec. 3.5. These solutions are more complex than those obtained in the ideal case. It is worth noting that, when the coefficients $\beta_{\mathrm{BS},12}$ and $\beta_{\mathrm{BS},21}$ are non-zero, the absolute squares of the outgoing fields ($|\varepsilon_{\mathrm{out,R}}|^2$ and $|\varepsilon_{\mathrm{out,L}}|^2$) depend on the phase φ that the field acquires as it passes through the bus waveguide between the two coupling regions. We will see later that this can be used to rotate the BS perturbation $\delta\beta$ around the EP.

The BS can also be seen as a perturbation that we want to detect in the system. In fact, we can think that the presence of a molecule/particle near the WG causes some BS [35, 98, 99, 100, 101]. To study how the ILMR behaves as a function of a BS perturbation, we assume that this perturbation is Hermitian, i.e., $\delta\beta := \beta_{\mathrm{BS},12} = -\beta^*_{\mathrm{BS},21}$. In this situation the eigenvalues of the system change to:

$$\lambda_{1/2} = \omega_0 \pm i\sqrt{-\left(4e^{i\varphi}\sqrt{\Gamma_L\Gamma_R}+\delta\beta\right)\delta\beta^*} - i\gamma_{\mathrm{tot}}\,. \tag{3.20}$$

$$\Delta\lambda_{2-1} := \lambda_2 - \lambda_1 = -2i\sqrt{-\left(4e^{i\varphi}\sqrt{\Gamma_L\Gamma_R}+\delta\beta\right)\delta\beta^*}\,. \tag{3.21}$$

We begin with the ideal case where we know the eigenvalues of the system exactly. We then plot the real part $\Re[\lambda]$ and the imaginary part $\Im[\lambda]$ of the two eigenvalues as a function of the real part $\Re[\delta\beta]$ and the imaginary part $\Im[\delta\beta]$ of the perturbation, see panels (a) and (b) of Fig. 3.4.

In Fig. 3.4, to make the plots independent of β_{12}, we normalized to this value. In panels (a) and (b), the Riemann surface corresponding to the first eigenvalue (λ_1) is shown in red, and that for the second eigenvalue (λ_2) is shown in blue. Note that in the real part of the eigenvalues we have removed ω_0 because it is simply a constant. From Fig. 3.4 (a) it can be seen that the real parts of the two eigenvalues are equal in the region where $\Im[\delta\beta/\beta_{12}] = 0$ and $-1 \leqslant \Re[\delta\beta/\beta_{12}] \leqslant 0$. Figure 3.4 (a) shows

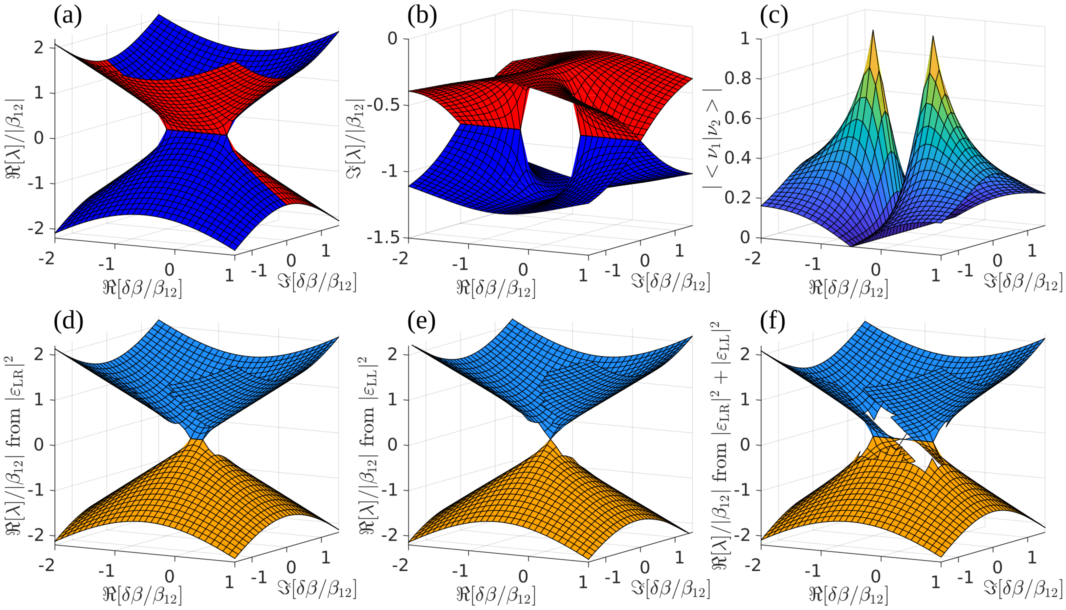

Figure 3.4: Normalized Riemann sheets for the ILMR as a function of the real $\Re[\delta\beta/\beta_{12}]$ and the imaginary $\Im[\delta\beta/\beta_{12}]$ part of the Hermitian BS perturbation ($\delta\beta$). All the quantities are normalized to β_{12} to make the graphs independent of this parameter. Panels (a) and (b) report the real $\Re[\lambda]$ and the imaginary $\Im[\lambda]$ parts of the eigenvalues. In $\Re[\lambda]$ the resonance angular frequency ω_0 is removed. The red Riemann surfaces correspond to the first eigenvalue λ_1, instead the blue ones to the second eigenvalue λ_2. Panel (c) shows the absolute value of the inner product between the two eigenvectors of the system as a function of $\Re[\delta\beta/\beta_{12}]$ and $\Im[\delta\beta/\beta_{12}]$. Panels (d), (e) and (f) show the dips position evaluated through the spectra of $|\varepsilon_{LR}|^2$, $|\varepsilon_{LL}|^2$ and $|\varepsilon_{LR}|^2+|\varepsilon_{LL}|^2$, respectively. In orange the position of the dip with lower angular frequency and in Dodger blue the position of the dip with higher angular frequency. The holes in panels (d), (e), and (f) are due to the inability to recognize two peaks. Here, we use $\Gamma_L=\Gamma_R=1/4$[a.u.] to get $\beta_{12}=1$[a.u.] and $\gamma=\Gamma_L$ ($\gamma_{tot}=3/4$ a.u.). [93]

that the imaginary parts of the two eigenvalues are equal only if $\Im[\delta\beta/\beta_{12}]=0$, $\Re[\delta\beta/\beta_{12}]\leqslant -1 \vee \Re[\delta\beta/\beta_{12}]\geqslant 0$. Consequently, the eigenvalues at $(0,0)$ and at $(-1,-1)$ are equal. Moreover, at these two points, the inner product of the two eigenvectors is 1, see Fig. 3.4 (c). So at $(0,0)$ and at $(-1,-1)$ the system is at an EP, because both eigenvalues and eigenvectors coalesce. Note also that the Riemann sheets intersect in panel (a) while they do not in panel (b).

The coefficient β_{12} in the case of the ILMR is equal to $4e^{i\varphi}\sqrt{\Gamma_L\Gamma_R}$, where φ is the phase acquired by the field propagating along the bus waveguide between the two coupling regions, see Fig. 3.1. By tuning this phase, e.g. by placing a microheater on the bus waveguide, it is possible to change the eigenvalues along a circular path around the EP in $(0,0)$ while keeping $\delta\beta$ constant. This encircling of the EP follows the Riemann surfaces given in Fig. 3.4. This is easily demonstrated by Eq. (3.20). Moreover, this phenomenon is also found in the output fields $\varepsilon_{\mathrm{out,R}}$ and $\varepsilon_{\mathrm{out,L}}$ when considering a Hermitian perturbation $\delta\beta$, see Eq. (3.18) and Eq. (3.19). In fact, in these equations [Eq. (3.18), Eq. (3.19) and Eq. (3.20)] it is observed that if $\delta\beta = \beta_{\mathrm{BS},12} = -\beta^*_{\mathrm{BS},21}$, then the change of φ (rotation in the complex plane of β_{12}) corresponds to a rotation of $\delta\beta$ in the negative direction ($e^{-i\varphi}$). This ability to rotate β_{12} in the complex plane with respect to $\delta\beta$ allows us to change the spectral sensitivity of the ILMR to the perturbation. In particular, by aligning β_{12} with $\delta\beta$ we can maximize the splitting of the real part of the eigenvalues, see Fig. 3.4 (a). In fact, aligning β_{12} with $\delta\beta$ corresponds to imposing $\Im[\delta\beta/\beta_{12}] = 0$ and $\Re[\delta\beta/\beta_{12}] \geqslant 0$.

As also reported in Sec. 2.4.2, it is not possible to directly measure the eigenvalues of the system using the single-side excitation. Normally, the spectral position of the two minima of the Autler-Townes splitting doublet [129, 35] is used to get an estimate of them. However, as we have already pointed out, the frequencies of the minima (maxima) of the spectral dips (peaks) in transmission (reflection) do not give the eigenvalues. In fact, we have seen that the eigenvalues degenerate into an EP, while in Fig. 3.2 (a) the transmission and reflection of the ILMR show a doublet. In order to study how to use the ILMR as a sensor of a $\delta\beta$ perturbation by exploiting the spectral responses, let us consider a symmetric ILMR having $\Gamma_L = \Gamma_R = 1/4$ a.u. and $\gamma = \Gamma_{L/R}$. The normalized spectral minima or maxima for the transmitted power ($|\varepsilon_{LR}|^2$), for the reflected power ($|\varepsilon_{LL}|^2$) and for the sum of the two ($|\varepsilon_{LR}|^2 + |\varepsilon_{LL}|^2$) are reported in panels (d), (e) and (f) of Fig. 3.4, respectively. In these three panels, the orange Riemann surfaces correspond to the dips/peaks at lower angular frequency, while the Dodger blue surfaces correspond to the dips/peaks at higher angular frequency. In some regions it is not possible to distinguish two distinct peaks and therefore holes are observed in panels (d), (e) and (f) of Fig. 3.4. In these regions, there is either only one dip/peak in the spectrum with non-zero detuning or the second dip/peak is masked by the first. In Fig. 3.4 it can be seen that the Riemann surfaces are different in the three cases [$|\varepsilon_{LR}|^2$, (d)], [$|\varepsilon_{LL}|^2$, (e)] and [$|\varepsilon_{LR}|^2 + |\varepsilon_{LL}|^2$, (f)]. In addition to the different trends, it can also be seen that the regions of insensitivity (when the two Riemann surfaces overlap or when one of them is undefined) are different in the three cases. In addition, it is worth noting that the Riemann surfaces corresponding to $|\varepsilon_{LR}|^2 + |\varepsilon_{LL}|^2$ [Fig. 3.4 (f)] curiously have a good correspondence with those for the eigenvalues [Fig. 3.4 (a)]. This can be explained by the fact that the spectrum of $|\varepsilon_{LR}|^2 + |\varepsilon_{LL}|^2$ yields the frequencies where the system has greater losses. Finally, by using the three spectra simultaneously and taking advantage of

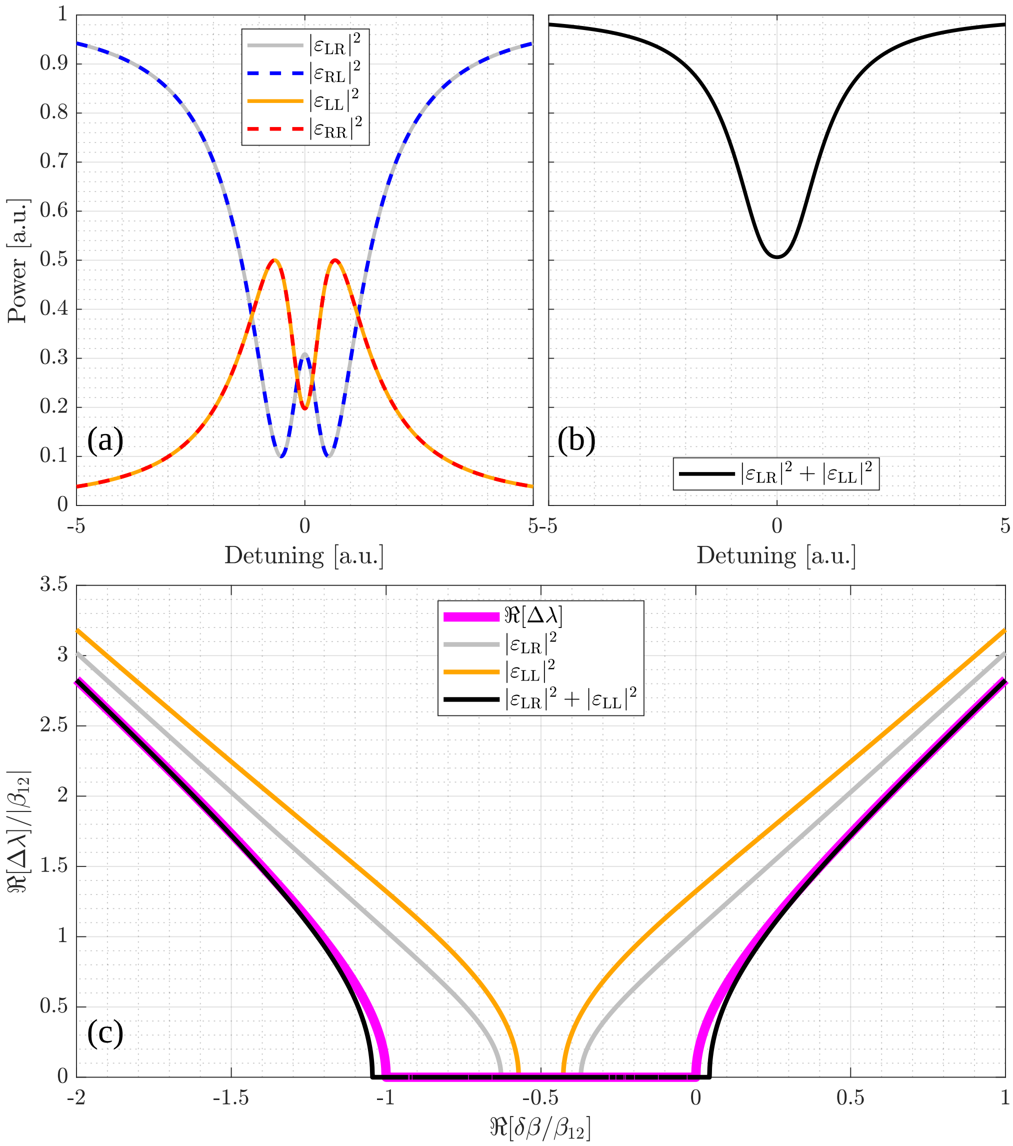

Figure 3.5: Theoretical results for a symmetric ILMR ($\Gamma_L = \Gamma_R$). Panel (a) shows the transmission and reflection spectra for left or right excitation. Panel (b) reports the sum of the output field intensities at the right (transmission) and left (reflection) ports when the ILMR is excited from left ($|\varepsilon_{LR}|^2 + |\varepsilon_{LL}|^2$). Panel (c) represents with different colors the splitting of the eigenvalues (magenta) or of the doublets observed in the spectra of $|\varepsilon_{LR}|^2$ (gray), $|\varepsilon_{LL}|^2$ (orange) and $|\varepsilon_{LR}|^2 + |\varepsilon_{LL}|^2$ (black) as a function of the backscattering perturbation $\Re[\delta\beta/\beta_{12}]$. Here, we use $\Gamma_L = \Gamma_R = 1/4$[a.u.] to get $\beta_{12} = 1$[a.u.] and $\gamma = \Gamma_L$ ($\gamma_{tot} = 3/4$ a.u.). [93]

the fact that one can encircle the EP, one is able to improve the accuracy in detecting the $\delta\beta$ perturbation.

To explore this concept further, we can set $\Im[\delta\beta/\beta_{12}] = 0$ with φ and observe the splitting ($\Re[\Delta\lambda]/|\beta_{12}|$) as a function of the perturbation ($\Re[\delta\beta/\beta_{12}]$), see Fig. 3.5. Looking at panels (a) and (b) of Fig. 3.5, it is observed that by summing the transmission ($|\varepsilon_{LR}|^2$) with the reflection ($|\varepsilon_{LL}|^2$) of an ideal ILMR ($\delta\beta = 0$), the spectrum changes from a doublet to a single dip. In panel (c) of Fig. 3.5 it is observed that the splitting of the eigenvalues (magenta curve) is well reproduced/represented by the splitting present in the spectrum of $|\varepsilon_{LR}|^2 + |\varepsilon_{LL}|^2$ (black curve), as in panels (a) and (f) of Fig. 3.4. However, for a small perturbation ($\Re[\delta\beta/\beta_{12}] \lesssim 0.044$) in the spectrum of $|\varepsilon_{LR}|^2 + |\varepsilon_{LL}|^2$, it is not possible to distinguish two dips, and therefore the splitting calculated using this spectrum is insensitive to the perturbation variation. In any case, as can also be verified by Eq. (3.20), the splitting follows a square root for small $\delta\beta$ perturbations, this is the characteristic trend of the EPs [35, 44, 47]. In contrast, the splitting in the transmission and reflection spectra (gray and orange curves) follow a linear trend for $\delta\beta$ around or greater than zero. Thus, by using the ILMR, one is able to simultaneously use both the enhanced sensitivity of the EP due to the square root trend and the linear trend, which can be used not only for calibration but also to remove the region of insensitivity observed for small perturbations. The ability to remove the region of insensitivity present in the structures used so far is a great advantage for a device that has to be used as a sensor.

3.3 Coherent perfect absorption condition

In this section, we will see how the Coherent Perfect Absorption (CPA) condition [186, 92] can be achieved and what it implies. To obtain the CPA condition, we need to study the eigenvalues of the scattering matrix of the ideal ILMR. For the ILMR we define the scattering matrix as follows:

$$\begin{pmatrix} E_{\text{out,L}} \\ E_{\text{out,R}} \end{pmatrix} = \mathbf{S}_{\text{ILMR}} \begin{pmatrix} E_{\text{in,R}} \\ E_{\text{in,L}} \end{pmatrix} \tag{3.22}$$

Hence

$$\begin{aligned} \mathbf{S}_{\mathrm{ILMR}} &= \begin{pmatrix} \varepsilon_{RL} & \varepsilon_{LL} \\ \varepsilon_{RR} & \varepsilon_{LR} \end{pmatrix} \\ &= e^{i\varphi} \begin{pmatrix} 1 - \frac{2(\Gamma_L+\Gamma_R)}{-i\Delta\omega+\gamma_{tot}} + \frac{8\Gamma_L\Gamma_R}{(-i\Delta\omega+\gamma_{tot})^2} & -\frac{4\sqrt{\Gamma_L\Gamma_R}}{-i\Delta\omega+\gamma_{tot}}\left(1-\frac{2\Gamma_L}{-i\Delta\omega+\gamma_{tot}}\right) \\ -\frac{4\sqrt{\Gamma_L\Gamma_R}}{-i\Delta\omega+\gamma_{tot}}\left(1-\frac{2\Gamma_R}{-i\Delta\omega+\gamma_{tot}}\right) & 1 - \frac{2(\Gamma_L+\Gamma_R)}{-i\Delta\omega+\gamma_{tot}} + \frac{8\Gamma_L\Gamma_R}{(-i\Delta\omega+\gamma_{tot})^2} \end{pmatrix} . \end{aligned} \tag{3.23}$$

Thus, the eigenvalues of the scattering matrix are:

$$\begin{aligned} \sigma_{1/2} = e^{i\varphi} \Bigg(& \frac{\Delta\omega - 2i\Gamma_R + i\gamma_{tot}}{\Delta\omega + i\gamma_{tot}} + \frac{2\Gamma_L\left(-i\Delta\omega - 4\Gamma_R + \gamma_{tot}\right)}{\left(\Delta\omega + i\gamma_{tot}\right)^2} \\ & \pm \frac{4\sqrt{\Gamma_L\Gamma_R\left(i\Delta\omega + 2\Gamma_L - \gamma_{tot}\right)\left(i\Delta\omega + 2\Gamma_R - \gamma_{tot}\right)}}{\left(\Delta\omega + i\gamma_{tot}\right)^2} \Bigg) \end{aligned} \tag{3.24}$$

Only the first eigenvalue of the scattering matrix (σ_1) has a zero, while only the second eigenvalue (σ_2) has a pole. The zero of σ_1 is for:

$$\omega_{\sigma_1,\mathrm{zero}} = \omega_0 - i\left(\gamma_{tot} - 2\left(\Gamma_L + \Gamma_R\right)\right) . \tag{3.25}$$

Instead, the pole of σ_2 is for:

$$\omega_{\sigma_2,\mathrm{pole}} = \omega_0 - i\gamma_{tot} . \tag{3.26}$$

Note that the pole of σ_2 corresponds to the eigenvalues of the Hamiltonian of the system [Eq. (3.3)].

The CPA condition is obtained when an eigenvalue of the scattering matrix is zero, restricted to the case of real frequencies [186]. This condition holds for $\gamma_{tot} = 2(\Gamma_L + \Gamma_R)$. Satisfying this condition $\omega_{\sigma_1,\mathrm{zero}}$ is only real [186, 92].

Figure 3.6 (a) shows the transmission and reflection spectral responses of an ideal and geometrically symmetric ILMR in the CPA condition ($\Gamma_L = \Gamma_R = \Gamma$, $\gamma_{tot} = 4\Gamma$, $\Gamma = 1/4$ a.u.). Here we can see the presence of a doublet (two dips/peaks) in both transmission and reflection. Note that at resonance both spectra are different from zero. Adding the two spectra of transmission and reflection ($|\varepsilon_{LR}|^2 + |\varepsilon_{LL}|^2$) yields a spectrum characterized by a quartic pattern, see the black curve in Fig. 3.6 (b). In fact, by expansion in Taylor series around $\Delta\omega = 0$ we get

$$|\varepsilon_{LR}|^2 + |\varepsilon_{LL}|^2 = \frac{1}{2} + \frac{\Delta\omega^4}{512\,\Gamma^4} - \frac{\Delta\omega^6}{4096\,\Gamma^6} + O\left[\Delta\omega^8\right] . \tag{3.27}$$

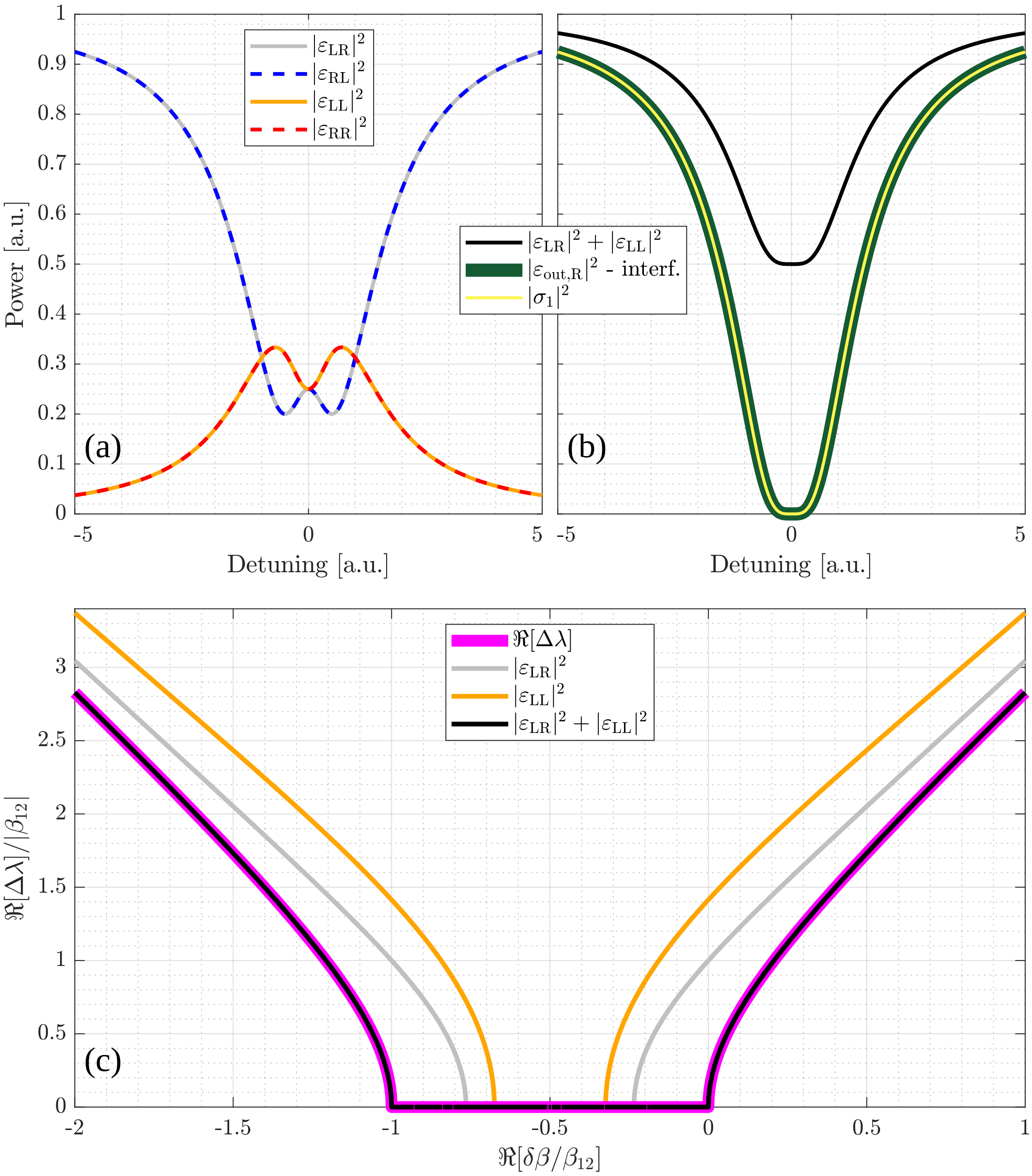

Figure 3.6: Theoretical results for a symmetric ILMR ($\Gamma_L = \Gamma_R$) in the Coherent Perfect Absorption (CPA) condition $\gamma_{tot} = 2(\Gamma_L + \Gamma_R)$. (a) Transmission and reflection spectra for left or right excitation. (b) Sum of the output field intensities at the right (transmission) and left (reflection) ports when the ILMR is excited from left ($|\varepsilon_{LR}|^2 + |\varepsilon_{LL}|^2$, black curve). The dark green line reports $|\varepsilon_{out,R}|^2$ when a symmetric interferometric excitation ($|\varepsilon_{in,L}|^2 = |\varepsilon_{in,R}|^2 = 1$) is used. The yellow curve shows the square absolute value of the first eigenvalue of the scattering matrix of the ILMR ($|\sigma_1|^2$). (c) Splitting of the eigenvalues or of the doublets observed in the spectra of $|\varepsilon_{LR}|^2$, $|\varepsilon_{LL}|^2$ and $|\varepsilon_{LR}|^2 + |\varepsilon_{LL}|^2$ as a function of the backscattering perturbation $\delta\beta/\beta_{12}$. The color code is given in the inset. Here we use $\Gamma_L = \Gamma_R = 1/4$ a.u. to get $\beta_{12} = 1$ a.u. and $\gamma = \Gamma_L + \Gamma_R = 1/2$ a.u. to reach the CPA condition. [93]

Note, however, that although we are in the CPA condition at resonance, the total absorption, $1-(|\varepsilon_{LR}|^2+|\varepsilon_{LL}|^2)$, turns out to be 0.5 a.u. instead of 1 a.u.. This is due to the fact that in our case, in order to have the CPA, it is necessary to use an interferometric excitation [102, 186], i.e. by exciting the ILMR from both sides of the bus waveguide. In this way, at resonance, the output electric field from both ports of the bus waveguide is zero, see the dark green curve in Fig. 3.6 (b). As expected, the spectrum obtained by symmetric interferometric excitation is equivalent to the spectrum of the squared modulus of the first eigenvalue of the scattering matrix ($|\sigma_1|^2$), see the yellow curve in Fig. 3.6 (b). $|\sigma_1|^2$ has a quartic trend around zero detuning ($\Delta\omega = 0$); in fact, expanding it in Taylor series around $\Delta\omega = 0$, we obtain:

$$|\sigma_1|^2 = \frac{\Delta\omega^4}{256\,\Gamma^4} - \frac{\Delta\omega^6}{2048\,\Gamma^6} + \frac{3\Delta\omega^8}{65536\,\Gamma^8} + O\left[\Delta\omega^{10}\right] . \tag{3.28}$$

As a result, even the absorption line shape of the first eigenchannel has the quartic dependence as observed in [186, 57, 92]. Note that, in this case, $|\sigma_1|^2 = 2(|\varepsilon_{LR}|^2 + |\varepsilon_{LL}|^2) - 1$.

Fig. 3.6 (c) shows the splitting of the eigenvalues or of the doublets observed in the spectra of $|\varepsilon_{LR}|^2$, $|\varepsilon_{LL}|^2$ and $|\varepsilon_{LR}|^2 + |\varepsilon_{LL}|^2$ as a function of the backscattering perturbation $\delta\beta/\beta_{12}$. Here the ILMR is in the CPA condition and the used parameters are: $\Gamma_L = \Gamma_R = \Gamma = 1/4$ a.u., $\beta_{12} = 4\Gamma = 1$ a.u., $\gamma = 2\Gamma = 1/2$ a.u. and $\gamma_{tot} = 4\Gamma$. Interestingly, the splitting of the spectrum of $|\varepsilon_{LR}|^2 + |\varepsilon_{LL}|^2$ [black curve in Fig. 3.6 (c)] equals the splitting of the eigenvalues (magenta curve). Consequently, there is no region of null splitting around the zero of the perturbation. In fact, at the CPA EP, the splitting evaluated from the spectrum of $|\varepsilon_{LR}|^2 + |\varepsilon_{LL}|^2$ depends as $2\sqrt{\delta\beta(\delta\beta + 4\Gamma)}$. This corresponds to the splitting of the Hamiltonian eigenvalues reported in Eq. (3.21). Here we have imposed: $\Gamma_L = \Gamma_R = \Gamma$, $\mathfrak{I}[\delta\beta] = 0$, $\mathfrak{R}[\delta\beta] \geqslant 0$ and $e^{i\varphi} = 1$.

3.4 Transfer Matrix Method with Backscattering

The ILMR can also be modeled using the TMM. In this section we will report the equations that characterize the electric fields inside the ILMR and, as in the Ch. 1, we will describe the backscattering as a single scatterer inside the ILMR. We will also report the relationships between the parameters of the TCMT and those of the TMM.

If we consider the crossing to be ideal, then the geometry we used to create this particular MR can be modified. In fact, the ILMR [Fig. 3.7 (a)] is also equivalent to a TJMR excited by the S-shaped WG [Fig. 3.7 (b)] or even to a two-point coupled MR with the bus waveguide and the crossing present in the bus waveguide between these two coupling regions [Fig. 3.7 (c)] [93]. The ILMR-equivalent structure shown in Fig. 3.7 (c) may appear similar to the device reported in [50]. However, the latter differs from the ILMR by the presence of an optical isolator that halves the coupling from α_1 to α_2. Thus, unlike the ILMR, the response of this device does not exhibit a doublet in the transmission spectrum when its response is not perturbed by the presence of a scatterer. Moreover, although the devices described in [52, 49, 50] have the same Hamiltonian as ILMR, they do not have the same spectral responses because their scattering matrix is different from that of ILMR.

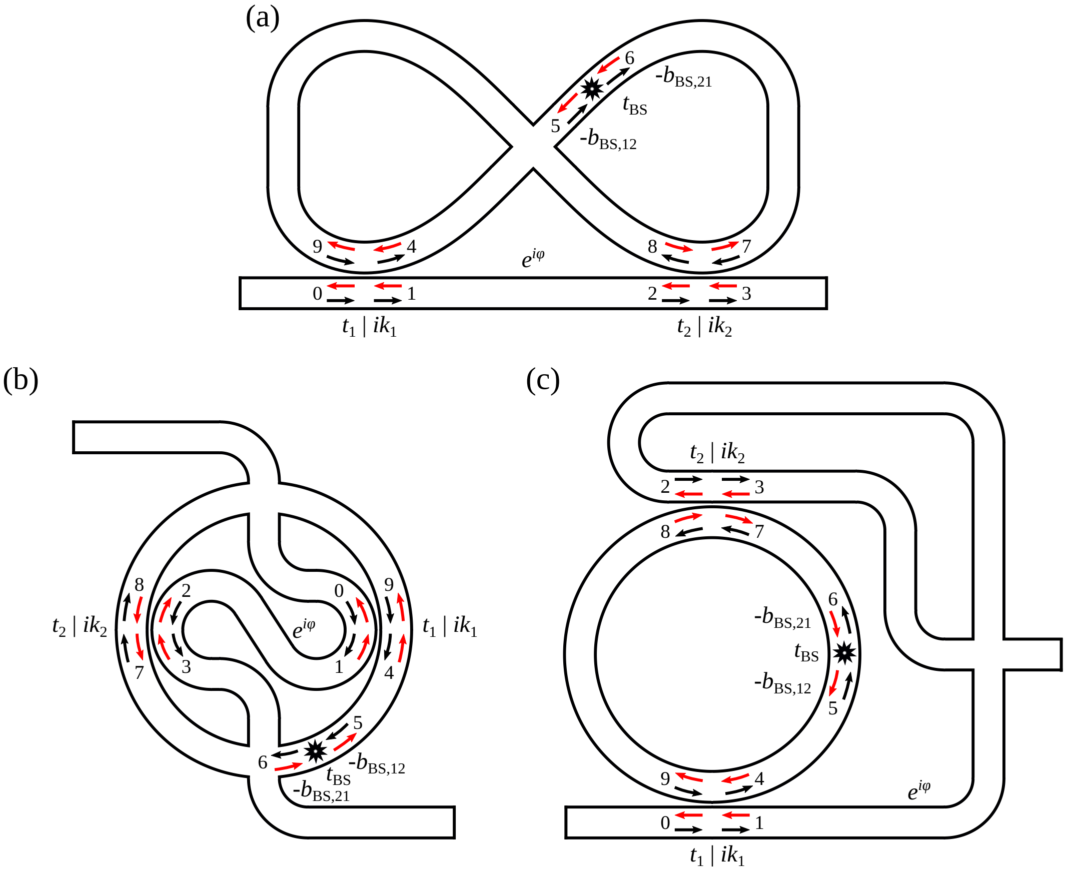

Figure 3.7: Sketches of MRs ideally equivalent to a ILMR. Panel (a) shows an ILMR, panel (b) schematizes a TJMR excited from the S-shaped WG, and panel (c) represents a MR having two couplings with the bus waveguide having within it a crossing. The black arrows identify the E_n fields, where $n = 0, ..., 9$, and their propagation direction. Instead, the red arrows identify the E_{nr} fields, which have opposite propagation directions. All the parameters are described in the text. [93]

To easily demonstrate the equality of the three structures schematized in Fig. 3.7, it is useful to use the TMM instead of the TCMT. In Fig. 3.7 the black arrows identify the E_n fields, where $n = 0, ..., 9$, and their propagation directions, instead the red arrows identify the E_{nr} fields, which have opposite propagation directions. By using Fig. 3.7, we can write the equations that connect the different fields:

$$
\begin{aligned}
E_1 &= t_1 E_0 + ik_1 E_9 \,, & E_{0r} &= t_1 E_{1r} + ik_1 E_{4r} \,,\\
E_2 &= e^{i\varphi} E_1 \,, & E_{1r} &= e^{i\varphi} E_{2r} \,,\\
E_3 &= t_2 E_2 + ik_2 E_{8r} \,, & E_{2r} &= t_2 E_{3r} + ik_2 E_7 \,,\\
E_4 &= t_1 E_9 + ik_1 E_0 \,, & E_{4r} &= \sigma_{45} e^{i\psi_{45}} E_{5r} \,,\\
E_5 &= \sigma_{45} e^{i\psi_{45}} E_4 \,, & E_{5r} &= t_{BS} E_{6r} - b_{BS,12} E_5 \,,\\
E_6 &= t_{BS} E_5 - b_{BS,21} E_{6r} \,, & E_{6r} &= \sigma_{67} e^{i\psi_{67}} E_{7r} \,,\\
E_7 &= \sigma_{67} e^{i\psi_{67}} E_6 \,, & E_{7r} &= t_2 E_{8r} + ik_2 E_2 \,,\\
E_8 &= t_2 E_7 + ik_2 E_{3r} \,, & E_{8r} &= \sigma_{89} e^{i\psi_{89}} E_{9r} \,,\\
E_9 &= \sigma_{89} e^{i\psi_{89}} E_8 \,, & E_{9r} &= t_1 E_{4r} + ik_1 E_{1r} \,,\\
\psi_{jl} &:= \frac{2\pi}{\lambda} n_{\text{eff}} L_{jl} \,, & L &:= L_{45} + L_{67} + L_{89} \,,\\
\sigma_{jl} &:= e^{-\alpha L_{jl}} \,, & \sigma &:= e^{-\alpha L} \,,\\
\psi &:= \frac{2\pi}{\lambda} n_{\text{eff}} L \,.
\end{aligned}
\tag{3.29}
$$

Note that these equations describe all three systems, so we can say that the three geometries reported in Fig. 3.7 are equivalent. The parameter L_{jl} identifies the WG length between the numbers j and l reported in Fig. 3.7. Here n_{eff} is the effective refractive index of the WG, α is the propagation loss coefficient, L is the perimeter of the infinity-shaped WG. In the following, for simplicity, we assume that all the couplings have no losses ($t_1^2 + k_1^2 = 1$ and $t_2^2 + k_2^2 = 1$).

The solution of the system of equations in Eq. (3.29) yields

$$
\varepsilon_{LR} = \varepsilon_{RL} = \frac{N}{D} \,, \quad \varepsilon_{LL} = \frac{N_{LL}}{D} \,, \quad \varepsilon_{RR} = \frac{N_{RR}}{D}
\tag{3.30}
$$

$$
\varepsilon_{\text{out},R} = \varepsilon_{\text{in},L} \varepsilon_{LR} + \varepsilon_{\text{in},R} e^{i\phi} \varepsilon_{RR} \,,
\tag{3.31}
$$

$$
\varepsilon_{\text{out},L} = \varepsilon_{\text{in},R} e^{i\phi} \varepsilon_{RL} + \varepsilon_{\text{in},L} \varepsilon_{LL} \,.
\tag{3.32}
$$

where

$$\begin{aligned} N = {} & \left[\left(t_2^2 - 2\right) t_1^2 - 2t_2^2 + 1\right] t_{BS} \sigma e^{i(\psi+\varphi)} + \\ & + t_1 \left(k_1 k_2 \sigma_{45}^2 \sigma_{89} e^{i(2\psi_{45}+\psi_{89})} b_{BS,12} + t_2 e^{i\varphi}\right) t_1 \sigma_{67}^2 \sigma_{89} e^{i(2\psi_{67}+\psi_{89}+\varphi)} \\ & \left[t_2 \sigma_{45}^2 \sigma_{89} e^{i(2\psi_{45}+\psi_{89})} \left(t_{BS}^2 - b_{BS,12} b_{BS,21}\right) - k_1 k_2 e^{i\varphi} b_{BS,21}\right] \end{aligned} \tag{3.33}$$

$$\begin{aligned} N_{LL} = {} & 2k_1 k_2 \sigma_{45} \sigma_{67} e^{i(\psi_{45}+\psi_{67}+\varphi)} \left[- t_1 t_{BS} + t_2 \sigma e^{i\psi} \left(t_{BS}^2 - b_{BS,12} b_{BS,21}\right) \right] \\ & + k_1^2 \sigma_{45}^2 e^{2i\psi_{45}} b_{BS,12} + k_2^2 t_1^2 \sigma_{67}^2 e^{2i(\psi_{67}+\varphi)} b_{BS,21} \end{aligned} \tag{3.34}$$

$$\begin{aligned} N_{RR} = {} & \sigma_{89}^2 e^{2i\psi_{89}} \left[k_2^2 t_1^2 \sigma_{45}^2 e^{2i\psi_{45}} b_{BS,12} + k_1^2 \sigma_{67}^2 e^{2i(\psi_{67}+\varphi)} b_{BS,21}\right] \\ & + 2k_1 k_2 \sigma_{89} e^{i(\psi_{89}+\varphi)} \left(-t_2 + t_1 \sigma e^{i\psi} t_{BS}\right) \end{aligned} \tag{3.35}$$

$$\begin{aligned} D = {} & 1 + t_2 \sigma_{67} \sigma_{89} e^{i(\psi_{67}+\psi_{89})} \Big[t_2 t_1^2 \sigma_{45} \sigma e^{i(\psi_{45}+\psi)} \left(t_{BS}^2 - b_{BS,12} b_{BS,21}\right) \\ & - 2k_1 k_2 \sigma_{67} e^{i(\psi_{67}+\varphi)} b_{BS,21} - 2t_1 \sigma_{45} e^{i\psi_{45}} t_{BS}\Big] \end{aligned} \tag{3.36}$$

Now, to simplify the discussion we impose the following conditions on the position of the scatterer inside the ILMR: $L_{89} = 2L_{45} = 2L_{67} = L/2$ ($\psi_{89} = 2\psi_{45} = 2\psi_{67} = \psi/2$ and $\sigma = \sigma_{89}^2 = \sigma_{45}^4 = \sigma_{67}^4$). If the conditions describing a situation of "low" couplings ($k_{1/2} \ll 1$, $t_{1/2} \simeq 1$, $|b_{BS,12/21}| \ll 1$, $t_{BS} \simeq 1$, $\sigma \simeq 1$) are met, and performing the following substitutions:

$$t_{1/2} \simeq 1 - \frac{\Gamma_{L/R}}{\tilde{f}}, \quad k_{1/2} \simeq \sqrt{\frac{2\Gamma_{L/R}}{\tilde{f}}} \tag{3.37}$$

$$t_{BS}\sigma \simeq 1 - \frac{\gamma}{\tilde{f}}, \quad \sigma := e^{-\alpha L} \tag{3.38}$$

$$\beta_{12} = 4e^{i\varphi} \sqrt{\Gamma_L \Gamma_R} \tag{3.39}$$

$$b_{BS,12} \simeq \frac{\beta_{BS,12}}{\tilde{f}}, \quad b_{BS,21} \simeq \frac{\beta_{BS,21}}{\tilde{f}} \tag{3.40}$$

$$\tilde{f} := \frac{c}{n_g L} = \frac{c\,\mathrm{FSR}}{\lambda_0^2}, \quad \mathrm{FSR} := \frac{\lambda_0^2}{n_g L}, \quad \psi = \frac{\Delta\omega}{\tilde{f}} \tag{3.41}$$

it is straightforward to verify that we obtain the same results derived in the steady state regime through the TCMT equations reported in Eq. (3.16), Eq. (3.17), namely Eq. (3.18) and Eq. (3.19).

Similar to what we did in Ch. 1 and Ch. 2, we have demonstrated that, if the following relations are satisfied ($k_{1/2} \ll 1$, $t_{1/2} \simeq 1$, $|b_{Bs,12/21}| \ll 1$, $t_{Bs}\sigma \simeq 1$) equivalent to ($\Gamma_L \& \Gamma_R \& \gamma_{tot} \& |\beta_{12}| \& |\beta_{Bs,12}| \& |\beta_{Bs,21}| \ll \tilde{f}$), to move from the coefficients of a TCMT to the ones of a TMM model one has to use the following relations:

$$\Gamma_{L/R} \simeq \tilde{f}(1 - t_{1/2})\,, \quad \Gamma_{L/R} \simeq \tilde{f} k_{1/2}^2/2 \tag{3.42}$$

$$\gamma \simeq \tilde{f}(1 - t_{Bs}\sigma)\,, \quad \sigma := e^{-\alpha L} \tag{3.43}$$

$$\beta_{12} = 4e^{i\varphi}\sqrt{\Gamma_L \Gamma_R} \simeq 4e^{i\varphi}\tilde{f}\sqrt{(1 - t_1)(1 - t_2)} \tag{3.44}$$

$$\beta_{12} \simeq 2e^{i\varphi}\tilde{f} k_L k_R \tag{3.45}$$

$$\beta_{Bs,12} \simeq \tilde{f} b_{Bs,12}\,, \quad \beta_{Bs,21} \simeq \tilde{f} b_{Bs,21} \tag{3.46}$$

$$\tilde{f} := \frac{c}{n_g L} = \frac{c\,\mathrm{FSR}}{\lambda_0^2}\,, \quad \mathrm{FSR} := \frac{\lambda_0^2}{n_g L}\,. \tag{3.47}$$

3.5 Experimental Measurements

3.5.1 Samples and experimental setup

To experimentally verify the theoretical model of the ILMR, we designed four ILMRs. Specifically, we fabricated one symmetric ILMR ($\Gamma_L = \Gamma_R$) and three asymmetric ILMRs ($\Gamma_L \neq \Gamma_R$) whose parameters are given by design in Tab. 3.1. The ILMRs are fabricated in Si using channels WGs with a cross section of 450 nm × 220 nm surrounded by a cladding in SiO_2. The samples were fabricated by the IMEC/Europractice facility within a multi-project wafer program (the design of the whole chip is shown in Fig. A.1 of Appendix A).

In Fig. 3.8 the designs of the two structures are shown, in panel (a) the symmetric ILMR and in panel (b) the asymmetric ILMR. The symmetric ILMR [Fig. 3.8 (a)] is realized by a crossing from which four Euler curves of 135° with minimum radius equal to 15 µm depart, these WGs are connected two by two by straight WGs; finally both lobes of the infinity-shaped WG are point coupled with the bus waveguide. Here the gap widths between the lobes and the bus waveguide are 165 nm. The three asymmetric ILMRs are formed by a crossing, four Euler curves of 45° and minimum radius of 10 µm, four straight WGs of 10 µm, four Euler curves of 90° and minimum radius of 10 µm connected by two straight WGs of about 17.24 µm;

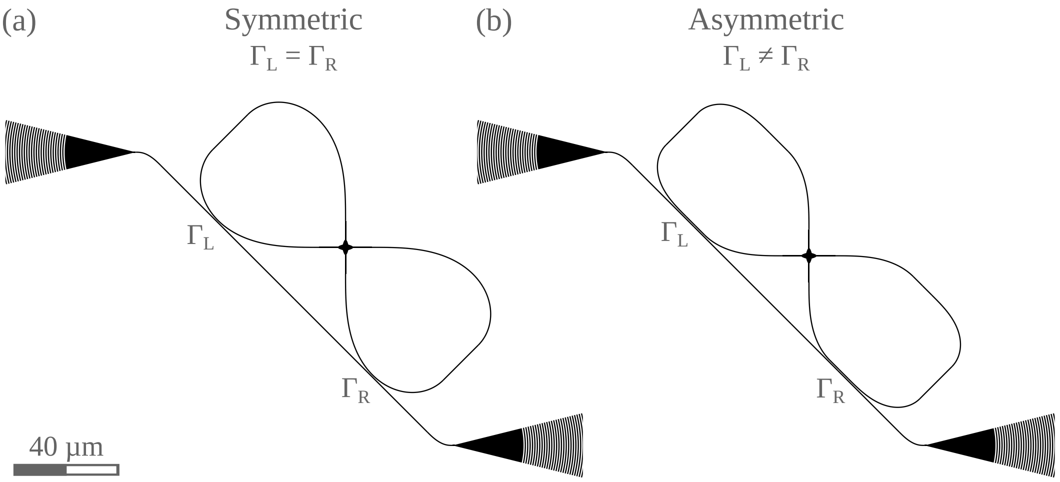

Figure 3.8: The design of a symmetric (a) and an asymmetric (b) ILMRs. The Si WGs are indicated by the black lines. Black triangles surmounted by white circular lines identify the input/output grating couplers.

finally, both lobes of the infinity-shaped WG are coupled with the bus waveguide. In this case, the gap widths between the bus waveguide and the infinity-shaped WG are $\text{gap}_L = [392, 288, 205]$ nm and $\text{gap}_R = [300, 326, 198]$ nm, for the left and right couplings, respectively. The crossings used in these structures are those of the design kit of the IMEC/Europractice facility, which from our measurements at 1550 nm have losses of 0.18 ± 0.01 dB/crossing and negligible reflections. To make the coupling between the fiber and the bus waveguide, we used grating couplers from the IMEC/Europractice design kit, see Fig. 3.8.

The same experimental setup described in Sec. 1.5.1 (Fig. 1.20) was used to measure these ILMRs. With this setup, we are actually able to measure both the transmission and reflection spectra of the structure under investigation simultaneously, and we can quickly change the excitation direction of the system.

3.5.2 Results

In Fig. 3.9 the experimental spectra and their theoretical fits for the four ILMRs are shown. The transmissions obtained by exciting the system from left and right are represented by gray and blue curves, while the reflections are shown in orange and red. The dashed black curves show the theoretical fits made by Eq. (3.18) and Eq. (3.19). The results of the fits are listed in Tab. 3.2.

Fig. 3.9 shows that the theoretical model can reproduce the experimental spectra. We also observe that the experimental spectra are similar to those expected by

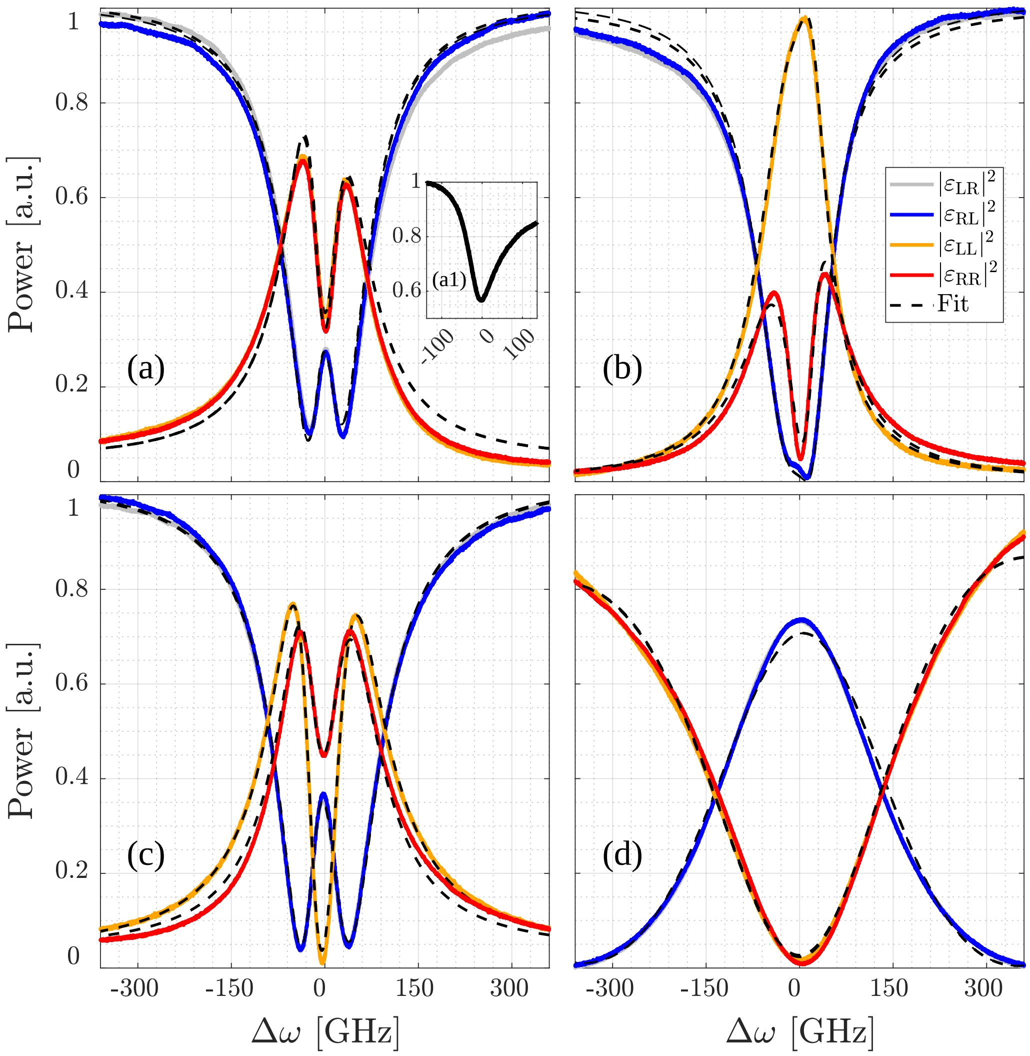

Figure 3.9: Experimental spectra of four different ILMRs. The solid curves report the experimental data instead the dashed black lines identify the fits with the TCMT equations [Eq. (3.18) and Eq. (3.19)]. The gray and blue curves show the transmission spectra while the orange and red ones show the reflection spectra. Moreover, the gray and orange lines correspond to an input excitation from left while the blue and red lines from right. The inset (a1) shows with a solid black curve the sum of the transmitted and reflected measured intensities as a function of $\Delta\omega$, when the ILMR is excited from left ($|\varepsilon_{LR}|^2 + |\varepsilon_{LL}|^2$). The coefficients derived at the design stage are listed in Tab. 3.1, while those derived from the fits are listed in Tab. 3.2. [93]

	Fig. 3.9 (a)	Fig. 3.9 (b)	Fig. 3.9 (c)	Fig. 3.9 (d)
design	symmetric	asymmetric	asymmetric	asymmetric
gap_L [nm]	165	392	288	205
gap_R [nm]	165	300	326	198
Γ_L [GHz]	12.86(7)	5.81(3)	23.90(6)	183(1)
Γ_R [GHz]	13.25(7)	30.8(3)	12.1(1)	182(1)
γ_{tot} [GHz]	39.9(3)	43.7(3)	47.0(3)	400(2)
$\lvert\beta_{12}\rvert$ [GHz]	52.2(8)	54(1)	68(1)	732(14)
$\arg[\beta_{12}]$	0.1436(6)	−2.148(3)	−1.865(6)	1.64(1)
$\lvert\beta_{Bs,12}\rvert$ [GHz]	2.21(2)	5.90(3)	5.93(6)	18.77(1)
$\arg[\beta_{Bs,12}]$	0.782(7)	1.567(8)	1.85(1)	1.000(9)
$\lvert\beta_{Bs,21}\rvert$ [GHz]	3.40(2)	13.1(1)	8.90(8)	23.12(1)
$\arg[\beta_{Bs,21}]$	1.11(1)	0.981(4)	1.047(7)	1.77(1)

Table 3.2: Design parameters and TCMT parameters derived through fits of experimental data reported in Fig. 3.9. For each ILMR, a simultaneous fit of the four spectral responses with the same parameters was performed using Eq. (3.18) and Eq. (3.19). [93]

the design (Fig. 3.2), where BS was not taken into account. This means that the simulations performed to obtain the correct gap widths of the coupling regions were quite accurate. In the design simulations, the coupling coefficients related to the TMM were calculated and then converted to those of the TCMT using the relations given in Sec. 3.4. Comparing the values of the parameters reported in Tab. 3.1 and in Tab. 3.2, a fair agreement is observed. The partial disagreement is mainly due to the presence of BS.

The presence of the non-Hermitian BS can also be detected by the asymmetry of the spectral responses with respect to the zero detuning axis ($\Delta\omega = 0$). Although the presence of the BS deforms the experimental spectra, we can also find the main features of each individual ILMR in the experimental measurements. In Fig. 3.9, as assured by the Lorentz reciprocity theorem, the system transmission spectra excited from left ($|\varepsilon_{LR}|^2$) are equivalent to those excited from right ($|\varepsilon_{RL}|^2$). In panel (a) [symmetric ILMR] we observe that the two reflections are also equivalent and that, like the transmission, they show an evident splitting (two peaks/dips). In panel (b), the transmission and reflection from the left show almost only a spectral dip/peak, while the reflection from the right shows a clear doublet. Note also that in Fig. 3.9 (b) the ILMR at resonance behaves approximately like a unidirectional reflector, in fact, the reflection on the left is much higher than that on the right ($|\varepsilon_{LL}|^2/|\varepsilon_{RR}|^2 \simeq 19$ at $\Delta\omega = 0$). In panel (c) we have that $|\varepsilon_{LL}|^2$ is close to zero at resonance and that all spectra show an evident doublet. As in panel (b), the asymmetric ILMR can be used as a unidirectional reflector, but in this case, the largest reflection at resonance is on the right. In panel (d), on the other hand, a peak at resonance is observed in the transmission spectra and a dip at resonance in the reflection spectra [as in Fig. 3.2 (d)].

In the inset (a1) of panel (a) of Fig. 3.9, the sum of the transmission spectrum and the reflection spectrum $|\varepsilon_{LR}|^2 + |\varepsilon_{LL}|^2$ is shown. This spectrum should ideally consist of only one symmetrical dip at resonance, similar to what we reported in Fig. 3.5 (b). Here we observe a dip at resonance, but because of the BS, there is an asymmetry with respect to the axis with $\Delta\omega = 0$. Also from Tab. 3.2 we can see that the BS is non-Hermitian and that in the complex plane the vector β_{12} is not aligned with the vector $\beta_{BS,12}$. Because we did not have the opportunity in the designed chip to insert the microheater over part of the bus waveguide between the two coupling regions, we were not able to vary the phase φ to perform the encircling of the EP.

In the theoretical model, we have not taken into account the non-idealities of the crossing present in the ILMR, but they can be incorporated in the other parameters of the system. In fact, the loss of the crossing can be taken into account in the coefficient γ_{tot}, while its possible reflections or cross-talk can be included in the coefficients $\beta_{BS,12}$ and $\beta_{BS,21}$, without loss of generality.

In conclusion, in this section, we have experimentally verified the presented theoretical model by also experimentally observing some of the interesting features of ILMRs.

Chapter 4

A comparison of the Microring, the Taiji, and the Infinity-Loop microresonators

In this chapter, we compare the three microresonators analyzed in chapters 1, 2 and 3. In Sec. 4.1 we will compare the spectral responses and in Sec. 4.2 their sensing performances.

4.1 Spectral responses

In this section, we will neglect the BS and discuss the ideal microring resonator (ideal MR), the ideal TJMR, and the ideal ILMR.

The MR, unlike the other two structures, has both zero reflections, in fact, its geometry does not create any intrinsic coupling between its two counterpropagating modes. The TJMR, on the other hand, is designed to transfer optical energy only from the CW field to the CCW field. This coupling causes the reflection on the right to have a peak at resonance, while the reflection on the left is zero, as in the case of the MR. This allows the TJMR to be used as a unidirectional reflector. The transmission spectra of these two devices (MR and TJMR) are characterized by a single Lorentzian dip. In contrast, the ILMR, although it also has degenerate eigenvalues, generally exhibits a transmission with two dips (a doublet). This peculiar phenomenon is given by a special interference between the outgoing fields of the ILMR and those of the bus waveguide.

The ILMR, unlike the other two structures, has two couplings to the bus waveguide instead of just one, which makes the ILMR much more tunable. In fact, it can have a variety of spectral responses. It can have both symmetrical and completely different reflections, so it can work at resonance as a unidirectional reflector (similar to TJMR). It can also have a single dip in transmission and a single peak in either reflection, or even a peak in transmission and a dip in reflection, see Fig. 3.2.

In the linear regime, these three structures cannot break Lorentz reciprocity (transmission relative to excitation from left is equal to that relative to excitation from right). In fact, the Lorentz reciprocity theorem is based on the linearity of the electric field and the absence of magnetic materials, as in this case. To break Lorentz reciprocity with these MRs, we need to enter the nonlinear regime, where the refractive index and thus the resonant frequency of the MR varies as a function of the optical intensity inside it. The simplest and most trivial way to get two different transmissions is to make sure that exciting the system in one direction (left, *forward*) couples less light inside the MR than when the system is excited from the other direction (right, *reverse*). To achieve this, it is sufficient to have greater losses in the left bus waveguide than in the right bus waveguide (MR not centered with respect to the bus waveguide). In this way, however, the maximum transmission that can be obtained is reduced due to the presence of this additional loss on the left side of the sample. If a symmetric system is used from the excitation point of view (excitation from both sides couples the same light intensity within the MR), then a simple passive MR cannot break Lorentz reciprocity. The TJMR and even an asymmetric ILMR, on the other hand, can break Lorentz reciprocity by going to the nonlinear regime. In fact, due to their special energy recirculation and non-Hermitianity, they exhibit a higher internal optical intensity when excited from one direction than from the other. In Sec. 2.3.1 we observed an isolation ratio of about 5.5 dB but by designing a TJMR or an asymmetric ILMR in the critical-coupling regime, much greater isolation can be achieved. However, we emphasize the fact that the optical isolator realized using the thermo optic nonlinearity of the system as a function of the electric field is strictly dependent on the input optical intensity.

4.2 Sensing performances

Let us now compare the three MRs from the point of view of their ability to detect a Hermitian perturbation $\delta\beta = \beta_{BS,12} = -\beta^*_{BS,21}$ of the BS. Note that the $\delta\beta$ perturbation changes the spectral shape of the resonances and is thus to a first approximation separable from the simple spectral shift caused, for example, by a change in temperature. To compare the three geometries, we assume that the propagation losses are the same ($\gamma_{\mathrm{ILMR}} = \gamma_{\mathrm{TJMR}} = \gamma_{\mathrm{MR}} = \gamma = 1/4$ a.u.) and that the coupling rates are also the same ($\Gamma_{\mathrm{MR}} = \Gamma_{\mathrm{TJMR}} = \Gamma_{\mathrm{S}} = \Gamma_{\mathrm{L}} = \Gamma_{\mathrm{R}} = \gamma = 1/4$ a.u. and $\beta_{12,\mathrm{TJMR}} = \beta_{12,\mathrm{ILMR}} = \beta_{12} = 1$ a.u.), see Fig. 4.1. Therefore, we consider a symmetric ILMR ($\Gamma_{\mathrm{L}} = \Gamma_{\mathrm{R}}$). Note that with these parameters, the MR is in the most favorable coupling regime, the critical coupling one.

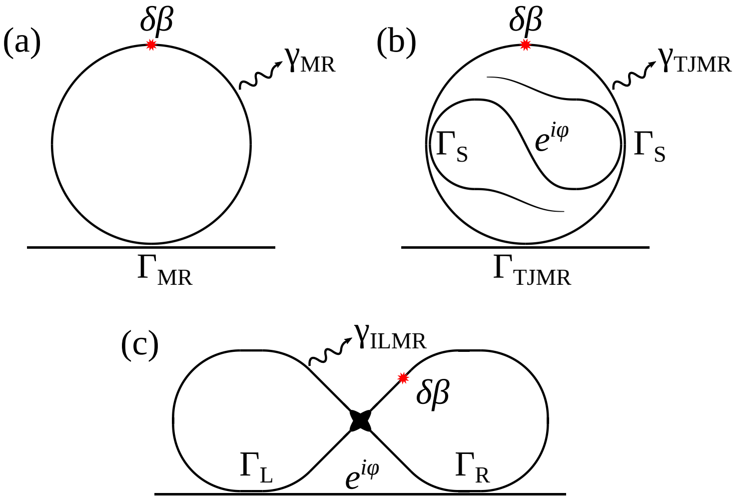

Figure 4.1: Sketch of a microring resonator (a), a TJMR (d), and a ILMR (c).

A very important difference between the MR and the other two structures is that it works at a DP, while the TJMR and the ILMR work at an EP. The former has degenerate eigenvalues and orthogonal eigenvectors, while for the other two both eigenvalues and eigenvectors coalesce. This causes a linear dependence of the eigenvalue splitting as a function of $\delta\beta$ in the case of a MR, while it has a square root dependence in the case of a TJMR and a ILMR, see Fig. 4.2. It is also worth noting that both the TJMR and the ILMR remain at an EP even when the characteristic parameters of the system, such as resonant frequency, propagation losses, or coupling coefficients, change. This means that, like the structures studied in [49, 50, 57], the TJMR and ILMR are on an exceptional surface. Consequently, a large class of unwanted perturbations will move the system along the exceptional surface, from one EP to another [49]. Thus, the TJMR and the ILMR are robust, and only a perturbation that causes backscattering leads to enhanced sensitivity. Equivalently, we can say that a simple MR is on a diabolic surface; in fact, it remains at a DP even if its resonant frequency, propagation losses, and coupling to the bus waveguide vary.

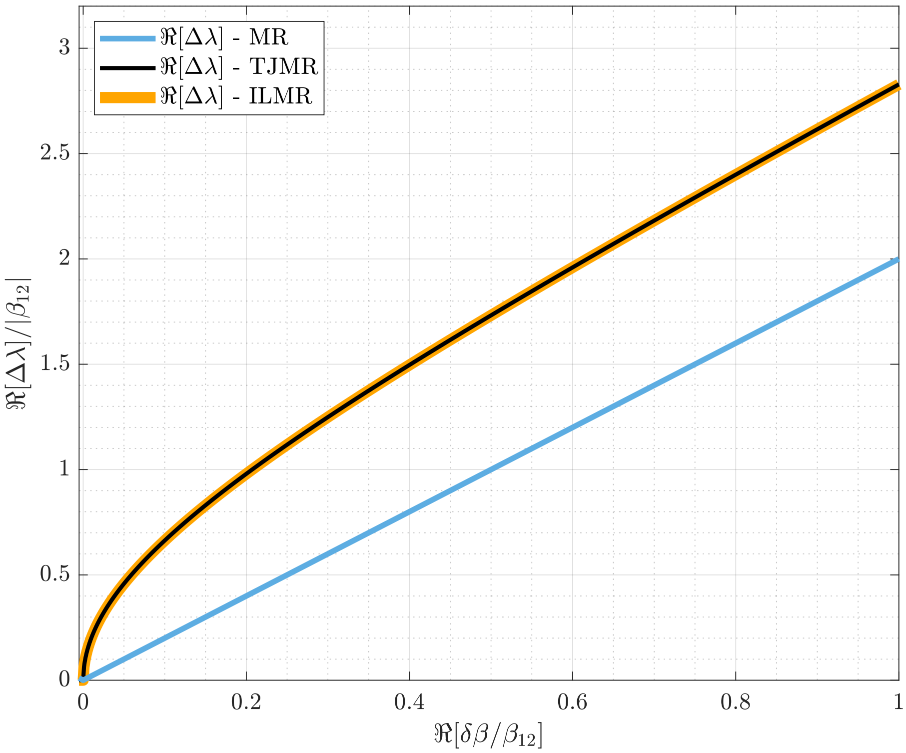

Figure 4.2: Eigenvalues splitting for a MR (light blue curve), a TJMR (black curve) and a ILMR (orange curve), as a function of the Hermitian perturbation $\delta\beta$. The used parameters are: $\gamma_{\mathrm{ILMR}} = \gamma_{\mathrm{TJMR}} = \gamma_{\mathrm{MR}} = \gamma = 1/4$ a.u., $\Gamma_{\mathrm{MR}} = \Gamma_{\mathrm{TJMR}} = \Gamma_{\mathrm{S}} = \Gamma_{\mathrm{L}} = \Gamma_{\mathrm{R}} = \gamma = 1/4$ a.u. and $\beta_{12,\mathrm{TJMR}} = \beta_{12,\mathrm{ILMR}} = \beta_{12} = 1$ a.u..

The Fig. 4.2 shows that the TJMR and ILMR have a higher sensitivity (slope of the curve) than the MR for small perturbations. At high perturbation values, however, the sensitivity of the three structures is equivalent, in fact all three curves converge to the same slope. Nevertheless, the splitting for the TJMR and the ILMR is larger than that found for the MR. We also note that the splitting of the real part of the eigenvalues is the same for the TJMR and the ILMR.

We now compare these three devices by calculating the splitting using the spectral responses (using the positions of the minimum/maximum dips/peaks), see Fig. 4.3.

In Fig. 4.3 the splittings corresponding to the MR, the TJMR and the ILMR are shown in light blue, black and orange. Since by varying the phase φ we have

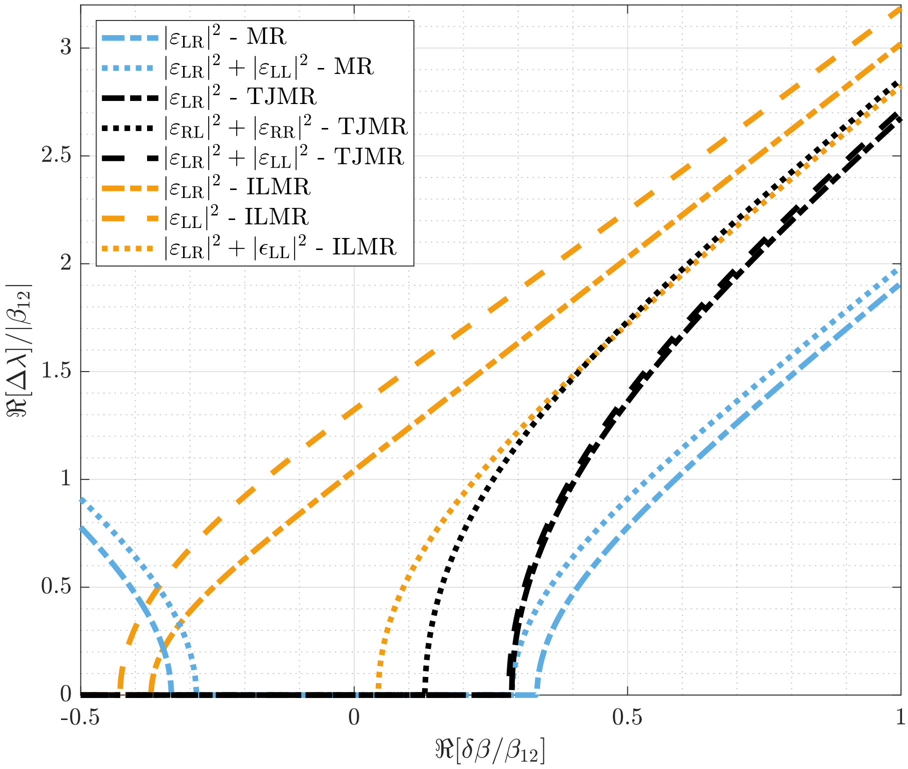

Figure 4.3: Spectral resonance splitting for a MR (light blue curves), a TJMR (black curves) and a ILMR (orange curves), as a function of the Hermitian perturbation $\delta\beta$. The used parameters are: $\gamma_{\mathrm{ILMR}} = \gamma_{\mathrm{TJMR}} = \gamma_{\mathrm{MR}} = \gamma = 1/4$ a.u., $\Gamma_{\mathrm{MR}} = \Gamma_{\mathrm{TJMR}} = \Gamma_{\mathrm{S}} = \Gamma_{\mathrm{L}} = \Gamma_{\mathrm{R}} = \gamma = 1/4$ a.u. and $\beta_{12,\mathrm{TJMR}} = \beta_{12,\mathrm{ILMR}} = \beta_{12} = 1$ a.u..

observed that we can perform an encircling of the EP for both the TJMR and the ILMR, we focus our attention on the region where $\Re[\delta\beta/\beta_{12}] \gtrsim 0$. From Fig. 4.3 it is clear that the ILMR is able to detect smaller perturbations than the TJMR, which in turn is better than the MR. Recall that the regions of insensitivity are given by the inability to observe two distinct dips/peaks in the spectra. This is largely due to the global losses of the system, which spectrally broaden the resonances. This causes all three types of MR to exhibit a nonlinear splitting behavior as a function of $\delta\beta$. Fig. 4.3 shows that by using the sum of the transmission and reflection spectra (dotted lines) it is possible to reduce the region of insensitivity.

Unlike the TJMR and the MR, the ILMR already exhibits transmission or reflection splitting for a zero $\delta\beta$ perturbation. Thus, only the ILMR does not have the insensitivity region. In fact, the splittings relative to $|\varepsilon_{\mathrm{LR}}|^2 = |\varepsilon_{\mathrm{RL}}|^2$ and $|\varepsilon_{\mathrm{LL}}|^2 = |\varepsilon_{\mathrm{RR}}|^2$

of the ILMR for perturbations around zero and larger are linear as a function of $\delta\beta$. This can then be used to remove the region of insensitivity and also for device calibration. We also note that the splitting relative to $|\varepsilon_{LR}|^2 + |\varepsilon_{LL}|^2 = |\varepsilon_{RL}|^2 + |\varepsilon_{RR}|^2$ of the ILMR (dotted orange curve) is the one that most closely matches the ideal splitting of eigenvalues near an EP (orange and black curves in Fig. 4.2). In Sec. 3.3 we saw that to get a perfect match between the splitting of the eigenvalues and that computed using the spectrum of $|\varepsilon_{LR}|^2 + |\varepsilon_{LL}|^2$, we need the ILMR to satisfy the CPA condition.

Let us define the responsivity enhancement as $\Re[\Delta\lambda]/\Re[\Delta\lambda_{MR}]$, i.e. the responsivity with respect to the ideal splitting of the eigenvalues of the MR. Figure 4.4 (a) shows the responsivity enhancement as a function of the perturbation. We see that for $\Re[\delta\beta/\beta_{12}] \simeq 0.1$, using the spectrum $|\varepsilon_{LR}|^2 + |\varepsilon_{LL}|^2$ of the ILMR yields a responsivity that is 2.5 times higher than that of the MR eigenvalues. This result is in agreement with the enhancement factor obtained experimentally in [35]. Furthermore, using the spectra $|\varepsilon_{LR}|^2$ and $|\varepsilon_{LL}|^2$ separately, we observe a 2.5 times larger splitting for $\Re[\delta\beta/\beta_{12}]$ values below about 0.4 [dash-dotted and dashed orange lines in Fig. 4.4 (a)]. If we look at the splitting curves obtained from the MR or the TJMR transmission spectra, we observe a lower responsivity than for ILMR with the same propagation losses.

Figure 4.4 (b) shows the relative sensitivity of the three structures with respect to the sensitivity computed by the splitting of the MR eigenvalues. The sensitivity is computed by the derivative of the splitting as a function of the backscattering perturbation $\delta\beta$. Figure 4.4 (b) shows that the ILMR has a higher sensitivity than the MR, which is about 2.5 times higher for $\Re[\delta\beta/\beta_{12}] \simeq 0.1$ (orange dotted curve, $|\varepsilon_{LR}|^2 + |\varepsilon_{LL}|^2$). Using the spectra of $|\varepsilon_{LR}|^2$ and $|\varepsilon_{LL}|^2$ separately, the sensitivity is almost constant and almost equal to 1 even for very small perturbations, whereas the sensitivity obtained using the MR or TJMR spectra is zero at very small perturbations since the splitting vanishes, see Fig. 4.3.

Although the ILMR has both higher responsivity and a larger sensitivity at small perturbations than the MR and the TJMR, in my thesis I did not investigate how the signal-to-noise ratio behaves in the three different structures [144]. The latter may penalize the ILMR more than a simple MR, partially reducing the advantage of using an ILMR. This aspect needs a dedicated study. In the future, we would like to investigate this experimentally. In particular, we have designed a new integrated sample with different types of Hermitian and non-Hermitian microresonators with integrated scatterers characterized by different backscattering strengths, see red

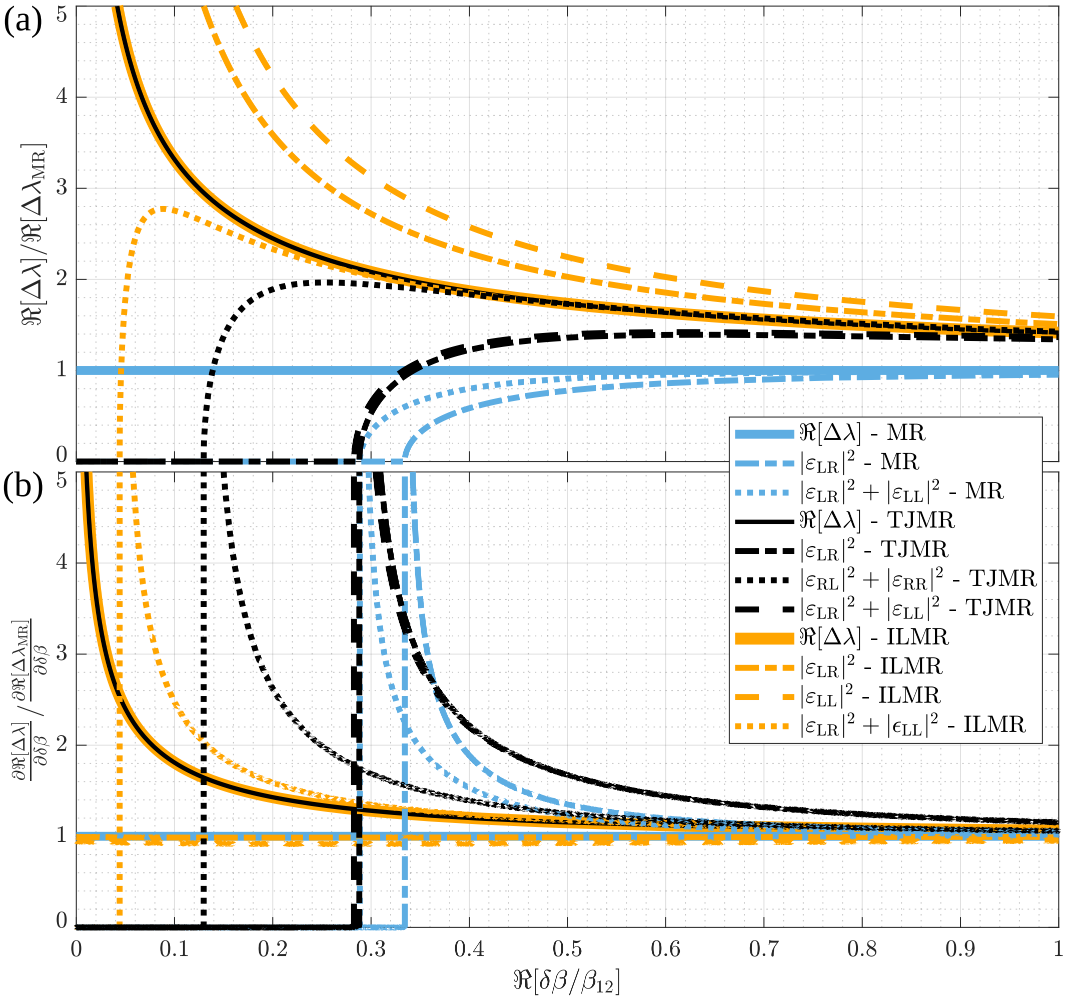

Figure 4.4: (a) Ratio of the splittings shown in Fig. 4.3 with the splitting of the MR eigenvalues as a function of the backscattering perturbation strength $\delta\beta$. (b) Ratio of the derivative of the splittings shown in Fig. 4.3 to that corresponding to the splitting of the MR eigenvalues as a function of $\delta\beta$. The used parameters are: $\gamma_{\rm ILMR} = \gamma_{\rm TJMR} = \gamma_{\rm MR} = \gamma = 1/4$ a.u., $\Gamma_{\rm MR} = \Gamma_{\rm TJMR} = \Gamma_{\rm S} = \Gamma_{\rm L} = \Gamma_{\rm R} = \gamma = 1/4$ a.u. and $\beta_{12,\rm TJMR} = \beta_{12,\rm ILMR} = \beta_{12} = 1$ a.u.. In this figure the conditions $\Im[\delta\beta/\beta_{12}] = 0$ and $\delta\beta = \beta_{\rm Bs,12} = -\beta^*_{\rm Bs,21}$ are used. The solid lines represent eigenvalues, while the dashed, dotted and dash-dotted lines represent experimentally measurable quantities. The light blue curves correspond to the MR, the black ones to the TJMR and the orange one to the ILMR.

boxes in Fig. A.3 in Appendix A.

Instead, comparing the structures analyzed here with those found in the literature that works at an EP, for example a SiO_2 microtoroid cavity with two silica nanotips [35], we observe that in this case it is very difficult to align β_{12} with $\delta\beta$, which leads to a very complicated use of these devices. Instead, for the TJMR, the ILMR and the structures reported in [49, 50, 57], it is sufficient to vary the phase φ using an integrated phase shifter to maximize the real splitting of the eigenvalues. However, it must be said that whispering gallery mode microresonators have the possibility of having higher Q (lower losses) than integrated MRs, and consequently the sensitivity of these devices will be higher.

A final comment concerns the role of the crossing in the ILMR, which is a critical element of the proposed geometry. If the crossing losses predominate over the other losses, the efficiency of the square root trend to detect small perturbations would decrease, but the linear trend still provides a way to detect the perturbation. This is another advantage of the ILMR that makes it robust to imperfections.

In conclusion, the ILMR seems to have potential as a sensor of a BS perturbation. In addition, the fact that the ILMR has both a linear and a square-root trend, can be both symmetric and asymmetric, and has the possibility of having very peculiar spectral responses is, in my opinion, one of the strong points of the geometry which can be used for cutting-edge applications.

Chapter 5

Matrix of Hermitian and non-Hermitian microresonators

Few works in the literature report on the possibility of using appropriately coupled resonator arrays to realize Hamiltonians corresponding to the quantum spin Hall effect [108, 187, 188, 69]. By creating this special configuration, topological edge states are created that are protected from local defects. These topological edge states have also been studied to realize topological laser insulators that can have higher efficiency and narrower bandwidth than those with the usual cavities [188, 69].

Therefore, we studied how our devices can be used to generate complex Hamiltonians or to generate synthetic magnetic fields. We also want to study in more detail what happens when the nodes of the array (MRs sites) are TJMRs. In fact, the TJMR has asymmetric responses and can therefore be used to break the symmetry between the two CW and CCW modes even in a topological structure [69].

In the following, I will briefly describe the basis for the construction of these arrays of MRs. In order to study these structures both theoretically and experimentally, we start with simple structures, characterized by few MRs, and then proceed to more complex structures, characterized by the generation of the synthetic magnetic field. In this way, we will also be able to study the limitations imposed by fabrication errors and find a way to compensate for them.

In Fig. 5.1 the key elements of a MRs structure with a synthetic magnetic field are given [108, 187, 188, 69]. We first distinguish two different types of MRs, the site MRs and the link MRs. The former are the main resonators characterized by two

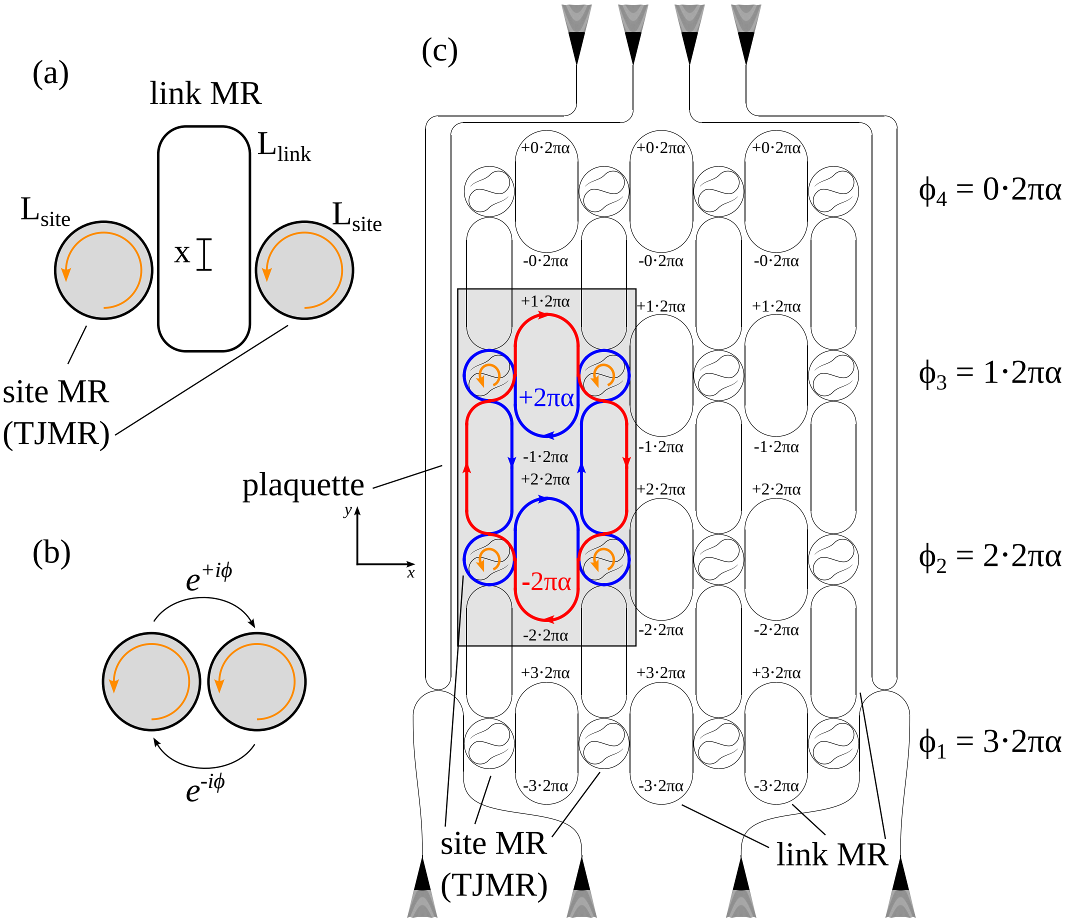

Figure 5.1: Panel (a) shows the scheme of coupling between site MRs using a link MR. Panel (b) highlights the asymmetric hopping phase. Panel (c) shows the design of the 4 × 4 TJMRs matrix. All asymmetric hopping phases and the composition of a plaquette are also shown in panel (c).

counterpropagating modes, the CCW and the CW. These can also be either ring microresonators or even TJMRs and are ideally thought to be identical. Instead, the link MRs are used to link the site MRs and play a key role in implementing the asymmetric hopping phase. The hopping phase is defined as the phase accumulated by an optical signal which propagates between two site MRs. In order to use the link MR to insert a hopping phase, it should be out of resonance with respect to the site MRs. We define L_{site} the perimeter of the site MR and L_{link} the perimeter of the link MR. We also connect the two perimeters as follows:

$$L_{\text{link}} = nL_{\text{site}} + \psi \frac{\lambda_{\text{res}}}{2\pi n_{\text{eff}}}, \quad \text{with} \quad n \in \mathbb{N}^+ , \tag{5.1}$$

where λ_{res} is the resonance wavelength of the MR site, for example 1550 nm. To impose the off-resonance condition of the link MR, we can for example use $n = [1, 2]$ and $\psi = \pi$. Instead, to have an asymmetric hopping phase by moving from the left to the right site MR and vice versa, we shift the link MR vertically by x, see Fig. 5.1 (a). As a result, the hopping phase is equal to

$$\phi = \frac{4\pi n_{\text{eff}}}{\lambda_{\text{res}}} x . \tag{5.2}$$

As shown in Fig. 5.1 (b), this hopping phase is asymmetric [108, 109, 187].

The next step is to create a two-dimensional (2D) array of MRs to implement a system that can be described by a Hamiltonian for charged bosons on a square lattice (tight-binding), but with the addition of a perpendicular, pseudo-spin-dependent effective uniform magnetic field [108]. To do this, we need to build the basic structure consisting of four site MRs and four link MRs. We call this structure a plaquette, see Fig. 5.1 (c). The link MRs responsible for tunneling in y direction are symmetrically positioned (zero hopping phase $\phi_y = 0$). In the x direction, the MRs links are positioned asymmetrically to obtain an asymmetric hopping phase. Furthermore, as shown in Fig. 5.1 (c), each row presents a different asymmetric hopping phase. In particular, two consecutive rows show a difference between the two hopping phases equal to $\phi_i - \phi_{i+1} = 2\pi\alpha$. Thus, if one moves counterclockwise (blue path), the field gains a phase of $+2\pi\alpha$, while if one moves clockwise (red path), the field gains a phase of $-2\pi\alpha$, as shown in Fig. 5.1 (c). α is the quanta of magnetic flux penetrating each plaquette [108, 189, 190]. Note that if instead we look at the CW mode of the site MRs, then the signs of the two phases are the opposite. To construct a larger matrix and thus be able to observe the topological edge state, it is sufficient to concatenate the plaquettes as shown in Fig. 5.1 (c). In particular, by changing the synthetic magnetic field, which is set by the parameter α, any finite lattice shows bulk and edge bands. The former are organized in the Hofstadter butterfly [189] and the latter are located in the gaps of the bulk dispersion [187, 108]. To study topologically protected edge modes, $\alpha = 1/4$ is usually used, as in [108]. In [108, 109, 69, 187] the authors show that this type of topological structure can have topological edge states that are protected against defects also present at the edges of the structure. This makes the study of this type of structure interesting for different applications, such as lasing [69].

To study this physics, we designed the various structures shown in Tabs. 5.1, 5.2 and 5.3 (the design of the whole chip is shown in Fig. A.1 of Appendix A). Tables 5.1, 5.2 and 5.3 refer to structures with 2 × 1, 2 × 2 and 4 × 4 site MRs, respectively, see Figs. 5.2 (a), 5.2 (b) and 5.1 (c). The S-bend parameter, if equal to 1, means that the site MRs are TJMRs [as shown in Figs. 5.2 (a1), 5.2 (b1) and 5.1 (c)], while if it is equal to 0 the S-shaped WG inside the TJMRs is cut [as shown in Fig. 5.2 (a2), (b2)]. The TJMR with the cut S-shaped WG is equivalent to a normal MR, but it has the same total losses (γ_{tot}) as the TJMR, which makes it easier to compare the considered structures.

2×1	n	ψ	ϕ	S-bend
1	1	0	0	1
2	2	0	0	1
3	2	$\pi/4$	0	1
4	2	$\pi/2$	0	1
5	1	π	0	1
6	2	π	0	1
7	2	π	0	0
8	2	$3\pi/2$	0	1

Table 5.1: Parameters of the TJMRs matrices 2 × 1, see Fig. 5.2 (a), Eq. (5.1) and Eq. (5.2).

From the Tabs. 5.1, 5.2 and 5.3 it can be seen that we chose to study structures characterized by link MRs in resonance or off-resonance with the site MRs, and that we used $\alpha = 1/4$ for the 4 × 4 structure, while for the single plaquette we listed more cases of α.

Even though the smaller structures (see Fig. 5.2) will not be able to exhibit the topological edge states because the number of site MRs is too small, we included them to study step by step each single part of the larger structure and at the same

2×2	n	ψ	ϕ_1	ϕ_2	S-bend
1	2	0	0	0	1
2	2	π	0	0	1
3	2	π	$\pi/3$	0	1
4	2	π	$\pi/2$	0	0
5	2	π	$\pi/2$	0	1

Table 5.2: Parameters of the TJMRs matrices 2×2, see Fig. 5.2 (b), Eq. (5.1) and Eq. (5.2).

4×4	n	ψ	ϕ_1	ϕ_2	ϕ_3	ϕ_4	S-bend
1	2	π	$3\pi/2$	π	$\pi/2$	0	1

Table 5.3: Parameters of the TJMRs matrix 4×4, see Fig. 5.1, Eq. (5.1) and Eq. (5.2).

time to study the non-idealities given by the fabrication (site MRs with different resonances, BS, lengths and displacements of the link MRs that are incorrect). The idea is to study these structures first in the linear regime and then move to the nonlinear regime. In addition, we want to observe if going to the nonlinear regime can eliminate/correct any differences between the resonances of the site MRs.

Our study of these structures is still in its very early stages. In the following, I will present some simulations for 2×1 structures [Fig. 5.2 (a1)] in the ideal case where we have zero BS and all parameters are as designed.

In Fig. 5.2 (a), the numbers identify the input/output ports of the structure. We call $|t_{io}|^2$ the intensity spectrum observed at port number o when the structure is excited from port i.

Using the TMM or TCMT, we can derive the transmission spectra of the 2×1 matrix, similar to what was done in previous chapters. Figure 5.3 reports the spectral responses of the 2×1 structure when the link MR is in resonance with the two site TJMRs ($\psi = 0$, S-bend$= 1$). When the three MRs have the same resonance $\lambda_{\text{res}} = 1550$ nm, they exhibit a strong Hermitian coupling. This strong coupling between the three modes of the system causes three dips/peaks in the spectral responses. Note from Fig. 5.2 (a) that the S-shaped WG does not couple the counterpropagating modes of the TJMR when the system is excited by ports 1 and 4. In fact, Fig. 5.3 shows that in these two cases the non-zero spectra are only those corresponding to the port on the same side of the structure and the symmetrically opposite one [blue and red curves, for excitation by 1(4): ports 2(3) and 3(2)]. In contrast, for the other two excitations (excitation from port 2 and

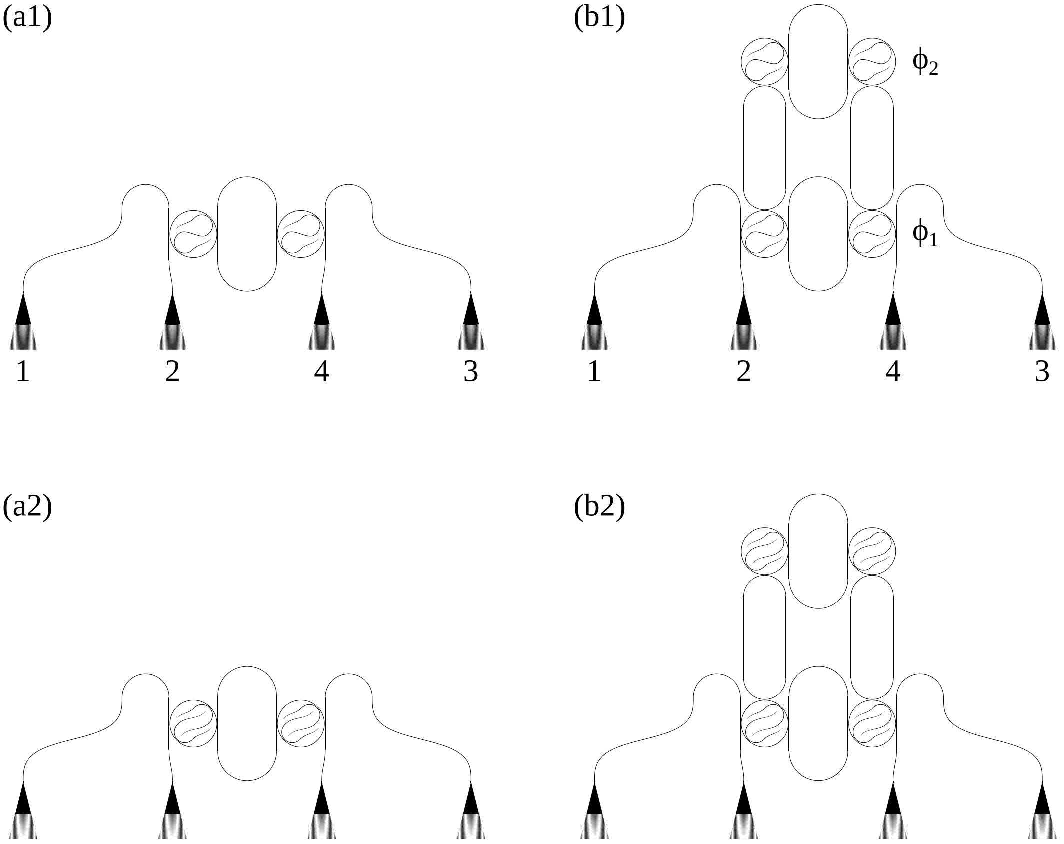

Figure 5.2: The design of the 2 × 1 (a) and 2 × 2 (b) TJMRs matrices. In panels (a1) and (b1) the S-shaped WG of the site TJMRs are not cut, while in (a2) and (b2) are cut. The numbers 1, 2, 3 and 4 identify the input/output ports of the structures. ϕ_1 and ϕ_2 are the asymmetric hopping phases corresponding to the two different rows of link MRs.

port 3), all the spectra are different from zero, because the S-shaped WG couples the counterpropagating modes of the TJMR. Since the structure is symmetric, symmetry is also present in the spectra shown in Fig. 5.3.

If instead the link MR is off-resonance with respect to the site TJMRs ($\psi = \pi$), then we no longer have the strong coupling between the three MRs and thus a single dip in transmission is observed (blue curves in Fig. 5.4). Here with $\psi = \pi$ the spectral peak of $|t_{13}|^2$, $|t_{24}|^2$, $|t_{31}|^2$ and $|t_{42}|^2$ is smaller than in the previous case where the three MRs had the same resonant frequency. Also here we can observe the symmetry of the spectra. Furthermore, Fig. 5.4 shows that the S-shaped WG is only relevant for the spectra $|t_{22}|^2$, $|t_{33}|^2$, $|t_{23}|^2$ and $|t_{32}|^2$. In fact, when the system is excited by port 1 or 4, the S-shaped WG contributes only to the losses (γ_{tot}).

This discussion is very preliminary since measurements are still in progress. Our

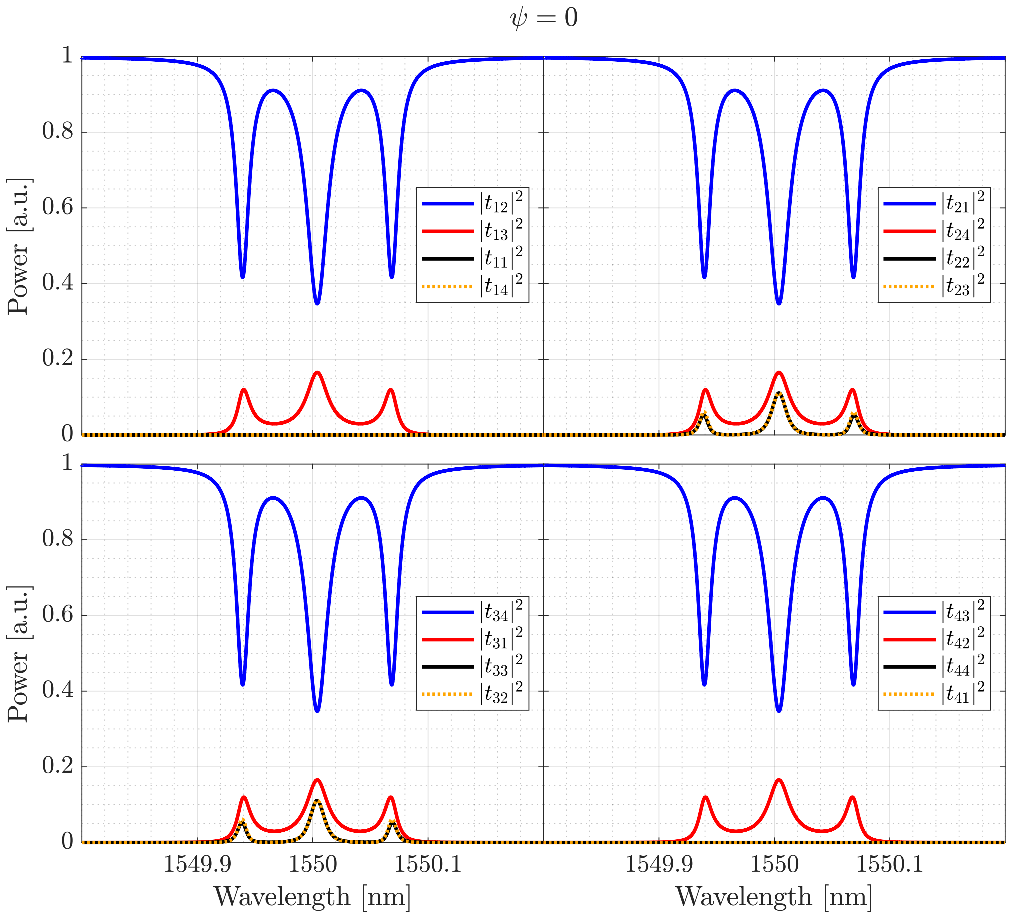

Figure 5.3: Theoretical spectral responses of a TJMRs matrix 2×1 with the link MR in resonance with the two site MRs ($\psi = 0$).

goal, before moving to topological effects, will be to model the system taking into account the fabrication errors and estimate them from experimental measurements and find a way to reduce or bypass the possible problems.

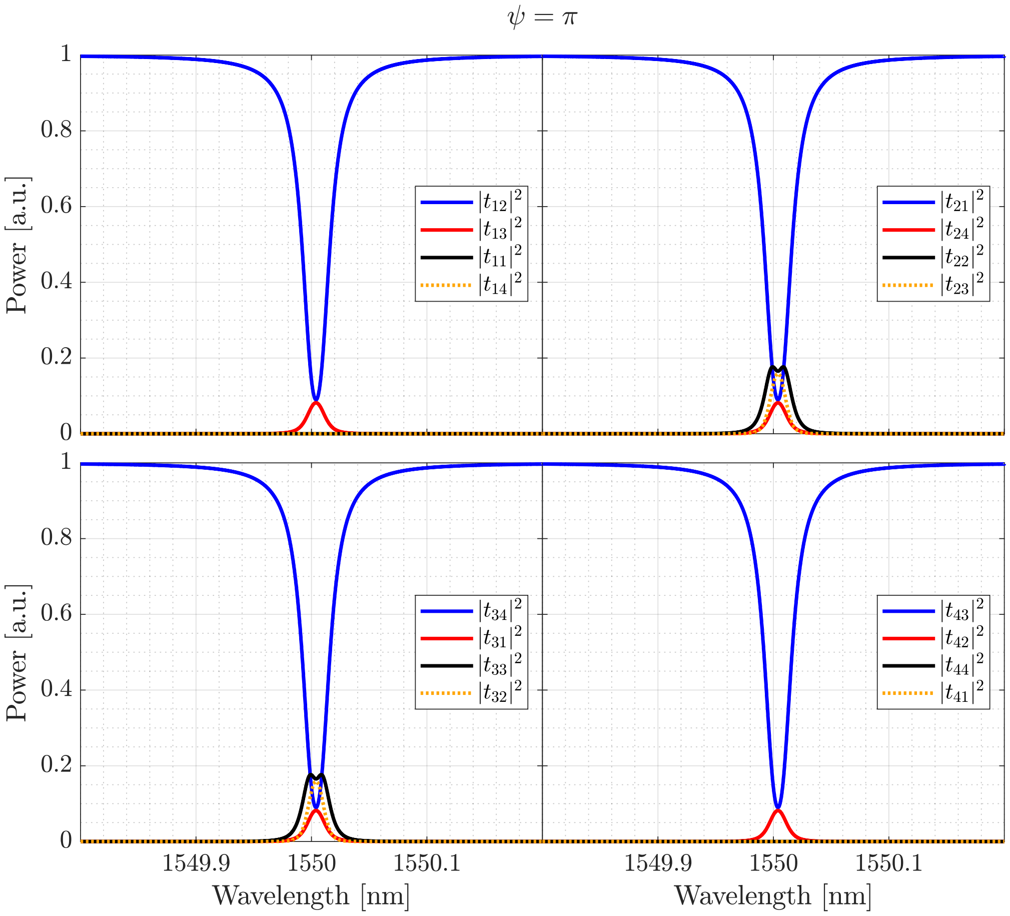

Figure 5.4: Theoretical spectral responses of a TJMRs matrix 2 × 1 with the link MR in off-resonance with the two site MRs ($\psi = \pi$).

Conclusions and Perspectives

In this thesis, I presented three different types of integrated microresonators: a microring resonator (MR), the Taiji Microresonator (TJMR) and the Infinity-Loop Microresonator (ILMR). They have been modeled by using either the Temporal Coupled Mode Theory (TCMT) or the Transfer Matrix Method (TMM). For all three resonant structures, the characteristic parameters of these two models were related. In this way, it is possible to design the Microresonators (MRs) using the advantages of both models. Although the TCMT is easier to handle and interpret, it describes only a single resonance and does not have the dimensions of the system within it. The formulas derived with TMM describe the complete spectral response of the system (multiple resonances) and are closely related to the system dimensions and the transmission and coupling coefficients that can be derived by simulation. At the same time, these formulas are more difficult to interpret and cannot be used to calculate the time response of a MR. Having the relation between the coefficients of the two models, allows to use the most appropriate one for the specific scope.

In addition to the study of the three ideal MRs, the backscattering (BS) has been introduced. The BS couples the counterpropagating modes of the MR, causing a splitting of both the eigenvalues of the system and its resonances. Indeed, the BS is an element that must be taken into consideration when designing integrated optical MRs with high Quality Factor (Q). In fact, as we have reported, by increasing the ideal Q of the MR, the BS mainly due to the waveguide (WG) surface-wall roughness becomes relevant. In our experiments with silicon (Si) structures, the measured BS coefficients (β) were found to be between 2 GHz and 20 GHz.

In my thesis, I introduced a new excitation method capable of exciting one of the supermodes of the MR at a time: the interferometric excitation. The interferometric excitation consists of a simultaneous and coherent excitation of the system from both sides. With this technique, it is possible to excite the proper combination of clockwise (CW) and counterclockwise (CCW) modes corresponding to one of the supermodes of the system by using a correct relationship between the amplitudes and phases of the excitation fields. Consequently, even in the presence of a non-Hermitian BS, it is possible to transform the doublet in transmission into a single Lorentzian, from which it is straightforward to calculate the real and imaginary parts of the eigenvalue corresponding to the excited supermode. In fact, its position corresponds to the real part of the eigenvalue, while its Full Width at Half Maximum (FWHM) is twice the absolute value of the eigenvalue's imaginary part. It is important to emphasize that in the non-Hermitian case, where the two input fields must have two different intensities, the required ratio between the excitation fields is easily measured by a single-side excitation measure of the two system reflections. In this way, the only parameter to be varied is the phase between the two fields. By using the interferometric excitation, it is also possible to increase the Q of the MR. In fact, one is able to remove the doublet caused, for example, by the BS. In Sec. 1.4 I have also shown that the interferometric method works not only in the stationary regime but also in the transient regime, i.e. when studying the charge and discharge of the MR (time response).

In the dissertation, I used TCMT to show that a normal MR is at a Diabolic Point (DP) while the TJMR is at an Exceptional Point (EP). The TJMR working at an EP has some very interesting features. First, the TJMR is chiral, i.e. one of its modes dominates over the other (in our case the CCW), in fact, the embedded S-shaped WG only transfers energy from the CW mode to the CCW one and not vice versa. For this reason, the TJMR is a unidirectional reflector at resonance, i.e. it exhibits a spectral peak in reflection only when excited from one side and not from the other side. We have also shown, both theoretically and experimentally, that in the nonlinear regime a TJMR breaks the Lorentz reciprocity. In fact, the transmission depends on the excitation direction of the system. This is a first step towards the creation of a passive integrated optical isolator without magnetic materials. The disadvantage of this technique is that the non-reciprocity of the transmission depends strongly on the input power, so that a signal of low intensity has the same transmission. One way to partially solve this problem is to use two different lasers, one high power and one low power, with a wavelength corresponding to a different resonance, so that the signal from the pump can be filtered. In this case, even the low-power signal, which is collinear with the pump, is affected by the transmission non-reciprocity.

In this work a new MR was also studied, which we called Infinity-Loop Microresonator (ILMR). The ILMR, which is characterized by an infinity-shaped WG coupled twice to a bus waveguide, is, like the TJMR, at an EP. The ILMR, which always works at an EP, also has some interesting features. Like the TJMR, it can be a unidirectional reflector, but thanks to the possibility of changing the two couplings with the bus waveguide (Γ_L and Γ_R), it is able to present a variety of spectral shapes while always remaining at an EP. In fact, the geometrically symmetric ILMR ($\Gamma_L = \Gamma_R$) has equal reflections and exhibits splitting in transmission, even if, being at an EP, its eigenvalues and eigenvectors coalesce. This splitting is in fact given by the interference between the fields leaving the ILMR and those present in the bus waveguide. In fact, we have shown that from the sum of the intensities in transmission and in reflection we are able to observe the resonance of the system, going from a doublet to a single dip. In addition, the condition for obtaining the Coherent Perfect Absorption (CPA) for the ILMR has been derived. Under this condition, and when the ILMR is geometrically symmetric, there is a quartic behavior as a function of detuning in the absorption spectrum of the system. We also showed that the geometrically asymmetric ILMR has a different total internal intensity when it is excited from left or from right. This implies that even the ILMR in the nonlinear regime is able to break the Lorentz reciprocity.

Perhaps the most interesting study, which I reported in my thesis, is the use of the three devices as sensors of a Hermitian perturbation of the BS ($\delta\beta$). In fact, the normal MR at a DP presents a linear dependence of the eigenvalue splitting as a function of $\delta\beta$, while both the TJMR and the ILMR at an EP present a square root dependence of the eigenvalue splitting as a function of a small $\delta\beta$ perturbation, obtaining a higher responsivity and sensitivity. I studied the Riemann surfaces not only of the eigenvalues but also of the spectra (the observables of the system). I demonstrated that the overlap caused by the imaginary part of the eigenvalues which spectrally broadens the resonances masks spectrally the resonance splitting. To reduce this region of insensitivity of the MRs, I observed that the sum of the intensities in transmission and reflection can be used. Using this method, it is observed that the spectral splitting for the symmetric ILMR more closely follows the splitting of the eigenvalues, presenting a much smaller region of insensitivity than that observed for the other two structures. Furthermore, since the transmission and reflection of the ILMR, taken individually, have a non-zero split even at $\delta\beta = 0$, and their trend is linear as a function of the $\delta\beta$ perturbation, using the ILMR not only makes it possible to calibrate the sensor more rigorously, but also to completely remove its region of insensitivity. I have also shown that using a simple phase shifter placed on the S-shaped WG (for the TJMR) or on the part of the bus waveguide between the two lobes of the ILMR, it is possible to encircle the EP and thus position the MRs at the point where the two Riemann surfaces are furthest apart (largest splitting). In this way, we can maximize the responsivity and the sensitivity of the sensor. In the future, it will be interesting to study whether dynamic encircling around the EP can be performed using an integrated phase shifter and to see if there are any applications that can take advantage of this phenomenon.

In my thesis I showed that both the TJMR and the ILMR are on an exceptional surface; in fact, they remain at an EP even if the characteristic parameters of the system (such as the resonant frequency, the propagation losses, and the coupling coefficients) are changed. This means that a large class of unwanted perturbations will move the system along the exceptional surface, from one EP to another [49]. Thus, the TJMR and the ILMR are robust and only a perturbation that causes backscattering leads to enhanced sensitivity.

A future perspective is, therefore, to use the ILMR as a sensor of a local perturbation, such as the one caused by a particle near the WG, as done in [35, 44, 45, 46, 32, 47, 48, 49, 50] with other types of MRs. Unlike traditional sensors, which exploit the change in refractive index caused by the presence of a substance or a particle, here we use the coupling between counterpropagating modes generated by the perturbation. This means that since we are interested in the spectral shape of the resonance and not its position in the spectrum, these types of sensors, are independent of temperature. To move further in this direction, we have designed different Hermitian and non-Hermitian integrated MRs, characterized by scatterers of different sizes, in order to verify experimentally the higher sensitivity of the structures operating at an EP.

As we have seen, the interferometric excitation method is able to excite the supermodes individually, allowing us to increase the Q of the MR and to more clearly determine the eigenvalues of the system. At present, this technique has been developed for two modes, but it may be useful to extend this excitation method to a system with n number of modes/levels, so that the eigenvalues of more complex systems can be measured.

As presented in Ch. 5, another perspective is to use matrices of Hermitian or non-Hermitian MRs to create a global Hamiltonian of the system corresponding to a physical phenomenon such as the quantum spin Hall effect [108, 109, 69, 187].

Finally, the study of the TJMR and the ILMR in the nonlinear regime may lead to interesting applications based on both the chirality of these structures and, for example, the four-wave mixing [80].

Publications

Research Articles

[158] Claudio Castellan, Riccardo Franchi, Stefano Biasi, Martino Bernard, Mher Ghulinyan, and Lorenzo Pavesi. Field-Induced Nonlinearities in Silicon Waveguides Embedded in Lateral p-n Junctions. *Frontiers in Physics*, 7:104, July 2019. `doi:10.3389/fphy.2019.00104`.

[191] Riccardo Franchi, Claudio Castellan, Mher Ghulinyan, and Lorenzo Pavesi. Second-harmonic generation in periodically poled silicon waveguides with lateral p-i-n junctions. *Optics Letters*, 45(12):3188, June 2020. Number: 12. `doi:10.1364/OL.391988`.

[77] Alberto Muñoz de las Heras, Riccardo Franchi, Stefano Biasi, Mher Ghulinyan, Lorenzo Pavesi, and Iacopo Carusotto. Nonlinearity-Induced Reciprocity Breaking in a Single Nonmagnetic Taiji Resonator. *Physical Review Applied*, 15(5):054044, May 2021. Number: 5. `doi:10.1103/PhysRevApplied.15.054044`.

[78] Riccardo Franchi, Stefano Biasi, Alberto Muñoz de las Heras, Mher Ghulinyan, Iacopo Carusotto, and Lorenzo Pavesi. Influence of the bus waveguide on the linear and nonlinear response of a taiji microresonator. *Optics Express*, 29(19):29615, September 2021. Number: 19. `doi:10.1364/OE.434239`.

[102] Stefano Biasi, Riccardo Franchi, Filippo Mione, and Lorenzo Pavesi. Interferometric method to estimate the eigenvalues of a non-Hermitian two-level optical system. *Photonics Research*, 10(4):1134, April 2022. `doi:10.1364/PRJ.450402`.

[103] Stefano Biasi, Riccardo Franchi, and Lorenzo Pavesi. Interferometric cavity ringdown technique for ultrahigh Q-factor microresonators. *Optics Letters*, 47(16):4083–4086, August 2022. Number: 16 Publisher: Optica Publishing Group. `doi:10.1364/OL.467590`.

[159] Stefano Biasi, Riccardo Franchi, Davide Bazzanella, and Lorenzo Pavesi. On the effect of the thermal cross-talk in a photonic feed-forward neural network based on silicon microresonators. *Frontiers in Physics*, 10, 2022. `doi:10.3389/fphy.2022.1093191`.

Preprints

[93] Riccardo Franchi, Stefano Biasi, Diego Piciocchi, and Lorenzo Pavesi. The infinity-loop microresonator: a new integrated photonic structure working at an exceptional surface. *Accepted in APL Photonics*, 2023. arXiv:2302.01108 [physics]. `doi:10.48550/arXiv.2302.01108`.

[192] Stefano Biasi, Riccardo Franchi, Lorenzo Cerini, and Lorenzo Pavesi. An array of microresonators as a Photonic Extreme Learning Machine. *Under peer review in APL Photonics*, May 2023. arXiv:2305.03066 [physics]. `doi:10.48550/arXiv.2305.03066`.

Conference Papers and Proceedings

[193] Riccardo Franchi, Chiara Vecchi, Mher Ghulinyan, and Lorenzo Pavesi. Electric Field Induced Second Harmonic Generation In Silicon Waveguides: the role of the disorder. In *2021 Conference on Lasers and Electro-Optics Europe & European Quantum Electronics Conference (CLEO/Europe-EQEC)*, pages 1–1, Munich, Germany, June 2021. IEEE. `doi:10.1109/CLEO/Europe-EQEC52157.2021.9541919`.

[141] R. Franchi, A. Muñoz de las Heras, S. Biasi, M. Ghulinyan, I. Carusotto, and L. Pavesi. Role of the bus waveguide in the nonlinear reciprocity breaking in a Taiji microresonator. In *2021 Conference on Lasers and Electro-Optics Europe and European Quantum Electronics Conference (2021), paper ec_6_3*, page ec_6_3. Optica Publishing Group, June 2021. URL: `https://opg.optica.org/abstract.cfm?uri=EQEC-2021-ec_6_3`.

[47] Riccardo Franchi, Stefano Biasi, Filippo Mione, and Lorenzo Pavesi. On the response of the Taiji microresonator against small perturbation of the counter propagating mode. In Sonia M. García-Blanco and Pavel Cheben, editors, *Integrated Optics: Devices, Materials, and Technologies XXVI*, page 13, San Francisco, United States, March 2022. SPIE. `doi:10.1117/12.2608157`.

Appendix A

Chips design

We designed two integrated chips, both with devices related to the study of non-Hermitian and Hermitian systems and other integrated circuits related to the projects BACKUP (`https://r1.unitn.it/back-up/`) and Photonic Extreme Learning Machine (PELM, `https://r1.unitn.it/pelm/`). The first chip, Fig. A.1, was designed at the end of 2020 and then realized by IMEC/Europractice facility within a multi-project wafer program, which delivered it to us at the end of 2021. The second chip, Fig. A.2 and Fig. A.3, was designed at the end of 2022. This second chip will be manufactured at the AMF facility (Singapore) within a multi-project wafer program and should reach us in mid-2023. We will call the first chip Mask2020 and the second chip Mask2022. Both designs were implemented using the nazca python library [194].

Figure A.1 shows the design of the Mask2020 chip. In Mask2020 we have included TJMRs (red boxes in Fig. A.1) with different couplings, some to achieve a very efficient unidirectional reflector [see Fig. 2.17 (a1)-(b1)], others to achieve the maximum internal intensity difference in the TJMRs when excited from left or right, so that there is a very pronounced Lorentz reciprocity break when used in the nonlinear regime. The geometry used to create the TJMRs is shown in Fig. 2.16. Scattered in the lower right corner of Fig. A.1, the four ILMRs are also visible (blue boxes). The spectra of these four ILMRs are shown in Fig. 3.9. The two types of designed ILMR geometries are shown in Fig. 3.8. In addition, various test structures (mainly placed on the left and right edges of the chip, cyan boxes in Fig. A.1) are designed, which are needed to calculate the propagation losses in the curved waveguides, the transmission, reflection and crosstalk coefficients of the crossings,

Figure A.1: Design of the Mask2020 chip. Red boxes highlight the TJMRs, the orange boxes the TJMRs matrices, the blue ones the ILMRs, the black ones the PELM structures, the fuchsia ones the microring resonators, the side-coupled integrated sequences of resonators (SCISSORs) and coupled resonators optical waveguides (CROWs) and lastly the cyan boxes highlight the test structures.

the reflection coefficient of the tapering of the WG, the coupling coefficients and the fiber-grating coupling losses. In this chip, mainly at the bottom center and in the middle (orange boxes), there are also the matrices of TJMRs described in Ch. 5, which will be used for an initial study of multi-MR structures and later to study the topological edge states. Note that some structures are designed to be coupled with one fiber on the left and another on the right, while others are designed to be coupled with an array of fibers, so that all gratings are oriented in the same direction and are 127 μm spaced. Using the fiber array, it is possible to couple several fibers simultaneously, and using it with the TJMRs matrices (see Fig. 5.2), for example, will allow us to measure all the combinations of transmissions reported in Fig. 5.3. We have also included simple MRs, side-coupled integrated sequences of resonators (SCISSORs) and coupled resonators optical waveguides (CROWs) [195], which can also be heated by an integrated resistor to change their resonant frequency (see fuchsia boxes in Fig. A.1). Finally, we have also included arrays of MRs coupled with WGs to realize a Photonic Extreme Learning Machine (see black/gray boxes in Fig. A.1) [196, 192]. This particular structure consists of a single input that is equally divided into four different paths whose optical intensity is varied by Mach Zhender Interferometers (MZIs) and phase shifters. This first part is used to insert the input with at most four features into our network. The network consists of 18 MRs whose internal intensity is measured by an infrared camera. The presence of the randomness of the perimeters of these 18 MRs (caused by the manufacturing errors), the various interferences established within this structure and the square absolute value given by the detector (nonlinear response of the camera), make this device capable of solving some nonlinear tasks. In [192] we have shown that by using this structure we are able, for example, to perform the logical operations (AND, OR and XOR) and to improve the classification of the three species of Iris flowers [197, 198] compared to a linear classifier. Using this structure, we were also able to see that the variation between the perimeters of the 18 MRs ($L \simeq 196.5$ μm) is about 25–100 nm and therefore $\Delta L/L \simeq 1\text{–}5\times10^{-4}$. This will cause the different resonance frequencies of the MRs to be taken into account in the TJMRs matrices reported in Ch. 5.

Figure A.2 shows the design of the Mask2022 chip. In the design of Mask2022 we have implemented new Hermitian and non-Hermitian MRs (red boxes in Fig. A.3). This time we also added the phase shifter inside the TJMRs and ILMRs to realize the EP encircling. In addition, in this new design, we have taken into account that the surface roughness of the WGs causes a BS of about 10–20 GHz (as shown

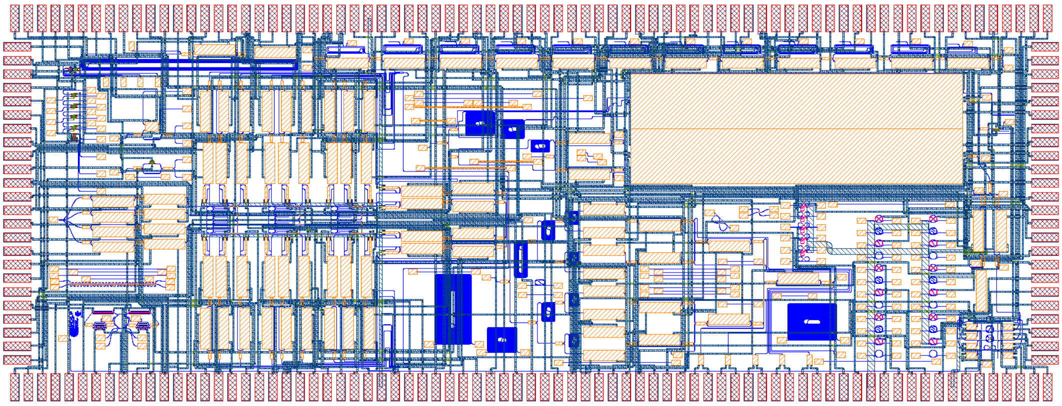

Figure A.2: Design of the Mask2022 chip.

in Fig. 2.18) and have therefore adjusted the coupling coefficients so that the BS is not dominant. In this design, we also included integrated scatterers within the different types of MRs to experimentally compare the sensitivity in detecting a BS perturbation (similar to what is reported in Fig. 4.3).

In the Mask2022 design, we also included a new version of the structure used to make Photonic Extreme Learning Machine (PELM), which also implemented integrated detectors (black/gray boxes in Fig. A.3). In this chip there are also structures for the BACKUP and ALPI (`https://r1.unitn.it/back-up/projects/projects/erc-poc-alpi-project/`) projects, which I have only marginally dealt with (fuchsia box in Fig. A.3). Finally, there are test structures to calculate e.g. propagation and insertion losses (cyan boxes).

As can be seen in Figure A.2, in Mask2022 many metal connections were made to connect the pins of the phase shifters, integrated detectors, and pn junctions to the PADs needed to realize the wire bounding. Given the number of connections to realize (more than 300 pins to connect) and the number of regions to avoid (all the gratings, phase shifters, detectors, and pn junctions), I developed a package in Python that would autonomously trace all the necessary electrical connections in an optimized manner. This program takes into account the minimum distances between layers from the design created with nazca, imports the regions where the metal cannot pass, imports the coordinates of the pins to be connected, and then uses two different metals to connect the pins to the closest metal PADs. In fact, there is an option in the program to use the two different metals that both AMF and IMEC use to create metal path crossings. In addition, it is possible to distinguish the pins that will later be connected to ground (GND) from the others, so that the

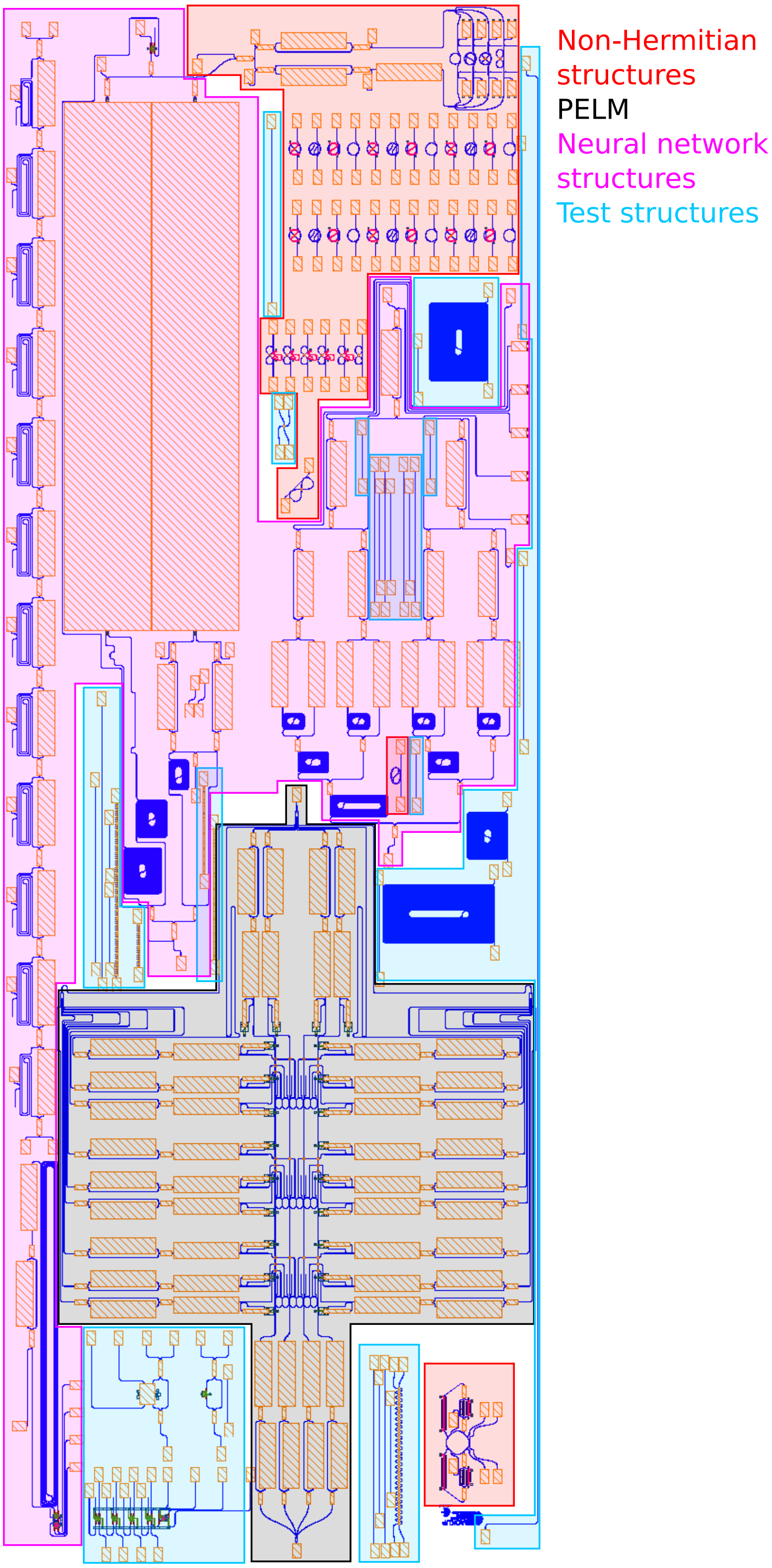

Figure A.3: Design of the Mask2022 chip without the metal layers. The colored boxes highlight the different types of structures.

GND pins can be connected in groups to the same PAD to save PADs. In fact, in Mask2022, the program connected more than 300 of pins even though it only had 200 of PADs available.

A.1 Couplings simulations

I designed the gap widths of the structures present in the two designs. I used both a COMSOL Multiphysics® [199] simulation and the Coupled Mode Theory (CMT) developed with MATLAB® [136]. In fact, using the CMT, I was able to simulate large coupling regions with MATLAB® in a short time without having to do a heavy simulation in COMSOL Multiphysics®.

To simulate the coupling between two adjacent waveguides (directional coupler), I first simulated in COMSOL Multiphysics® the Si waveguide with the proper cross section. In this way, I calculated the electric and magnetic fields in and around the WG (silica (SiO_2) cladding). Then, I used MATLAB® to calculate the coefficients needed to the CMT [200, 201, 202, 203, 204, 205] as a function of the gap width between two WGs. Namely, the mode coupling coefficients (k_{12} and k_{21}), the butt coupling coefficients (c_{12} and c_{21}), and the propagation constant change coefficients (χ_1 and χ_2).

Assuming that the two WGs are far enough that the modes of the two WGs are not deformed by the presence of the second WG, the equations of the CMT are as follows [200, 201, 202, 203, 204, 205]:

$$\frac{dA}{dz} + c_{12}\frac{dB}{dz}e^{-i(\beta_2-\beta_1)z} + i\chi_1 A + ik_{12}Be^{-i(\beta_2-\beta_1)z} = 0\,, \tag{A.1}$$

$$\frac{dB}{dz} + c_{21}\frac{dA}{dz}e^{+i(\beta_2-\beta_1)z} + i\chi_2 B + ik_{21}Be^{+i(\beta_2-\beta_1)z} = 0\,, \tag{A.2}$$

where A and B are the amplitude of the first and the second mode (first and second waveguide). *z* is wave the propagation direction. In our case, using two equal WGs, the two modes will also be equal and $\delta = \beta_2 - \beta_1 = 0$. The mode coupling coefficient is [200]:

$$k_{pq} = \frac{\omega\varepsilon_0 \int_{-\infty}^{\infty}\int_{-\infty}^{\infty}(\varepsilon_r - \varepsilon_{r,q})\vec{E}_p^* \cdot \vec{E}_q \, dx\, dy}{\int_{-\infty}^{\infty}\int_{-\infty}^{\infty} \hat{z} \cdot \left(\vec{E}_p^* \times \vec{H}_p + \vec{E}_p \times \vec{H}_p^*\right) dx\, dy}\,, \tag{A.3}$$

where ε_r is the dielettric function containing both WGs, $\varepsilon_{r,q}$ is the dielettric function containing only the q WG and $p, q \in \{1, 2\}$. The butt coupling coefficient is defined as [200]:

$$c_{pq} = \frac{\int_{-\infty}^{\infty}\int_{-\infty}^{\infty} \hat{z}\cdot\left(\vec{E}_p^{*}\times\vec{H}_q+\vec{E}_q\times\vec{H}_p^{*}\right)dx\,dy}{\int_{-\infty}^{\infty}\int_{-\infty}^{\infty} \hat{z}\cdot\left(\vec{E}_p^{*}\times\vec{H}_p+\vec{E}_p\times\vec{H}_p^{*}\right)dx\,dy}\,. \tag{A.4}$$

The change in propagation constant is instead [200]:

$$\chi_p = \frac{\omega\varepsilon_0\int_{-\infty}^{\infty}\int_{-\infty}^{\infty}(\varepsilon_r-\varepsilon_{r,q})\vec{E}_p^{*}\cdot\vec{E}_p\,dx\,dy}{\int_{-\infty}^{\infty}\int_{-\infty}^{\infty} \hat{z}\cdot\left(\vec{E}_p^{*}\times\vec{H}_p+\vec{E}_p\times\vec{H}_p^{*}\right)dx\,dy}\,. \tag{A.5}$$

Normalizing for the power in the p WG and assuming that the coupling is lossless, we can rewrite the CMT [200]:

$$\frac{dA}{dz} = -ik_aBe^{-i2\delta z}+i\alpha_aA\,, \tag{A.6}$$

$$\frac{dB}{dz} = -ik_bAe^{+i2\delta z}+i\alpha_bB\,, \tag{A.7}$$

where

$$k_a = \frac{k_{12}-c_{12}\chi_2}{1-|c_{12}|^2} \qquad \alpha_a = \frac{k_{21}c_{21}-\chi_1}{1-|c_{12}|^2}\,, \tag{A.8}$$

$$k_b = \frac{k_{21}-c_{12}^{*}\chi_1}{1-|c_{12}|^2} \qquad \alpha_b = \frac{k_{12}c_{12}^{*}-\chi_2}{1-|c_{12}|^2}\,. \tag{A.9}$$

For each directional coupler, I first calculated the gap width as a function of the wave propagation direction (z). Then, using this parameter, I calculated the coefficients given in Eq. (A.8) and Eq. (A.9) as a function of z. At this point I solved the system of equations given in Eq. (A.6) and Eq. (A.7) starting from the initial condition where the whole field is in a waveguide ($A[0] = 1$ and $B[0] = 0$). At this point, using the final intensities in the two WGs, I calculated the coupling and transmission coefficients corresponding to the TMM ($k = |B[z_{end}]|/|A[0]|$ and $t = |A[z_{end}]|/|A[0]|$). For the coupling between three WGs I followed a similar procedure, but I used the formulas for the coupling between three WGs [206, 207, 208, 209, 210].

Appendix B

Experimental procedure for the interferometric excitation

In this section, we describe the experimental procedure used to obtain a symmetric interferometric excitation by using the experimental setup reported in Fig. 1.20 [102]. First of all, we have measured the losses of each of the components of the experimental setup and we have calibrated the responses of the detectors. Then, the light was coupled into the MR. Calibration can be done using a straight waveguide, but for greater accuracy and precision, we used the bus waveguide and the MR system under test. In fact, when the MR is out of resonance, its presence is negligible and the system can be considered as consisting only of the bus waveguide. Using the detectors PD_{C1}, PD_{C2}, PD_L and PD_R and Variable Optical Attenuators (VOAs), we set the intensity in the two arms almost equal and low enough not to observe nonlinear effects. At this stage, the first step is to balance the length of the two optical paths after the first splitter. This is necessary to reduce the relative phase variation between the two input fields as a function of wavelength $(2\pi n_{\mathrm{eff}}\Delta L/\lambda)$, and thus to achieve an almost constant relative phase ϕ for a MR resonant wavelength. To find the condition where the period of the observed oscillations at the PD_R and PD_L detectors is maximum, we performed repeated wavelength scans at a scan rate of 100 nm/s over the entire spectrum and we varied the optical length of the right arm.

Once the delay line was set, we used the following procedure to apply the same intensities to the bus waveguide sides, i.e., to perform a symmetrical interferometric excitation.

1. We block one of the two arms of the setup. Then we maximize the transmission of the device at a non-resonant wavelength (1530 nm).
2. We repeat step 1. for the other arm.
3. We set the VOAs to guarantee the same transmissions from both device outputs (taking into account the different loss of the Optical Circulators (OCs) and the sensitivity of the photodetectors (PDs)).
4. We determine the ratio of the powers at the two detectors PD_{C1} and PD_{C2} $(I_{3,C1}/I_{3,C2})$.
5. We set the VOAs to get the same reflections from both device outputs.
6. We determine the ratio of the powers at the two detectors PD_{C1} and PD_{C2} $(I_{5,C1}/I_{5,C2})$.
7. By using these data, we derive the relation between the grating couplers coefficients:

   $$\frac{g_L}{g_R} = \sqrt{\frac{I_{5,C2}}{I_{5,C1}} \frac{I_{3,C1}}{I_{3,C2}}}, \tag{B.1}$$

   where g_L and g_R are the coupling coefficients with the fibers for the left and right gratings at the bus waveguide edges.
8. Considering the ratio of the coupling coefficients (g_L/g_R), we set the VOAs such that the field intensities within the bus waveguide are the same for both the excitation directions.

Bibliography

[1] Carl M. Bender and Stefan Boettcher. Real Spectra in Non-Hermitian Hamiltonians Having PT Symmetry. *Physical Review Letters*, 80(24):5243–5246, June 1998. Publisher: American Physical Society. `doi:10.1103/PhysRevLett.80.5243`.

[2] Carl M Bender. $\mathcal{PT}$-symmetric quantum theory. *Journal of Physics: Conference Series*, 631:012002, July 2015. `doi:10.1088/1742-6596/631/1/012002`.

[3] Ramy El-Ganainy, Konstantinos G. Makris, Mercedeh Khajavikhan, Ziad H. Musslimani, Stefan Rotter, and Demetrios N. Christodoulides. Non-Hermitian physics and PT symmetry. *Nature Physics*, 14(1):11–19, January 2018. Number: 1 Publisher: Nature Publishing Group. `doi:10.1038/nphys4323`.

[4] Ş K. Özdemir, S. Rotter, F. Nori, and L. Yang. Parity–time symmetry and exceptional points in photonics. *Nature Materials*, 18(8):783–798, August 2019. Number: 8 Publisher: Nature Publishing Group. `doi:10.1038/s41563-019-0304-9`.

[5] Martino De Carlo, Francesco De Leonardis, Richard A. Soref, Luigi Colatorti, and Vittorio M. N. Passaro. Non-Hermitian Sensing in Photonics and Electronics: A Review. *Sensors*, 22(11):3977, January 2022. Number: 11 Publisher: Multidisciplinary Digital Publishing Institute. `doi:10.3390/s22113977`.

[6] A. Guo, G. J. Salamo, D. Duchesne, R. Morandotti, M. Volatier-Ravat, V. Aimez, G. A. Siviloglou, and D. N. Christodoulides. Observation of $\mathcal{PT}$-Symmetry Breaking in Complex Optical Potentials. *Physical Review Let-*

ters, 103(9):093902, August 2009. Publisher: American Physical Society. `doi:10.1103/PhysRevLett.103.093902`.

[7] S. Longhi. Bloch Oscillations in Complex Crystals with $\mathcal{PT}$ Symmetry. *Physical Review Letters*, 103(12):123601, September 2009. Publisher: American Physical Society. `doi:10.1103/PhysRevLett.103.123601`.

[8] Stefano Longhi. Optical Realization of Relativistic Non-Hermitian Quantum Mechanics. *Physical Review Letters*, 105(1):013903, June 2010. `doi:10.1103/PhysRevLett.105.013903`.

[9] Christian E. Rüter, Konstantinos G. Makris, Ramy El-Ganainy, Demetrios N. Christodoulides, Mordechai Segev, and Detlef Kip. Observation of parity–time symmetry in optics. *Nature Physics*, 6(3):192–195, March 2010. Number: 3 Publisher: Nature Publishing Group. `doi:10.1038/nphys1515`.

[10] Liang Feng, Maurice Ayache, Jingqing Huang, Ye-Long Xu, Ming-Hui Lu, Yan-Feng Chen, Yeshaiahu Fainman, and Axel Scherer. Nonreciprocal Light Propagation in a Silicon Photonic Circuit. *Science*, 333(6043):729–733, August 2011. `doi:10.1126/science.1206038`.

[11] Zin Lin, Hamidreza Ramezani, Toni Eichelkraut, Tsampikos Kottos, Hui Cao, and Demetrios N. Christodoulides. Unidirectional Invisibility Induced by $\mathcal{PT}$-Symmetric Periodic Structures. *Physical Review Letters*, 106(21):213901, May 2011. Publisher: American Physical Society. `doi:10.1103/PhysRevLett.106.213901`.

[12] Hamidreza Ramezani, D. N. Christodoulides, V. Kovanis, I. Vitebskiy, and Tsampikos Kottos. $\mathcal{PT}$ -Symmetric Talbot Effects. *Physical Review Letters*, 109(3):033902, July 2012. `doi:10.1103/PhysRevLett.109.033902`.

[13] Luca Razzari and Roberto Morandotti. Gain and loss mixed in the same cauldron. *Nature*, 488(7410):163–164, August 2012. Number: 7410 Publisher: Nature Publishing Group. `doi:10.1038/488163a`.

[14] Alois Regensburger, Christoph Bersch, Mohammad-Ali Miri, Georgy Onishchukov, Demetrios N. Christodoulides, and Ulf Peschel. Parity–time synthetic photonic lattices. *Nature*, 488(7410):167–171, August 2012. Number: 7410 Publisher: Nature Publishing Group. `doi:10.1038/nature11298`.

[15] Chao Hang, Guoxiang Huang, and Vladimir V. Konotop. $\mathcal{PT}$ Symmetry with a System of Three-Level Atoms. *Physical Review Letters*, 110(8):083604, February 2013. Publisher: American Physical Society. `doi:10.1103/PhysRevLett.110.083604`.

[16] G. Q. Liang and Y. D. Chong. Optical Resonator Analog of a Two-Dimensional Topological Insulator. *Physical Review Letters*, 110(20):203904, May 2013. Publisher: American Physical Society. `doi:10.1103/PhysRevLett.110.203904`.

[17] Xiaobing Luo, Jiahao Huang, Honghua Zhong, Xizhou Qin, Qiongtao Xie, Yuri S. Kivshar, and Chaohong Lee. Pseudo-Parity-Time Symmetry in Optical Systems. *Physical Review Letters*, 110(24):243902, June 2013. Publisher: American Physical Society. `doi:10.1103/PhysRevLett.110.243902`.

[18] Alois Regensburger, Mohammad-Ali Miri, Christoph Bersch, Jakob Näger, Georgy Onishchukov, Demetrios N. Christodoulides, and Ulf Peschel. Observation of Defect States in PT-Symmetric Optical Lattices. *Physical Review Letters*, 110(22):223902, May 2013. Publisher: American Physical Society. `doi:10.1103/PhysRevLett.110.223902`.

[19] Y. D. Chong, Li Ge, and A. Douglas Stone. $\mathcal{PT}$-Symmetry Breaking and Laser-Absorber Modes in Optical Scattering Systems. *Physical Review Letters*, 106(9):093902, March 2011. Publisher: American Physical Society. `doi:10.1103/PhysRevLett.106.093902`.

[20] M. Liertzer, Li Ge, A. Cerjan, A. D. Stone, H. E. Türeci, and S. Rotter. Pump-Induced Exceptional Points in Lasers. *Physical Review Letters*, 108(17):173901, April 2012. Publisher: American Physical Society. `doi:10.1103/PhysRevLett.108.173901`.

[21] B. Dietz, H. L. Harney, O. N. Kirillov, M. Miski-Oglu, A. Richter, and F. Schäfer. Exceptional Points in a Microwave Billiard with Time-Reversal Invariance Violation. *Physical Review Letters*, 106(15):150403, April 2011. Publisher: American Physical Society. `doi:10.1103/PhysRevLett.106.150403`.

[22] S. Bittner, B. Dietz, U. Günther, H. L. Harney, M. Miski-Oglu, A. Richter, and F. Schäfer. PT Symmetry and Spontaneous Symmetry Breaking in a Microwave Billiard. *Physical Review Letters*, 108(2):024101, January 2012. Publisher: American Physical Society. `doi:10.1103/PhysRevLett.108.024101`.

[23] J. Rubinstein, P. Sternberg, and Q. Ma. Bifurcation Diagram and Pattern Formation of Phase Slip Centers in Superconducting Wires Driven with Electric Currents. *Physical Review Letters*, 99(16):167003, October 2007. Publisher: American Physical Society. `doi:10.1103/PhysRevLett.99.167003`.

[24] N. M. Chtchelkatchev, A. A. Golubov, T. I. Baturina, and V. M. Vinokur. Stimulation of the Fluctuation Superconductivity by $\mathcal{PT}$ Symmetry. *Physical Review Letters*, 109(15):150405, October 2012. Publisher: American Physical Society. `doi:10.1103/PhysRevLett.109.150405`.

[25] K. F. Zhao, M. Schaden, and Z. Wu. Enhanced magnetic resonance signal of spin-polarized Rb atoms near surfaces of coated cells. *Physical Review A*, 81(4):042903, April 2010. `doi:10.1103/PhysRevA.81.042903`.

[26] Joseph Schindler, Ang Li, Mei C. Zheng, F. M. Ellis, and Tsampikos Kottos. Experimental study of active LRC circuits with $\mathcal{PT}$ symmetries. *Physical Review A*, 84(4):040101, October 2011. Publisher: American Physical Society. `doi:10.1103/PhysRevA.84.040101`.

[27] N. Bender, S. Factor, J. D. Bodyfelt, H. Ramezani, D. N. Christodoulides, F. M. Ellis, and T. Kottos. Observation of Asymmetric Transport in Structures with Active Nonlinearities. *Physical Review Letters*, 110(23):234101, June 2013. Publisher: American Physical Society. `doi:10.1103/PhysRevLett.110.234101`.

[28] Carl M. Bender, Bjorn K. Berntson, David Parker, and E. Samuel. Observation of PT phase transition in a simple mechanical system. *American Journal of Physics*, 81(3):173–179, March 2013. Publisher: American Association of Physics Teachers. `doi:10.1119/1.4789549`.

[29] Maurizio Fagotti, Claudio Bonati, Demetrio Logoteta, Paolo Marconcini, and Massimo Macucci. Armchair graphene nanoribbons: $\mathcal{PT}$-symmetry breaking and exceptional points without dissipation. *Physical Review B*, 83(24):241406, June 2011. Publisher: American Physical Society. `doi:10.1103/PhysRevB.83.241406`.

[30] Alexander Szameit, Mikael C. Rechtsman, Omri Bahat-Treidel, and Mordechai Segev. $\mathcal{PT}$-symmetry in honeycomb photonic lattices. *Physical Review A*, 84(2):021806, August 2011. Publisher: American Physical Society. `doi:10.1103/PhysRevA.84.021806`.

[31] W. D. Heiss. Exceptional points of non-Hermitian operators. *Journal of Physics A: Mathematical and General*, 37(6):2455, January 2004. `doi:10.1088/0305-4470/37/6/034`.

[32] Yuto Ashida, Zongping Gong, and Masahito Ueda. Non-Hermitian Physics. *Advances in Physics*, 69(3):249–435, July 2020. Number: 3 arXiv:2006.01837 [cond-mat, physics:quant-ph]. `doi:10.1080/00018732.2021.1876991`.

[33] W. D. Heiss. The physics of exceptional points. *Journal of Physics A: Mathematical and Theoretical*, 45(44):444016, October 2012. Publisher: IOP Publishing. `doi:10.1088/1751-8113/45/44/444016`.

[34] Liang Feng, Xuefeng Zhu, Sui Yang, Hanyu Zhu, Peng Zhang, Xiaobo Yin, Yuan Wang, and Xiang Zhang. Demonstration of a large-scale optical exceptional point structure. *Optics Express*, 22(2):1760–1767, January 2014. Publisher: Optica Publishing Group. `doi:10.1364/OE.22.001760`.

[35] Weijian Chen, Şahin Kaya Özdemir, Guangming Zhao, Jan Wiersig, and Lan Yang. Exceptional points enhance sensing in an optical microcavity. *Nature*, 548(7666):192–196, August 2017. Number: 7666 Publisher: Nature Publishing Group. `doi:10.1038/nature23281`.

[36] Jinhan Ren, Yuzhou G. N. Liu, Midya Parto, William E. Hayenga, Mohammad P. Hokmabadi, Demetrios N. Christodoulides, and Mercedeh Khajavikhan. Unidirectional light emission in PT-symmetric microring lasers. *Optics Express*, 26(21):27153, October 2018. Number: 21. `doi:10.1364/OE.26.027153`.

[37] Jung-Wan Ryu, Soo-Young Lee, and Sang Wook Kim. Coupled nonidentical microdisks: Avoided crossing of energy levels and unidirectional far-field emission. *Physical Review A*, 79(5):053858, May 2009. Publisher: American Physical Society. `doi:10.1103/PhysRevA.79.053858`.

[38] Sang-Bum Lee, Juhee Yang, Songky Moon, Soo-Young Lee, Jeong-Bo Shim, Sang Wook Kim, Jai-Hyung Lee, and Kyungwon An. Observation of an Exceptional Point in a Chaotic Optical Microcavity. *Physical Review Letters*, 103(13):134101, September 2009. Publisher: American Physical Society. `doi:10.1103/PhysRevLett.103.134101`.

[39] Bo Peng, Şahin Kaya Özdemir, Fuchuan Lei, Faraz Monifi, Mariagiovanna Gianfreda, Gui Lu Long, Shanhui Fan, Franco Nori, Carl M. Bender, and Lan Yang. Parity–time-symmetric whispering-gallery microcavities. *Nature Physics*, 10(5):394–398, May 2014. Number: 5 Publisher: Nature Publishing Group. `doi:10.1038/nphys2927`.

[40] C. Dembowski, H.-D. Gräf, H. L. Harney, A. Heine, W. D. Heiss, H. Rehfeld, and A. Richter. Experimental Observation of the Topological Structure of Exceptional Points. *Physical Review Letters*, 86(5):787–790, January 2001. Publisher: American Physical Society. `doi:10.1103/PhysRevLett.86.787`.

[41] Jörg Doppler, Alexei A. Mailybaev, Julian Böhm, Ulrich Kuhl, Adrian Girschik, Florian Libisch, Thomas J. Milburn, Peter Rabl, Nimrod Moiseyev, and Stefan Rotter. Dynamically encircling an exceptional point for asymmetric mode switching. *Nature*, 537(7618):76–79, September 2016. Number: 7618 Publisher: Nature Publishing Group. `doi:10.1038/nature18605`.

[42] Youngwoon Choi, Sungsam Kang, Sooin Lim, Wookrae Kim, Jung-Ryul Kim, Jai-Hyung Lee, and Kyungwon An. Quasieigenstate Coalescence in an Atom-Cavity Quantum Composite. *Physical Review Letters*, 104(15):153601, April 2010. Publisher: American Physical Society. `doi:10.1103/PhysRevLett.104.153601`.

[43] Kun Ding, Guancong Ma, Meng Xiao, Z. Q. Zhang, and C. T. Chan. Emergence, Coalescence, and Topological Properties of Multiple Exceptional Points and Their Experimental Realization. *Physical Review X*, 6(2):021007, April 2016. Publisher: American Physical Society. `doi:10.1103/PhysRevX.6.021007`.

[44] Hossein Hodaei, Absar U. Hassan, Steffen Wittek, Hipolito Garcia-Gracia, Ramy El-Ganainy, Demetrios N. Christodoulides, and Mercedeh Khajavikhan. Enhanced sensitivity at higher-order exceptional points. *Nature*, 548(7666):187–191, August 2017. Number: 7666. `doi:10.1038/nature23280`.

[45] Jun-Hee Park, Abdoulaye Ndao, Wei Cai, Liyi Hsu, Ashok Kodigala, Thomas Lepetit, Yu-Hwa Lo, and Boubacar Kanté. Symmetry-breaking-induced plasmonic exceptional points and nanoscale sensing. *Nature Physics*, 16(4):462–468, April 2020. Number: 4 Publisher: Nature Publishing Group. `doi:10.1038/s41567-020-0796-x`.

[46] Alexander McDonald and Aashish A. Clerk. Exponentially-enhanced quantum sensing with non-Hermitian lattice dynamics. *Nature Communications*, 11(1):5382, December 2020. Number: 1. `doi:10.1038/s41467-020-19090-4`.

[47] Riccardo Franchi, Stefano Biasi, Filippo Mione, and Lorenzo Pavesi. On the response of the Taiji microresonator against small perturbation of the counter propagating mode. In Sonia M. García-Blanco and Pavel Cheben, editors, *Integrated Optics: Devices, Materials, and Technologies XXVI*, page 13, San Francisco, United States, March 2022. SPIE. `doi:10.1117/12.2608157`.

[48] Martino De Carlo, Francesco De Leonardis, Richard A. Soref, and Vittorio M. N. Passaro. Design of a Trap-Assisted Exceptional-Surface- Enhanced Silicon-on-Insulator Particle Sensor. *Journal of Lightwave Technology*, 40(17):6021–6029, September 2022. Publisher: IEEE. URL: `https://opg.optica.org/jlt/abstract.cfm?uri=jlt-40-17-6021`.

[49] Q. Zhong, J. Ren, M. Khajavikhan, D. N. Christodoulides, Ş. K. Özdemir, and R. El-Ganainy. Sensing with Exceptional Surfaces in Order to Combine Sensitivity with Robustness. *Physical Review Letters*, 122(15):153902, April 2019. Publisher: American Physical Society. `doi:10.1103/PhysRevLett.122.153902`.

[50] Guo-Qing Qin, Ran-Ran Xie, Hao Zhang, Yun-Qi Hu, Min Wang, Gui-Qin Li, Haitan Xu, Fuchuan Lei, Dong Ruan, and Gui-Lu Long. Experimental Realization of Sensitivity Enhancement and Suppression with Exceptional Surfaces. *Laser & Photonics Reviews*, 15(5):2000569, 2021. _eprint: https://onlinelibrary.wiley.com/doi/pdf/10.1002/lpor.202000569. `doi:10.1002/lpor.202000569`.

[51] Liang Feng, Ye-Long Xu, William S. Fegadolli, Ming-Hui Lu, José E. B. Oliveira, Vilson R. Almeida, Yan-Feng Chen, and Axel Scherer. Experimental demonstration of a unidirectional reflectionless parity-time metamaterial at optical frequencies. *Nature Materials*, 12(2):108–113, February 2013. Number: 2 Publisher: Nature Publishing Group. `doi:10.1038/nmat3495`.

[52] A. Calabrese, F. Ramiro-Manzano, H. M. Price, S. Biasi, M. Bernard, M. Ghulinyan, I. Carusotto, and L. Pavesi. Unidirectional reflection from

an integrated "taiji" microresonator. *Photonics Research*, 8(8):1333, August 2020. Number: 8. `doi:10.1364/PRJ.393070`.

[53] W.D. Heiss and H.L. Harney. The chirality of exceptional points. *The European Physical Journal D - Atomic, Molecular, Optical and Plasma Physics*, 17(2):149–151, November 2001. `doi:10.1007/s100530170017`.

[54] C. Dembowski, B. Dietz, H.-D. Gräf, H. L. Harney, A. Heine, W. D. Heiss, and A. Richter. Observation of a Chiral State in a Microwave Cavity. *Physical Review Letters*, 90(3):034101, January 2003. Publisher: American Physical Society. `doi:10.1103/PhysRevLett.90.034101`.

[55] Bo Peng, Şahin Kaya Özdemir, Matthias Liertzer, Weijian Chen, Johannes Kramer, Huzeyfe Yılmaz, Jan Wiersig, Stefan Rotter, and Lan Yang. Chiral modes and directional lasing at exceptional points. *Proceedings of the National Academy of Sciences*, 113(25):6845–6850, June 2016. Publisher: Proceedings of the National Academy of Sciences. `doi:10.1073/pnas.1603318113`.

[56] Changqing Wang, Xuefeng Jiang, Guangming Zhao, Mengzhen Zhang, Chia Wei Hsu, Bo Peng, A. Douglas Stone, Liang Jiang, and Lan Yang. Electromagnetically induced transparency at a chiral exceptional point. *Nature Physics*, 16(3):334–340, March 2020. Number: 3 Publisher: Nature Publishing Group. `doi:10.1038/s41567-019-0746-7`.

[57] S. Soleymani, Q. Zhong, M. Mokim, S. Rotter, R. El-Ganainy, and Ş K. Özdemir. Chiral and degenerate perfect absorption on exceptional surfaces. *Nature Communications*, 13(1):599, February 2022. Number: 1 Publisher: Nature Publishing Group. `doi:10.1038/s41467-022-27990-w`.

[58] Junda Zhu, Changqing Wang, Can Tao, Zhoutian Fu, Haitao Liu, Fang Bo, Lan Yang, Guoquan Zhang, and Jingjun Xu. Imperfect chirality at exceptional points in optical whispering-gallery microcavities, August 2022. arXiv:2208.07077 [physics]. `doi:10.48550/arXiv.2208.07077`.

[59] L. Jin and Z. Song. Incident Direction Independent Wave Propagation and Unidirectional Lasing. *Physical Review Letters*, 121(7):073901, August 2018. Number: 7. `doi:10.1103/PhysRevLett.121.073901`.

[60] A. Muñoz de las Heras and I. Carusotto. Unidirectional lasing in nonlinear

Taiji microring resonators. *Physical Review A*, 104(4):043501, October 2021. Publisher: American Physical Society. `doi:10.1103/PhysRevA.104.043501`.

[61] Liang Feng, Zi Jing Wong, Ren-Min Ma, Yuan Wang, and Xiang Zhang. Single-mode laser by parity-time symmetry breaking. *Science*, 346(6212):972–975, November 2014. Publisher: American Association for the Advancement of Science. `doi:10.1126/science.1258479`.

[62] Jing Zhang, Bo Peng, Şahin Kaya Özdemir, Kevin Pichler, Dmitry O. Krimer, Guangming Zhao, Franco Nori, Yu-xi Liu, Stefan Rotter, and Lan Yang. A phonon laser operating at an exceptional point. *Nature Photonics*, 12(8):479–484, August 2018. Number: 8 Publisher: Nature Publishing Group. `doi:10.1038/s41566-018-0213-5`.

[63] G. Fasching, Ch Deutsch, A. Benz, A. M. Andrews, P. Klang, R. Zobl, W. Schrenk, G. Strasser, P. Ragulis, V. Tamošiūnas, and K. Unterrainer. Electrically controllable photonic molecule laser. *Optics Express*, 17(22):20321–20326, October 2009. Publisher: Optica Publishing Group. `doi:10.1364/OE.17.020321`.

[64] M. Brandstetter, M. Liertzer, C. Deutsch, P. Klang, J. Schöberl, H. E. Türeci, G. Strasser, K. Unterrainer, and S. Rotter. Reversing the pump dependence of a laser at an exceptional point. *Nature Communications*, 5(1):4034, June 2014. Number: 1 Publisher: Nature Publishing Group. `doi:10.1038/ncomms5034`.

[65] Hossein Hodaei, Mohammad-Ali Miri, Matthias Heinrich, Demetrios N. Christodoulides, and Mercedeh Khajavikhan. Parity-time–symmetric microring lasers. *Science*, 346(6212):975–978, November 2014. Publisher: American Association for the Advancement of Science. `doi:10.1126/science.1258480`.

[66] Pei Miao, Zhifeng Zhang, Jingbo Sun, Wiktor Walasik, Stefano Longhi, Natalia M. Litchinitser, and Liang Feng. Orbital angular momentum microlaser. *Science*, 353(6298):464–467, July 2016. Publisher: American Association for the Advancement of Science. `doi:10.1126/science.aaf8533`.

[67] B. Peng, Ş. K. Özdemir, S. Rotter, H. Yilmaz, M. Liertzer, F. Monifi, C. M. Bender, F. Nori, and L. Yang. Loss-induced suppression and revival of lasing. *Science*, 346(6207):328–332, October 2014. `doi:10.1126/science.1258004`.

[68] Jinuk Kim, Juman Kim, Jisung Seo, Kyu-Won Park, Songky Moon, and Kyungwon An. Practical lineshape of a laser operating near an exceptional point. *Scientific Reports*, 11(1):6164, March 2021. Number: 1 Publisher: Nature Publishing Group. `doi:10.1038/s41598-021-85665-w`.

[69] Miguel A. Bandres, Steffen Wittek, Gal Harari, Midya Parto, Jinhan Ren, Mordechai Segev, Demetrios N. Christodoulides, and Mercedeh Khajavikhan. Topological insulator laser: Experiments. *Science*, 359(6381):eaar4005, March 2018. Number: 6381. `doi:10.1126/science.aar4005`.

[70] H. Xu, D. Mason, Luyao Jiang, and J. G. E. Harris. Topological energy transfer in an optomechanical system with exceptional points. *Nature*, 537(7618):80–83, September 2016. Number: 7618 Publisher: Nature Publishing Group. `doi:10.1038/nature18604`.

[71] Yuzhou G. N. Liu, Pawel S. Jung, Midya Parto, Demetrios N. Christodoulides, and Mercedeh Khajavikhan. Gain-induced topological response via tailored long-range interactions. *Nature Physics*, 17(6):704–709, June 2021. Number: 6. `doi:10.1038/s41567-021-01185-4`.

[72] Mohammad P. Hokmabadi, Alexander Schumer, Demetrios N. Christodoulides, and Mercedeh Khajavikhan. Non-Hermitian ring laser gyroscopes with enhanced Sagnac sensitivity. *Nature*, 576(7785):70–74, December 2019. Number: 7785 Publisher: Nature Publishing Group. `doi:10.1038/s41586-019-1780-4`.

[73] Xuan Mao, Guo-Qing Qin, Hong Yang, Hao Zhang, Min Wang, and Gui-Lu Long. Enhanced sensitivity of optical gyroscope in a mechanical parity-time-symmetric system based on exceptional point. *New Journal of Physics*, 22(9):093009, September 2020. Publisher: IOP Publishing. `doi:10.1088/1367-2630/abaacd`.

[74] Yu-Hung Lai, Yu-Kun Lu, Myoung-Gyun Suh, Zhiquan Yuan, and Kerry Vahala. Observation of the exceptional-point-enhanced Sagnac effect. *Nature*, 576(7785):65–69, December 2019. Number: 7785 Publisher: Nature Publishing Group. `doi:10.1038/s41586-019-1777-z`.

[75] Martino De Carlo, Francesco De Leonardis, Francesco Dell'Olio, Pietro Peliti, Fabrizio Berton, Mario Lucchesini, and Vittorio M. N. Passaro. Indirectly-coupled optical resonators for anti-parity-time-symmetric gyroscopes. In *2022*

IEEE International Symposium on Inertial Sensors and Systems (INERTIAL), pages 1–4, May 2022. ISSN: 2377-3480. `doi:10.1109/INERTIAL53425.2022.9787722`.

[76] O. Dietz, H.-J. Stöckmann, U. Kuhl, F. M. Izrailev, N. M. Makarov, J. Doppler, F. Libisch, and S. Rotter. Surface scattering and band gaps in rough waveguides and nanowires. *Physical Review B*, 86(20):201106, November 2012. Publisher: American Physical Society. `doi:10.1103/PhysRevB.86.201106`.

[77] Alberto Muñoz de las Heras, Riccardo Franchi, Stefano Biasi, Mher Ghulinyan, Lorenzo Pavesi, and Iacopo Carusotto. Nonlinearity-Induced Reciprocity Breaking in a Single Nonmagnetic Taiji Resonator. *Physical Review Applied*, 15(5):054044, May 2021. Number: 5. `doi:10.1103/PhysRevApplied.15.054044`.

[78] Riccardo Franchi, Stefano Biasi, Alberto Muñoz de las Heras, Mher Ghulinyan, Iacopo Carusotto, and Lorenzo Pavesi. Influence of the bus waveguide on the linear and nonlinear response of a taiji microresonator. *Optics Express*, 29(19):29615, September 2021. Number: 19. `doi:10.1364/OE.434239`.

[79] Dimitrios Chatzidimitriou, Alexandros Pitilakis, Traianos Yioultsis, and Emmanouil E. Kriezis. Breaking Reciprocity in a non-Hermitian Photonic Coupler with Saturable Absorption. *Physical Review A*, 103(5):053503, May 2021. Number: 5 arXiv:2102.07483 [physics]. `doi:10.1103/PhysRevA.103.053503`.

[80] A. Muñoz de las Heras and I. Carusotto. Optical isolators based on nonreciprocal four-wave mixing. *Physical Review A*, 106(6):063523, December 2022. Publisher: American Physical Society. `doi:10.1103/PhysRevA.106.063523`.

[81] John Heebner, Rohit Grover, and Tarek Ibrahim. *Optical Microresonators: Theory, Fabrication, and Applications*, volume 138 of *Optical Sciences*. Springer New York, New York, NY, 2008. `doi:10.1007/978-0-387-73068-4`.

[82] W. Bogaerts, P. De Heyn, T. Van Vaerenbergh, K. De Vos, S. Kumar Selvaraja, T. Claes, P. Dumon, P. Bienstman, D. Van Thourhout, and R. Baets. Silicon microring resonators. *Laser & Photonics Reviews*, 6(1):47–73, January 2012. `doi:10.1002/lpor.201100017`.

[83] L.B. Soldano and E.C.M. Pennings. Optical multi-mode interference devices based on self-imaging: principles and applications. *Journal of Lightwave Tech-*

nology, 13(4):615–627, April 1995. Conference Name: Journal of Lightwave Technology. `doi:10.1109/50.372474`.

[84] Po Dong. Silicon photonic integrated circuits for WDM applications. In *2015 International Conference on Photonics in Switching (PS)*, pages 25–27, September 2015. `doi:10.1109/PS.2015.7328941`.

[85] Mack Johnson, Mark G. Thompson, and Döndü Sahin. Low-loss, low-crosstalk waveguide crossing for scalable integrated silicon photonics applications. *Optics Express*, 28(9):12498–12507, April 2020. Publisher: Optica Publishing Group. `doi:10.1364/OE.381304`.

[86] Hongnan Xu, Daoxin Dai, and Yaocheng Shi. Silicon Integrated Nanophotonic Devices for On-Chip Multi-Mode Interconnects. *Applied Sciences*, 10(18):6365, January 2020. Number: 18 Publisher: Multidisciplinary Digital Publishing Institute. `doi:10.3390/app10186365`.

[87] Weijie Chang and Minming Zhang. Silicon-based multimode waveguide crossings. *Journal of Physics: Photonics*, 2(2):022002, April 2020. Publisher: IOP Publishing. `doi:10.1088/2515-7647/ab8698`.

[88] Sailong Wu, Xin Mu, Lirong Cheng, Simei Mao, and H. Y. Fu. State-of-the-Art and Perspectives on Silicon Waveguide Crossings: A Review. *Micromachines*, 11(3):326, March 2020. Number: 3 Publisher: Multidisciplinary Digital Publishing Institute. `doi:10.3390/mi11030326`.

[89] Lirong Cheng, Simei Mao, Zhi Li, Yaqi Han, and H. Fu. Grating Couplers on Silicon Photonics: Design Principles, Emerging Trends and Practical Issues. *Micromachines*, 11(7):666, July 2020. Number: 7. `doi:10.3390/mi11070666`.

[90] Riccardo Marchetti, Cosimo Lacava, Ali Khokhar, Xia Chen, Ilaria Cristiani, David J. Richardson, Graham T. Reed, Periklis Petropoulos, and Paolo Minzioni. High-efficiency grating-couplers: demonstration of a new design strategy. *Scientific Reports*, 7(1):16670, November 2017. Number: 1 Publisher: Nature Publishing Group. `doi:10.1038/s41598-017-16505-z`.

[91] Clara Zaccaria, Mattia Mancinelli, and Lorenzo Pavesi. A FEM Enhanced Transfer Matrix Method for Optical Grating Design. *Journal of Lightwave Technology*, 39(11):3521–3530, June 2021. Number: 11. `doi:10.1109/JLT.2021.3067153`.

[92] Changqing Wang, William R. Sweeney, A. Douglas Stone, and Lan Yang. Coherent perfect absorption at an exceptional point. *Science*, 373(6560):1261–1265, September 2021. Publisher: American Association for the Advancement of Science. `doi:10.1126/science.abj1028`.

[93] Riccardo Franchi, Stefano Biasi, Diego Piciocchi, and Lorenzo Pavesi. The infinity-loop microresonator: a new integrated photonic structure working at an exceptional surface. *Accepted in APL Photonics*, 2023. arXiv:2302.01108 [physics]. `doi:10.48550/arXiv.2302.01108`.

[94] Brent E. Little, Juha-Pekka Laine, and Sai T. Chu. Surface-roughness-induced contradirectional coupling in ring and disk resonators. *Optics Letters*, 22(1):4, January 1997. Number: 1. `doi:10.1364/OL.22.000004`.

[95] Ang Li, Thomas Van Vaerenbergh, Peter De Heyn, Peter Bienstman, and Wim Bogaerts. Backscattering in silicon microring resonators: a quantitative analysis: Backscattering in silicon microring resonators: a quantitative analysis. *Laser & Photonics Reviews*, 10(3):420–431, May 2016. `doi:10.1002/lpor.201500207`.

[96] Stefano Biasi, Fernando Ramiro-Manzano, Fabio Turri, Pierre-Elie Larre, Mher Ghulinyan, Iacopo Carusotto, and Lorenzo Pavesi. Hermitian and Non-Hermitian Mode Coupling in a Microdisk Resonator Due to Stochastic Surface Roughness Scattering. *IEEE Photonics Journal*, 11(2):1–14, April 2019. Number: 2. `doi:10.1109/JPHOT.2018.2880281`.

[97] Chengle Sui, Qiangmin Wang, Shilin Xiao, and Pingqing Li. Analysis of Microdisk/Microring's Surface Roughness Effect by Orthogonal Decomposition. *Optics and Photonics Journal*, 03(02):288–292, 2013. Number: 02. `doi:10.4236/opj.2013.32B068`.

[98] Andreas Ø. Svela, Jonathan M. Silver, Leonardo Del Bino, Shuangyou Zhang, Michael T. M. Woodley, Michael R. Vanner, and Pascal Del'Haye. Coherent suppression of backscattering in optical microresonators. *Light: Science & Applications*, 9(1):204, December 2020. Number: 1. `doi:10.1038/s41377-020-00440-2`.

[99] Jiangang Zhu, Sahin Kaya Ozdemir, Yun-Feng Xiao, Lin Li, Lina He, Da-Ren Chen, and Lan Yang. On-chip single nanoparticle detection and sizing by

mode splitting in an ultrahigh-Q microresonator. *Nature Photonics*, 4(1):46–49, January 2010. Number: 1 Publisher: Nature Publishing Group. `doi:10.1038/nphoton.2009.237`.

[100] Lina He, Şahin Kaya Özdemir, Jiangang Zhu, Woosung Kim, and Lan Yang. Detecting single viruses and nanoparticles using whispering gallery microlasers. *Nature Nanotechnology*, 6(7):428–432, July 2011. Number: 7 Publisher: Nature Publishing Group. `doi:10.1038/nnano.2011.99`.

[101] Frank Vollmer and Lan Yang. Review Label-free detection with high-Q microcavities: a review of biosensing mechanisms for integrated devices. *Nanophotonics*, 1(3-4):267–291, December 2012. Publisher: De Gruyter. `doi:10.1515/nanoph-2012-0021`.

[102] Stefano Biasi, Riccardo Franchi, Filippo Mione, and Lorenzo Pavesi. Interferometric method to estimate the eigenvalues of a non-Hermitian two-level optical system. *Photonics Research*, 10(4):1134, April 2022. `doi:10.1364/PRJ.450402`.

[103] Stefano Biasi, Riccardo Franchi, and Lorenzo Pavesi. Interferometric cavity ringdown technique for ultrahigh Q-factor microresonators. *Optics Letters*, 47(16):4083–4086, August 2022. Number: 16 Publisher: Optica Publishing Group. `doi:10.1364/OL.467590`.

[104] Qi Zhong, Mercedeh Khajavikhan, Demetrios N. Christodoulides, and Ramy El-Ganainy. Winding around non-Hermitian singularities. *Nature Communications*, 9(1):4808, November 2018. Number: 1 Publisher: Nature Publishing Group. `doi:10.1038/s41467-018-07105-0`.

[105] Xu-Lin Zhang, Tianshu Jiang, and C. T. Chan. Dynamically encircling an exceptional point in anti-parity-time symmetric systems: asymmetric mode switching for symmetry-broken modes. *Light: Science & Applications*, 8(1):88, October 2019. Number: 1 Publisher: Nature Publishing Group. `doi:10.1038/s41377-019-0200-8`.

[106] Midya Parto, Yuzhou G. N. Liu, Babak Bahari, Mercedeh Khajavikhan, and Demetrios N. Christodoulides. Non-Hermitian and topological photonics: optics at an exceptional point. *Nanophotonics*, 10(1):403–423, January 2021. Publisher: De Gruyter. `doi:10.1515/nanoph-2020-0434`.

[107] Bahaa Saleh and Malvin Teich. *Fundamentals of Photonics, 2nd Edition*. June 2007. Journal Abbreviation: Canada Wiley Interscience Publication Title: Canada Wiley Interscience.

[108] Mohammad Hafezi, Eugene A. Demler, Mikhail D. Lukin, and Jacob M. Taylor. Robust optical delay lines with topological protection. *Nature Physics*, 7(11):907–912, November 2011. Number: 11 Publisher: Nature Publishing Group. `doi:10.1038/nphys2063`.

[109] M. Hafezi, S. Mittal, J. Fan, A. Migdall, and J. M. Taylor. Imaging topological edge states in silicon photonics. *Nature Photonics*, 7(12):1001–1005, December 2013. Number: 12 Publisher: Nature Publishing Group. `doi:10.1038/nphoton.2013.274`.

[110] Stefano Biasi, Pierre Guillemé, Andrea Volpini, Giorgio Fontana, and Lorenzo Pavesi. Time Response of a Microring Resonator to a Rectangular Pulse in Different Coupling Regimes. *Journal of Lightwave Technology*, 37(19):5091–5099, October 2019. Conference Name: Journal of Lightwave Technology. `doi:10.1109/JLT.2019.2928640`.

[111] Lorenzo Pavesi. Thirty Years in Silicon Photonics: A Personal View. *Frontiers in Physics*, 9, 2021. URL: `https://www.frontiersin.org/articles/10.3389/fphy.2021.786028`.

[112] Shanhui Fan, Pierre R. Villeneuve, J. D. Joannopoulos, M. J. Khan, C. Manolatou, and H. A. Haus. Theoretical analysis of channel drop tunneling processes. *Physical Review B*, 59(24):15882–15892, June 1999. Publisher: American Physical Society. `doi:10.1103/PhysRevB.59.15882`.

[113] Min-Suk Kwon and William H. Steier. Microring-resonator-based sensor measuring both the concentration and temperature of a solution. *Optics Express*, 16(13):9372–9377, June 2008. Publisher: Optica Publishing Group. `doi:10.1364/OE.16.009372`.

[114] A. Ksendzov and Y. Lin. Integrated optics ring-resonator sensors for protein detection. *Optics Letters*, 30(24):3344–3346, December 2005. Publisher: Optica Publishing Group. `doi:10.1364/OL.30.003344`.

[115] Chung-Yen Chao, W. Fung, and L.J. Guo. Polymer microring resonators for biochemical sensing applications. *IEEE Journal of Selected Topics in Quantum*

Electronics, 12(1):134–142, January 2006. Conference Name: IEEE Journal of Selected Topics in Quantum Electronics. `doi:10.1109/JSTQE.2005.862945`.

[116] Paul V Lambeck. Integrated optical sensors for the chemical domain. *Measurement Science and Technology*, 17(8):R93–R116, August 2006. `doi:10.1088/0957-0233/17/8/R01`.

[117] Kevin D. Heylman, Niket Thakkar, Erik H. Horak, Steven C. Quillin, Charles Cherqui, Kassandra A. Knapper, David J. Masiello, and Randall H. Goldsmith. Optical microresonators as single-particle absorption spectrometers. *Nature Photonics*, 10(12):788–795, December 2016. Number: 12 Publisher: Nature Publishing Group. `doi:10.1038/nphoton.2016.217`.

[118] E. Gavartin, P. Verlot, and T. J. Kippenberg. A hybrid on-chip optomechanical transducer for ultrasensitive force measurements. *Nature Nanotechnology*, 7(8):509–514, August 2012. Number: 8 Publisher: Nature Publishing Group. `doi:10.1038/nnano.2012.97`.

[119] S. Forstner, S. Prams, J. Knittel, E. D. van Ooijen, J. D. Swaim, G. I. Harris, A. Szorkovszky, W. P. Bowen, and H. Rubinsztein-Dunlop. Cavity Optomechanical Magnetometer. *Physical Review Letters*, 108(12):120801, March 2012. Publisher: American Physical Society. `doi:10.1103/PhysRevLett.108.120801`.

[120] Bipin Bhola and William H. Steier. A Novel Optical Microring Resonator Accelerometer. *IEEE Sensors Journal*, 7(12):1759–1766, December 2007. Conference Name: IEEE Sensors Journal. `doi:10.1109/JSEN.2007.910070`.

[121] P. Rabiei, W.H. Steier, Cheng Zhang, and L.R. Dalton. Polymer microring filters and modulators. *Journal of Lightwave Technology*, 20(11):1968–1975, November 2002. Conference Name: Journal of Lightwave Technology. `doi:10.1109/JLT.2002.803058`.

[122] Francesco Testa, Claudio J. Oton, Christophe Kopp, Jong-Moo Lee, Ruben Ortuno, Reinhard Enne, Stefano Tondini, Guido Chiaretti, Alberto Bianchi, Paolo Pintus, Min-Su Kim, Daivid Fowler, Jose Angel Ayucar, Michael Hofbauer, Mattia Mancinelli, Maryse Fournier, Giovan Battista Preve, Nikola Zecevic, Costanza L. Manganelli, Claudio Castellan, Gabriel Pares, Olivier Lemonnier, Fabrizio Gambini, Pierre Labeye, Marco Romagnoli, Lorenzo Pavesi, Horst Zimmermann, Fabrizio Di Pasquale, and Stefano Stracca. Design and Implementation of an Integrated Reconfigurable Silicon Photonics Switch Matrix in

IRIS Project. *IEEE Journal of Selected Topics in Quantum Electronics*, 22(6):155–168, November 2016. Number: 6. `doi:10.1109/JSTQE.2016.2547322`.

[123] M. L. Gorodetsky and V. S. Ilchenko. Optical microsphere resonators: optimal coupling to high-Q whispering-gallery modes. *JOSA B*, 16(1):147–154, January 1999. Publisher: Optica Publishing Group. `doi:10.1364/JOSAB.16.000147`.

[124] Yisheng Fang and Zhichao Ruan. Temporal Coupled-Mode Theory for Light Scattering and Absorption by Nanostructures. In Eugene Kamenetskii, Almas Sadreev, and Andrey Miroshnichenko, editors, *Fano Resonances in Optics and Microwaves: Physics and Applications*, Springer Series in Optical Sciences, pages 157–183. Springer International Publishing, Cham, 2018. `doi:10.1007/978-3-319-99731-5_7`.

[125] Wonjoo Suh, Zheng Wang, and Shanhui Fan. Temporal coupled-mode theory and the presence of non-orthogonal modes in lossless multimode cavities. *IEEE Journal of Quantum Electronics*, 40(10):1511–1518, October 2004. Conference Name: IEEE Journal of Quantum Electronics. `doi:10.1109/JQE.2004.834773`.

[126] Qiang Li, Tao Wang, Yikai Su, Min Yan, and Min Qiu. Coupled mode theory analysis of mode-splitting in coupled cavity system. *Optics Express*, 18(8):8367–8382, April 2010. Publisher: Optica Publishing Group. `doi:10.1364/OE.18.008367`.

[127] Hua-Xing Xu, Li Ke, Li Yang, and Jing-Ren Qian. Temporal coupled-mode theory for resonators. In *Proceedings of 2011 Cross Strait Quad-Regional Radio Science and Wireless Technology Conference*, volume 1, pages 82–84, July 2011. `doi:10.1109/CSQRWC.2011.6036890`.

[128] M Borghi, C Castellan, S Signorini, A Trenti, and L Pavesi. Nonlinear silicon photonics. *Journal of Optics*, 19(9):093002, September 2017. Number: 9. `doi:10.1088/2040-8986/aa7a6d`.

[129] Bo Peng, Şahin Kaya Özdemir, Weijian Chen, Franco Nori, and Lan Yang. What is and what is not electromagnetically induced transparency in whispering-gallery microcavities. *Nature Communications*, 5(1):5082, December 2014. `doi:10.1038/ncomms6082`.

[130] Dana Z. Anderson, Josef C. Frisch, and Carl S. Masser. Mirror reflectometer based on optical cavity decay time. *Applied Optics*, 23(8):1238–1245, April 1984. Publisher: Optica Publishing Group. `doi:10.1364/AO.23.001238`.

[131] Kevin K. Lehmann and Daniele Romanini. The superposition principle and cavity ring-down spectroscopy. *The Journal of Chemical Physics*, 105(23):10263–10277, December 1996. Publisher: American Institute of Physics. `doi:10.1063/1.472955`.

[132] D. K. Armani, T. J. Kippenberg, S. M. Spillane, and K. J. Vahala. Ultra-high-Q toroid microcavity on a chip. *Nature*, 421(6926):925–928, February 2003. Number: 6926 Publisher: Nature Publishing Group. `doi:10.1038/nature01371`.

[133] J. Barnes, B. Carver, J. M. Fraser, G. Gagliardi, H.-P. Loock, Z. Tian, M. W. B. Wilson, S. Yam, and O. Yastrubshak. Loss determination in microsphere resonators by phase-shift cavity ring-down measurements. *Optics Express*, 16(17):13158–13167, August 2008. Publisher: Optica Publishing Group. `doi:10.1364/OE.16.013158`.

[134] Gianluca Gagliardi and Hans-Peter Loock, editors. *Cavity-Enhanced Spectroscopy and Sensing*, volume 179 of *Springer Series in Optical Sciences*. Springer, Berlin, Heidelberg, 2014. `doi:10.1007/978-3-642-40003-2`.

[135] Dean G. Duffy. *Green's Functions with Applications*. Chapman and Hall/CRC, New York, 2 edition, March 2015. `doi:10.1201/9781315371412`.

[136] MATLAB®. URL: `https://www.mathworks.com/`.

[137] J. P. Hohimer, G. A. Vawter, and D. C. Craft. Unidirectional operation in a semiconductor ring diode laser. *Applied Physics Letters*, 62(11):1185–1187, March 1993. Number: 11. `doi:10.1063/1.108728`.

[138] Yuan Shi, M. Sejka, and O. Poulsen. A unidirectional Er/sup 3+/-doped fiber ring laser without isolator. *IEEE Photonics Technology Letters*, 7(3):290–292, March 1995. Conference Name: IEEE Photonics Technology Letters. `doi:10.1109/68.372749`.

[139] Svyatoslav Kharitonov and Camille-Sophie Brès. Isolator-free unidirectional thulium-doped fiber laser. *Light: Science & Applications*, 4(10):e340–e340, October 2015. Number: 10. `doi:10.1038/lsa.2015.113`.

[140] Wesley D. Sacher, Michael L. Davenport, Martijn J. R. Heck, Jared C. Mikkelsen, Joyce K. S. Poon, and John E. Bowers. Unidirectional hybrid silicon ring laser with an intracavity S-bend. *Optics Express*, 23(20):26369–26376, October 2015. Publisher: Optica Publishing Group. `doi:10.1364/OE.23.026369`.

[141] R. Franchi, A. Muñoz de las Heras, S. Biasi, M. Ghulinyan, I. Carusotto, and L. Pavesi. Role of the bus waveguide in the nonlinear reciprocity breaking in a Taiji microresonator. In *2021 Conference on Lasers and Electro-Optics Europe and European Quantum Electronics Conference (2021), paper ec_6_3*, page ec_6_3. Optica Publishing Group, June 2021. URL: `https://opg.optica.org/abstract.cfm?uri=EQEC-2021-ec_6_3`.

[142] Yuzhou G. N. Liu, Omid Hemmatyar, Absar U. Hassan, Pawel S. Jung, Jae-Hyuck Choi, Demetrios N. Christodoulides, and Mercedeh Khajavikhan. Engineering interaction dynamics in active resonant photonic structures. *APL Photonics*, 6(5):050804, May 2021. Number: 5. `doi:10.1063/5.0045228`.

[143] Huibo Fan, Hongwei Fan, and Huili Fan. Multiple Fano resonance refractive index sensor based on a plasmonic metal-insulator-metal based Taiji resonator. *JOSA B*, 39(1):32–39, January 2022. Publisher: Optica Publishing Group. `doi:10.1364/JOSAB.441882`.

[144] Jan Wiersig. Review of exceptional point-based sensors. *Photonics Research*, 8(9):1457, September 2020. Number: 9. `doi:10.1364/PRJ.396115`.

[145] William E. Hayenga, Midya Parto, Jinhan Ren, Fan O. Wu, Mohammad P. Hokmabadi, Christian Wolff, Ramy El-Ganainy, N. Asger Mortensen, Demetrios N. Christodoulides, and Mercedeh Khajavikhan. Direct Generation of Tunable Orbital Angular Momentum Beams in Microring Lasers with Broadband Exceptional Points. *ACS Photonics*, 6(8):1895–1901, August 2019. Publisher: American Chemical Society. `doi:10.1021/acsphotonics.9b00779`.

[146] Jan Wiersig, Alexander Eberspächer, Jeong-Bo Shim, Jung-Wan Ryu, Susumu Shinohara, Martina Hentschel, and Henning Schomerus. Nonorthogonal pairs of copropagating optical modes in deformed microdisk cavities. *Physical Review A*, 84(2):023845, August 2011. Publisher: American Physical Society. `doi:10.1103/PhysRevA.84.023845`.

[147] William B. Ribbens. An Optical Circulator. *Applied Optics*, 4(8):1037–1038, August 1965. Publisher: Optica Publishing Group. `doi:10.1364/AO.4.001037`.

[148] Dirk Jalas, Alexander Petrov, Manfred Eich, Wolfgang Freude, Shanhui Fan, Zongfu Yu, Roel Baets, Miloš Popović, Andrea Melloni, John D. Joannopoulos, Mathias Vanwolleghem, Christopher R. Doerr, and Hagen Renner. What is — and what is not — an optical isolator. *Nature Photonics*, 7(8):579–582, August 2013. Number: 8 Publisher: Nature Publishing Group. `doi:10.1038/nphoton.2013.185`.

[149] D.A.B. Miller. Rationale and challenges for optical interconnects to electronic chips. *Proceedings of the IEEE*, 88(6):728–749, June 2000. Conference Name: Proceedings of the IEEE. `doi:10.1109/5.867687`.

[150] Ivan P. Kaminow. Optical Integrated Circuits: A Personal Perspective. *Journal of Lightwave Technology*, 26(9):994–1004, May 2008. Conference Name: Journal of Lightwave Technology. `doi:10.1109/JLT.2008.922149`.

[151] Radhakrishnan Nagarajan, Masaki Kato, Jacco Pleumeekers, Peter Evans, Scott Corzine, Sheila Hurtt, Andrew Dentai, Sanjeev Murthy, Mark Missey, Ranjani Muthiah, Randal A. Salvatore, Charles Joyner, Richard Schneider, Mehrdad Ziari, Fred Kish, and David Welch. InP Photonic Integrated Circuits. *IEEE Journal of Selected Topics in Quantum Electronics*, 16(5):1113–1125, September 2010. Conference Name: IEEE Journal of Selected Topics in Quantum Electronics. `doi:10.1109/JSTQE.2009.2037828`.

[152] Li Fan, Jian Wang, Leo T. Varghese, Hao Shen, Ben Niu, Yi Xuan, Andrew M. Weiner, and Minghao Qi. An All-Silicon Passive Optical Diode. *Science*, 335(6067):447–450, January 2012. Publisher: American Association for the Advancement of Science. `doi:10.1126/science.1214383`.

[153] Ang Li and Wim Bogaerts. Reconfigurable nonlinear nonreciprocal transmission in a silicon photonic integrated circuit. *Optica*, 7(1):7, January 2020. Number: 1. `doi:10.1364/OPTICA.7.000007`.

[154] Parinaz Aleahmad, Mercedeh Khajavikhan, Demetrios Christodoulides, and Patrick LiKamWa. Integrated multi-port circulators for unidirectional optical information transport. *Scientific Reports*, 7(1):2129, May 2017. Number: 1 Publisher: Nature Publishing Group. `doi:10.1038/s41598-017-02340-9`.

[155] Long Chang, Xiaoshun Jiang, Shiyue Hua, Chao Yang, Jianming Wen, Liang Jiang, Guanyu Li, Guanzhong Wang, and Min Xiao. Parity–time symmetry and

variable optical isolation in active–passive-coupled microresonators. *Nature Photonics*, 8(7):524–529, July 2014. Number: 7 Publisher: Nature Publishing Group. `doi:10.1038/nphoton.2014.133`.

[156] Leonardo Del Bino, Jonathan M. Silver, Sarah L. Stebbings, and Pascal Del'Haye. Symmetry Breaking of Counter-Propagating Light in a Nonlinear Resonator. *Scientific Reports*, 7(1):43142, February 2017. Number: 1 Publisher: Nature Publishing Group. `doi:10.1038/srep43142`.

[157] Leonardo Del Bino, Jonathan M. Silver, Michael T. M. Woodley, Sarah L. Stebbings, Xin Zhao, and Pascal Del'Haye. Microresonator isolators and circulators based on the intrinsic nonreciprocity of the Kerr effect. *Optica*, 5(3):279–282, March 2018. Publisher: Optica Publishing Group. `doi:10.1364/OPTICA.5.000279`.

[158] Claudio Castellan, Riccardo Franchi, Stefano Biasi, Martino Bernard, Mher Ghulinyan, and Lorenzo Pavesi. Field-Induced Nonlinearities in Silicon Waveguides Embedded in Lateral p-n Junctions. *Frontiers in Physics*, 7:104, July 2019. `doi:10.3389/fphy.2019.00104`.

[159] Stefano Biasi, Riccardo Franchi, Davide Bazzanella, and Lorenzo Pavesi. On the effect of the thermal cross-talk in a photonic feed-forward neural network based on silicon microresonators. *Frontiers in Physics*, 10, 2022. `doi:10.3389/fphy.2022.1093191`.

[160] J. Leuthold, C. Koos, and W. Freude. Nonlinear silicon photonics. *Nature Photonics*, 4(8):535–544, August 2010. Number: 8. `doi:10.1038/nphoton.2010.185`.

[161] John Kerr. XL. A new relation between electricity and light: Dielectrified media birefringent. *The London, Edinburgh, and Dublin Philosophical Magazine and Journal of Science*, 50(332):337–348, November 1875. Publisher: Taylor & Francis. `doi:10.1080/14786447508641302`.

[162] John Kerr. LIV. A new relation between electricity and light: Dielectrified media birefringent (Second paper). *The London, Edinburgh, and Dublin Philosophical Magazine and Journal of Science*, 50(333):446–458, December 1875. Publisher: Taylor & Francis. `doi:10.1080/14786447508641319`.

[163] F. Ramiro-Manzano, N. Prtljaga, L. Pavesi, G. Pucker, and M. Ghulinyan. Thermo-optical bistability with Si nanocrystals in a whispering gallery mode resonator. *Optics Letters*, 38(18):3562, September 2013. `doi:10.1364/OL.38.003562`.

[164] Tal Carmon, Lan Yang, and Kerry J Vahala. Dynamical thermal behavior and thermal selfstability of microcavities. page 9, 2004.

[165] V. S. Il'chenko and M. L. Gorodetskii. Thermal Nonlinear Effects in Optical Whispering Gallery Microresonators. *Laser Physics*, 1992. URL: `https://www.semanticscholar.org/paper/Thermal-Nonlinear-Effects-in-Optical-Whispering-Il%27chenko-Gorodetskii/0dc6fa8823bb6029cbffe8586d09e437a8f93cf2`.

[166] C. Schmidt, A. Chipouline, T. Pertsch, A. Tünnermann, O. Egorov, F. Lederer, and L. Deych. Nonlinear thermal effects in optical microspheres at different wavelength sweeping speeds. *Optics Express*, 16(9):6285–6301, April 2008. Publisher: Optica Publishing Group. `doi:10.1364/OE.16.006285`.

[167] Alberto Muñoz de las Heras. *Non-Hermitian and Topological Features of Photonic Systems*. PhD thesis. URL: `https://iris.unitn.it/retrieve/e3835199-7027-72ef-e053-3705fe0ad821/MunozDeLasHerasPhD_A.pdf`.

[168] J.k. Doylend and A.p. Knights. The evolution of silicon photonics as an enabling technology for optical interconnection. *Laser & Photonics Reviews*, 6(4):504–525, 2012. _eprint: https://onlinelibrary.wiley.com/doi/pdf/10.1002/lpor.201100023. `doi:10.1002/lpor.201100023`.

[169] Arnab Dewanjee, Jan Niklas Caspers, James Stewart Aitchison, and Mo Mojahedi. Demonstration of a compact bilayer inverse taper coupler for Si-photonics with enhanced polarization insensitivity. *Optics Express*, 24(25):28194–28203, December 2016. `doi:10.1364/OE.24.028194`.

[170] Assia Barkai, Ansheng Liu, Daewoong Kim, Rami Cohen, Nomi Elek, Hsu-Hao Chang, Bilal H. Malik, Rami Gabay, Richard Jones, Mario Paniccia, and Nahum Izhaky. Double-Stage Taper for Coupling Between SOI Waveguides and Single-Mode Fiber. *Journal of Lightwave Technology*, 26(24):3860–3865, December 2008. Conference Name: Journal of Lightwave Technology. `doi:10.1109/JLT.2008.928199`.

[171] Guillaume Maire, Laurent Vivien, Guillaume Sattler, Andrzej Kazmierczak, Benito Sanchez, Kristinn B. Gylfason, Amadeu Griol, Delphine Marris-Morini, Eric Cassan, Domenico Giannone, Hans Sohlström, and Daniel Hill. High efficiency silicon nitride surface grating couplers. *Optics Express*, 16(1):328, 2008. `doi:10.1364/OE.16.000328`.

[172] Matteo Cherchi, Sami Ylinen, Mikko Harjanne, Markku Kapulainen, and Timo Aalto. Dramatic size reduction of waveguide bends on a micron-scale silicon photonic platform. *Optics Express*, 21(15):17814–17823, July 2013. Publisher: Optica Publishing Group. `doi:10.1364/OE.21.017814`.

[173] H. G. Unger. Normal mode bends for circular electric waves. *The Bell System Technical Journal*, 36(5):1292–1307, September 1957. Conference Name: The Bell System Technical Journal. `doi:10.1002/j.1538-7305.1957.tb01509.x`.

[174] Guoliang Li, Jin Yao, Hiren Thacker, Attila Mekis, Xuezhe Zheng, Ivan Shubin, Ying Luo, Jin-hyoung Lee, Kannan Raj, John E. Cunningham, and Ashok V. Krishnamoorthy. Ultralow-loss, high-density SOI optical waveguide routing for macrochip interconnects. *Optics Express*, 20(11):12035–12039, May 2012. Publisher: Optica Publishing Group. `doi:10.1364/OE.20.012035`.

[175] Mohammad Reza Bonyadi and Zbigniew Michalewicz. Particle Swarm Optimization for Single Objective Continuous Space Problems: A Review. *Evolutionary Computation*, 25(1):1–54, March 2017. `doi:10.1162/EVCO_r_00180`.

[176] J. Kennedy and R. Eberhart. Particle swarm optimization. In *Proceedings of ICNN'95 - International Conference on Neural Networks*, volume 4, pages 1942–1948 vol.4, November 1995. `doi:10.1109/ICNN.1995.488968`.

[177] J. Kennedy. The particle swarm: social adaptation of knowledge. In *Proceedings of 1997 IEEE International Conference on Evolutionary Computation (ICEC '97)*, pages 303–308, April 1997. `doi:10.1109/ICEC.1997.592326`.

[178] Y. Shi and R. Eberhart. A modified particle swarm optimizer. In *1998 IEEE International Conference on Evolutionary Computation Proceedings. IEEE World Congress on Computational Intelligence (Cat. No.98TH8360)*, pages 69–73, May 1998. `doi:10.1109/ICEC.1998.699146`.

[179] T. Gao, E. Estrecho, K. Y. Bliokh, T. C. H. Liew, M. D. Fraser, S. Brodbeck, M. Kamp, C. Schneider, S. Höfling, Y. Yamamoto, F. Nori, Y. S. Kivshar, A. G.

Truscott, R. G. Dall, and E. A. Ostrovskaya. Observation of non-Hermitian degeneracies in a chaotic exciton-polariton billiard. *Nature*, 526(7574):554–558, October 2015. Number: 7574 Publisher: Nature Publishing Group. `doi:10.1038/nature15522`.

[180] Raam Uzdin, Alexei Mailybaev, and Nimrod Moiseyev. On the observability and asymmetry of adiabatic state flips generated by exceptional points. *Journal of Physics A: Mathematical and Theoretical*, 44(43):435302, October 2011. Publisher: IOP Publishing. `doi:10.1088/1751-8113/44/43/435302`.

[181] M. V. Berry and R. Uzdin. Slow non-Hermitian cycling: exact solutions and the Stokes phenomenon. *Journal of Physics A: Mathematical and Theoretical*, 44(43):435303, October 2011. Publisher: IOP Publishing. `doi:10.1088/1751-8113/44/43/435303`.

[182] Thomas J. Milburn, Jörg Doppler, Catherine A. Holmes, Stefano Portolan, Stefan Rotter, and Peter Rabl. General description of quasiadiabatic dynamical phenomena near exceptional points. *Physical Review A*, 92(5):052124, November 2015. Publisher: American Physical Society. `doi:10.1103/PhysRevA.92.052124`.

[183] S. N. Ghosh and Y. D. Chong. Exceptional points and asymmetric mode conversion in quasi-guided dual-mode optical waveguides. *Scientific Reports*, 6(1):19837, April 2016. Number: 1 Publisher: Nature Publishing Group. `doi:10.1038/srep19837`.

[184] Youngsun Choi, Choloong Hahn, Jae Woong Yoon, Seok Ho Song, and Pierre Berini. Extremely broadband, on-chip optical nonreciprocity enabled by mimicking nonlinear anti-adiabatic quantum jumps near exceptional points. *Nature Communications*, 8(1):14154, January 2017. Number: 1 Publisher: Nature Publishing Group. `doi:10.1038/ncomms14154`.

[185] Absar U. Hassan, Bo Zhen, Marin Soljačić, Mercedeh Khajavikhan, and Demetrios N. Christodoulides. Dynamically Encircling Exceptional Points: Exact Evolution and Polarization State Conversion. *Physical Review Letters*, 118(9):093002, March 2017. Publisher: American Physical Society. `doi:10.1103/PhysRevLett.118.093002`.

[186] William R. Sweeney, Chia Wei Hsu, Stefan Rotter, and A. Douglas Stone. Perfectly Absorbing Exceptional Points and Chiral Absorbers. *Physical Review*

Letters, 122(9):093901, March 2019. Publisher: American Physical Society. `doi:10.1103/PhysRevLett.122.093901`.

[187] Tomoki Ozawa, Hannah M. Price, Alberto Amo, Nathan Goldman, Mohammad Hafezi, Ling Lu, Mikael C. Rechtsman, David Schuster, Jonathan Simon, Oded Zilberberg, and Iacopo Carusotto. Topological photonics. *Reviews of Modern Physics*, 91(1):015006, March 2019. Publisher: American Physical Society. `doi:10.1103/RevModPhys.91.015006`.

[188] Gal Harari, Miguel A. Bandres, Yaakov Lumer, Mikael C. Rechtsman, Y. D. Chong, Mercedeh Khajavikhan, Demetrios N. Christodoulides, and Mordechai Segev. Topological insulator laser: Theory. *Science*, 359(6381):eaar4003, March 2018. Number: 6381. `doi:10.1126/science.aar4003`.

[189] Douglas R. Hofstadter. Energy levels and wave functions of Bloch electrons in rational and irrational magnetic fields. *Physical Review B*, 14(6):2239–2249, September 1976. Publisher: American Physical Society. `doi:10.1103/PhysRevB.14.2239`.

[190] Dieter Langbein. The Tight-Binding and the Nearly-Free-Electron Approach to Lattice Electrons in External Magnetic Fields. *Physical Review*, 180(3):633–648, April 1969. Publisher: American Physical Society. `doi:10.1103/PhysRev.180.633`.

[191] Riccardo Franchi, Claudio Castellan, Mher Ghulinyan, and Lorenzo Pavesi. Second-harmonic generation in periodically poled silicon waveguides with lateral p-i-n junctions. *Optics Letters*, 45(12):3188, June 2020. Number: 12. `doi:10.1364/OL.391988`.

[192] Stefano Biasi, Riccardo Franchi, Lorenzo Cerini, and Lorenzo Pavesi. An array of microresonators as a Photonic Extreme Learning Machine. *Under peer review in APL Photonics*, May 2023. arXiv:2305.03066 [physics]. `doi:10.48550/arXiv.2305.03066`.

[193] Riccardo Franchi, Chiara Vecchi, Mher Ghulinyan, and Lorenzo Pavesi. Electric Field Induced Second Harmonic Generation In Silicon Waveguides: the role of the disorder. In *2021 Conference on Lasers and Electro-Optics Europe & European Quantum Electronics Conference (CLEO/Europe-EQEC)*, pages 1–1, Munich, Germany, June 2021. IEEE. `doi:10.1109/CLEO/Europe-EQEC52157.2021.9541919`.

[194] Ronald Broeke and Xaveer Leijtens. Nazca design, photonic IC design framework. URL: `https://nazca-design.org/`.

[195] Marco Masi, Mattia Mancinelli, Paolo Bettotti, and Lorenzo Pavesi. Light Combining for Interferometric Switching. *International Journal of Optics*, 2012:e130517, June 2012. Publisher: Hindawi. `doi:10.1155/2012/130517`.

[196] Guang-Bin Huang, Qin-Yu Zhu, and Chee-Kheong Siew. Extreme learning machine: Theory and applications. *Neurocomputing*, 70(1):489–501, December 2006. `doi:10.1016/j.neucom.2005.12.126`.

[197] R. A. Fisher. The Use of Multiple Measurements in Taxonomic Problems. *Annals of Eugenics*, 7(2):179–188, 1936. _eprint: https://onlinelibrary.wiley.com/doi/pdf/10.1111/j.1469-1809.1936.tb02137.x. `doi:10.1111/j.1469-1809.1936.tb02137.x`.

[198] R. A. Fisher. Iris Data Set. URL: `https://archive.ics.uci.edu/ml/datasets/Iris`.

[199] COMSOL Multiphysics®. URL: `www.comsol.com`.

[200] Raymond C. Rumpf. Coupled Mode Theory, January 2020. URL: `https://empossible.net/wp-content/uploads/2020/01/Lecture-Coupled-Mode-Theory.pdf`.

[201] 21st Century Electromagnetics. URL: `https://empossible.net/academics/emp6303/`.

[202] Wei-Ping Huang. Coupled-mode theory for optical waveguides: an overview. *JOSA A*, 11(3):963–983, March 1994. Publisher: Optica Publishing Group. `doi:10.1364/JOSAA.11.000963`.

[203] A. Yariv. Coupled-mode theory for guided-wave optics. *IEEE Journal of Quantum Electronics*, 9(9):919–933, September 1973. `doi:10.1109/JQE.1973.1077767`.

[204] E. Marcatili. Improved coupled-mode equations for dielectric guides. *IEEE Journal of Quantum Electronics*, 22(6):988–993, June 1986. Conference Name: IEEE Journal of Quantum Electronics. `doi:10.1109/JQE.1986.1073042`.

[205] R. R. A. Syms. Improved coupled-mode theory for codirectionally and contradirectionally coupled waveguide arrays. *JOSA A*, 8(7):1062–1069, July 1991. Publisher: Optica Publishing Group. `doi:10.1364/JOSAA.8.001062`.

[206] Ary Syahriar, Helmi Adam, Dwi Astharini, Ahmad Husin Lubis, and Danny M. Gandana. Analysis of three paralel waveguides using coupled mode theory and the method of lines. In *2016 International Seminar on Application for Technology of Information and Communication (ISemantic)*, pages 174–178, Semarang, Indonesia, August 2016. IEEE. `doi:10.1109/ISEMANTIC.2016.7873833`.

[207] P Ganguly, J.C Biswas, S Das, and S.K Lahiri. A three-waveguide polarization independent power splitter on lithium niobate substrate. *Optics Communications*, 168(5-6):349–354, September 1999. Number: 5-6. `doi:10.1016/S0030-4018(99)00368-5`.

[208] Chang-Min Kim and Young-Joon Im. Switching operations of three-waveguide optical switches. *IEEE Journal of Selected Topics in Quantum Electronics*, 6(1):170–174, January 2000. Number: 1 Conference Name: IEEE Journal of Selected Topics in Quantum Electronics. `doi:10.1109/2944.826885`.

[209] H. Ogiwara and H. Yamamoto. Optical waveguide switch (3×3) for an optical switching system. *Applied Optics*, 17(8):1182–1186, April 1978. Publisher: Optica Publishing Group. `doi:10.1364/AO.17.001182`.

[210] Haruo Ogiwara. Optical waveguide 3X3 switch: theory of tuning and control. *Applied Optics*, 18(4):6, February 1979.